A Thesis entitled

" The Physics and Instrumental Development

of

Inelastic Electron Tunnelling Spectroscopy."

by Robert Nayler.

Submitted for the degree of

Doctor of Philosophy

at

The Department of Chemistry,

The City University, London.

September, 1982

Contents

LIST OF DIAGRAMS

(S indicates a spectrum)

LIST OF TABLES

LIST OF PHOTOGRAPHS

1. General view of the vacuum system and power supply.
2. Close-up of sample preparation chamber.
3. View of tunnel junction soldered to the probe assembly.
4. General view of the computerised spectrometer.
5. T.E.M. aluminium electrode: thin region, (No. 83,80kV) a final magnification X 12,000.
6. T.E.M. aluminium electrode: medium thickness region (No. 87,80kV) x 12,000.
7. T.E.M. aluminium electrode: thickest region (No. 84,80kV) x 12,000.
8. E.D. aluminium electrode, Specimen untilted (No.143,80kV) L20.
9. E.D. aluminium electrode. Specimen tilted 25°(No.85,80kV) L.20
10. E.D. aluminium electrode. Specimen tilted 35.26° (No.142 80kV) L20.
11. R.E.D. aluminium electrode No. 151, 60kV).
12. T.E.M. lead electrode thinnest region (No. 88, 80kV) x 12,00
13. T.E.M. lead electrode thicker region (No.141, 80kV) x 12,00
14. T.E.M. lead electrode thick region (No. 91, 80kV) x 12,00
15. T.E.M. lead electrode showing pores in thinnest continuous region (No. 140, 80kV) x 12,000.
16. T.E.M. lead electrode showing pores in thicker region (No. 90, 80kV) x 12,000.
17. S.E.M. of aluminium electrode on p.c.b. substrate (No. 156, 80kV) x 12,000.
18. S.E.M. of aluminium electrode on silica substrate (No. 158, 80kV) x 12,000.
19. S.E.M. of lead electrode on p.c.b. substrate (No. 157, 80kV) x 12,000.
20. S.E.M. of printed circuit board substrate (Nos. 3 & 4, 80kV) x 10,000.
21. Translucent lead electrode x 10.

Notes:
- T.E.M. Transmission Electron Micrograph
- E.D. Electron Diffraction
- R.E.D. Reflection Electron Diffraction
- S.E.M. Scanning Electron Micrograph

ACKNOWLEDGEMENTS

I would like to thank the following people whose help and co-operation has been essential to this work:

[redacted] for his excellent technical help and advice concerning the vacuum system and the spectrometer;

[redacted], Pye-Unicam of Cambridge and the S.E.R.C. for providing a C.A.S.E. award studentship :

[redacted] for allowing me to use the transmission electron microscope and for help with the reflection electron diffraction experiment;

The Physics Department for loan of their liquid helium dewars and transfer equipment;

[redacted] and the Marconi Research photographic section for producing the photographs;

[redacted] for designing and building the computerised spectrometer, and then leaving without drawing a circuit diagram for it;

[redacted] the Senior Programming Adviser of the computer unit, University College of Wales, Aberystwyth, for building and modifying the Pet/Honeywell interface;

The Computer Unit at The City University, and in particular [redacted] and [redacted] for allowing me to interface the microprocessor with the University's Honeywell computer;

[redacted] and [redacted] for typing the manuscript.

I would also especially like to thank [redacted] of the Department of Mathematics for allowing me to attend his

series of lectures on Quantum Mechanics, and for the many enthusiastic discussions and tutorials.

Finally, I would like to give my sincerest thanks to my Supervisor - Mr. Brian O. Field whose untiring enthusiasm and willingness to listen to new ideas has provided the inspiration for this work.

ABSTRACT

A new doping technique called Electrode Penetration Doping has been developed in order to produce inelastic electron tunnelling spectra of volatile solvents such as benzene which previously had proved impossible to dope by other methods. An investigation into the doping mechanism revealed a large number of pores in the upper (lead) electrode through which the organic molecules are thought to pass. Additionally, the same investigation revealed the rough surface nature of both the aluminium and lead electrodes as being due to the rough substrate used for tunnelling experiments. Using a model of the junction deduced from the above investigation, it has been possible to explain several previously unexplained phenomena such as boosting and instabilities.

A computerised spectrometer has been constructed in order to average several scans of one spectrum thus reducing random low frequency noise which cannot be removed by increasing the detector time constant. The microprocessor used for controlling the spectrometer is also able to store spectral data on minifloppy discs. The microprocessor has also been interfaced to the University's mainframe computer to allow larger spectral processing programmes to be implemented.

Finally, a new form of spectroscopy is proposed. A.S.E.T. (Anti-Stokes' Electron Tunnelling) spectroscopy has been devised in order to circumvent insulator breakdown problems occurring in normal inelastic electron tunnelling spectroscopy. The technique involves using a tunnel junction with a translucent upper electrode, selectively exciting the adsorbed species using a tuneable radiation source and then interacting tunnelling electrons with the excited species. The results presented are of a preliminary nature only, yet they do show that an effect is occurring and that a future investigation will prove worthwhile.

' To the ignorant, nothing is profound.'

Mervyn Peake.

CHAPTER 1. INTRODUCTION AND THEORY

1.1 INTRODUCTION

Inelastic Electron Tunnelling Spectroscopy (I.E.T.S.) is a new analytical technique which uses tunnelling electrons to probe the vibrational structure of molecules adsorbed on a thin insulating oxide barrier.

The concept of electron tunnelling is well known and has its origins in basic quantum mechanics, the phenomenon has been studied most extensively over the past twenty-five years by physicists mainly in connection with solid-state physics and superconductivity (1, 2, 3, 4, 5, 6), the commonest example of electron tunnelling is that of the tunnel diode developed by Leo Esaki in 1957 (3).

However, it was not until 1966 when Jaklevic and Lambe (7) utilized the phenomena to study the vibrational spectra of molecules. Their discovery of I.E.T.S. was quite accidental. Hoping to observe band structure effects due to metal electrodes, they instead noticed that the conductance of a metal-insulator-metal junction changed very slightly at voltages characteristic of molecular vibrations and they surmised that the tunnelling electrons were interacting with the vibrational states of the molecules trapped on the insulator.

The idea is a simple one and the experimental procedures for producing the tunnel junctions and detecting the

minute changes in conductance are relatively straightforward. First, a metal electrode (usually aluminium) about one millimeter wide and 2000 Angstroms thick is vacuum deposited on a clean silica or pyrex microscope slide. The electrode surface is then carefully oxidised to a thickness somewhere between 25 to 30 Angstroms to form an insulating layer. The oxide is then "doped" with a small amount of chemical sample, usually in the form of a vapour or a liquid, and a top electrode (usually lead) is vacuum deposited across the oxide to complete the junction. (Figure 1.1.1). Electron tunnelling is achieved by applying a small d.c. bias voltage (typically 0-500 mV) across the oxide barrier. The current-voltage characteristic of the junction, i.e. its conductance, is not perfectly linear, but shows some small changes in slope which arise from the tunnelling electrons interacting with the dopant molecules adsorbed on the oxide layer. When the d.c. voltage, V, is applied to the junction, electrons tunnel from one electrode through the insulator (which they experience as a potential barrier) and into the second electrode. Usually the electrons tunnel through without energy loss and the process is termed Elastic Tunnelling. However, at certain bias voltages, when the tunnelling electron has the same energy as a vibrational mode in a molecule trapped in the barrier, then some (approximately 1%) of the electrons on tunnelling through the barrier interact with the vibrational states

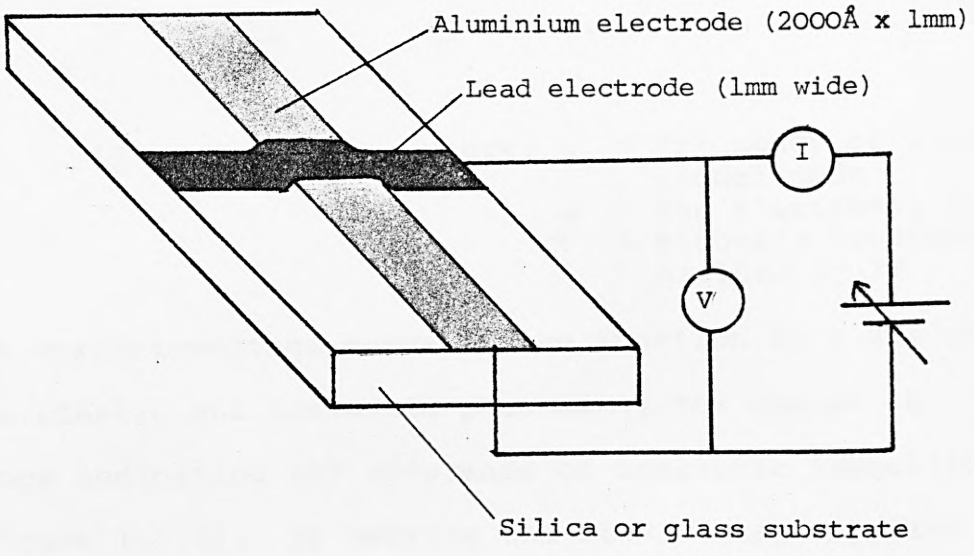

Figure 1.1.1. A typical tunnel junction.

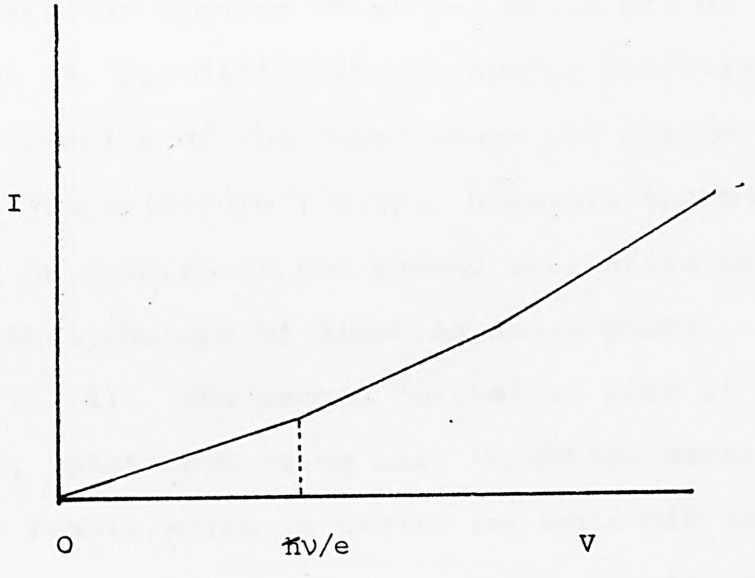

Figure 1.1.2. Schematic current-voltage curve of a tunnel junction.

of the trapped molecules and loose energy as they do so. This process is termed Inelastic Electron Tunnelling. The voltage, V, at which an inelastic interaction occurs is given by:

(1.1)

$$V = \frac{\hbar \omega_o}{e}$$

where: ω_o = frequency of vibrational mode
e = the electronic charge
$\hbar$ = Planck's constant divided by 2Π

The current-voltage curve of the junction is a sum of the elastic and inelastic phenomena, the change in slope indicating the occurence of inelastic tunnelling (Figure 1.1.2). By varying the bias voltage applied to the junction, an energy range is effectively scanned, producting a spectrum of interaction verses energy. Since the current-voltage curve is only very weakly non-linear, the changes of slope, which are of the order of 0.5 to 1%, are difficult to observe directly. The first derivative of the curve shows the changes of slope as jumps (Figure 1.1.3). However, the most useful quantity to observe is the second derivative which shows the original changes of slope as sharp peaks . (Figure 1.1.4). The second derivative plot of d^2I/dV^2 verses V, apart from being easy to obtain experimentally, yields a result which is easily recognisable as a spectrum of intensity verses energy. Practically speaking, nearly all inelastic electron tunnelling spectra are displayed in this form.

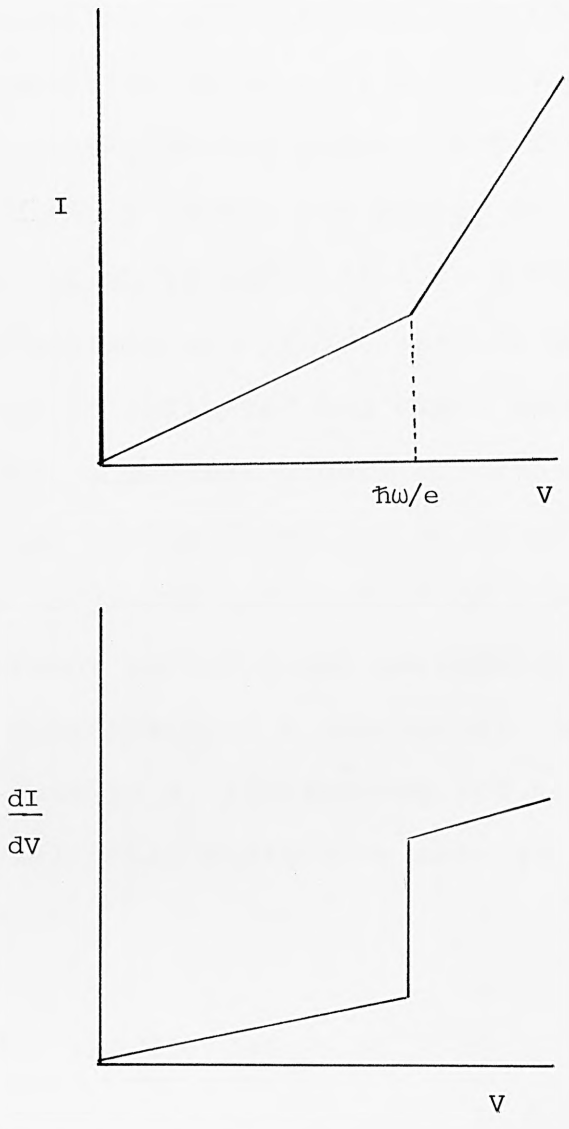

Figure 1.1.3.

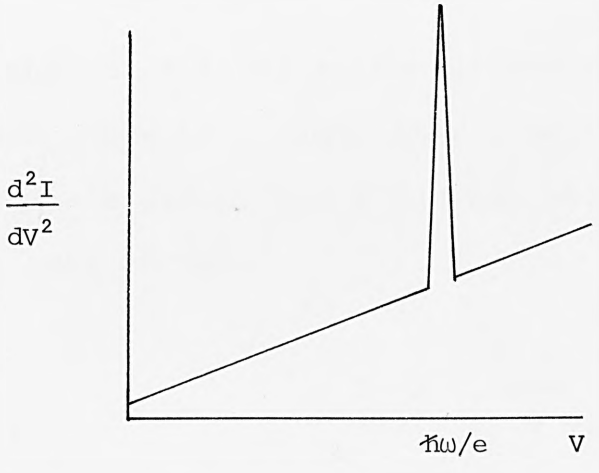

Figure 1.1.4.

The current-voltage measurements have to be performed at low temperatures (typically 4.2 kelvin and lower) to give acceptably narrow peaks. I.E.T.S. with the present technology covers the energy range 0-16,000 wavenumbers (which is equivalent to a bias voltage from zero to two volts), and yields spectra which are similar in appearance to infra-red and Raman spectra. However, the technique is several orders of magnitude more sensitive than either infra-red or Raman spectroscopy, and because it yields information on adsorbed molecules it has important applications particularly in the fields of surface spectroscopy, biochemistry, adhesion, corrosion, catalysis, lubrication and most other branches of interfacial solid-state chemistry (8,9,10,11,12).

1.2 THEORETICAL PRINCIPLES

1.2.1 The Schrödinger Wave Equation

> "By this time I had solved Schrödinger's equation enough times to believe that electrons sometimes behave as waves, and I did not worry much about that part anymore".
>
> Ivor Giaever 1959
> (Reference 6)

Quantum mechanical tunnelling, or the passing of a particle through a classically forbidden region of negative kinetic energy, from one allowed region to another, was one of the first major successes of Schrödinger's wave equation (13). One of the original applications of particle tunnelling was by Oppenheimer (14) who applied it to the ionization of hydrogen in the presence of an external electric field. In the same year Fowler and Nordheim (15) explained the phenomenon of electron emission from cold metals in the presence of large electric fields in terms of electron tunnelling.

Many other phenomena were also explained successfully by tunnelling, for example in 1928 Gammow (16) and Gurney & Condon (17) treated alpha decay as a tunnelling process. In 1930 Frenkel (18) accounted for the current flow between two metal electrodes separated by a vacuum. Sommerfield and Bethé (19) subsequently extended Frenkel's calculations to metal-insulator-metal systems.

Up until the early 1960's almost all tunnelling experiments were performed using either pressed bi-metallic contacts (20, 21) with insulating material or semiconductor powder sandwiched in between them (22), or deposited insulator films (23, 24). Unfortunately, the results obtained were far from reproducible and varied from one laboratory to another. In 1961, Fisher

and Giaever (25) reported that thermal oxidation of metals gave relatively uniform thin oxide barriers. This discovery constituted perhaps one of the greatest technological advances in tunnelling physics: since it was possible to obtain reproducible results from tunnelling experiments.

To show how particle tunnelling arises as a consequence of quantum mechanics, a simple stationary state solution to Schrödinger's wave equation is outlined. Although the stationary state solution is suitable for providing an insight into what happens when a particle (in this case an electron) encounters a potential barrier, it is not strictly adequate for describing the actual motion of a single particle, since we are considering plane waves with a well defined momentum. The results, therefore, do not contain information concerning the position of the particle as a function of time. In order to obtain a more accurate picture, it would be necessary to consider a wave packet of particles and obtain a solution to Schrödinger's time-dependent wave equation (26). However, at this stage, the stationary state solution will suffice.

Schrödinger's time-dependent wave equation for one dimension is:-

$$\left[-\frac{\hbar^2}{2m} \frac{d^2}{dx^2} + V(x) \right] \psi(x) = E\psi(x) \qquad (1.2\text{-}1)$$

where m is the mass of the particle

and $\hbar$ = Planck's constant divided by 2π

For a free electron in the absence of any potential field, V(x), the equation becomes:-

$$-\frac{\hbar^2}{2m} \frac{d^2\psi(x)}{dx^2} = E\psi(x) \qquad (1.2\text{-}2)$$

i.e. writing:-

$$\frac{d^2\psi(x)}{dx^2} + k^2\psi(x) = 0 \qquad (1.2\text{-}3)$$

where $k^2 = 2mE/\hbar^2$

and the electron momentum, p, thus $\hbar k$

The general solution to (1.2-3) is:-

$$\psi_{(x)} = Ae^{ikx} + Be^{-ikx} \qquad (1.2\text{-}4)$$

Thus, for one dimension the stationary wave solution for a free electron is a linear combination of e^{ikx} and e^{-ikx}; where electrons travelling in the +x direction are described by e^{ikx} and electrons travelling in the -x direction are described by e^{-ikx}.

1.2.2 The Potential Step

Now we examine the case of an electron moving in a region where there is a potential step, V, which is considered to be the limit as $\varepsilon \to o$ of the continuous curve in the interval $-\varepsilon$ to $+\varepsilon$ (Figure 1.2.1) and $V=0$ for $x<o$ (region I) and $V=Vo$ for $x>o$ (region II). Although such a step is physically unrealisable, it does yield results which give a good indication as to what really happens.

The classical behaviour of an electron arriving at the potential step from the $x = -\infty$ direction is straightfoward:-

(1) If the electron energy is greater than the height of the step (i.e. if $\frac{1}{2}mv^2 > Vo$) the electron will enter region II with a reduced velocity V', which can be calculated by applying conservation of momentum:-

$$\tfrac{1}{2}mv^2 = \tfrac{1}{2}mv'^2 + Vo$$

(2) If the energy of the electron is less than the height of the step, (i.e. if $\frac{1}{2}mv^2 < Vo$), then the electron will be reflected at $x = o$. It will not be able to pass from region I into region II as its energy would be negative, which is impossible; so region II is classically forbidden for $E<Vo$.

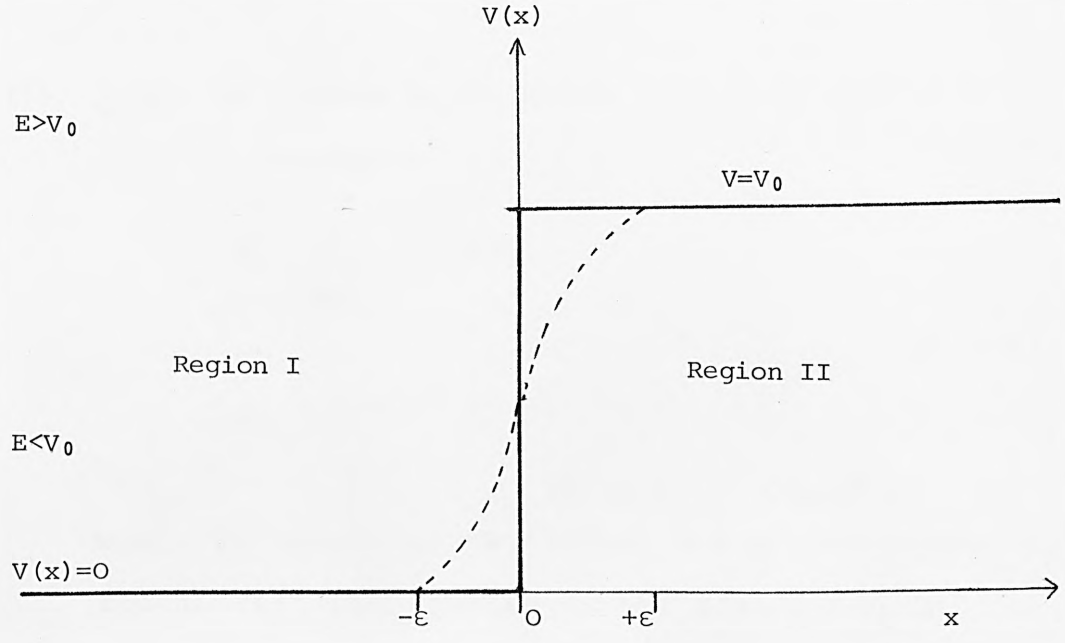

Figure 1.2.1. The Potential Step.

The quantum mechanical behaviour of the particle is, however, quite different. Again there are two cases, one where the electron energy is greater than the potential step (E>Vo) and one where the electron energy is less than the potential step (E<Vo).

(1) E>Vo: In region I, in which V(x) = 0, equation (1.2-2) becomes:-

$$-\frac{\hbar^2}{2m}\frac{d^2\psi_1}{dx^2} = E\psi_1$$

or

$$\frac{d^2\psi_1}{dx^2} + k^2\psi_1 = 0 \qquad (1.2\text{-}5)$$

where $k^2 = 2mE/\hbar^2$

which is identical to (1.2-2) for a free electron. Its general solution is of the form given in (1.2-4), i.e.

$$\psi_1(x) = Ae^{ikx} + Be^{-ikx} \qquad (1.2\text{-}6)$$

In region II, in which V(x) = Vo, Schrödinger's equation becomes:-

$$-\frac{h^2}{2m}\frac{d^2\psi_2}{dx^2} + V_0\psi_2 = E\psi_2$$

or

$$\frac{d^2\psi_2}{dx^2} + k'^2\psi_2 = 0 \qquad (1.2\text{-}7)$$

where $k'^2 = 2m(E-Vo)/\hbar^2$, and $p' = \hbar k'$ is the electron momentum in region II

In region II we will have only electrons travelling to the right and thus the correct solution to (1.2-7) is not of the form (1.2-4) but:

$$\psi_2(x) = Ce^{ik'x} \qquad (1.2\text{-}8)$$

Classically speaking, all the particles incident on the potential step with E>Vo pass into Region II. However, this is not the quantum mechanical picture. If the constants A, B and C in equations (1.2-6) and (1.2-8) are calculated it can be shown that B, which describes electrons travelling in the -X direction, is non-zero. This indicates that some of the electrons are reflected at x=o even though their energy is greater than the step height.

(2) E<Vo: In region I the Schrödinger's equation is the same as (1.2-5) and the solution is given by (1.2-6), where, as before, e^{ikx} represents an electron travelling the +x direction.

In region II where V(x)=Vo the Schrödinger equation is:

$$-\frac{\hbar^2}{2m}\frac{d^2\psi_2}{dx^2} + V_0\psi_2 = E\psi_2$$

or

$$\frac{d^2\psi_2}{dx^2} - \alpha^2\psi_2 = 0 \qquad (1.2\text{-}9)$$

where $\alpha = 2m(E-V_0)/\hbar^2$

The solution to (1.2-9) is again a linear combination of $e^{\alpha x}$ and $e^{-\alpha x}$, however, the increasing exponential term is not an acceptable solution as the amplitude of the wave must decrease in region II; therefore only the decreasing term is used.

$$\psi_2(x) = Ce^{-\alpha x} \qquad (1.2\text{-}10)$$

Since $\psi_2(x)$ is non-zero this implies that there is a finite probability of finding the electron in region II, this probability decreasing exponentially with x.

(The constants A, B and C can be determined by applying continuity conditions to the wave functions at x=o. In other words, the wave function must be continuous and change smoothly at x=o. This requires:

$$\psi_1(x) = \psi_2(x) \qquad \text{for } x=o$$

and $$d\psi_1/dx = d\psi_2/dx \qquad \text{for } x=o$$

1.2.3 The Potential Barrier

An ideal potential barrier is shown in Figure 1.2.2 and is defined by:-

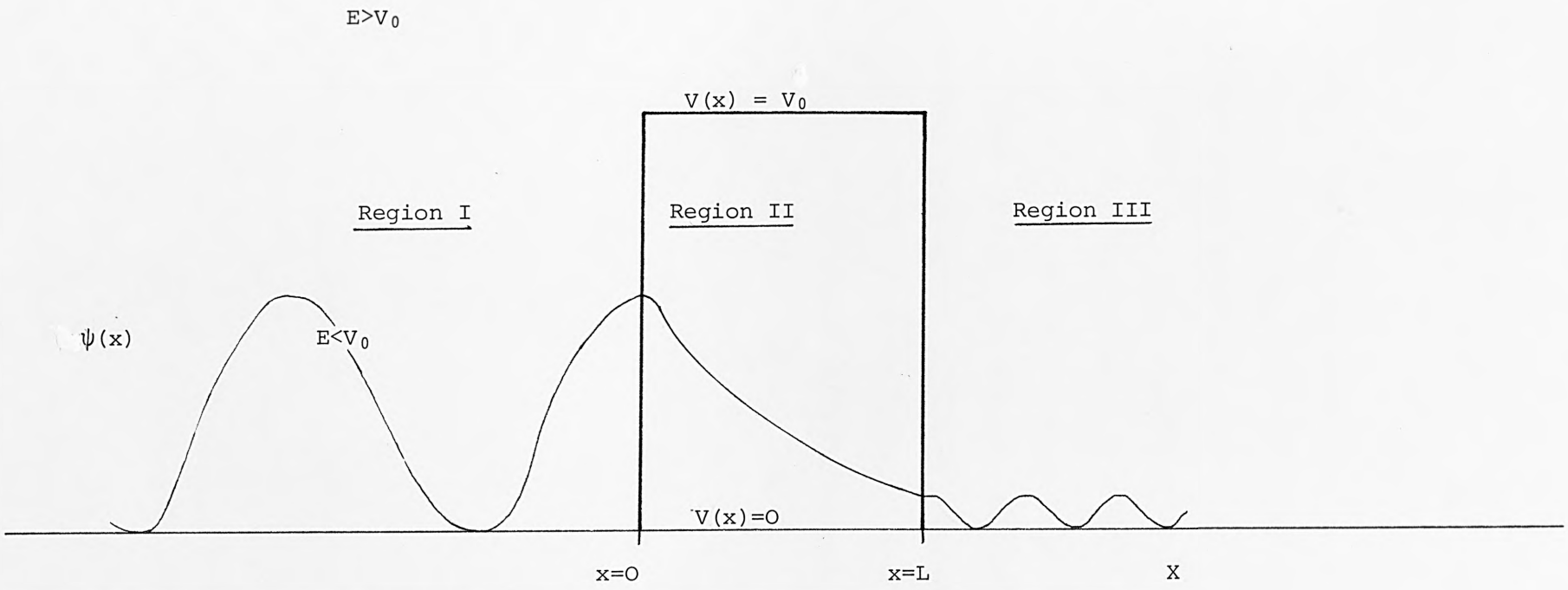

Figure 1.2.2. The rectangular potentialbarrier. The wavefunction incident from $x=-\infty$ is oscillatory only on regions I an III, and of an exponentialnature in region II.

V=0	x<o	region I
V=Vo	o<x<L	region II
V=0	x>L	region III

In classical mechanics an electron with energy less than Vo incident on the barrier at x=o will be reflected and never reach the far side. However, quantum mechanics tells us that the wave function of the electron incident on region II (the barrier) from region I is not zero, but decreases in an expotential manner. Thus, if the barrier is narrow enough (L small) the wave functions, although considerably diminished in amplitude, will be non-zero at x=L, and there will thus be a certain probability of finding the electron on the other side of the barrier in region III. This possibility of an electron penetrating through a classically forbidden region is known as the tunnelling effect.

1.3 The Tunnel Effect

Tunnelling behaviour can now be demonstrated in more practical terms. Figure 1.3.1 shows a schematic cross section through a metal-insulator-metal junction at absolute zero. Under such conditions all energy levels up to and including the fermi levels of each metal (Ef_1, Ef_2) are occupied by conduction band electrons. Above

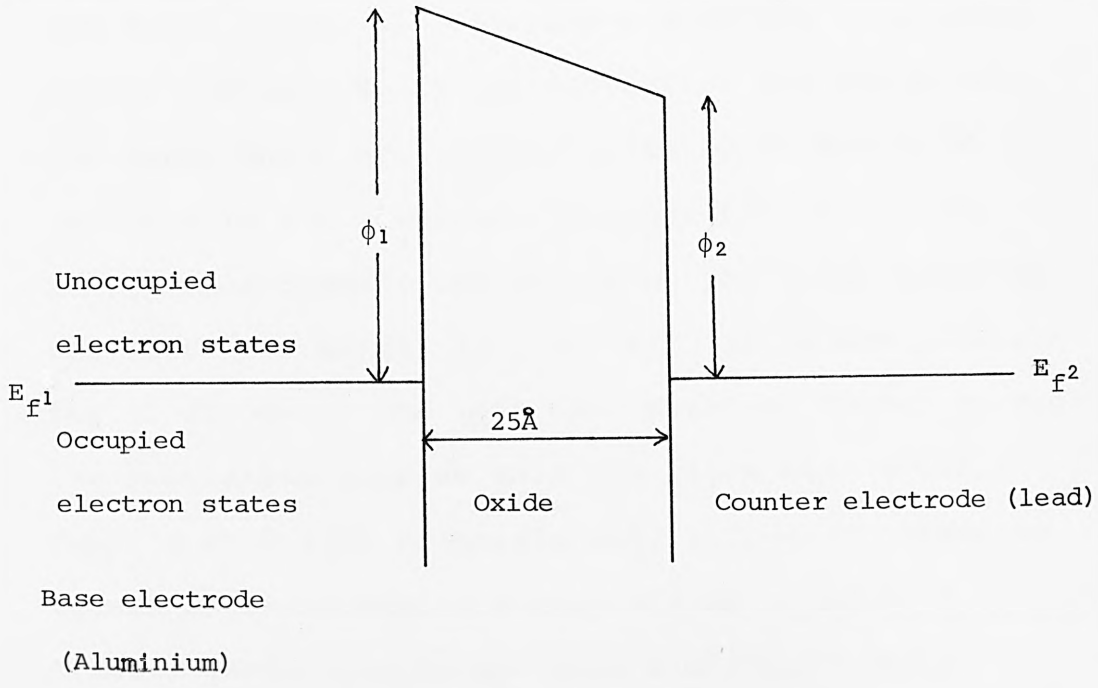

Figure 1.3.1. Tunnel junction at OK with no applied bias

Ef_1 and Ef_2 are the Fermi levels of the two electrodes, ϕ_1 ϕ_2 are their work functions.

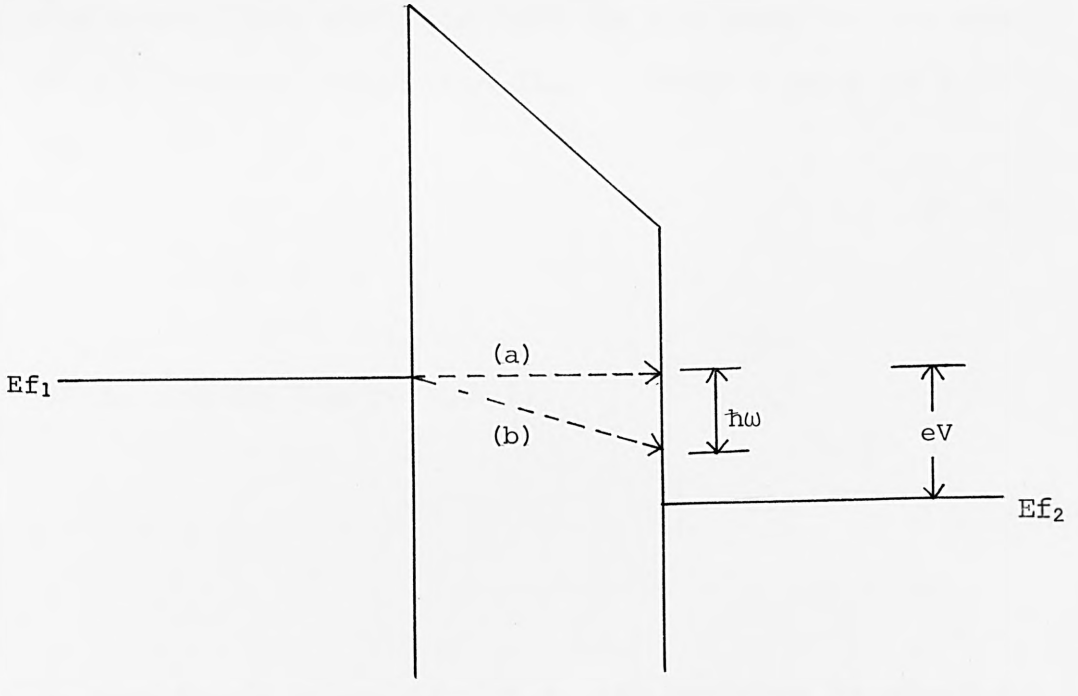

Figure 1.3.2. The same junction under an applied bias.

Path (a) : elastic tunneling

Path (b) : inelastic tunneling.

the fermi levels all electron states are unoccupied. When a voltage, V, is applied across the two metals, the fermi levels are shifted apart by an energy eV (where e is the electronic charge; Figure 1.3-2). All energy measurements are made from the fermi level of the left hand metal (i.e. $Ef_1 = 0$). It is now possible for electrons in the left hand metal to tunnel through the insulating barrier into the right hand metal. Pauli's exclusion principle only allows electrons to tunnel into unoccupied energy states in metal 2. Elastic tunnelling occurs when electrons tunnel horizontally across the barrier without energy loss (path (a) in Figure 1.3-2).

Inelastic tunnelling can only occur when the energy of the tunnelling electron (eV) is the same as the energy of a molecular vibration ($\hbar\omega$). This occurs at a voltage of:

$$V = \hbar\omega/e \qquad (1.3\text{-}1)$$

(Path (b) in Figure 1.3-2)

As mentioned in section 1.1, the changes in slope of the current-voltage curve due to the onset of inelastic

tunnelling, are small ($\leq 1\%$) and there are thus plotted as a second derivative. In practice, the dopant molecules will have many vibrations and a real spectrum is much more complicated. Figure 1.3-3 shows the tunnelling spectrum of benzaldehyde; the majority of the peaks are assignable to the vibrational modes of the molecule.

1.4 Mathematical Models for Peak Intensities

Various models have been suggested to account for electron-molecule interactions in tunnel junctions. One of the first was that due to Scalapino and Marcus (27). In this one-electron model, the height of the potential barrier is perturbed by molecular impurities in such a way that electrons can couple with the molecular vibrations. In one type of coupling infra-red selection rules arise, another type of coupling yields Raman-like selection rules. In practice, both infra-red and Raman vibrations are observed in tunnelling spectra.

Scalapino and Marcus' theory is best explained using a specific example of water doped on an aluminium-aluminium-oxide-lead junction. (The junction is fabricated as described in Section 1.1). The water molecules are physisorbed by hydrogen bonding to hydroxyl groups which

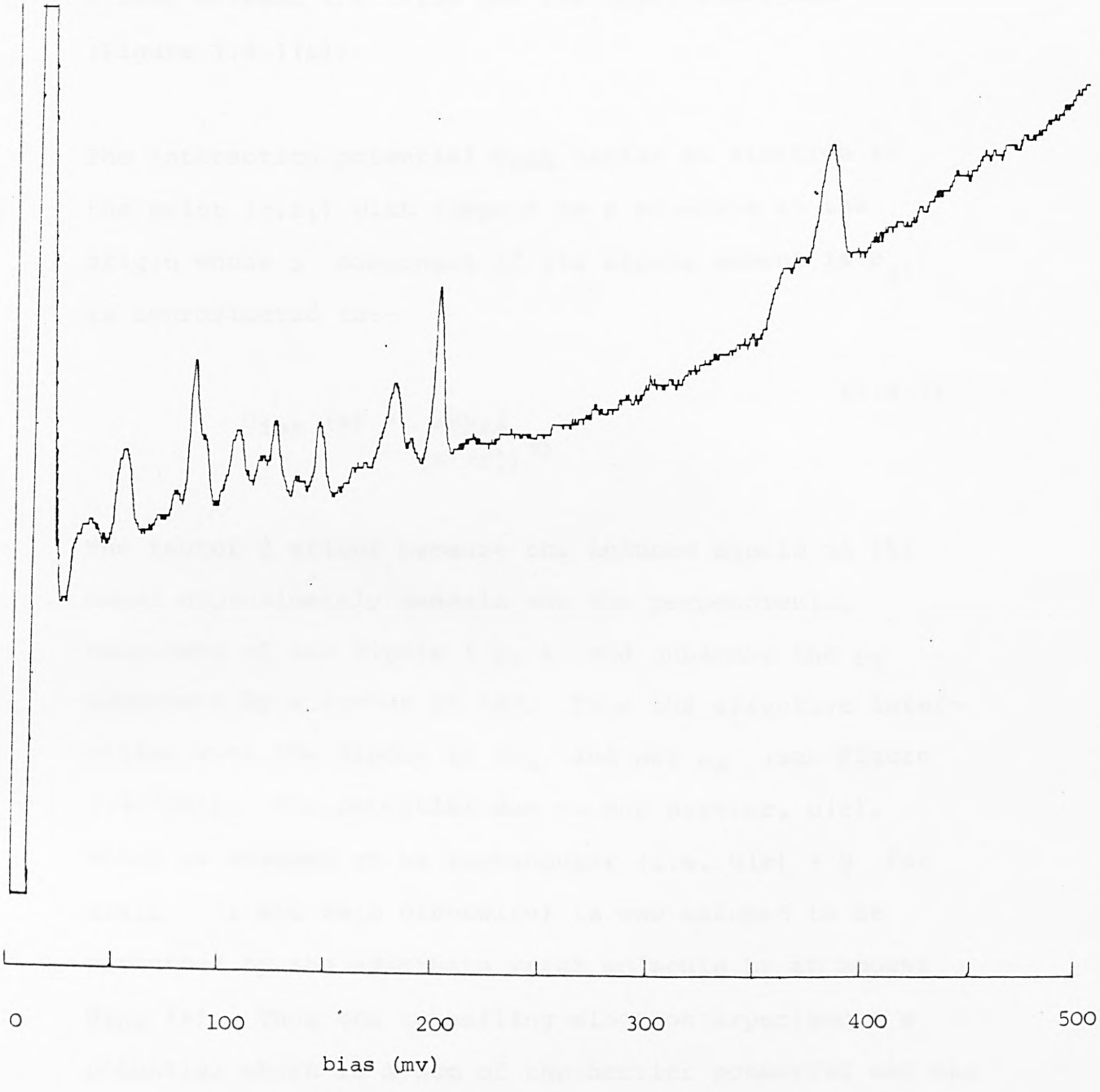

Figure 1.3.3. Inelastic electron tunnelling spectrum of benzaldehyde on alumina at 4.2k.

are present on the oxide surface and are thus sandwiched between the oxide and the upper electrode (Figure 1.4.1(a)).

The interaction potential $U_{int}(z)$ for an electron at the point (z, r_1) with respect to a molecule at the origin whose z component of its dipole moment is p_z, is approximated to:-

$$U_{int}(z) = \frac{2ep_z Z}{(z^2+r_1^2)^{3/2}} \qquad (1.4\text{-}1)$$

The factor 2 arises because the induced dipole in the metal approximately cancels out the perpendicular component of the dipole (p_1) and enhances the p_z component by a factor of two. Thus the effective interaction with the dipole is $2p_z$ and not p_z (see Figure 1.4-1(b)). The potential due to the barrier, U(z), which is assumed to be rectangular (i.e. $U(z) = U$ for $o \leqq z \leqq L$; and zero otherwise) is now assumed to be perturbed by the adsorbate water molecule by an amount $U_{int}(z)$. Thus the tunnelling electron experiences a potential which is a sum of the barrier potential and the interaction potential.

Using a W.K.B. approximation (31) the tunnelling matrix element M for the transfer of electrons from metal 1 to metal 2 is given by:-

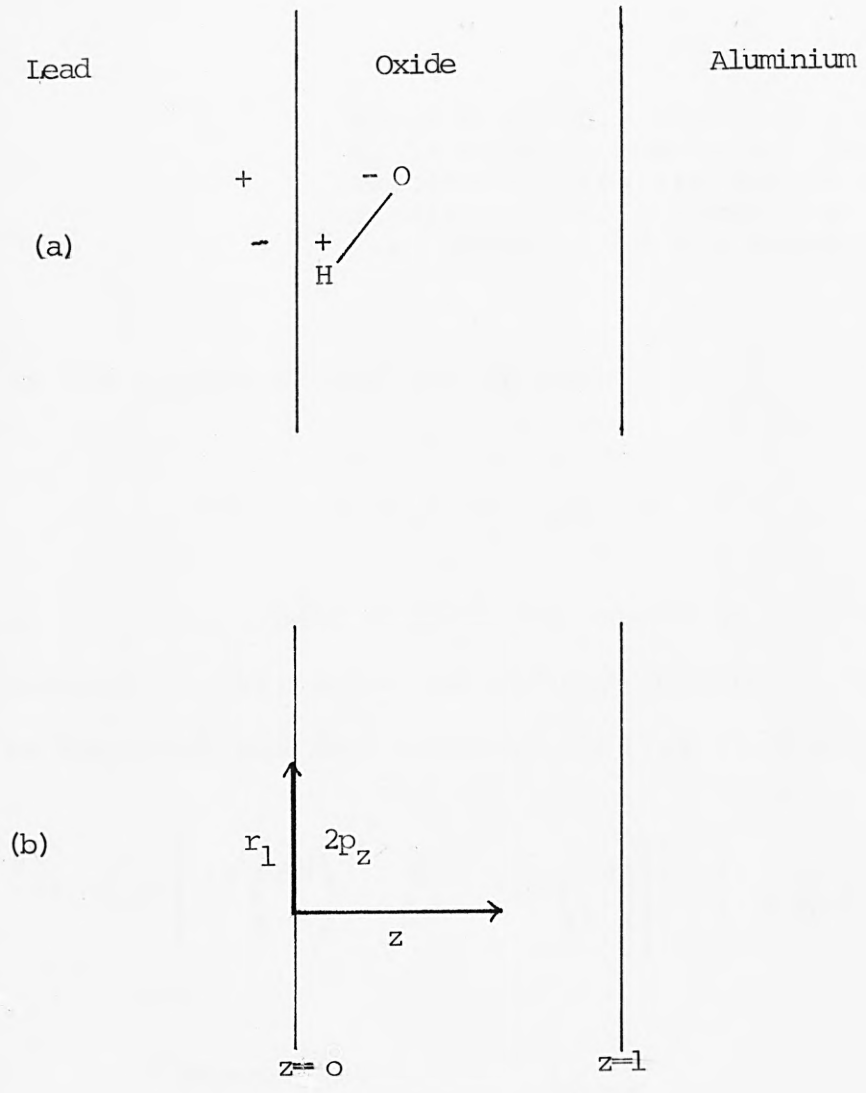

Figure 1.4.1 (a). Hydroxyl group orientation near the aluminium -oxide - lead interface. The mirror image charges in the lead are shown.

(b). The dipole 2pz and the coordinate system used in evaluating the matrix element. (Reference 27)

$$\left|M_{1,2}\right| \propto \exp\left\{-\int_0^L \left(\frac{2m}{\hbar}\right)^{\frac{1}{2}} \left(U(z)+Uint(z)-(E-E_1)\right)^{\frac{1}{2}} dz\right\} \quad (1.4\text{-}2)$$

where E = total electron energy,
E_1 = kinetic energy of the electron associated with its motion perpendicular to the z direction.
i.e. parallel to the barrier.

In the region around the OH group

$$U(z) - (E-E_1) >> U_{int}(z)$$

so by letting $U(z) - (E-E_1) \cong \phi$, where ϕ is the maximum barrier height, which is assumed constant; $U_{int}(z)$ can be expanded and the integral in (1.4-2) evaluated giving:

(1.4-3)

$$|M_{1,2}| \propto \left[1+\left(\frac{2m}{\phi}\right)^{\frac{1}{2}} \frac{epz}{\hbar L} \cdot g\left(\frac{r_1}{L}\right)\right] \exp\left[-\left(\frac{2m\phi}{\hbar^2}\right)^{\frac{1}{2}} L\right]$$

(1.4-4)

$$\text{where } g(x) = \frac{1}{x} - \frac{1}{(x^2+1)^{\frac{1}{2}}}$$

The first term gives rise to the inelastic tunnelling current, and the second term gives the elastic contribution. It is now possible to calculate the ratio of the inelastic conductance to the elastic conductance for a single given vibrational mode. i.e. The ratio:-

(1.4-5)

$$\frac{(dIi/dV)}{(dIe/dV)}$$

Before calculating this ratio, it is worth noting several points:

(1) Current, (and hence conductance) in tunnelling is proportioned to the square of the relevant matrix element. This is merely a statement of Fermi's "Golden Rule" of perturbation theory:-

$$W = \frac{2\pi}{\hbar} \left| \langle \Psi_1 \left| U_{int}(z) \right| \Psi_2 \rangle \right|^2 \delta(E_1 - E_2 - \hbar\omega) \qquad (1.4\text{-}6)$$

where $\langle \Psi_1 | U_{int}(z) | \Psi_2 \rangle$ is the matrix element describing the interaction of the electron with the dipole potential $U_{int}(z)$,
$\langle \Psi_1 | U_{int}(z) | \Psi_2 \rangle \equiv M_{1,2}$
Ψ_1, Ψ_2 are the wavefunctions of the electron in metal 1 and metal 2 respectively,
$\delta(E_1 - E_2 \mp \hbar\omega)$ is a delta function which ensures the conservation of energy. $\delta(x) = 0$ unless $x = o$ in which case $E_1 = E_2 + \hbar\omega$. E_1, E_2 are the energies of the electron in the two metals. (The delta function is just another way of stating that the electron can only tunnel when $eV \geq \hbar\omega$.

(2) The relevant matrix element for inelastic tunnelling is taken between the ground state $\langle 0 |$ and the first excited state $|1\rangle$. This represents the tunnelling of an electron which gives energy $\hbar\omega$ to the molecular vibration. (It should be noted that in this calculation all molecules are in their ground vibrational state at

absolute zero and that any energy radiating - or anti Stokes - processes are neglected. At temperatures above absolute zero, broadening effects become significant, (these are discussed later in section 1.8.1)

(3) Finally, it is assumed that the density of states for the metal electrodes are independent of energy, which is approximately true for normal (i.e. non-superconducting) metals; and that transverse momentum for inelastic tunnelling is conserved, just as it is for elastic tunnelling; then the quantities multiplying the square of the matrix element are identical for the elastic and inelastic current. Thus the ratio $(dIi/dV)/(dIe/dV)$ at a distance r_1 from an impurity is just the square of the matrix element of second term in brackets in equation (1.4-3).

$$\frac{(dIi/dV)}{(dIe/dV)} = \frac{2m}{\phi}\left(\frac{e}{\hbar L}\right)^2 \left[g^2\left(\frac{r_1}{L}\right)\right] \left|\langle 1|pz|0\rangle\right|^2 \delta(eV-\hbar\omega) \qquad (1.4\text{-}7)$$

The total inelastic conductance due to one vibrational mode of one impurity molecule is obtained by integrating (1.4-7) over all r_1. The integration is simplified by using the fact:

$$2\pi\int_0^L r_1\, g^2\left(\frac{r_1}{L}\right) dr_1 \cong 2\pi L^2 \ln\left(\frac{L}{ro}\right) \qquad (1.4\text{-}8)$$

The lower limit r_o is a cut-off distance near to the dipole. Below r_o the approximation for the potential $U_{int}(z)$ (equation 1.4-1) begins to fail. Fortunately, it enters as a logarithm so its exact magnitude is not too critical; it does, however, preclude quantitative accuracy.

Multiplying the integrated form of (1.4-7) by N, the number of impurities per unit area, and summing over all the possible vibrations for the impurity, (1.4-7) becomes:

$$\frac{(dIi/dV)}{(dIe/dV)} = N\left(\frac{4\Pi me^2}{\hbar^2}\right) \ln\left(\frac{L}{r_o}\right)\sum_{\substack{\text{all}\\ m}} |\langle m|pz|o\rangle|^2 \delta(eV-\hbar\omega_m) \qquad (1.4\text{-}9)$$

where: $\langle m|$ is the first excited state of the mth vibrational mode, $\hbar\omega_m$ is the energy of the mth vibrational mode, and

$\sum |\langle m|Pz|0\rangle|^2 \delta(eV-\hbar\omega)$ is also known as the Dipole spectral weight function of the OH group (27).

The above equation only holds for T=OK. For T>OK, terms involving the fermi function:
$f(E) = [1+\exp(E/kT)]^{-1}$ have to be included.
For example, see Jaklevic and Lambe (32). For a surface coverage of N ≅ 1 molecule per 10Å^2; a cut-off value of $r_o \cong 1$Å; and $\sum |\langle m|Pz|0\rangle|^2 \cong 10^{-38}$ e.s.u.^{2},cm^2, the change in conductance is of the order

of one percent, which is in agreement with the experimental results.

The important aspect of (1.4-9) is that the size of the conductance change is proportional to the square of the dipole matrix element of a given mode:

(1.4-10)

$$|\langle m|p_z|o\rangle|^2$$

This is the same quantity which predicts the integrated peak intensity in an infra-red spectrum. Thus all infra-red active modes of a given impurity should be present in an inelastic electron tunnelling spectrum. (In fact, some infra-red peaks are not present; but this is due to the operation of orientational selection rules which will be explained in Section 1.9.)

Scalapino and Marcus' theory does not explain the presence of Raman-active modes in tunnel spectra. However, Jaklevic and Lambe (32) extended Scalapino and Marcus' theory to include Raman type interactions.

Although a dopant molecule may not have a dipole moment associated with a given vibrational mode, there will usually be a polarisability associated with that mode. The tunnelling electron will induce a dipole moment in the molecule and interact with the induced dipole.

Jaklevic and Lambe calculated the interaction energy to be:-

(1.4-11)

$$U_{int}^{R}(z) = \frac{-4e^2\alpha z^2}{(z^2+r_1^2)^3}$$

where: α is the polarisability of the molecule, superscript ^{R} indicates Raman, since vibrational modes that have a polarisability associated with them are called "Raman-active" modes,
z: the z axis (see Figure 1.4-2)

The tunnelling matrix element can now be calculated as before:

(1.4-12)

$$|M_{1,2}^{R}| \propto \left[1+\left(\frac{2m}{\Phi}\right)^{\frac{1}{2}} \frac{\alpha e^2}{4\hbar L^3} t\left(\frac{r_1}{L}\right)\right] \exp\left\{-\left[\frac{2m\Phi}{\hbar^2}\right]^{\frac{1}{2}} L\right\}$$

which is analogous to (1.4-3) where ϕ is the maximum barrier height; and

$$t(x) = \frac{1}{x^2}\left[\frac{1-x^2}{(1+x)^2} + \tan^{-1}\left(\frac{1}{x}\right)\right]$$

and the ratio of the two conductances is:

(1.4-13)

$$\frac{(dIi/dV)}{(dIe/dV)} = \left[\frac{4\pi m}{\hbar^2\phi} \frac{e^3}{16 L^2}\right]\left[t^2\left(\frac{r_1}{L}\right)\right] |\langle 1|\alpha|0\rangle|^2 \delta(eV-\hbar\omega)$$

The total inelastic conductance change due to N impurities per unit area, and m possible vibrations is thus:

$$\frac{(dIi/dV)}{(dIe/dV)_{TOTAL}} = N\left[\frac{4\Pi me^3}{\hbar^2\phi 16L^6}\right]\int_0^L t^2\left(\frac{r_1}{L}\right) r_1^2 dr_1 \sum_m |\langle m|\alpha|o\rangle|^2 \delta(eV-\hbar\omega)$$

(1.4-15)

which is analogous to (1.4-9) where $\langle m|\alpha|o\rangle$ is the matrix element for the polarisability.

Unfortunately, t(x) is strongly divergent for small x and has to be estimated numerically; it is also strongly dependent on the cut-off distance r_o.

Jaklevic and Lambe, estimated the conductance change for a purely Raman-active vibration to be between 0.1 and 0.5% compared with a 1% conductance change for an infra-red interaction (see Figure (1.4.2).

There is no doubt that the simple formalism of Scalapino and Marcus' theory (and that extended by Jaklevic and Lambe) is successful since it is able to predict the correct order of magnitude for tunnelling currents; however the theory has several drawbacks:

(1) It assumes transverse momentum (P_1) is conserved: usually scattering by an impurity molecule will alter the transverse momentum. Such off axis scattering terms have been neglected, and if included, substantially modify the selection rules (33).

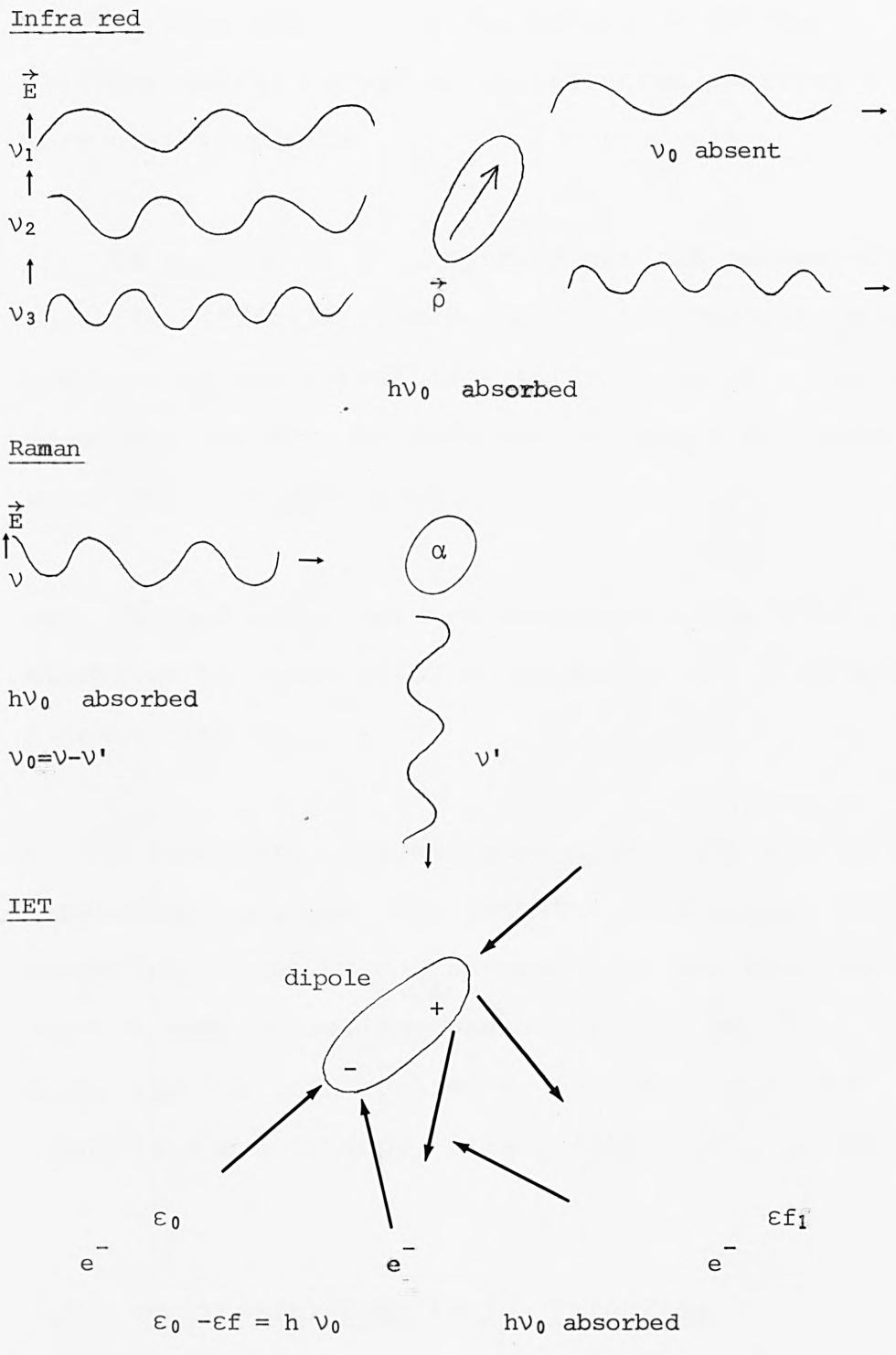

Figure 1.4.2. A semiclassical representation of interaction occuring in infra red, Raman and I.E.T. spectroscopies. The figure shows infrared absorption, Raman scattering and interaction of the tunneling electron with the molecule.

(2) It does not include the effect of decreased electron energy caused by the electron exciting a molecular vibration.

(3) It depends on an arbitrary cut-off parameter, r_o , which is difficult to determine. For example, when calculating the vibrational intensities of a complex molecule, would r_o be constant or have a different value for each vibration.

(4) It implicitly assumes localised tunnelling of electrons by first calculating $Ii(r_1)$ and then integrating over r_1.

It is, therefore, necessary to search for a "second generation" theory. The transfer Hamiltonian formalism, first originated by J. B. Bardeen (34) has been used to explain many tunnelling phenomena (35, 36, 37). This formalism has been applied to inelastic electron tunnelling spectroscopy with a fair degree of success.

1.5 The Transfer Hamiltonian Formalism

The Transfer Hamiltonian formalism assumes that the total Hamiltonian, $\hat{H}$, for a metal-insulator-metal system can be written as the sum of three terms:-

(1.5-1)

$$H = H_L + H_R + H_T$$

H_L and H_R are the two complete Hamiltonians of the left and right electrode, and H_T is a perturbing operator, the transfer Hamiltonian, which can be regarded as driving electrons across the tunnelling barrier according to the golden rule.

(1.5-2)

$$W_{L\to R} = \frac{2\pi}{\hbar} |\langle \Psi_R | H | \Psi_L \rangle|^2 \quad N_f(E_R) \; \delta(E_L - E_R)$$

where $N_f(E_R)$ is the density of states of the right hand electrode

In this approach, the electrodes are regarded as almost completely isolated systems with their own Hamiltonians, H_L and H_R, and eigenstates ψ_L and ψ_R, which are weakly coupled to each other by the perturbing operator term H .

For a rectangular potential barrier of height Vo, and thickness L, the W.K.B. approximated wavefunctions for Ψ_L and Ψ_R are of the form (40):-

$$\Psi_L = \begin{cases} (Cpx)^{-\frac{1}{2}} \exp(i(p_y y + p_z z)) \sin(p_x x + \gamma) & (1.5\text{-}3) \\ \qquad \text{for } x<o \text{ (in the left electrode)} & \\ \frac{1}{2}(Cp_x)^{-\frac{1}{2}} \exp(i(p_y y + p_z z)) \exp\left(-\int_0^L |p_x| dx\right) & (1.5\text{-}4) \\ \qquad \text{for } o<x<L \text{ (in the insulator)} & \\ 0 \qquad \text{for } x>L & (1.5\text{-}5) \end{cases}$$

where C = normalisation constant
and p is the dipole moment

(for tunnelling occuring from left to right)

The wavefunctions for Ψ_R is of a similar form. The wavefunctions Ψ_L, Ψ_R are standing waves in the two electrodes with weakly overlapping exponential tails in the barrier (Figure 1.5-1). The W.K.B. approximation assumes that Ψ_L does not perturb the right hand electrode and vice versa. In other words:

$$\Psi_L(x) = 0 \qquad x>L \qquad (1.5\text{-}6)$$

$$\Psi_R(x) = 0 \qquad x<0 \qquad (1.5\text{-}7)$$

For the barrier region the magnitude of the dipole moment normal to the electrode surface is approximated to (34):

$$|p_x| = (2\mu V(x) - p_y^2 - p_z^2)^{\frac{1}{2}} \qquad (1.5\text{-}8)$$

where V(x) is the barrier height and $\hbar \equiv 1$.

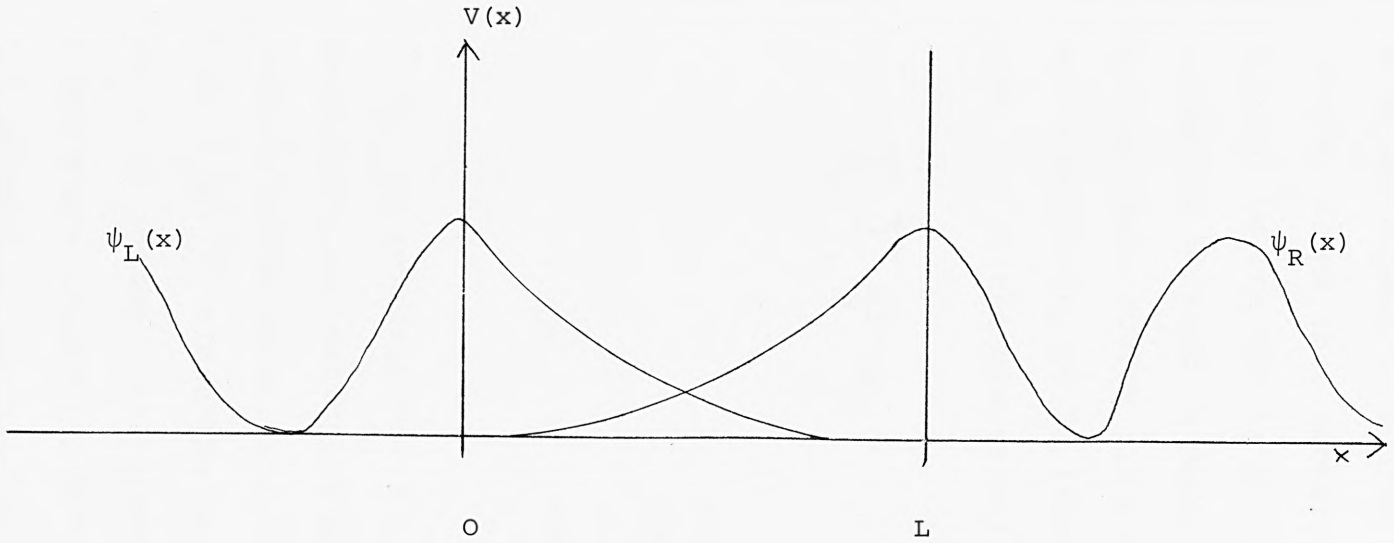

$$\psi_L = \begin{cases} (Cp_x)^{-\frac{1}{2}} \exp(i(p_y y - p_z z)) \sin(p_x x + \gamma) & x<0 \\ \frac{1}{2}(Cp_x)^{-\frac{1}{2}} \exp(i(p_y y + p_z z)) \exp(p_x x)\, dx & 0<x<L \\ 0 & x>L \end{cases}$$

Figure 1.5.1. The WKB approximated wavefunctions for the electron in the left and right electrodes and the insulator.

The inelastic tunnelling process is now viewed as a transition between the metal state on one side (Ψ_L) to the metal state on the other (Ψ_R) via an interaction with the dopant molecules trapped in the barrier. The rate at which this occurs, i.e. the current flow, depends on the matrix product of the two metals. The inelastic current is obtained by summing over all initial full states (i) and all final empty states (f) and multiplying by 2e (this factor arises from the spin sum of the electrons). Thus:

(1.5-9)

$$I_i = 2e \sum_{\Psi_i} \sum_{\Psi_f} \frac{2\pi}{\hbar} |M_{fi}|^2 \, f_i(1-f_f) \, \delta(E_i - E_f)$$

where f_i, and f_f are fermi-functions which ensure the initial states are unoccupied, and $|M_{fi}|^2 = |\langle \Psi_R | H_T | \Psi_L \rangle|^2$

If H_T is represented as a sum of terms Mi and Me, describing inelastic and elastic tunnelling respectively, then no cross terms will appear in the matrix element $|(Me + Mi)|^2$, since the two tunnelling terms Me and Mi share no common final states; the inelastic tunnelling final state includes a molecular excitation which is not present in the elastic terms. Consequently, the inelastic current (Ii) and the elastic current (Ie) can be evaluated separately:

$$I_i \propto |\langle M_i \rangle_{fi}|^2 \qquad (1.5\text{-}10)$$

$$I_e \propto |\langle M_e \rangle_{fi}|^2 \qquad (1.5\text{-}11)$$

A more detailed theoretical account of the Transfer Hamiltonian formalism is given elsewhere: (31, 34, 38, 39, 41).

An alternative to the dipole approximation given by (1.5-8) was proposed by Kirtley, Scalapino and Hansma (33). Essentially they assumed that changes in the charge distribution within the molecule can be broken up into partial charges each localised on a particular atom. (The partial charges arise from uneven electron sharing and can be calculated from infra-red theory.) Interaction at distances comparable to atomic lengths can now be calculated. Previously this was not possible as the earlier dipole approximation does not hold for small distances. The tunnelling electron-molecule interaction is thus:

$$V(\vec{r}) = \sum_j \frac{-e^2 z_j}{|\vec{r} - R_j|} \qquad (1.5\text{-}12)$$

where R_j = position of jth atom,
$z_j e$ its partial charge,
$\vec{r}$ position of the tunnelling electron
(See Figure 1.5-2)

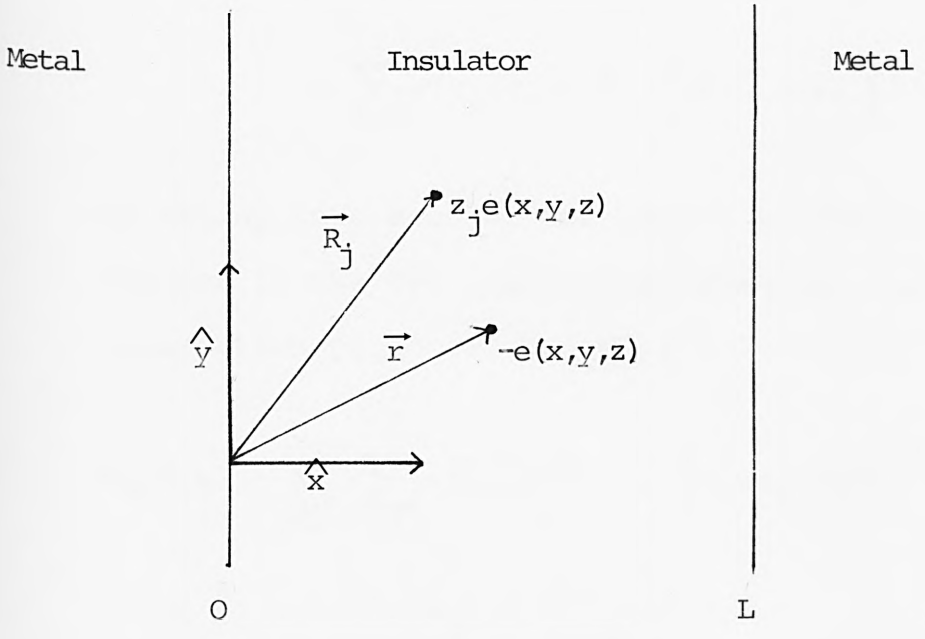

Figure 1.5.2. Coordinate system used in partial charge formalism for calculating the electron-molecule interaction. (Reference 33)

In order to connect initial and final states which are of different energies, the component of the total interaction potential, which oscillates at the frequency of the vibrational mode of interest (ω), is separated out. Then expanding R_j:

$$\vec{R}_j = \vec{R}_j(o) + \delta\vec{R}_j$$

we obtain:

(1.5-13)

$$V_I(\vec{r}) \cong \sum_j -e^2 z_j \delta\vec{R}_j \cdot \vec{\nabla}_j \left(|\vec{r}-\vec{R}_j(o)| \right)^{-1}$$

By taking into account the images of the partial charges in the two electrodes, the electron-molecule interaction potential becomes:

(1.5-14)

$$V_I(\vec{r},\omega) = \sum_{n=-\infty}^{+\infty} \sum_j \frac{-e^2 z_j \delta\vec{R}_j \cdot \vec{\nabla}_j}{\varepsilon} \left\{ (\vec{r}-R_j-2n\hat{x})^{-1} - \right.$$

$$\left. (|\vec{r} - \vec{R}_j - (2nL-2a_j)\,\hat{x}|)^{-1} \right\}$$

where ε is the dielectric constant of the insulator,
a_j the distance of the j^{th} atom from one electrode

The matrix element can then be defined as:

(1.5.15)

$$M_{fi} = \int_0^L \Psi_f^* (V_I(\vec{r},\omega))\ \Psi_i\ d^3x$$

The total inelastic current can then be calculated as before using the Transfer Hamiltonian formalism, by summing over the transition rate (obtained from the Golden Rule) and the initial and final state.

$$I_i = 2e \sum_{\Psi_i} \sum_{\Psi_f} \frac{2\pi}{\hbar} |M_{fi}|^2 f_i(1-f_f)\delta(E_i-E_f) \qquad (1.5\text{-}16)$$

which is analogous to (1.5-9)

Since the change in conductance is so small, the second derivative of (1.5-16) is calculated i.e. the quantity d^2Ii/dV^2. (In performing this calculation the summations can be replaced by intergrals and M_{fi} explicitly expressed as a result of calculating (1.5-15)).

The final form of (1.5-16) is multiplied by the surface density of impurity molecules before the ratio of the change in inelastic current to the change in elastic current can be evaluated. Kirtley, Scalapino and Hansma (33) have calculated this ratio for a monolayer of hydroxyl ions and have found:

$$\frac{(dIi/dV)}{(dIe/dV)} \cong 0.5\%$$

which is in excellent agreement with the average experimental value of 0.4% (33).

Although the Transfer Hamiltonian formalism, and the modified form used by Kirtley, Scalapino and Hansma, predicts the correct order of magnitude for the tunnelling current, there is still some controversy as to whether the Transfer Hamiltonian formalism is applicable. There are a number of alternative theories which do not use this approach or that of the Golden Rule, but these are much more complex and in general are only applicable at absolute zero.

1.6. Second Harmonic Detection System

One of the most sensitive ways to electronically detect a small deviation in an otherwise linear signal is to use an a.c. modulation technique in which the second harmonic of a fundamental modulation current is detected using a special synchronous detector called a lock-in amplifier. This technique is not unique to I.E.T.S. but is employed whenever minute signal changes have to be detected. For example, in four probe Hall effect measurements, capacitance measurements, l.e.e.d and auger, N.M.R., E.S.R and optical spectroscopy (41). Apart from its high sensitivity, the technique enables signals to be obtained from very noisy environments. A typical commercial lock-in amplifier is capable of detecting signals at least 100,000 X (100dB) smaller than the noise generated in the circuit, and one of the

advantages applying a fairly well established detection technology is that most of the electronic hardware is commercially available.

Theoretically it is easiest to calculate the dynamic conductance $G = dI/dV$ and its derivative $dG/dV = d^2I/dV^2$, and whilst it is possible to obtain these quantities experimentally, it is much easier and far more sensitive to electronically measure the dynamic tunnel resistance $R = dV/dI$ and its first derivative $dR/dI = d^2V/dI^2$. The above four quantities are related by the following two identities:

(1.6-1)

Identity 1:

$$\frac{dI}{dV} = \left[\frac{dV}{dI}\right]^{-1}$$

(1.6-2)

Identity 2:

$$\frac{d^2I}{dV^2} = -G^3 \frac{d^2V}{dI^2}$$

where $G = \frac{dI}{dV}$, the dynamic conductance

Equation (1.6-2) is obtained thus:-

$$\frac{d^2I}{dV^2} = \frac{d}{dV}\left[\frac{dI}{dV}\right]$$

$$= \frac{dI}{dV}\,\frac{d}{dI}\left[\frac{dV}{dI}\right]^{-1}$$

$$= \frac{dI}{dV}\,\frac{d^2I}{dV^2}\,-1\left[\frac{dV}{dI}\right]^{-2}$$

$$= -\left[\frac{dI}{dV}\right]^{3}\,\frac{d^2V}{dI^2}$$

$$= -G^3\,\frac{d^2V}{dI^2} \qquad (1.6\text{-}2)$$

Using the two identities the conversion of R and dR/dI into G and dG/dV is trivial. However, when studying molecular vibrations it is not necessary to obtain absolute values of dI/dV and d^2I/dV^2 for two reasons. Firstly, there is very little theoretical data on d^2I/dV^2 magnitudes for comparison; besides which the current theories discussed only give a qualitative result anyway. Secondly, in the regions of interest (that is, away from zero bias where superconductivity effects dominate), the conductance G is very nearly constant and so $d^2I/dV^2 \propto d^2V/dI^2$. Consequently, peak shapes and positions are virtually identical. Indeed results of computer generated d^2I/dV^2 measurements [calculated from dV/dI] and d^2I/dV^2 values measured directly show very little difference (74).

The second harmonic detection technique applied to electron tunnelling has been described by many authors (43,44,45). Essentially, the technique entails applying a constant amplitude, high purity sine wave to the tunnel junction. Since the junction has a non-linear current voltage characteristic, the resultant signal will now contain a significant percentage of higher harmonics of the fundamental frequency. These harmonics, which are a measure of the distortion, and hence the deviation from linearity, can be detected by the lock-in amplifier. The description of the system outlined below follows the analysis of the Adler and Jackson (45).

A sinusoidally varying modulation current of small amplitude δ (typically 2mv peak to peak) and of angular frequency ω is applied to a tunnel junction which has a weakly non-linear current-voltage characteristic (Figure 1.6-1). For a given amplitude, the voltage developed across the junction is not a pure sinewave but is distorted and consequently contains some higher harmonics of the fundamental frequency. A schematic circuit to realise this is shown in Figure 1.6-2. The modulation current, whose freqency is typically 1kHz, is applied to the junction R_j through R_1. A slowly varying bias voltage V, which in effect provides the energy sweep, is also applied to R_j through R_2. Both R_1 and $R_2 >> R_j$ hence the current is insensitive to changes in R_j which varies as the bias voltage is increased. The resulting distorted a.c. voltage is then synchro-

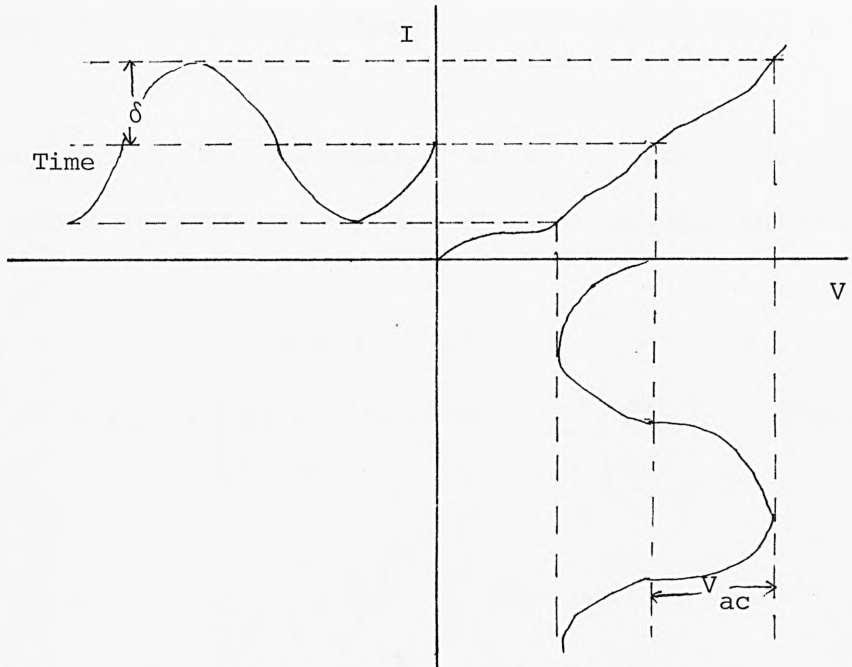

Figure 1.6.1. Hypothetical I-V curve with sinewave modulation of current. The resulting output voltage is distorted due to the non-linear I-V characteristic.

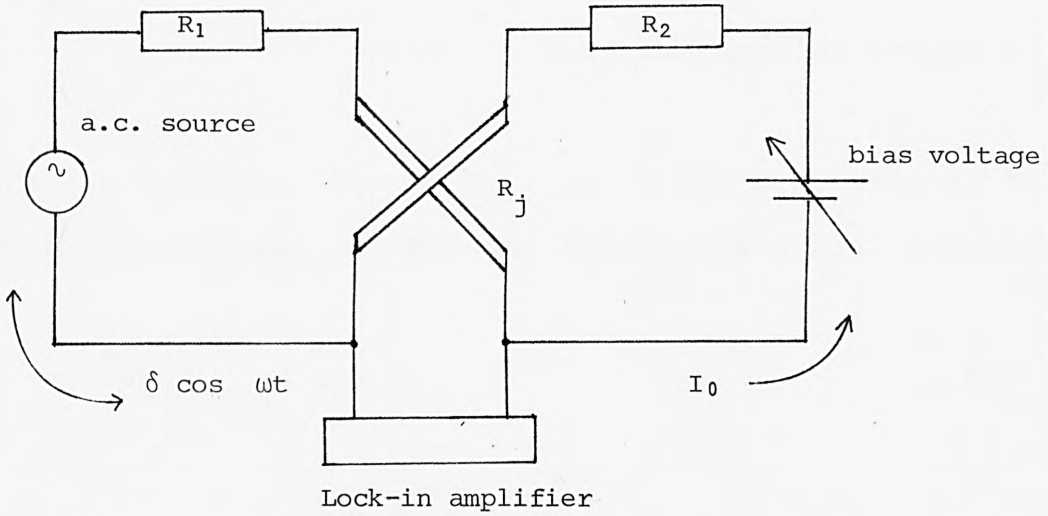

Figure 1.6.2. Schematic circuit for second harmonic detection measurements.

nously detected using the lock-in amplifier.

Since δ is small compared with I_o, the voltage across the junction can be expressed as a Taylor Series

(1.6-3)

$$V(I) = V(I_o + \delta\cos\omega t)$$

$$= V(I_o) + \left[\frac{dV}{dI}\right]_{I_o} \delta \cos \omega t + \frac{1}{2!}\left[\frac{d^2V}{dI^2}\right]_{I_o} \delta^2\cos^2\omega t + \ldots$$

$$+ \frac{1}{n!}\left[\frac{d^nV}{dI^n}\right]_{I_0} \delta^n \cos^n \omega t \qquad (1.6\text{-}4)$$

neglecting terms for $n \geq 3$ and substituting

$\cos^2\omega t = \frac{1}{2}(1 + \cos 2\omega t)$, (1.6-4) becomes:

(1.6-5)

$$V(I_o) + \frac{dV}{dI}\delta \cos \omega t + \frac{1}{4}\frac{d^2V}{dI^2} \delta^2(1 + \cos 2\omega t)$$

where $\omega = 2\pi f$, the angular frequency.

Thus 2 voltages, $V\omega$ and $V_{2\omega}$, which are proportional to their derivatives, are present across the tunnel junction.

$$V\omega \propto \left[\frac{dV}{dI}\right]_{I_o} \delta \cos\omega t \qquad (1.6\text{-}6)$$

$$V_{2\omega} \propto \left[\frac{d^2V}{dI^2}\right]_{I_o} \delta^2\cos 2\omega t \qquad (1.6\text{-}7)$$

Therefore, in order to obtain dV/dI and d^2V/dI^2 it is only necessary to measure the amplitudes of the voltages at the fundamental frequency (ω) and at twice the fundamental frequency (2ω). These small voltages can be measured using the lock-in amplifier, which only detects signals which are in phase with a reference signal, which in this case is the fundamental modulation voltage $\delta \cos \omega t$.

Obviously, (from 1.6-4), the higher harmonic terms ($n \geq 3$) are also present across the junction, and although they can be detected and measured, they are rarely used.

The dynamic conductance G and its derivative dG/dV can be obtained in a similar way but by maintaining a fixed voltage across R_j and examining the Taylor expansion of:

$$I = I(V_o + V \cos \omega t)$$

This method is experimentally more difficult to perform and is less sensitive; consequently direct dynamic conductance meansurements are rarely performed (46).

The practical details, circuit diagrams of the detection system and the principle of operation of the lock-in amplifier are left to Chapter Two.

1.7. Superconductivity Effects

In order to obtain sufficient resolution most tunnelling experiments are carried out at temperatures of 4.2K or lower. In this temperature region, the effects of the metal electrodes becoming superconducting substantially modify some of the characteristices of the current-voltage curve.

In order to understand what happens when one or two superconducting electrodes are used in tunnelling experiments, it is necessary to be aware of some of the consequences of the B.C.S. (Bardeen, Cooper, Schrieffer) theory of superconductivity (28,29). The main feature of the B.C.S. theory is that a significant change in a metal's density of states occurs when the metal becomes superconducting. In a normal metal at absolute zero, all the electron energy states are full up to and including the fermi surface, E_f. At OK the fermi surface is sharply defined; all states above E_f are empty. However, for a superconductor at absolute zero there is a forbidden energy gap of width 2Δ centred on the fermi level. Electrons are not allowed to have energies within this region. The gap occurs as a consequence of the electrons condensing into pairs, called 'Cooper Pairs', which have a binding energy of 2Δ . (The precise details of the B.C.S. theory need not concern us here). Figures 1.7-1 and 1.7-2 show the difference in the density of states

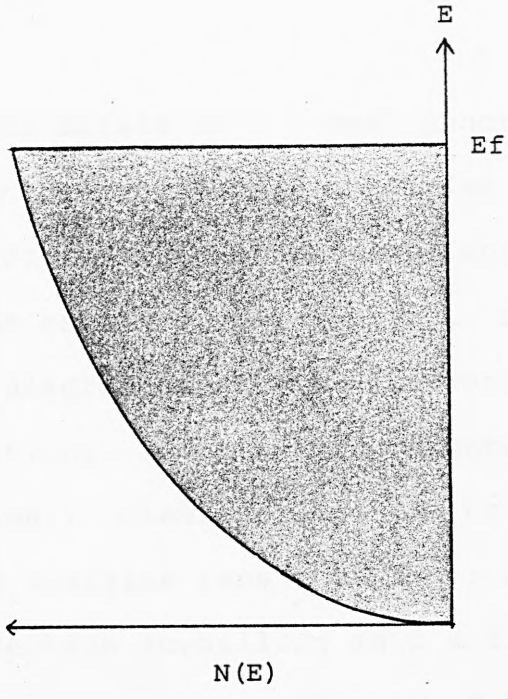

Figure 1.7.1. Density of states plot for a normal metal at OK.

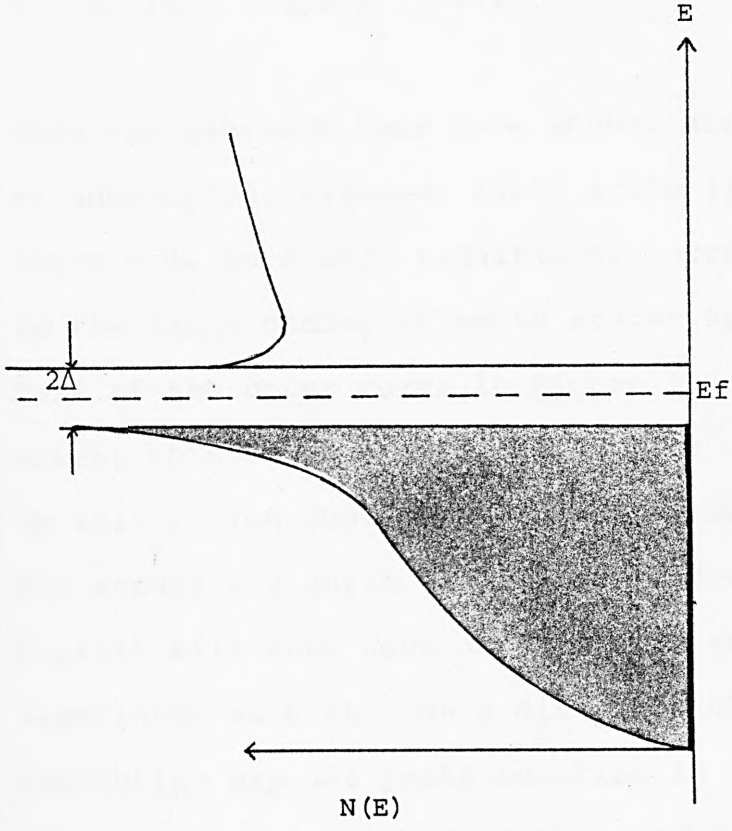

Figure 1.7.2. Density of states plot for a superconductor at OK. showing the forbidden energy gap of width 2Δ.

plot for a normal metal and a superconductor at absolute zero.

If one or both metals in a tunnel junction are superconducting the energy gap 2Δ modifies the I-V curve and new structure appears which reflects the density of states in the region around the gap. Figure 1.7-3 is a schematic diagram of a metal-insulator-superconductor [M-I-S] junction. (Compare with Figure 1.3-1 for a M-I-M junction.) Clearly there can be no tunnelling of any sort for energies less than 2Δ ; since this would entail an electron tunnelling into a final state within the forbidden energy gap. Thus the I-V curve for such a system would show no detail at voltages below $V = 2\Delta/e$ (Figure 1.7.4)

When the electron does have enough energy to tunnel into an unoccupied, allowed, final state (i.e. when $eV \geq 2\Delta$), there will be a very significant increase in current due to the large number of empty states at $E \geq 2\Delta$, (the tail of the upper curve in Figure 1.7-3), and to an extent this current will reflect the density of states in this region just above the superconducting gap (34). The actual I-V curve (and corresponding d^2I/dV^2 against V plot) will thus have at $V = 2\Delta/e$ sharp structure associated with it. As a direct result of the superconducting gap all peaks occuring in a tunnelling spectrum have been shifted by an energy equal to 2Δ ; and thus have to be corrected in the final spectral analysis.

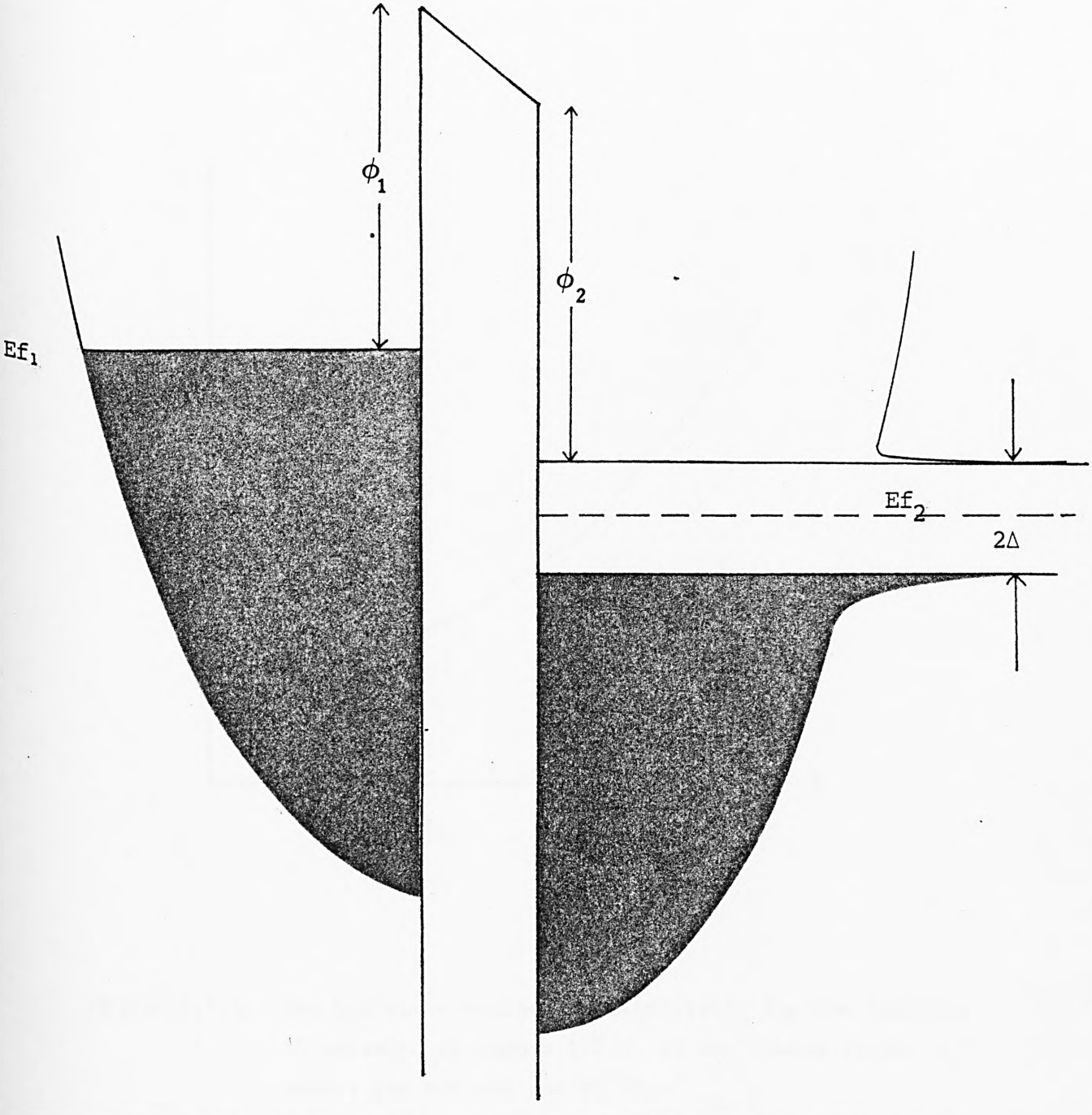

Figure 1.7.3. Schematic diagram of a M-I-S tunnel junction at T=OK showing the forbidden gap. No tunnelling can occur for $eV<2\Delta$, as there are no empty states below $Ef_1 + 2\Delta$.

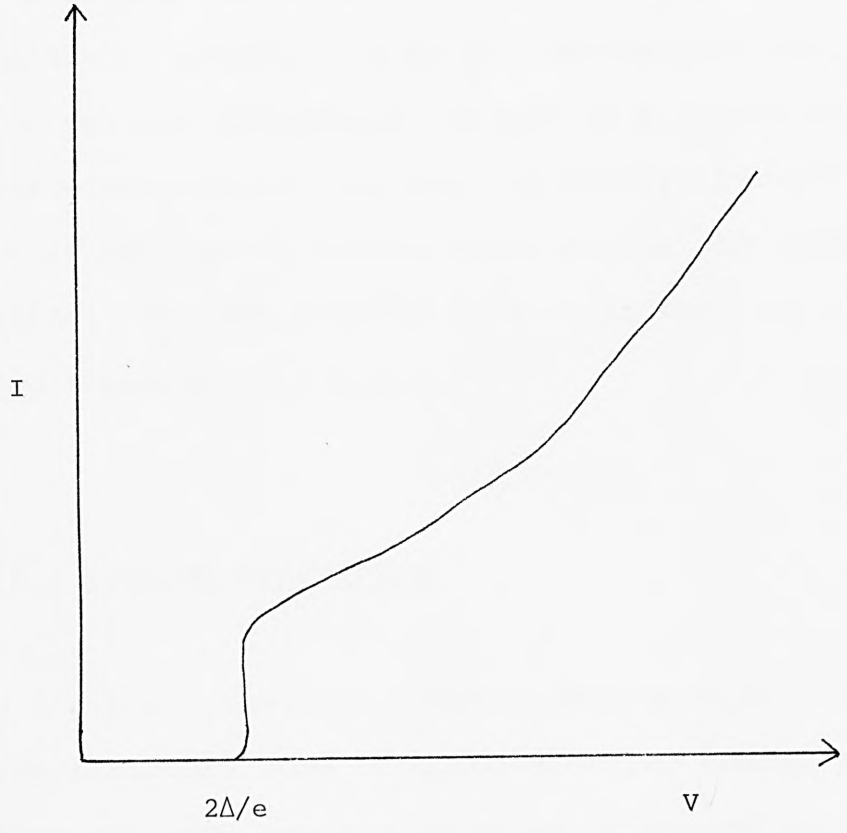

Figure 1.7.4. The current - voltage characteristic for the junction illustrated in Figure 1.7.3. at OK. There is no tunnelling current for $V < 2\Delta/e$.

The advantages of having a superconducting gap structure and that of using superconducting electrodes are discussed in the following section on resolution.

1.8 Resolution

In practice the peaks are not perfectly sharp but are broadened, principally by two mechanisms: one, modulation voltage broadening, arises as a consequence of the measurement technique; and the other, thermal broadening, arises because at finite temperatures the fermi surfaces are not sharply defined as they are in the zero temperature limit.

1.8.1 Thermal Broadening

In a normal metal at temperatures greater than absolute zero there are some occupied electron energy states above and some unoccupied electron energy states below the fermi level. The occupational probability is given by the fermi (distribution) function:

$$f(E) = [1 + \exp (E/kT)]^{-1} \qquad (1.8\text{-}1)$$

This "smearing out" of the fermi level means that for a given voltage applied to a M-I-M tunnel junction,

the electrons have a distribution of energies, central at E_f (Figure 1.8-1). Consequently, electrons whose energy is greater than E_f can, for a given molecular vibration $\hbar\omega$, tunnel at a lower bias voltage than is otherwise necessary. Similarly those electrons with less energy than E_f, can only tunnel at a greater bias voltage than is needed to satisfy the energy conservation equation:

(1.8-2)

$$eV = \hbar\omega$$

The exact shape of the thermally broadened peak can be calculated since it depends principally on the fermi function (1.8-1).

The total inelastic current is given by (47,50):

(1.8-3)

$$I_i = C\int_{-\infty}^{\infty} dE f(E_1)\ [1-f(E_2+eV-\hbar\omega)].N_1(E_1).N_2(E_2+eV-\hbar\omega)$$

where: $f(E_1)$, $f(E_2)$ are the fermi functions of the left and right metals respectively; $1-f(E_2)$ represents the unfilled states in metal 2, $N_1(E_1)$, $N_2(E_2+eV-\hbar\omega)$ are the density of states for the electrodes; which for normal metals are set equal to unity. C a constant taking into account tunnelling parameters independent of E or T.

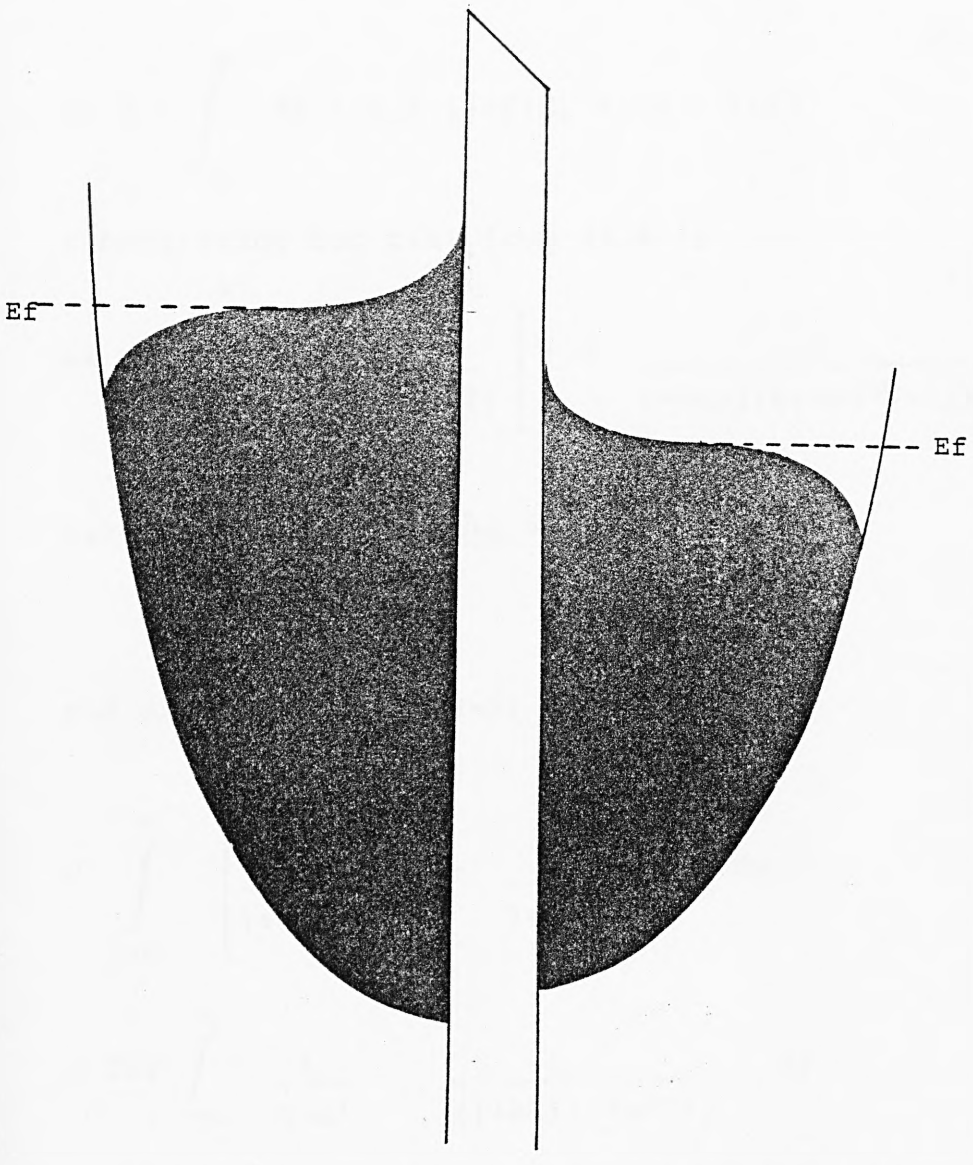

Figure 1.8.1. Density of states plot for a M-I-S junction at T>OK. There are now some occupied electron states above Ef, and some unoccupied states below Ef. This 'smearing out' of the Fermi level is the cause of thermal broadening.

For normal (non-superconducting) metals (1.8-3) becomes:

$$Ii = C \int_{-\infty}^{\infty} dE\ f(E_1)\ [1-f(E_2 + eV - \hbar\omega)] \qquad (1.8\text{-}4)$$

substituting for f(E) from (1.8-1)

$$Ii = C \int_{-\infty}^{\infty} \frac{1}{1+\exp(E_1/kT)} \left[1 - \frac{1}{1+\exp[(E_2+eV-\hbar\omega)/kT]}\right] dE \qquad (1.8\text{-}5)$$

letting $E/kT = y$, $\frac{eV-\hbar\omega}{kT} = x$

and $dE = kTdy$, (1.8-5) becomes:

$$C \int_{-\infty}^{\infty} \left[\frac{1}{1+e^{y}}\right] \left[1 - \frac{1}{1+e^{x+y}}\right] kT\ dy$$

$$= CkT \int_{-\infty}^{\infty} \frac{1}{1+e^{y}} - \frac{1}{(1+e^{y})(1+e^{x+y})}\ dy$$

$$= CkT \int_{-\infty}^{\infty} \frac{(1+e^{x+y}) + 1}{(1+e^{y})(1+e^{x+y})}\ dy$$

$$= CkT \int_{-\infty}^{\infty} \frac{e^{x}\ e^{y}}{(1+e^{y})(1+e^{x+y})}\ dy \qquad (1.8\text{-}6)$$

letting $e^Y=z$ and $dz=e^Y dy$, (1.8-6) becomes:

(1.8-7)

$$= CkTe^X \int_{-\infty}^{\infty} \frac{1}{(1+z)(1+e^X z)} \, dz$$

solving for A, B

$$\frac{1}{(1+z)(1+e^X z)} = \frac{A}{(1+z)} + \frac{B}{(1+e^X z)}$$

$$1 = A(1+e^X z)+B(1+z)$$

letting $z = o \Rightarrow A + B = 1$

letting $z = 1 \Rightarrow A = \frac{1}{1-e^X}$

$$\Rightarrow B = \frac{-e^X}{1-e^X}$$

Substituting A and B into (1.8-7)

$$= CkTe^X \int_{-\infty}^{\infty} \frac{(1-e^X)^{-1}}{(1+z)} - \frac{e^X(1-e^X)^{-1}}{(1+e^X z)} \, dz$$

$$= CkT \frac{e^X}{(1-e^X)} \int_{-\infty}^{\infty} \frac{1}{1+z} - \frac{e^X}{1+e^X z} \, dz$$

$$= CkT \frac{e^x}{(1-e^x)} \left[\ln \frac{(1+z)}{(1+e^x z)} \right]_0^\infty$$

$$= CkT \frac{e^x}{(1-e^x)} x$$

substituting $x = \frac{eV-\hbar\omega}{kT}$

$$Ii = C(eV-\hbar\omega) \frac{e^x}{(e^x-1)} \qquad (1.8\text{-}8)$$

Hence $$\frac{d^2 I}{dV^2} = \frac{d^2}{dV^2} \left[CkT \frac{xe^x}{(e^x-1)} \right] \qquad (1.8\text{-}9)$$

changing variables $$\frac{d}{dV} = \frac{d}{dx} \frac{dx}{dV}$$

$$= \frac{d}{dx} \frac{e}{kT}$$

hence $$\frac{d^2}{dV^2} = \frac{e^2}{k^2T^2} \frac{d^2}{dx^2}$$

(1.8-9) becomes

$$\frac{d^2 I}{dV^2} = \frac{Ce^2}{kT} \frac{d^2}{dV^2} \left[\frac{xe^x}{(e^x-1)} \right]$$

$$= \frac{Ce^2}{kT} \frac{d}{dV} \left[\frac{e^{2x} - xe^x - e^x}{(e^x-1)^2} \right]$$

The final expression for the peak shape is thus:-

(1.8-10)

$$\frac{d^2I}{dV^2} = \frac{Ce^2}{kT} \frac{e^x}{(e^x-1)^3} [(x-2)e^x + (x+2)]$$

$$\text{where} \quad x = \frac{eV-\hbar w}{kT}$$

Equation (1.8-10) is plotted in Figure (1.8-2). Taking the limit as $x \rightarrow o$ gives a miximum height of

$$\frac{1}{6} \frac{kT}{e}$$

and hence a full-width half maximum of 5.4kT. This value has been experimentally confirmed by the work of Jennings and Merril (49).

Thus, in order to obtain a spectrum with sufficeintly good resolution all measurements have to be made at liquid helium temperatures or lower. Table 1.8.1 shows thermal broadening that can be expected at various temperatures.

Whereas (1.8-4) is the most manageable form when discussing thermal and instrumental broadening, it

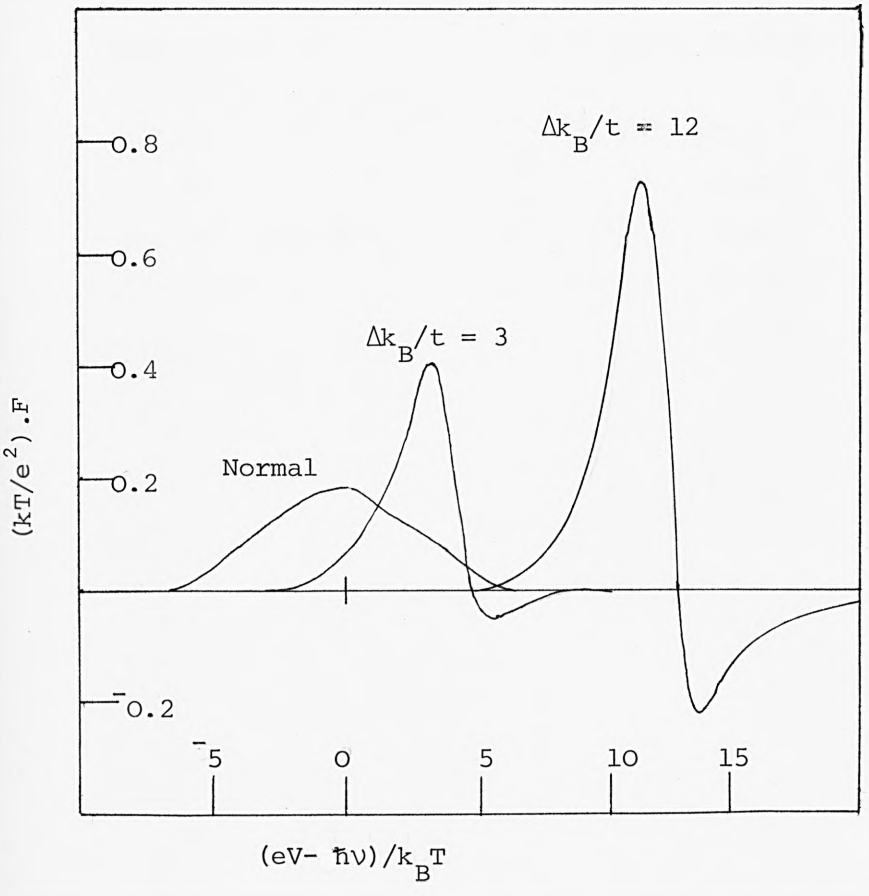

Figure 1.8.2. The thermal broadening function F with both electrodes normal and one electrode superconducting, with $\Delta k_B/t = 3$ and 12. When one electrode goes superconducting the peaks shift by 2Δ, and become taller and narrower. They also develop an undershoot.

(Reference 54)

Table 1.8.1. Thermal broadening at various temperatures

Temperature (k)	Full Width Half Maximum (cm^{-1})
298	1120.0
77	289.0
20 (liquid H_2)	75.0
4.2	15.8
1.1	4.13

represents only a single vibrational excitation of energy. However, to be strictly accurate, it is necessary to consider a distribution of oscillator frequencies to represent the real excitation spectrum. Thus, the master equation (1.8-3) has to be modified to include a dipole spectral weight function $D^S(\hbar\omega)$ which represents the vibrational density of oscillator strenghts for the Sth vibrational band at a frequency $\hbar\omega$. Infact:

$$D^S \propto N\langle m|pz|o\rangle$$

where N is the number of molecules
$\langle m|pz|o\rangle$ dipole strength of the individual oscillators (32).

Integrating $D^S(\hbar\omega)$ amounts to summing over all possible vibrational frequencies. Equation (1.8-3) then becomes:

$$Ii = K \int_0^\infty D^S(\hbar\omega)\, d\omega \int_{-\infty}^{\infty} f(E_1)\,[1-f(E_2+eV-\hbar\omega)]\,N_1(E_1)\,N_2(E_2+eV-\hbar\omega)\, dE \qquad (1.8\text{-}11)$$

If, however, one or both of the electrodes are in a superconducting state, (for example, in an Aluminium-aluminium oxide-lead junction at 4.2, Pb is superconducting, and in a tin-tinoxide-tin junction at 1.2K when tin is a superconductor), the situation is different and $N_1(E_1)$ and $N_2(E_2)$, the tunnelling density

of states, can no longer be set equal to unity, and equation (1.8-3) [or (1.8-11)] has to be integrated numerically (51).

Practically speaking, the presence of one superconducting electrode is a distinct advantage for two reasons. Firstly, it improves peak resolution and, secondly, the intense structures due to the superconducting gap that appears in the second deriviative plot (Section 1.7) is indicative of a good tunnel junction.

The increase in peak resolution occurs because the number of electrons that can be thermally excited across the superconducting gap is governed by the fermi distribution which in the low temperature limit is approximately Boltzman (exp-(E+Δ/kT). At low temperatures, in the region of 1 Kelvin, Δ may be 10 to 20 times kT, so very few electrons will be excited across the gap. The superconducting gap effectively truncates the "tail" of the fermi function which gives a sharper onset to tunnelling occuring over a much narrower range than for normal electrodes. For example Giaever (53) reported an increase in resolution by a factor of five when going from normal to superconducting electrodes for a tin-tinoxide-tin junction at 0.3K. The width of the onset of tunnelling was 0.25 cm^{-1} compared to 1.2 cm^{-1} for the electrodes in their normal state.

The usefulness of superconducting bandgap structure arises because the superconducting density of states, Ns, at the gap is very large and sharp:

(1.8-12)

$$Ns = \frac{N_N|E|}{(E^2-\Delta^2)^{\frac{1}{2}}}$$ reference (52)

where N_N is the normal density of states

E = electron energy

2Δ = superconducting gap energy

Since the number of states in a very small energy range is so very large, electrons tunnelling into these states dominate and result in a very sharp second derivative peak at $V = 2\Delta/e$. This structure indicates that the conduction mechanism under examination is solely electron tunnelling. The presence of other conduction mechanisms, (pin-holes, metallic bridges, tunnelling via traps, ionic conduction, etc) would degrade this superconducting gap structure or eliminate it entirely.

1.8.2 Modulation Voltage Broadening

The second principal source of peak broadening is due to the detection technique itself. It arises as a consequence of using a finite modulation voltage. The

analysis presented here is that essentially due to Leger (48, 88).

f"(eV) is the exact (theoretically obtained) second derivative and F"(eV) is the experimentally obtained function. The current through the junction as a function of time can be expressed as:

(1.8-13)

$$I = f(Vo+V\omega.\cos\ \omega t)$$

where f(Vo) is the junction characteristic at bias voltage Vo, $V\omega$ is the modulation amplitude at frequency w.

The second harmonic current $I_{2\omega}$ at a bias voltage Vo is:

(1.8-14)

$$I_{2\omega} = \frac{1}{\tau}\int_{\tau} f(Vo+V\omega.\cos\ \omega t)\cos 2\omega t\ dt$$

where τ = period of oscillation, $\cos 2\omega t$ is the second harmonic voltage component (see (1.6-7))

Substitution $U = V\omega\ \cos\ \omega t\ dt$

and $dU = -\omega V\omega[1-(U^2/V\omega^2)]^{\frac{1}{2}}\ dt,$

(1.8-14) becomes:-

(1.8-15)

$$I_2\omega = \frac{1}{2\pi V\omega} \int_{-V\omega}^{+V\omega} -f(Vo+U)\ \frac{2U^2-V\omega^2}{(V\omega^2-U^2)^{\frac{1}{2}}}\ dU$$

Integrating twice by parts to obtain f"(Vo+U)

Once

(1.8-16)

$$2\pi V\omega I_2\omega = O - \int_{-V\omega}^{+V\omega} f'(Vo+U)\ \ U(V\omega^2-U^2)^{\frac{1}{2}}\ \ dU$$

(substituting $V\omega^2-U^2 = z$

and $-2UdU = dz$ gives

$$2\pi V\omega I_2\omega = \frac{1}{z}\int z^{\frac{1}{2}}\ dz\ )$$

Twice

(1.8-17)

$$2\pi V\omega I_2\omega = \int_{-V\omega}^{+V\omega} f"(Vo+U)\ \frac{(V\omega^2-U^2)^{\frac{3}{2}}}{3}\ dU$$

finally:

(1.8-18)

$$F"(Vo) = \int_{-V\omega}^{+V\omega} f"(Vo+U)\ \Phi\ (U)dU$$

where: (1.8-19)

$$\Phi(U) = \frac{8}{3\pi V\omega^4}\ (V\omega-U^2)^{\frac{3}{2}}$$

for $|V| < V\omega$ and 0 otherwise

[The substitution of (1.8-19) into (1.8-17) to obtain (1.8-18) is a complete mystery and is due entirely to Leger (88).]

The experimentally observed quantity F"(Vo) is a convolution product of the exact second derivative f"(Vo+Vωcosωt) with an instrumental broadening function Φ(U).

(1.8-20)

$$F'' = f'' \otimes \Phi(U)$$

where ⊗ denotes convolution

The function (1.8-19) is plotted in Figure (1.8-3). The full width half maximum is 1.22eVω, and as expected, is zero outside the range $|eVo| \geq eV\omega$. Table 1.8-2 shows the broadening due to (1.8-19) for a series of modulation voltages.

Thus the observed second harmonic signal is a double convolution of the spectral weight function $D^S(\hbar\omega)$ with a thermal broadening function (1.8-10) and a modulation broadening function (1.8-19). The combined instrumental line widths are shown in Figure (1.8-4)

Table 1.8.2. Broadening at 4.2 K for a series of Modulation voltages, V_ω

V_ω (peak to peak) (in millivolts)	Broadening (cm^{-1})
1	9.9
2	19.7
4	39.5
6	59.0
8	79.0
10	98.5
12	118.0

Notes: (1) V_ω (peak to peak) = $(V_\omega^{r.m.s.})$. $\sqrt{2}$

(2) Actual linewidths arecalculated according to equation 1.8-21.

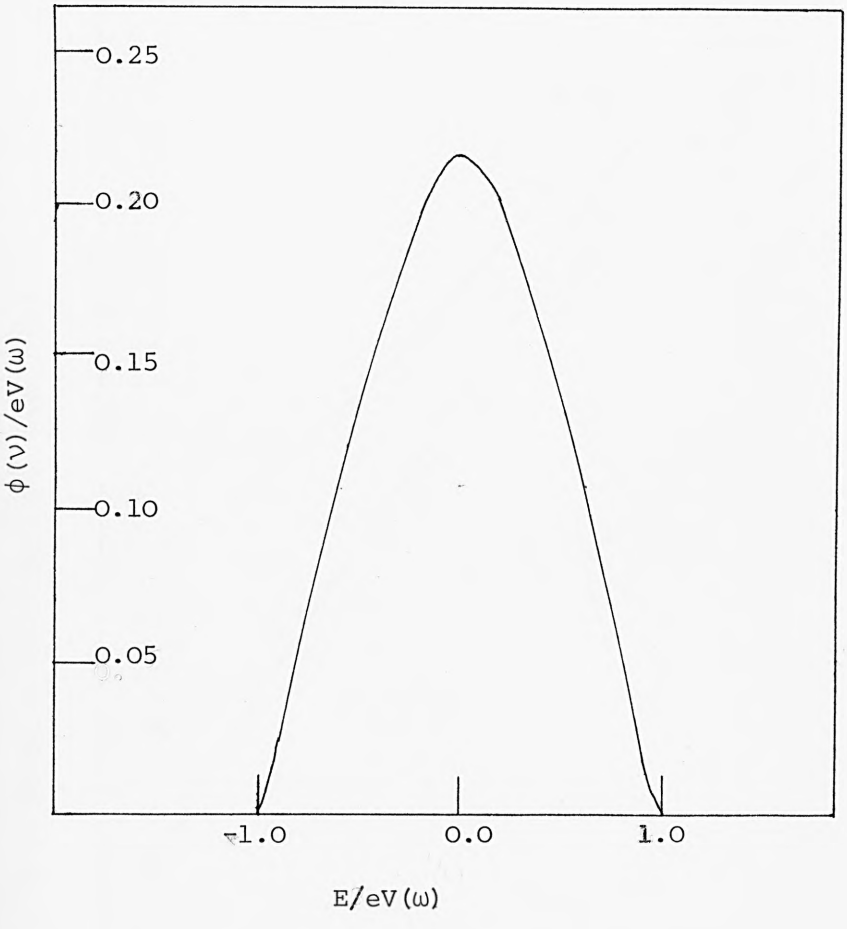

Figure 1.8.3. The modulation broadening function $\phi(u)$. The observed peaks are a double convolution of the spectral weight function $D^{s}(\hbar\omega)$ with the thermal broadening function F, and the modulation broadening function $\phi(u)$. (Reference 54)

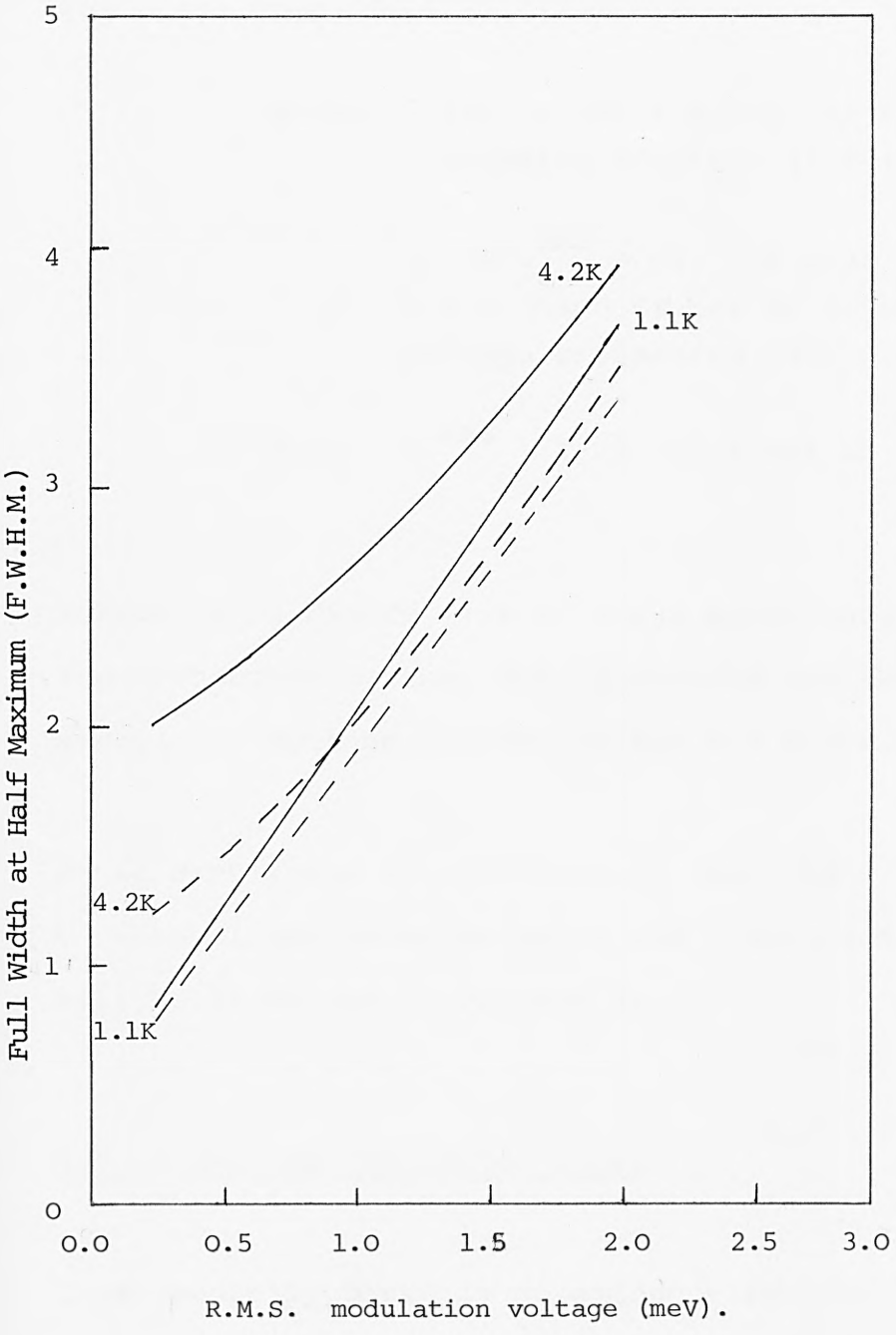

Figure 1.8.4. Instrumental linewidths for an infintiely narrow density of states with one electrode superconducting (----) or normal (———). (Reference 54).

The total instrumental width δV closely follows the expression (54).

(1.8-21)

$$\delta V = [(1.73eV\omega^{RMS})^2 + (5.4kT)^2]^{\frac{1}{2}}$$

where: 5.4kT is the f.w.h.m. of the thermal broadening function (1.8-10)

$1.73eV\omega^{RMS}$ = Wo, the peak width at T = O which is due to modulation voltage broadening (49).

Note: $V\omega^{RMS} = 1/\sqrt{2}\ V\omega$ (peak to peak)

Referring to Figure (1.8-4) for a metal-insulator-superconductor system, the linewidths are dominated by modulation voltage broadening for V > 0.5 mv.

As in many forms of spectroscopy there is a trade-off between signal-to-noise ratio and resolution; this will be discussed in Chapter 2.

1.9 Geometrical Selection Rules

Experimentally there is no evidence for any strong selection rules except for orientational selection rules. Thus providing the molecule is the correct orientation with respect to the surface of the electrodes, infra-red and Raman active vibrational modes are seen in

the tunnelling spectrum. This is consistent with the theoretical predictions discussed in sections 1.4 and 1.5.

The only aparent selection rules in evidence are of a geometrical nature. If a particular bond is parallel to the insulator surface then its vibration is not detected, or more precisely, the tunnelling electron interacts with the electron density in the bond either very weakly or not at all. If a bond is perpendicular to the oxide surface then its vibration (whether infra-red, Raman or both) is detected. (Figure 1.9-1). Thus, from the absence or presence of particular vibrations in a tunnelling spectrum it is possible to deduce the orientation molecule with respect to the oxide surface.

For example, the tunnelling and infra-red spectra of benzaldehyde are shown in part if Figure (1.9-2). In this energy region the positions of the major peaks are in agreement to a few tenths of a percent. However, two c=o bond modes, the asymmetric stretch at 1560 cm^{-1} and the symmetric strectch at 1435 cm^{-1}, are absent from the tunnelling spectrum but are both present in the infra-red spectrum. Field and Shott (55) have interpreted this evidence to suggest that the benzaldehyde chemisorbs onto the alumina surface "end on" with the benzene ring away from the surface (Figure 1.9-3). Supporting evidence for this orientation is threefold.

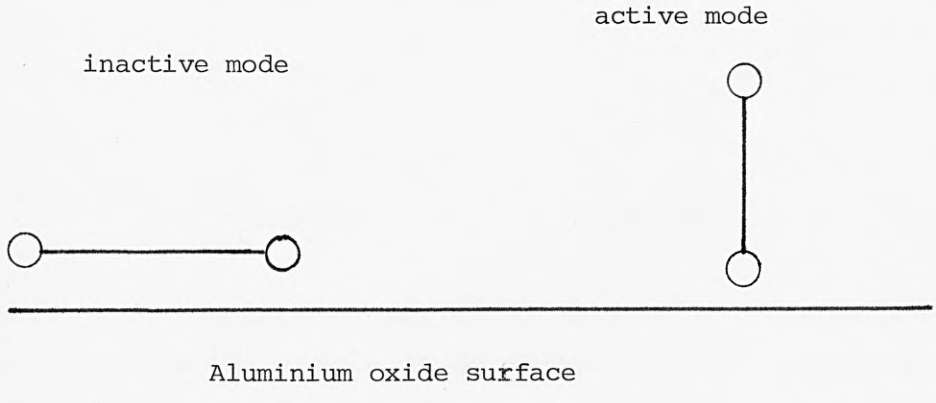

Figure 1.9.1. Orientational selection rules operating in I.E.T.S. Vibrational modes parallel to the surface are inactive and much weaker or non existent, whereas vibrational modes perpendicular to the surface give rise to strong peaks in the i.e.t. spectrum.

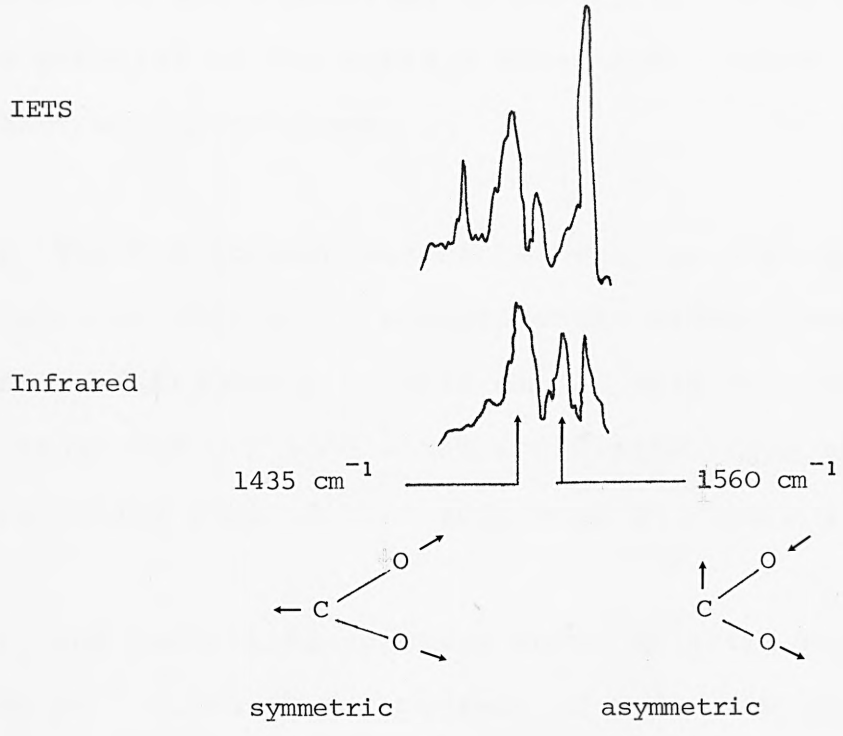

Figure 1.9.2. Comparison of IET and IR spectra of benzaldehyde on alumina. Note the absence of the asymmetric COO- stretch in the **IET** spectrum. (Reference 47).

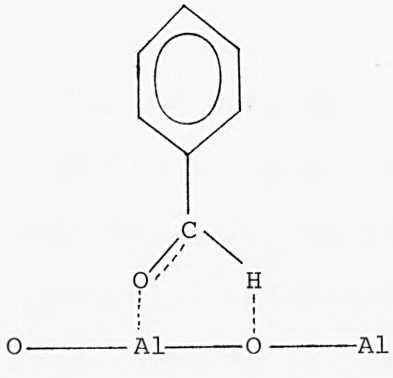

Figure 1.9.3. Proposed orientation of benzaldehyde on alumina surface. (After Field and Shott (55)).

(1) The ring vibration modes below 1600 cm^{-1} are present in the tunnelling spectrum, if the molecule was parallel to the surface these modes would be much weaker or non-existent.

(2) The C-H stretch associated with an aryl group is present at 2904 cm^{-1}, significantly higher than the infra-red frequency of 2820 cm^{-1}. This indicates a strengthened C-H bond which would arise from an orientation such as that indicated in Figure (1.9-3).

(3) The tunnelling spectrum shows an extra peak at 1331 cm^{-1} which is not present in the infra-red spectrum of aluminium benzoate. This suggests a structure in which the c=o bond is much weaker than it would be in the benzoate. Again this evidence supports the proposed orientation.

Another elegant piece of work that demonstrates the operation of orientational selection rules was performed by Field and Shott (56). Figure (1.9-4) is the molecular structure of N^3-benzoyl-3',5'-diacetyl-2'-bromo-2'-deoxyuridine. This compound is interesting since the two rings are perpendicular. The tunnelling spectrum of this compound (Figure 1.9-5) shows the carbonyl absorptions of the acetyl and benzoyl groups at 1629 and 1677 cm^{-1} respectively, and a band at 1072 cm^{-1} which is associated with the cyclic ether of ring 1.

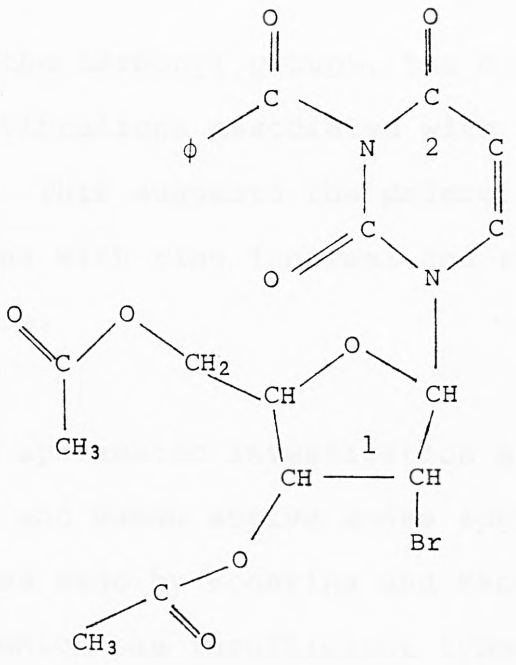

Figure 1.9.4. N^3-benzoyl- $3^1,5^1$-diacetyl-2^1-bromo-2^1-deoxyuridine. The two rings, 1 and 2, are perpendicular.

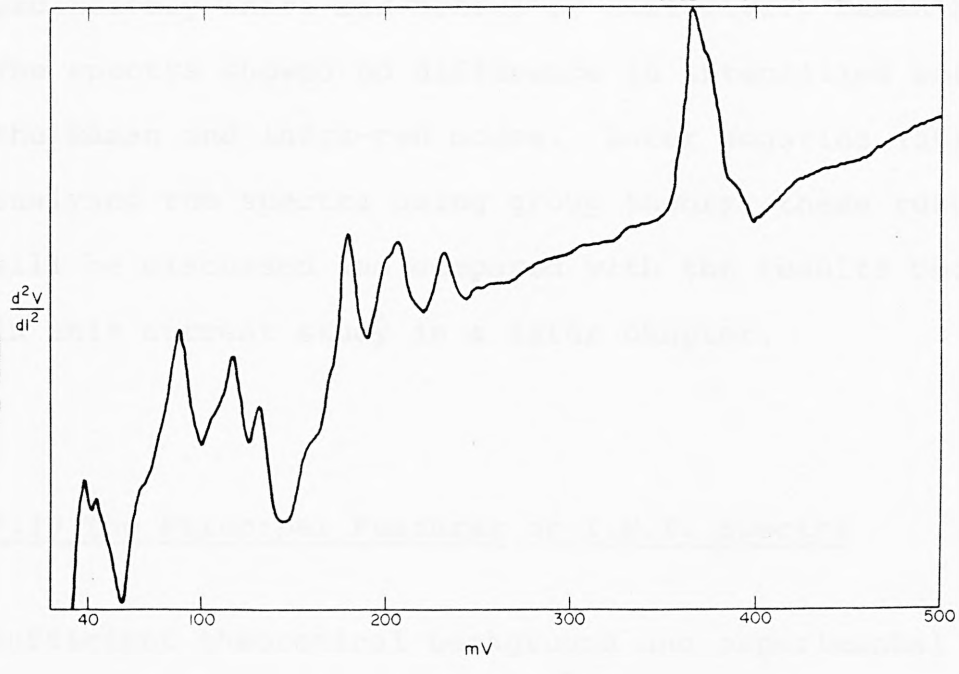

Figure 1.9.5. IET spectrum of the above molecule. (Reference 55).

However, the carbonyl groups, the C-N bonds and the skeletal vibrations associated with ring 2 are not observed. This suggests the molecule is adsorbed onto the alumina with ring 1 normal and ring 2 parallel to the surface.

The first systematic investigation as to whether both infra-red and Raman active modes appeared in tunnelling spectra was made by Bogatina and Yanson (57). In a molecule which has insufficient symmetry there are no vibrational modes which are exclusively infra-red or Raman active: both dipole moment and polarizability oscillate during its vibrations. Bogatina et. al. have made an attempt to study highly symmetrical molecules such as benzene, tetrachloromethane and acetone. These molecules have some vibrations which are either exclusively infra-red active or exclusively Raman active. The spectra showed no difference in intensities between the Raman and infra-red modes. Later Bogatina (56) analysed the spectra using group theory; these results will be discussed and compared with the results obtained in this current study in a later chapter.

1.10 The Principal Features of I.E.T. Spectra

Sufficient theoretical background and experimental effects have now been discussed to enable a series of I.E.T. Spectra to be presented and their principal features

examined in the light of the previous work.

1.10.1 An Undoped Spectrum

Figure 1.10.1 is a clean, undoped spectrum obtained from an aluminium-aluminium/oxide-lead junction at a temperature of 4.2K. At this temperature the lead electrode is superconducting and its superconducting gap and density of states effects are labelled A. The small peaks at 23 and 34 mv (185 and 274 cm^{-1} respectively) are due to aluminium phonons, (labelled B and C). Peak D at 120 mv (968 cm^{-1}) which was originally attributed to OH bending motions (32) is now believed to be predominantly due to aluminium oxide phonons, with the OH bending mode occuring as a small shoulder on the low voltage side of the peak (47). Peak E at 240 mv (1936 cm^{-1}) is the first overtone of the OH bend, Peak F at 450 mv (3630 cm^{-1}) is the OH stretch. At first, it seems unusual that an apparently clean spectrum exhibits any peaks due to hydroxyl groups; since this implies that water has at some stage been introduced into the junction during its manufacture. The hydroxyl groups are present in all spectra and as yet it has not been possible to produce a junction without these peaks: even with ultra-high vaccuum chambers. The gently sloping background is due to elastic tunnelling effects.

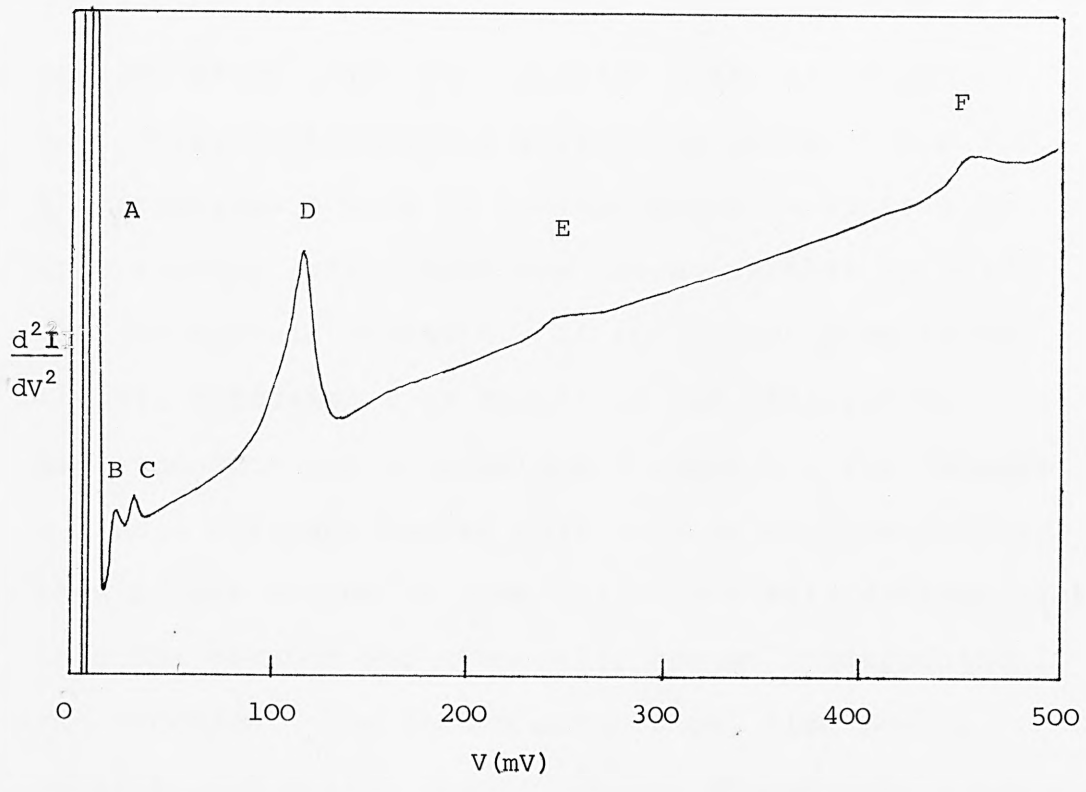

Figure 1.10.1. Idealised IET spectrum of a clean, undoped Aluminium-aluminiumoxide-lead junction at 4.2K The peaks are as follows:

A: 0-20 mV. Density of states effects.

B: 23 mV Al phonon.

C: 34 mV Al phonon.

D: 120 mV Al-oxide phonon. (OH bend as shoulder on low-voltage side.)

E: 240mV.OH bend, first overtone.

F: 450mV. OH stretch.

1.10.2 Contamination

Contamination which is a problem with all sensitive analytical techniques is especially acute in I.E.T.S. The principal source of contamination in tunnelling spectroscopy arises from the vacuum chamber in which the junction is prepared. If the vacuum pump is of the oil diffusion type and it is not efficiently isolated from the preparation chamber by, for example, a liquid nitrogen cooled cold trap or chevron baffle, then minute traces of pump oil vapour will diffuse back into the chamber and eventually become incorporated in the junction. The vacuum chamber may also become contaminated whilst exposed to the atmosphere, contamination arising from organic impurities in the laboratory atmosphere. Before junction preparation commences the vacuum chamber is cleaned up using a high voltage discharge in a pure oxygen atmosphere. Figure 1.10.2 shows hydrocarbon contamination resulting from backstreaming pump oil contaminating the preparation chamber and the junction. (It is worth noting that the vacuum system constructed and used for the work presented here utilises a turbomolecular vacuum pump which does not use oil as a pumping medium and is, therefore, not susceptable to backstreaming problems.) The extra structure in Figure 1.10.2 is due to pump oil on a conventional diffusion type vacuum system. The peaks at 90, 175 and 360 mv are the C-H rocking, bending and stretching modes of the contaminating oil.

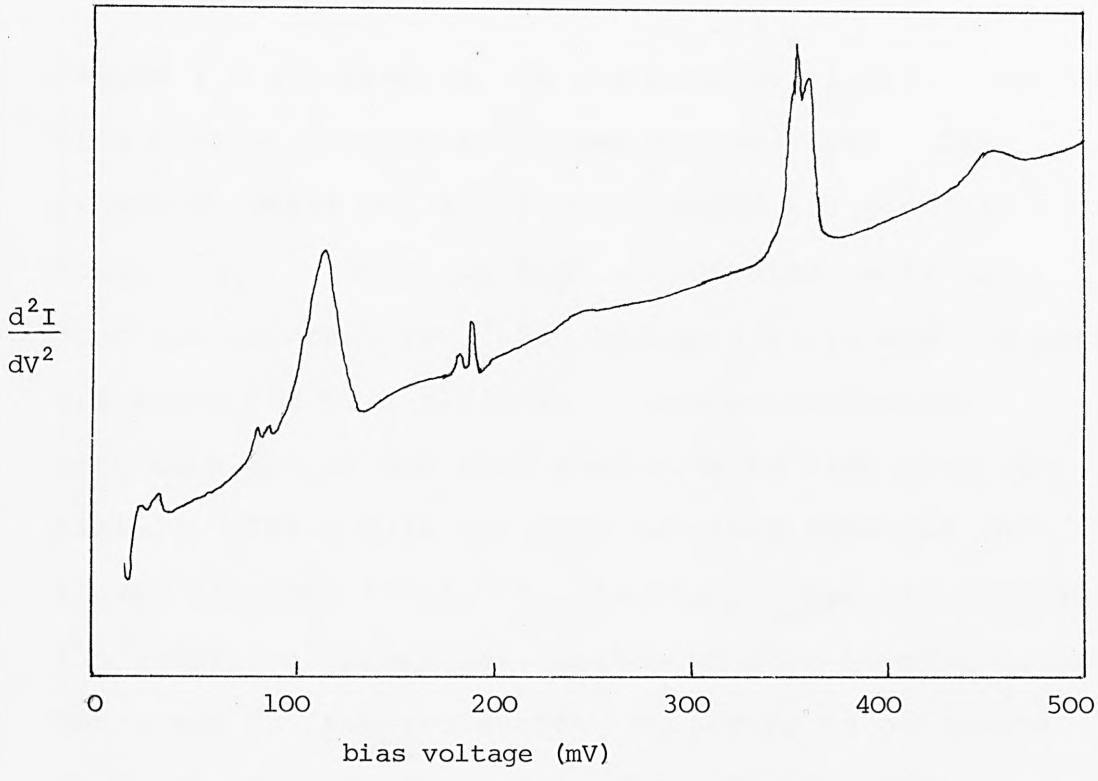

Figure 1.10.2. Tunnelling spectrum showing hydrocarbon contamination due to pump oil backstreaming into the chamber. The extra structure at 90, 175, and 360 mV are the C-H rocking, bending and stretching modes. (Compare with figure 1.10.1.)

1.10.3 Benzaldehyde

Figure 1.10.3, Trace A, is the complete I.E.T. spectrum of a typical organic molecule, benzaldehyde. The principal peaks and their assignments are given in Table 5.1. This spectrum was obtained with the junction immersed in liquid helium (4.2K), and the peaks are sharp and well defined. The superconducting structure due to the lead electrode is also clearly visible. Trace B is the same junction immersed in liquid nitrogen (77K). All resolution has disappeared: the individual peaks have coalesced into several broad bands and the superconducting structure is no longer present. Finally Trace C is the same junction at 298K; all traces of peaks have now been smeared out. These three spectra (A, B and C) dramatically illustrate thermal broadening operating in inelastic electron tunnelling spectroscopy.

1.10.4 Anthracene

Anthracene is a highly symmetrical molecule (point group D_{2h}). Consequently, the infra-red and Raman(and some optically forbidden) vibrations all occur separately. Figure 1.10.4 shows the I.E.T. spectrum of anthracene with the infra-red and Raman absorptions occuring with comparable intensity: a result which is in agreement with the theoretical interpretation discussed in Section 1.4.

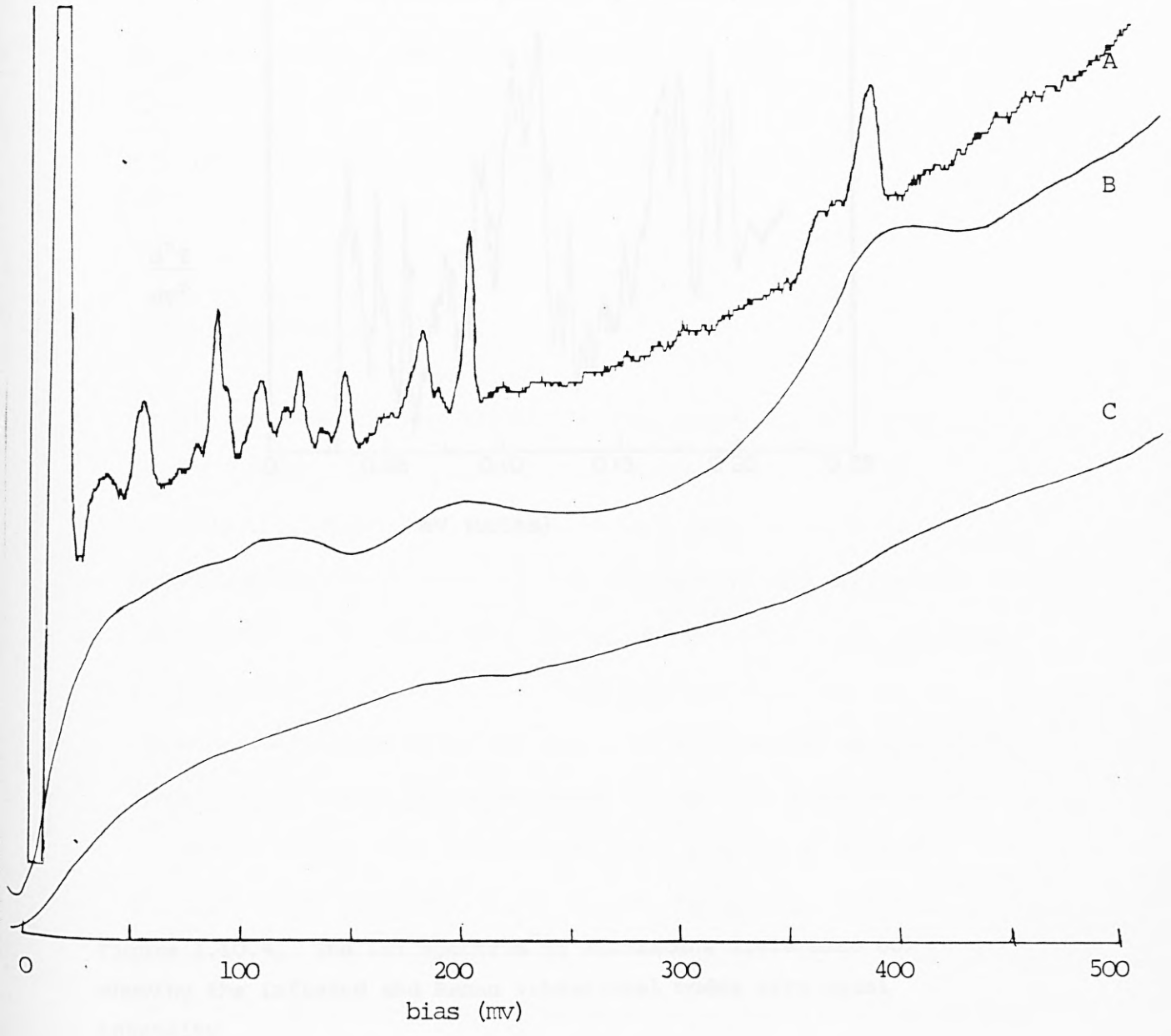

Figure 1.10.3. Benzaldehyde spectrum at three different temperatures showing the effect of temperature on resolution.

Trace A: 4.2K

Trace B: 77K

Trace C: 298K

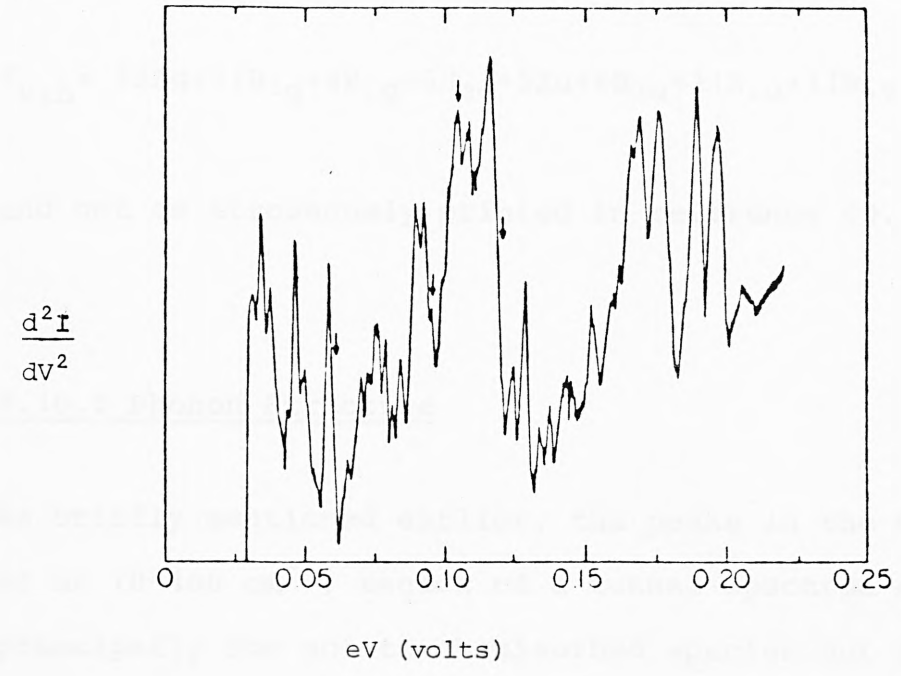

Figure 1.10.4. The IET spectrum of anthracene (reference 60) showing the infrared and Raman vibrational modes with equal intensity.

The correct irreducible representation for the vibrations of anthracene is:-

$$\Gamma_{vib} = 12Ag+11B_{1g}+4B_{2}g+6B_{3g}+5Au+6B_{1u}+11B_{2u}+11B_{3}v$$

and not as erroneously printed in reference 60.

1.10.5 Phonon Structure

As briefly mentioned earlier, the peaks in the 0 to 50 mv (0-400 cm^{-1}) region of a tunnel spectrum are principally due not to chemisorbed species but to quantised crystal lattice vibrations of the oxide and electrodes i.e. Phonons. Under an applied bias voltage V, elastically tunnelling electrons arrive in the second metal electrode in excited states above the fermi level, E_f. Upon relaxing back to E_f, if they have the correct energy, the electrons will excite a phonon. Only phonons excited by electrons relaxing in the vicinity of the insulator-metal interface are observable in I.E.T. spectroscopy. Phonons have been studied using tunnel junctions fabricated from many different metals (59, 61, 62, 63). Figure 1.10.5A shows a series of regularly spaced peaks which are due to the excitation of one, two and three transverse acoustical (T.A.) phonons in the lead electrode (64). The longitudinal acoustical (L.A.) phonon at 8 mv (64 cm^{-1}) of the lead,

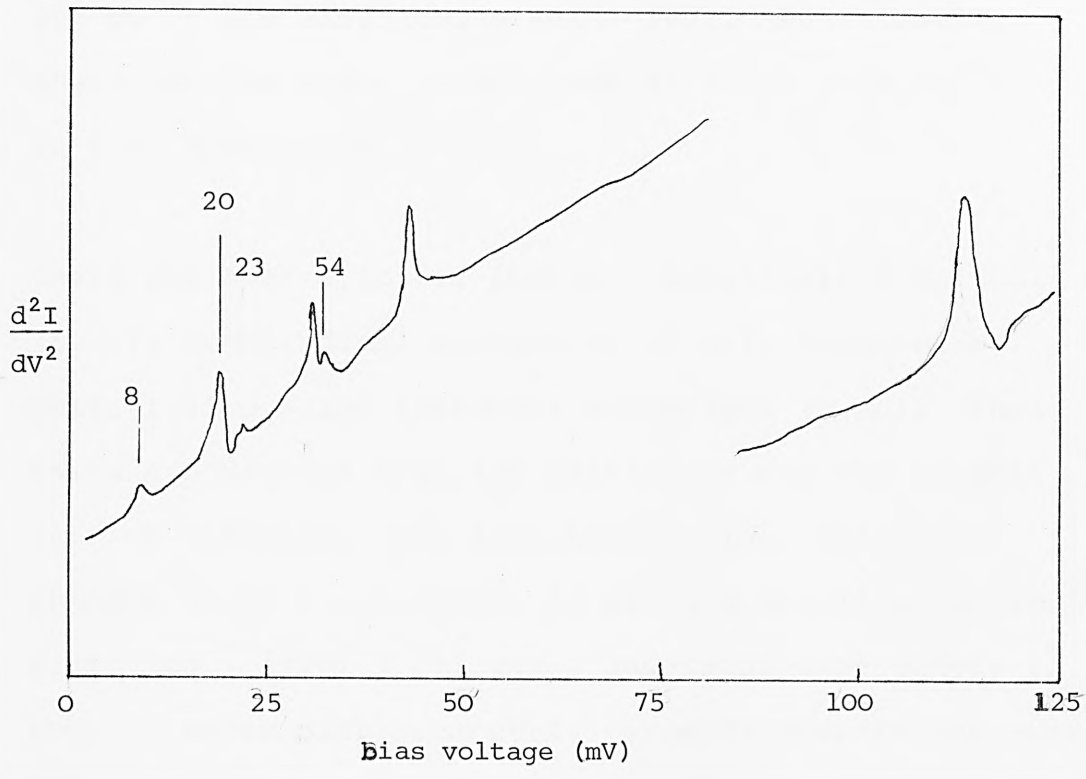

Figure 1.10.5.a. Detailed phonon structure of an Al- Al oxide- Pb tunnelling junction at 1.6K with both electrodes superconducting. (After references 59 & 64.)

and the aluminium phonons at 23 and 34mv (185 and 258 cm^{-1}) are also just visible (64). Additionally, the aluminium oxide phonon peak at 120mv (968 cm^{-1}) is also observable.

There are four types of phonon: Longitudinal Optical (L.O.); Longitudinal Acoustical (L.A.); Transverse Optical (T.O.) and Transvers Acoustical (T.A.). Their names are derived from the particular way the crystal lattice vibrates. The term Longitudinal refers to phonons whose displacement is along a specified crystal direction ([100] [110] etc), and Transverse refers to phonons whose displacement is perpendicular to the same direction. (Figure 1.10.5, B and C)

Optical and Acoustical denote the ways in which the crystal lattice vibrates. For example, in a lattice consisting of two different types of atoms per primitive unit cell (e.g.NaCl), then the two sorts of atoms can vibrate against each other or together. If the atoms vibrate against each other (their centres of mass remaining fixed) and the atoms are carrying opposite charges, then this type of phonon can be excited by the oscillation electric field of light wave and hence is termed Transverse Optical (Figure 1.10.5D). If the atoms vibrate with each other (and their centres of mass also), then the situation is similar to long wave-length acoustical vibrations and the phonons are termed

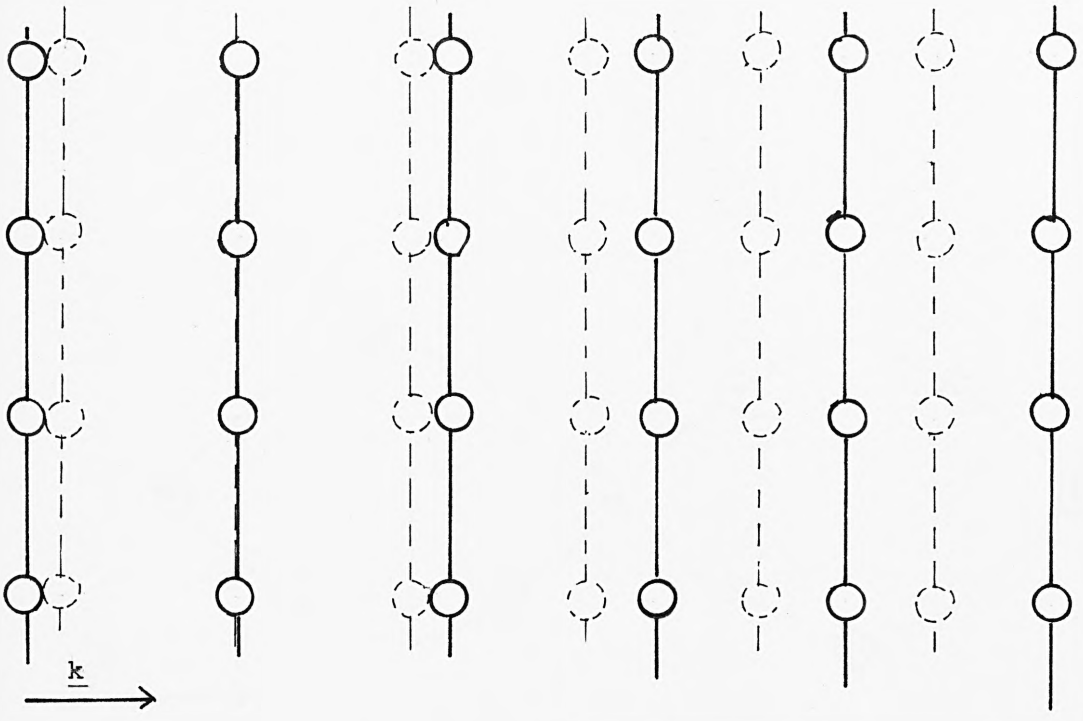

Figure 1.10.5.b. Longitudinal Phonon. The dashed lines are planes of atoms when in equilibrium. The solid lines show displacement due to longitudinal wave.

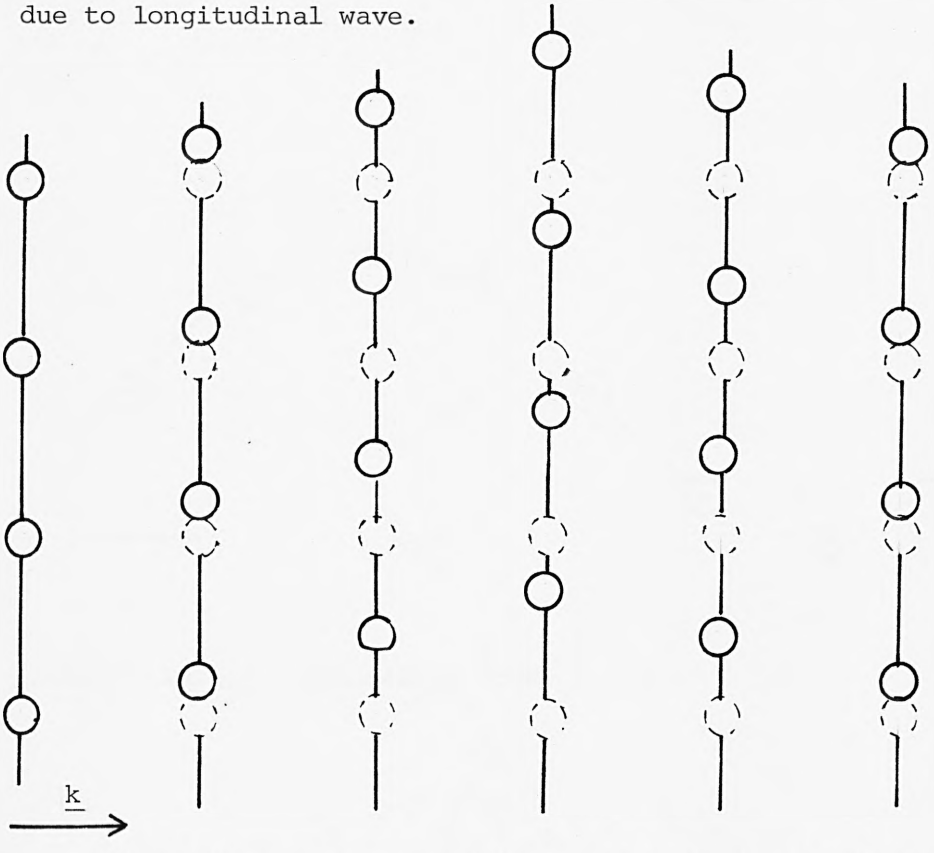

Figure 1.10.5.c. Transverse Phonon. Displacement of atoms is perpendicular to the crystal direction.

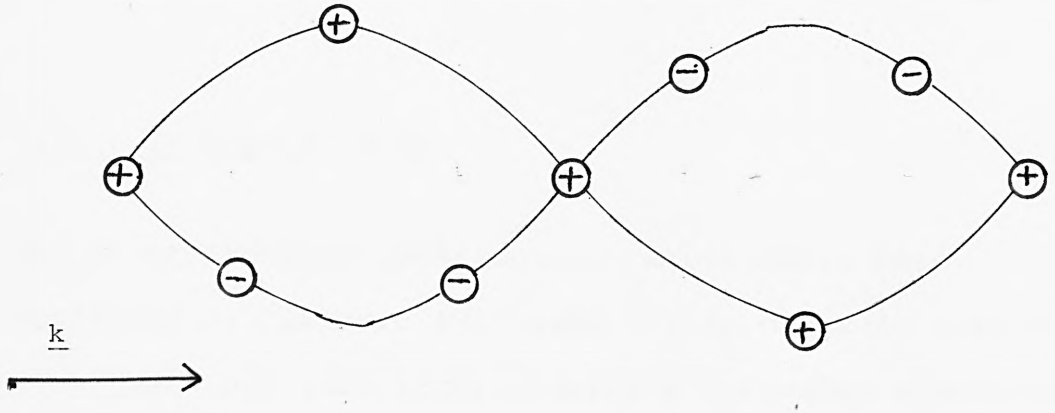

Figure 1.10.5.d. Optical mode .

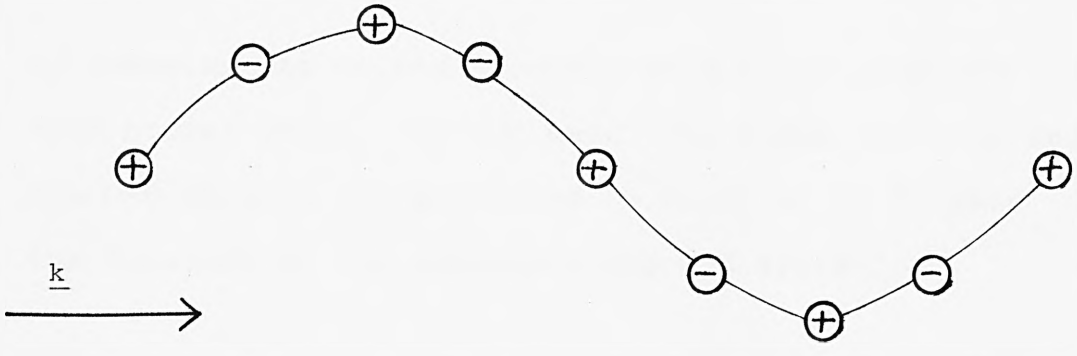

Figure 1.10.5.e. Acoustical mode.

Transverse Acoustical (Figure 1.10.5E). (A fuller account of phonons and their properties, especially concerned with layered structures can be found in references 84 and 85).

1.10.6 Isotope Effects

The first isotopic substitution experiments were performed by Jaklevic and Lambe (7) in order to establish that they were truly observing molecular vibrations. Trace A in Figure 1.10.6 is of normal acetic acid. Trace B is of deuterated acetic acid. Note in particular the C-D peaks near 275mv (2218 cm^{-1}) for approximately $1/\sqrt{2}$ times the position for the undeuterated sample.

If measurements on the spectrum of D_2o are compared with normal water, the O-D bend, its first overtone and the O-D stretch are all found to occur at $1/\sqrt{2}$ times the position of the corresponding O-H vibrations.

1.10.7 The Effects of Bias-Voltage Reversal

Trace A, Figure 1.10.7 is of a toluene doped aluminium-aluminium oxide-lead junction with the aluminium electrode biased negatively. Trace B is the same junction

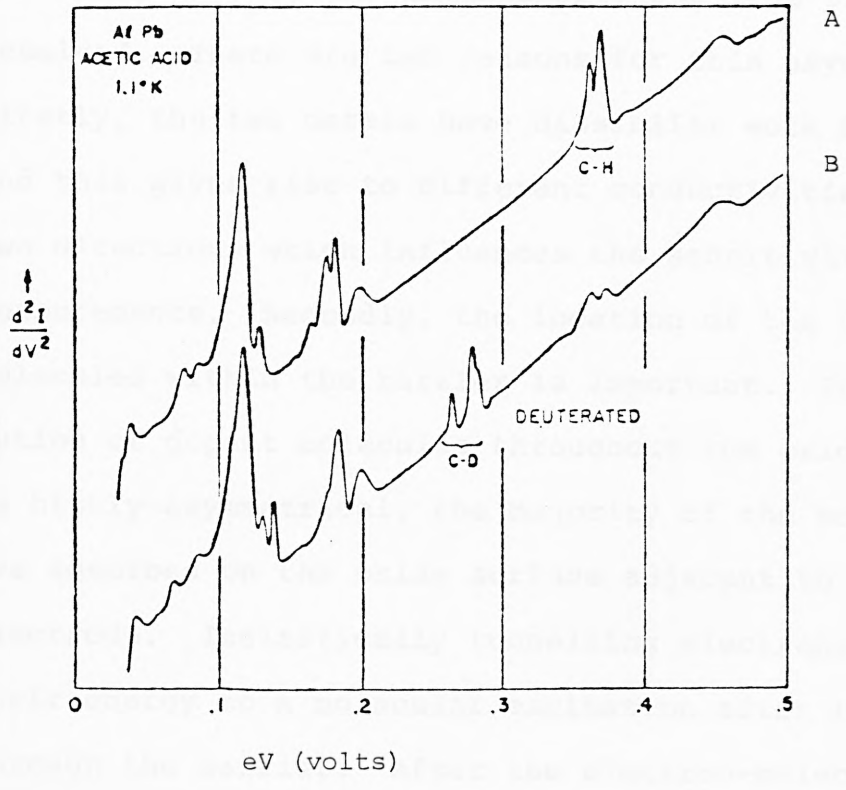

Figure 1.10.6. Tunnelling spectrum of normal acetic acid (traceA), CH_3COOH, and deuterated acetic acid (trace B), CH_3COOD.(Reference 32).

but with the d.c. bias voltage polarity reversed. The reversed biased spectrum exhibits peaks which although they occur at the same voltage as the forward biased peaks are much weaker in intensity and less finely resolved. There are two reasons for this asymmetry. Firstly, the two metals have dissimilar work functions and this gives rise to different conductivities in the two directions which influences the sensitivity of the measurements. Secondly, the location of the dopant molecules within the barrier is important. The distribution of dopant molecules throughout the oxide barrier is highly asymmetrical, the majority of the molecules are adsorbed on the oxide surface adjacent to the lead electrode. Inelastically tunnelling electrons give up their energy to a molecular excitation after tunnelling through the barrier. After the electron-molecule interaction the electron energy is now lower by a few tenths of an electronvolt, which is a few tenths of the barrier height. The probability that an electron has enough energy to traverse the remaining part of the barrier depends principally on the width of the latter. If the electron collides with a molecule after having traversed the barrier, the probability of detecting it is quite high (Figure 1.10.7A). Conversely, if the electron interacts with a molecular vibration and then has to tunnel through the barrier the probability of observing it is much smaller. (Figure 1.10.7B). Consequently, the forward-biased process illustrated in Figure 1.10.7A

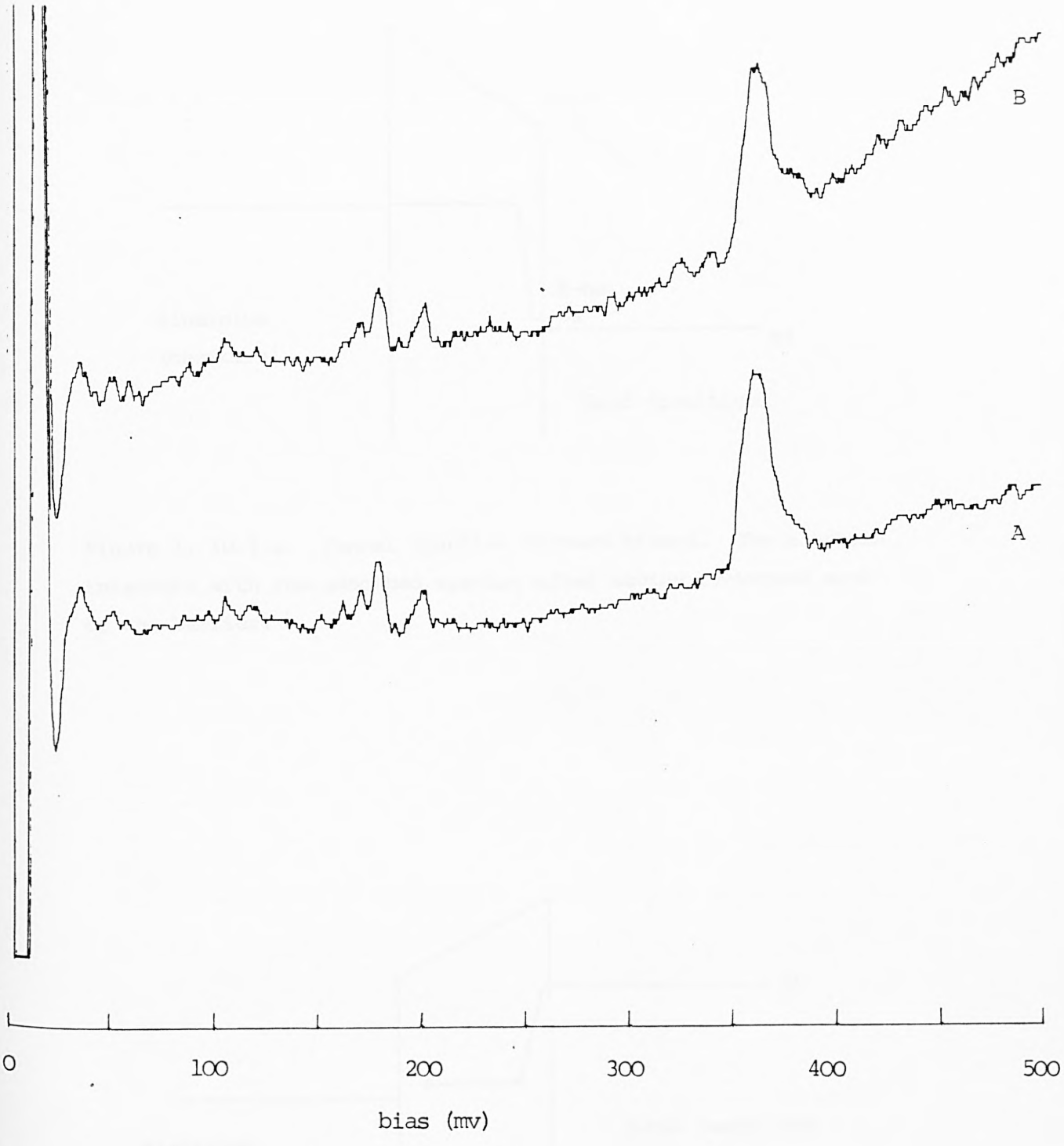

Figure 1.10.7. Toluene 4.2K.

Trace A: Forward biased, aluminium electrode negative.

Trace B: Reversed biased, aluminium electrode positive.

Note the broadening of the peaks and increased sloping baseline of the reversed biased spectrum.

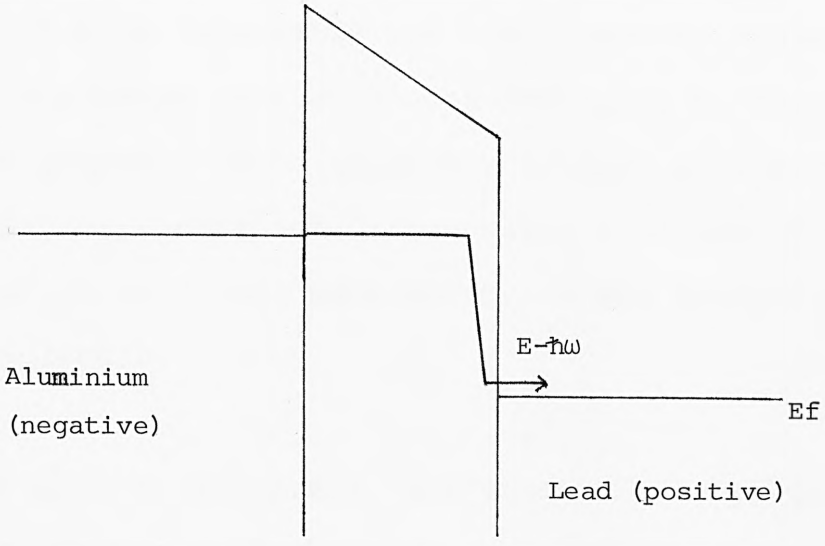

Figure 1. 10.7.a. Tunnel junction forward biased. The electron interacts with the adsorbed species after having traversed most of the barrier.

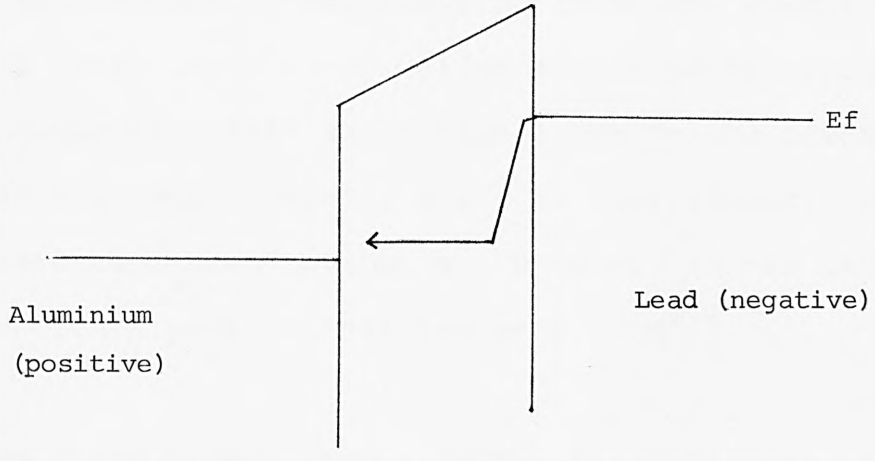

Figure 1.10.7.b. Reversed-biased tunnel junction. Electrons have to tunnel through the barrier after interaction with the adsorbate species.

is much more favourable for spectroscopic measurements. (The asymmetry obviously does not apply to the aluminium oxide phonon). Bias asymmetry is much more pronounced for higher excitation frequencies, principally because the electron looses more energy in its interaction with the molecule.

Consequently, all I.E.T. spectra are run by biasing the lower electrode (the one which is oxidised) negatively. Quantitative accounts of bias asymmetry are given in references 65 and 80.

1.11 Intensity as a Function of Surface Coverage

The theoretical ideas discussed in sections 1.4 and 1.5 all assume that the adsorbate-electron interaction is independent of neighbouring adsorbate species, and that there is no co-operative adsorbate behaviour. Consequently, this assumption leads to the prediction that the peak intensity ought to vary linearly with adsorbate concentration, n. However, it has been found that peak intensities vary as $n^{1.3}$.

Langan and Hansma (83) were the first workers to systematically investigate this non-linear dependence, using standard aluminium-aluminium oxide-lead junctions doped with tritium labelled benzoic acid. They found

that for sub-monolayer coverages the peak intensity decreases more rapidly than the surface concentration. This apparent anomaly can be explained quite easily. Doped junctions have a resistance of at least two orders of magnitude greater than undoped junctions; the tunnelling conductance through the insulator alone is much greater than through the insulator plus adsorbate. When the surface coverage is below a monolayer, there will be regions where the top electrode is in direct contact with the insulator only. Since the conductance per unit area through these undoped regions is much greater than through the doped regions, and assuming that only electrons which travel through a doped region excite the adsorbate molecule, then the fraction of inelastic electron tunnelling events (and hence the measured peak intensity) will decrease more rapidly than the surface coverage. From their experimental data, Langan and Hansma showed that the intensity of the peaks vary as $n^{1.3}$, where n is the surface concentration of the adsorbate molecules.

The non-linear dependence can be quantitatively understood if the collective behaviour of the adsorbate layer is taken into account. Such a simple model has been proposed by Cunningham and Weinberg (78).

Essentially, they assume that any coupling between vibrational modes of adjacent molecules is large enough

for the adsorbate layer to exhibit collective vibrational behaviour. The interaction between a tunnelling electron and the adsorbate layer is then of the form:

(1.11-1)

$$H_T = \sum_{ki}\sum_{kf}\sum_{q} \langle k_f | U(\underline{r},q) | ki \rangle$$

where ki, k_f are the initial and final states of the tunnelling electron,

$U(\underline{r}q)$ is the potential due to the qth vibrational mode the oscillating dipoles in the adsorbate layer at a point $\underline{r}$.

Due to the screening effect of the electrodes, $(U(\underline{r}q)$ only has a definite value in the insulating region, and is effectively zero in both electrodes. Consequently, only the wavefunctions in the barrier need be specified in order to calculate the matrix element in (1.11-1). This is conveniently evaluated using the Transfer Hamiltonian formalism described earlier (section 1.5). After obtaining an expression for $U(\underline{r}q)$ the total transition probability from all initial states to all final states where in the qth vibrational mode is generated, is calculated using the Golden Rule:

(1.11-2)

$$W_{i\to f}(q) = \frac{2\pi}{\hbar} \sum_{ki}\sum_{kf} |\langle kf | U(\underline{r},q) | ki \rangle|^2 \delta(E_f - Ei - q)$$

Finally, logarithmically plotting the magnitude of the transition probability as a function of adsorbate concentration, n, yields a line, which although not perfectly straight can be very closely approximated by a straight line of gradient 1.3. This theoretical result agrees to within 5% of the experimental results. However, for low surface coverages (less than 0.05 monolayer) the model is not valid: at such low coverages the adsorbate molecules are so far apart as not to exhibit any co-operative surface vibrational behaviour.

Using this model it is hoped that I.E.T.S. will be able to provide kinetic parameters valuable in chemisorption and heterogeneous catalysis; however, several objections are immediately obvious. Firstly, the oxide surface is not characterised well enough to determine the exact nature and number of active sites: different workers produce their oxides by different methods (elaborated in Chapter 2) and although this seems to have very little effect on the qualitative results obtained worldwide, it may prove to be a crucial factor in quantitative measurements. Secondly, the surface potential $U(\underline{r}q)$ will vary with the type and size of the adsorbate molecules and how it is bonded to the surface; clearly if any useful quantitative information is to be extracted from I.E.T. spectra, a much more detailed model would be an advantage. Alternatively, it should be possible to produce a series of standard spectra for each

particular dopant and oxide substrate, the surface concentrations having been determined by isotopic labelling using a similar technique to that described by Langan and Hansma (83).

1.12 Peak Shifts Due to Oxide and Upper Electrode Interactions

1.12.1 Upper Electrode Interactions

Although there is no evidence for any chemical reaction between the upper electrode and the dopant molecules, there is a physical interaction which, depending on the type of metal used, can cause a broadening and shift in the peak position by up to 5%. Figure 1.12.1 shows that the spectra of magnesium-magnesium oxide-gold and magnesium-magnesium oxide-lead junctions which have been vapour doped with H_2O and D_2O (66). The O-H stretching mode at450 mV and the OD stretching mode at 370 mV are both visible. However, both the O-D and the O-H vibrational frequencies for the gold upper electrode are broadened and shifted down by approximately 5% compared with the lead electrode. Peak shifts and broadening can be explained using the image-dipole concept discussed in section 1.4, and a more sophisticated theory by H. Morawitz (77).

An oscillating charge of frequency w, present outside the plane metal surface of the upper electrode induces

an image charge inside the metal. There is an attractive potential, U, between the charge and its image which is proportional to 1/d where d is the separation between the charge and the metal surface. The attractive potential will shift the oscillator frequency downwards. Assuming the molecules (in this example H_2O and D_2O) occur on non-equivalent sites on the oxide surface, then there will be an effective distribution of d values and consequently there will be a corresponding distribution of vibrational frequencies. The metals that produce larger overall peak shifts can be expected to have a larger distribution in peak shifts and thus larger bandwidths as shown in Figure 1.12.2. To give the experimentally observed peak shifts, d needs to be of the order of one Angstrom (66). Furthermore, the effective d values correlate with the atomic radius which suggests that metal with smaller atomic radii pack more closely around the adsorbate molecules and thus have smaller effective d values, and hence give a greater shift.

Thus tunnelling spectra with a lead top electrode have their peak positions shifted by about 2%. This shift could cause considerable difficulty expecially at lower energies ($\leqq$200mv or 1600 cm^{-1}) where there are a large number of vibrational modes, especially for organic

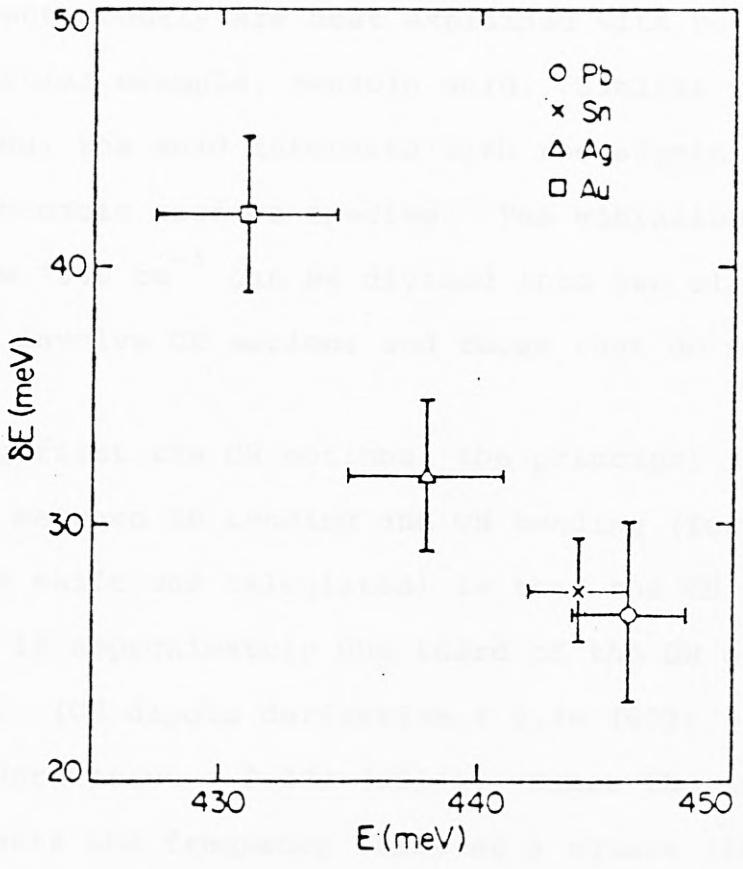

Figure 1.12.2. Plot of peak position against bandwidth (full width at half maximum) for the OH stretch on an aluminium- aluminium oxide junction with four different upper electrodes. Larger frequency shifts to lower energies correlate with larger bandwidths. (Reference 66)

molecules. Fortunately, this is not the case, and the observed shifts are much smaller. The reasons for this apparent anomaly are best explained with reference to a particular example, benzoic acid. Similar to benzaldehyde, the acid interacts with the aluminium forming a benzoic surface species. The vibrational modes below 1600 cm^{-1} can be divided into two classes: those that involve CH motions and those that do not.

Considering first the CH motions: the principal difference between CH bending and OH bending (for which the 2% peak shift was calculated) is that the CH dipole derivative is approximately one third of the OH dipole derivative. [CH dipole derivative $\cong$ 0.1e (67); OH dipole derivative $\cong$ 0.32e (68)]. Since the image dipole affects the frequency shift as a square (66), CH peak shifts can be of the order of a few tenths of a percent. When, infact, the position of a peak near 200 mv (1600 cm^{-1}) is measured, the difference in position between that of a normal lead electrode and that of a gold electrode is about 0.4mv (3 cm^{-1}). The position of the same peak measured by infra-red reflectance spectroscopy (i.e. with no upper electrode) is 0.2mv greater than for the value for lead (69). Considering the other modes of vibrations, principally the ring deformation modes, the effective mass is six times larger (the dipole derivatives are approximately equal to C-C and C-H bonds), and hence the peak shift

will be an order of magnitude smaller. Since the resolution is also of the order of 0.2mv (1.5 cm^{-1}) C-C and C-H peak shifts due to the upper electrode are not observed. This is a fortunate occurence since it renders compound identification by vibrational mode analysis and infra-red and Raman comparison directly possible.

1.12.2 Oxide Interaction

The consequences of adsorbate molecules chemically reacting with the oxide is far more important than upper electrode effects, since (as mentioned in section 1.9) valuable orientational information may be deduced. For example, the spectrum of formic acid, although directly comparable with the infra- red spectrum, gives all the peak positions at lower energies as for the infra-red data, also the carboxylate stretch near 220 mv (1774cm^{-1}) is absent in the I.E.T. spectrum. Klein and Leger (48) inferred from this absence that the acid had reacted with the surface giving a formate species. This would also explain the slight shift in the other frequencies. When the I.E.T. spectrum of formic acid was compared with an infra-red spectrum of sodium formate the peak positions were in much better agreement.

Even in the presence of minute traces of water,aluminium oxide becomes covered with hydroxyl groups (70). In-

fact, even the partial pressure of water at ambient temperatures is enought to saturate the oxide surface making it basic. One proposed interaction mechanism (81) of the surface and an acid is for one of the surface O-H groups to accept a proton from the acid and desorb as water. The remaining ion is ionically bound to the oxide surface.

The reactivity of the alumina surface is extremely useful. It is possible for example, to monitor reactions occuring on the oxide surface and examine the products and intermediates as they are formed (71, 72). The precise nature of the oxide surface is discussed in Chapter 3.

1.13 Alternative Electrode-Insulator Systems

Although aluminium-aluminium oxide-lead tunnel junctions are by far the commonest systems used for I.E.T.S., other metal-insulator systems have been used yielding quite acceptable results. The other principal systems in use for I.E.T.S. are magnesium-magnesium oxide-magnesium (48) and aluminium-aluminium oxide-gold (54). Table 1.13.1 lists some of the metal-metal oxide systems that have been investigated: none of these systems are in common use in inelastic electron tunnelling spectroscopy, research work on these systems is primarily

concerned with other physical effects such as density of states experiments, interband tunnelling, superconductivity and Josephson effects, both a.c. and d.c. Other insulators such as nitrides (89), rare earth sulphides and selenides (74, 90) and micas (91) have been used to fabricate tunnel devices, but they have only been used for studying the solid state effects mentioned above and not as a junction system for inelastic electron tunnelling spectroscopy. However, Burrafato et. al. (75) have investigated tunnelling junctions using a nominally 75 Angstrom thick layer of polyvinyl formate (Formvar) as the insulator. As yet their investigations have been confined to low bias voltages $\leqq$500mv ($\leqq$4000 cm^{-1}) at such energies only the vibrational modes of the insulator are observed. It may be possible to use the formvar insulator junctions at much higher bias voltages than conventional aluminium oxide tunnel junctions and hopefully observe electronic transitions of adsorbed species. As yet, no such results have been published.

1.14 The Energy Range of I.E.T.S.

This chapter has primarily been concerned with the lower energy region of tunnelling spectroscopy focusing on the vibrational spectra of molecules which occur at bias voltages of 500mv (4032 cm^{-1}) or below.

Theoretically, there is no reason why it is not possible to examine the higher inelastic electron tunnelling range (>4032 cm^{-1}) and examine the lower lying electronic transitions. (Jaklevic and Lambe (7) have observed an overtone of the O-H vibration at about 930mv, but no electronic transitions). The major obstacle to scanning higher energy regions is the dielectric strength of the insulator. At a bias voltage of two volts a 50 Angstrom thick insulator is supporting an electric field strength of 4×10^8 volts per metre, which is very close to the insulators dielectric breakdown voltage. Applying a bias voltage greater than about 2.2 volts to a standard aluminium-aluminium oxide-lead junction will cause the insulator to break down, irrepairably damaging the junction.

Consequently, using normal metal-metal oxide-metal junctions, the highest energy range attainable is governed by the dielectric strength of the insulator, and is usually limited to about 2.2 volts ($\cong 17{,}750 cm^{-1}$). Even so low lying electronic transitions (below 2.2 volts) have been studied (73, 86, 87, 102). However, because of enhanced conduction at greater bias voltages the second derivative technique is much less sensitive.

Leger and Klein (73) have observed electronic transitions in several large molecules including copper phthalocyanine, tetracene and β-carotene. Figure 1.14.1 is the I.E.T.

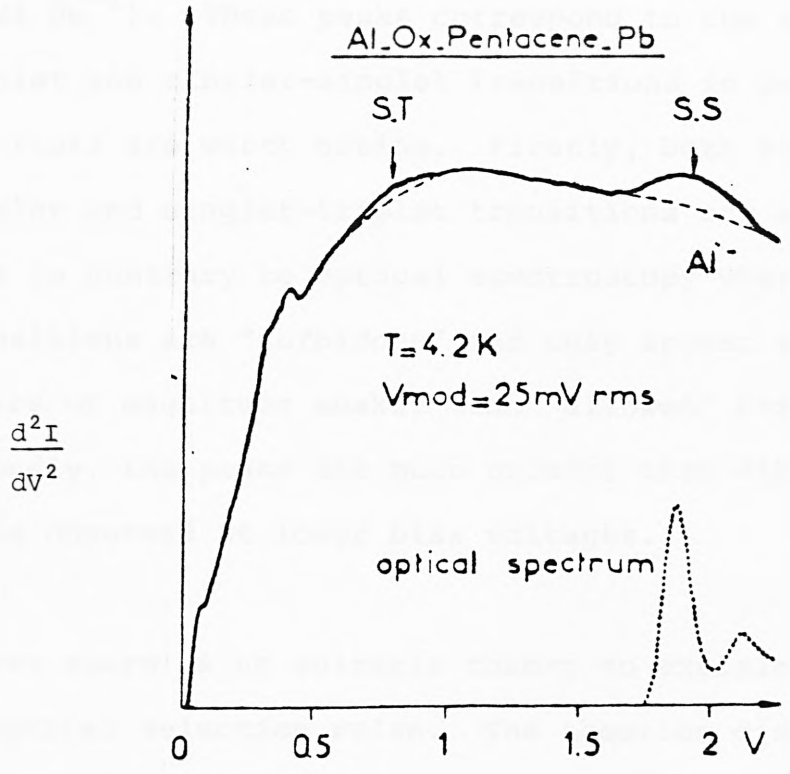

Figure 1.14.1. Tunnelling spectrum of pentacene over the bias range o to 2 volts. The S-T transition at 0.9 volts and the S-S transition at 1.9 volts are clearly visible. (Reference 86)

spectrum of pentacene in an aluminium-aluminium oxide-lead junction. The main features of interest are two small broad peaks at 0.9 and 1.9 volts (7260 and 15325 cm^{-1}). These peaks correspond to the singlet-triplet and singlet-singlet transitions in pentacene. Two facts are worth noting. Firstly, both singlet-singlet and singlet-triplet transitions are abserved. This is contrary to optical spectroscopy where S-T transitions are "forbidden" and only appear several orders of magnitude weaker than "allowed" S-S transitions. Secondly, the peaks are much broader than vibrational peaks observed at lower bias voltages.

As yet there is no suitable theory to explain the lifting of optical selection rules. The theories discussed in sections 1.4 and 1.5 which are based on a dipole model, showed that the inelastic conductance was proportional to the square of the matrix element taken between the initial and final states. However, when these calculations are performed, (taking into account the observed changes in inelastic conductance) for electronic transitions an oscillator strength is obtained which is an order of magnitude larger than the value obtained for the same compound by optical methods. This disagreement has led workers to conclude that the change in inelastic conductance is not a good measure of the intensity of transition at high energies.(86, 102).

The broad peaks observed in electronic transitions are probably due to co-operative thin film behaviour of the adsorbate. Figure 1.14.2 shows the optical and tunnelling spectra of xenocyanine. In the optical spectrum (which was made from a solution) the peaks are much narrower than the thin film spectrum which suggests the broadening effect is caused by surface interaction between the oxide and the adsorbate molecules.

In conclusion, it seems that inelastic electron tunnelling spectroscopy will be confirmed to the 0 to 2 eV energy range unless a dielectrically stronger insulator can be found. Apart from the alternative insulators mentioned in section 1.13, Adane et. al. has proposed the use of a fluoride insulator (102). However, as yet no results have been published.

Table 1.14 summarises the principal types of interaction in I.E.T.S. and the energy region in which they occur.

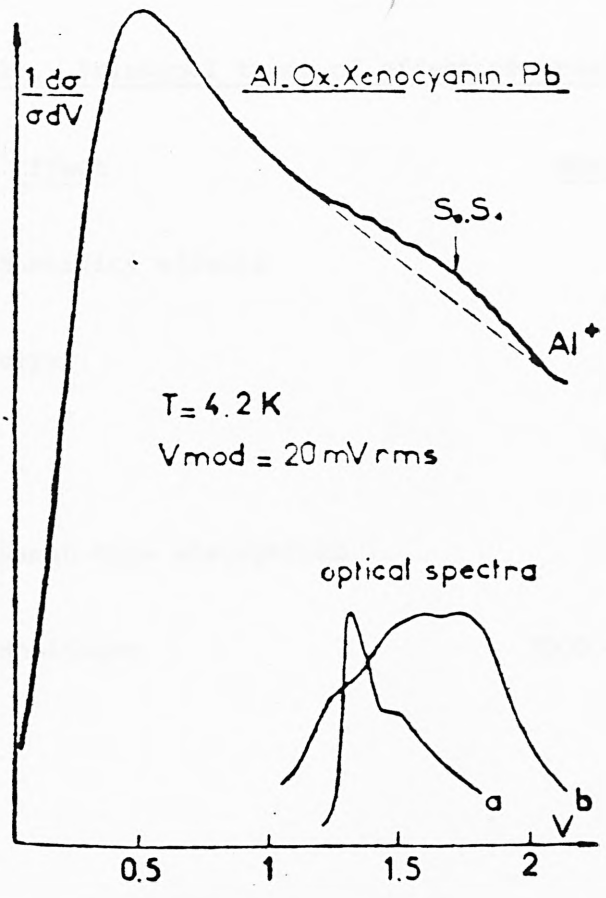

Figure 1.14.2. The optical and IET spectra of xenocyanine at 4.2K. Note the large modulation voltage. (Reference 86)

Table 1.14. Principal types of effect observable in I.E.T.S.

Effect	Energy (cm^{-1})
Zero-bias conductivity effects	0
Superconductivity	0-30
Phonons	0 - 400
Infrared and Raman-type absorptions	> 200
Electronic transitions	7000 - 18000

CHAPTER 2. EXPERIMENTAL CONSIDERATIONS

2.1 THE VACUUM SYSTEM

The preparation of tunnelling junctions requires a clean hydrocarbon-free, high vacuum system capable of attaining a pressure of about 10^{-8} torr with the provision for vacuum depositing metals and a means of accurately controlling gas pressure within the system. Furthermore, the system should have a reasonably fast pumpdown speed enabling a large number of junctions to be manufactured. One of the major influencing factors affecting the design of the vacuum system was the choice of a vacuum pump. Eventually a turbomolecular pump was chosen because of its advantages over more conventional pumps.

The choice of a vacuum pump for the pressure region from 10^{-5} to 10^{-8} torr and below is limited to three types. Mercury or oil diffusion pumps, ion-getter pumps and turbomolecular pumps. Diffusion pumps will operate from about 10^{-4} torr and in practice achieve a minimum pressure of about 10^{-7} torr, ion-getter pumps operate from about 10^{-3} to 10^{-8} torr, and turbomolecular pumps can reach a pressure of 10^{-9} torr from atmospheric pressure (113). Diffusion pumps suffer from several weaknesses, principally the backstreaming of oil vapour from the pump into the preparation chambers. Although

this can be minimised by using a liquid nitrogen cold trap, it means the system needs almost constant maintenance in the filling of the cold trap with liquid nitrogen and its periodic warming up to remove the condensed vapours in the trap. Oil-diffusion pumps are also susceptable to being accidentally exposed to atmosphere pressure. Prolonged exposure will cause the oil to crack depositing harmful organic residues throughout the vacuum system. Diffusion pumps are adequate if they are handled with care, however, with repeated pumping down from high pressures the oil soon becomes saturated with vapours and the pumping speed becomes much longer. An oil-diffusion pump based vacuum system also requires a backing pump and a roughing pump to evacuate the chamber to $<10^{-3}$ torr before the diff. pump can be used. The large number of vacuum lines and the necessity to water cool the diff. pump means that diffusion pump systems are often quite complicated (106).

Ion-getter pumps do not use oil as a pumping medium and thus provide a hydrocarbon-free vacuum pump. However, their pumping speed is slow and they are difficult to start at non-optimum pressures.

Finally, turbomolecular pumps (whose principle of operation is described in section 2.1.3) have many advantages over diffusion pumps and ion pumps. Since

they do not use a pumping medium (the only oil present is used to lubricate turbine bearings which, because of the fast pumping speed, cannot backstream) they provide a clean hydrocarbon-free vacuum. Turbomolecular pumps can also start pumping from atmospheric pressure, consequently accidental gas bursts cause no harm and recovery of a good vacuum is vary rapid. The turbo's ability to repeatedly pump down from a rough fore-vacuum very quickly (without showing any signs of fatigue) makes it ideal for use in a system which must be frequently let up to atmospheric pressure. Air-cooled turbomolecular pumps need only a mains electricity supply to function, and require only minimal maintenance: typically 14 hours in 25,000 running time, compared with 300 hours maintenance in the same period for a diffusion pump (113). Thus, a vacuum system based around a turbomolecular pump is simple and straight-forward to operate and requires a minimum of overall maintenance.

A turbomolecular pump based system was therefore chosen for this study, principally because of its short recycling time and its ability to provide a hydrocarbon-free vacuum.

Figure 2.1.1 is a schematic diagram of the vacuum system used in this project (see also photograph No. 1). It is

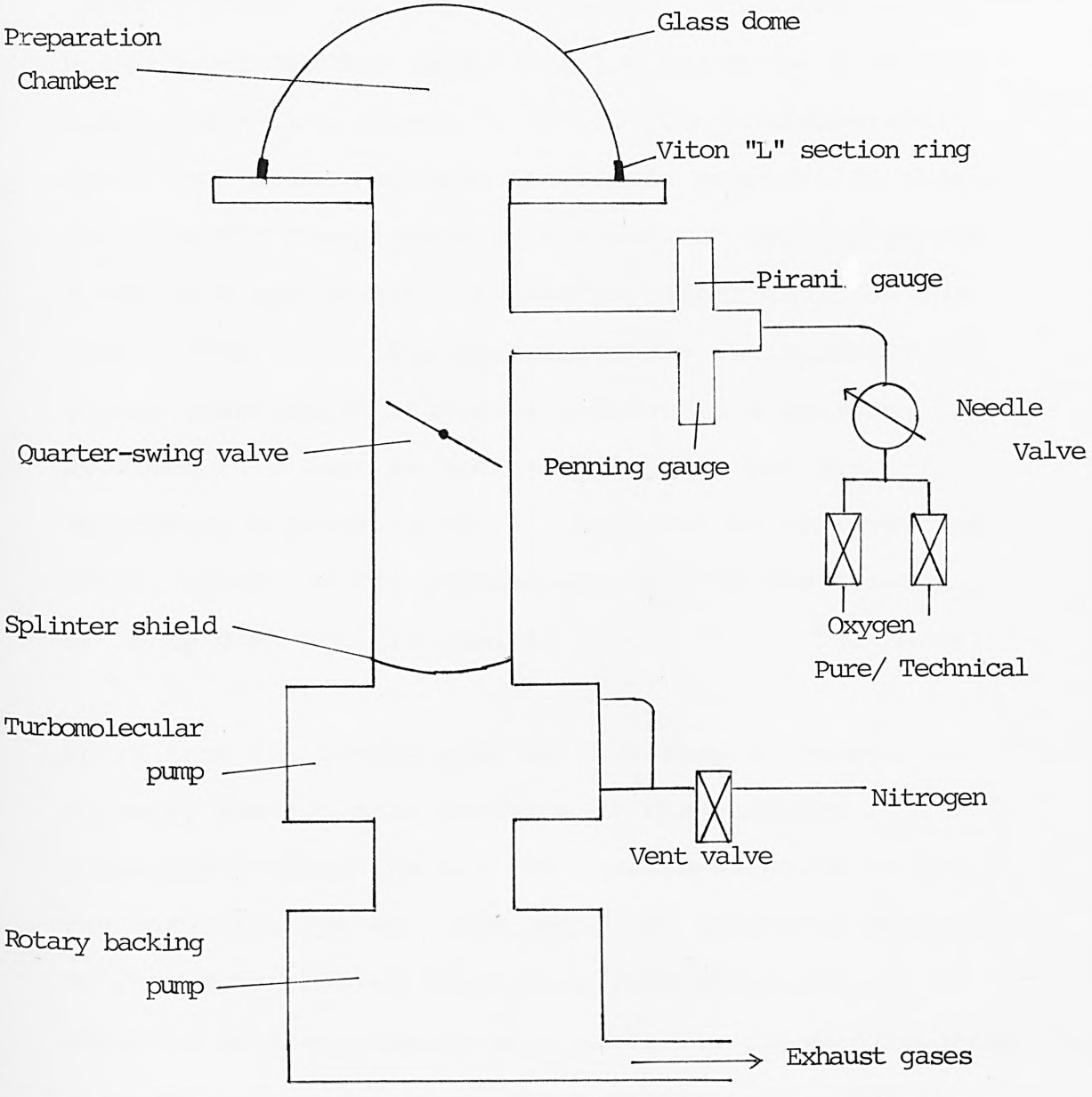

Figure 2.1.1. Schematic diagram of vacuum system.
(See also Photograph 1)

constructed entirely out of stainless steel except for the baseplate of the sample preparation chamber which is mild steel. All the high-vacuum joints are sealed with copper gaskets except for the column-to-baseplate joint which is a rubber 'o' ring. The hemispherical glass dome which encloses the sample preparation chamber seals to the baseplate with a viton 'L' section gasket. Viton is a compressable synthetic rubber designed for high vacuum work. The material has a sufficiently low vapour pressure to reduce de-gassing to a minimum. Provided this seal is treated with care and not scratched, a pressure of 10^{-7} torr can be achieved and after baking out the turbomolecular pump the system can pump down to less than 10^{-8} torr within two hours.

Apart from the vacuum pump and the sample preparation chamber, the two main features of the junction preparation apparatus are the quarter-swing valve and the gas inlet system. The gas inlet system is designed so that a controlled fixed flow rate of oxygen can be admitted to the preparation chamber for plasma-discharge cleaning and oxidation of the aluminium electrode to produce the insulating layer in the junction.

The oxygen source, technical grade for cleaning and ultra-pure for oxidation, is selected using the appropriate valve and the flow rate is adjusted using an Edwards fine control needle valve which permits a

continuously variable gas flow rate from zero up to a maximum of 0.09 litres a second. The flow rate is adjusted on an 18 turn dial. The dial controls a lever arrangement which pushes on a brass rod, the other end of which is honed to a fine needle. When fully closed, the needle seats against a brass collar. Turning the dial anti-clockwise raises the needle thus opening the valve. Three dial turns correspond to a vertical needle movement of ≅ 0.254 mm (0.01 inches) giving a flow rate of approximately 0.025 litres a second. The large rotary movement coupled to such a small vertical needle movement permits extremely fine control of the gas flow rate. When the needle valve was used for admitting gas into the chamber the dial was only opened about nine tenths of one turn (117).

In order for the gas to remain in the sample preparation chamber without being immediately removed by the turbo-molecular pump, (whose maximum pumping speed is 230 litres a second), the flow of gas to the turbo has to be throttled. When the vacuum system is operational, the turbo pump runs at a constant speed of 60,000 r.p.m.; because of its principle of operation it is not possible to reduce the pumping rate by slowing the rotor speed. Instead, the flow rate is reduced by a quarter-swing valve. This valve, which is situated half way between the pump and the sample chamber, consists of a circular

plate which is just smaller in diameter than the stack. The plate is pivoted about its diameter and can swing freely through 90 degrees from a position parallel to the air flow, to a position which almost completely blocks off the gas flow to the pump. Movement of the plate is achieved with a lever arrangment which is operated via a threaded pushrod. With the valve in position, it is possible to maintain a steady gas pressure of 10^{-1} torr above the valve in the sample preparation chamber.

2.1.1 The Junction Preparation Chamber

The junction preparation chamber (figure 2.1.2 and photograph No. 2) consists of the evaporation sources and an H.T. cathode. The evaporation sources are used for evaporating the aluminium and lead electrodes and the H.T. cathode (in the form of a ring) is used for creating a plasma discharge for oxidising the aluminium and also for removal of organic contamination in the vacuum chamber.

The aluminium evaporation source consists of a tungsten wire basket 1 cm in diameter which is positioned 3 cm below a stainless steel mask with a 3.5 cm long adjustable-width slit. The lead evaporation source

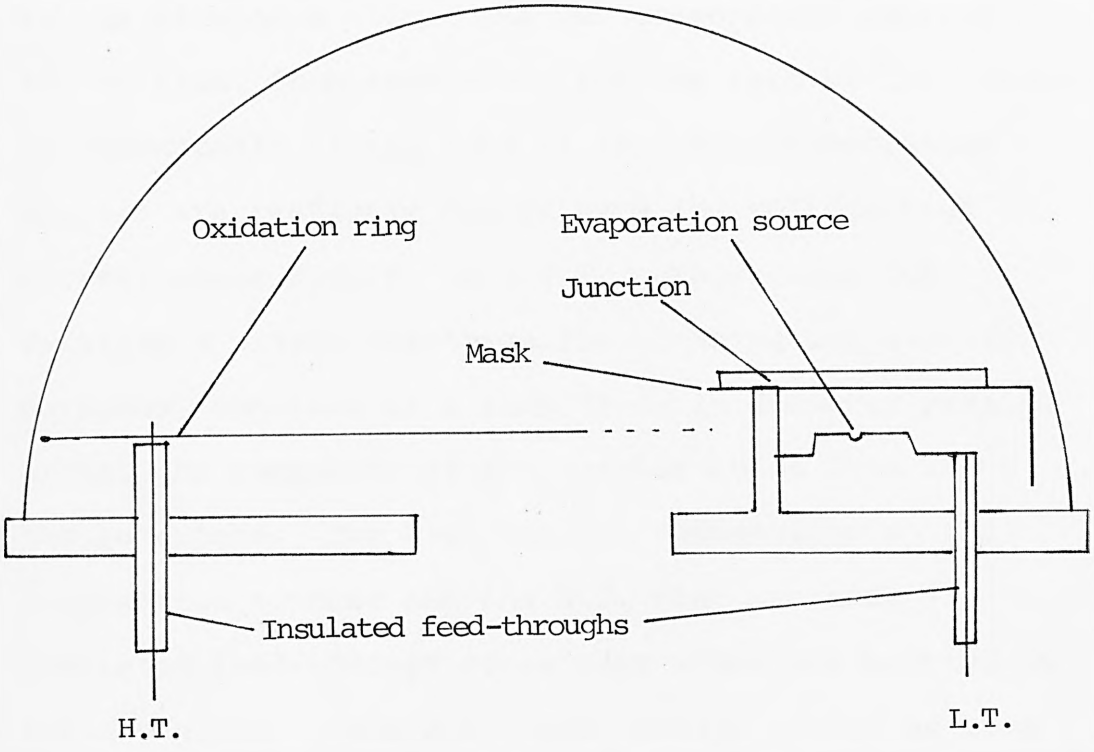

Figure 2.1.2. Schematic diagram of junction preparation chamber. (See also Photograph 2.)

consists of a molybdenum "boat" (a strip of molybdenum foil with a small dimple in it) which is again positioned 3 c.m. below a stainless steel mask with a 1cm long adjustable width slit. The lead slit is perpendicular to the aluminium slit. The two evaporation sources are shielded from each other and the rest of the chamber by demountable nickel foil masks. Both evaporation sources are restively heated by a low voltage high current power supply. The H.T. cathode used for creating a plasma discharge for cleaning and oxidation purposes, consists of a ring 15 cm in diameter passing around the perimeter of the chamber about 5 cm above the baseplate. The high current connections to the evaporation sources and the H.T. ring are made via insulated feed-through connectors which are mounted in the baseplate. (The H.T. feed through connector uses a pyrophylite insulator, whilst the L.T. insulators are p.t.f.e.) In addition to these high power connectors there is a small low power nine-way feed through. Three of these connectors are used to monitor the integrity of the aluminium electrode and measuring the junction resistance, and another two for a thermocouple.

The chamber itself is a 7 mm thick 32 cm diameter glass dome which is sealed to the baseplate with the viton 'L' section ring. This arrangement will permit east removal of the dome for access to the chamber and give an air

tight seal. To confine shattered glass to the vacuum chamber in the unlikely event of the glass dome imploding, it is covered with two layers of transparent cling film, which, so Edwards High Vacuum claim, will stop any glass splinters.

2.1.2 Pressure measurement

The vacuum system employs two pressure gauges, the heads of which are situated just below the junction preparation chamber on a 'T' section pipe which is also connected to a gas inlet pipe. The system requires two types of pressure gauge since there is no single gauge which will accurately measure the pressure from atmosphere to $< 10^{-8}$ torr. A Piranii gauge covers the pressure region from atmospheric to about 10^{-3} torr and a Penning ionization gauge is used for pressure measurement from 10^{-3} torr downwards to lower pressures.

The Piranni Gauge (115)

The Piranni gauge measures the variation in thermal conductivity of a gas as a function of pressure by measuring the resistance of a heated metal filament.

A coiled tungsten filament is heated by a small electric current (Figure 2.1.3). Eventually, the wire reaches an equilabrium temperature when the heat generated is balanced

by conduction, convection and radiation losses. Gas molecules striking the heated filament gain kinetic energy which they transfer to other molecules or the vessel walls. At a high pressure (≅ 500 torr) a large number of molecules are striking the filament whose heat losses are correspondingly high. At this pressure the mean free path of the molecules is short compared with the filament-wall distance, and nearly all energy transferred is by molecular collisions. In this pressure region heat losses are not proportional to pressure. As the pressure decreases the mean free path becomes comparable with the filament-wall distance and the heat lost is a complex function of pressure. When the pressure is below about 1 torr, energy losses by molecule-wall collisions become dominant and heat loss is directly proportional to pressure. Below a pressure of about 10^{-3} torr there are not enough molecules to cool the filament by collision, and it thus reaches an equilibrium temperature governed by conductive and radiative losses. The useful range of the Piranni gauge is between 1 and 5×10^{-3} torr. In this region heat loss from the filament (and hence the temperature of the filament) is proportional to pressure. The resistance of the filament, which will also vary linearly with pressure, can be measured using a wheatstone bridge circuit. (Figure 2.1.4)

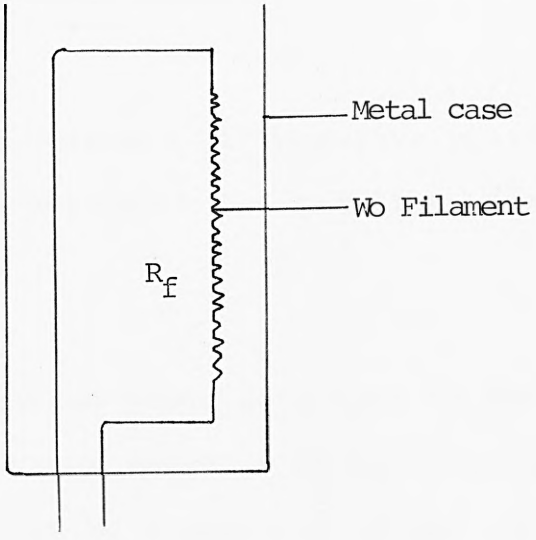

Figure 2.1.3. The Pirani Gauge.

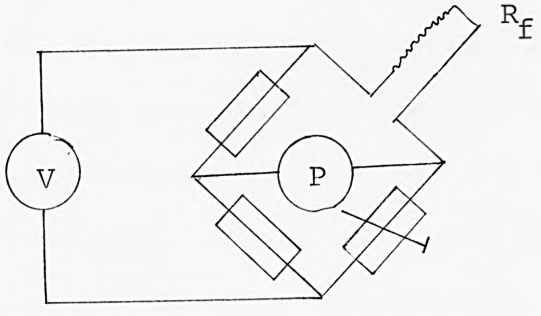

Figure 2.1.4. Wheatstone bridge used to measure variation in R_f.
P = Voltmeter calibrated in pressure units.

The Penning Gauge (116)

The Penning gauge measures air pressure by ionizing gas molecules and measuring the resulting ionization current.

In the cold ionization gauge developed by Penning there are two parallel rectangular cathodes about 15 x 40 mm separated by a space of 20 mm. A rectangular loop of thin wire situated halfway between the cathodes serves as an anode. There is a potential difference of 2 kV between the anode and cathode. The electrode assembly is housed in a permanent magnet which provides a magnetic field of about 400 Gauss perpendicular to the plane of the electrodes (Figure 2.1.5). Electrons near the cathode accelerated towards the anode by the electric field travel in a spiral due to the effect of the magnetic field. Since the anode has a small cross section, most of the electrons miss it and travel towards the other cathode where they are repelled. The electrons oscillate in between the two cathodes. Because of this oscillation and the long spiral path length there is a large probability that an electron will strike a gas molecule and ionize it. The secondary electron produced by ionization also performs similar oscillations, and the ionization rate quickly increases. The normalized number of ions produced is proportional to the pressure of the gas over the pressure region 10^{-2} to 10^{-6} torr.

The migration of the ionized gas molecules to the cathode and the eventual capture of some of the electrons by the anode results in an ionization current which flows in an external circuit. This current (which is of the order of milliamps for cold cathode gauges) is measured directly on an ammeter to give a pressure reading. (Figure 2.1.6).

The only minor problem with the Penning gauge is getting the gauge to "strike" at low pressures ($<10^{-3}$ torr). Normally, the Penning is switched on when the Piranii gauge shows a pressure of about 10^{-2} torr, however, this procedure is sometimes neglected. The simplest way to start the Penning gauge at lower pressures is to admit a short burst of gas into the chamber. This momentarily raises the pressure at the gauge head allowing it to strike and because of the turbomolecular pump's ability to cope with increases in pressure, this method does not endanger the pumping system.

The calibration of the Penning gauge wavies slightly for each gas used due to their differing ionization energies. The unit is usually calibrated for dry air.

As the pressure of the vacuum chamber decreases, the gas composition changes and the pressure readings must

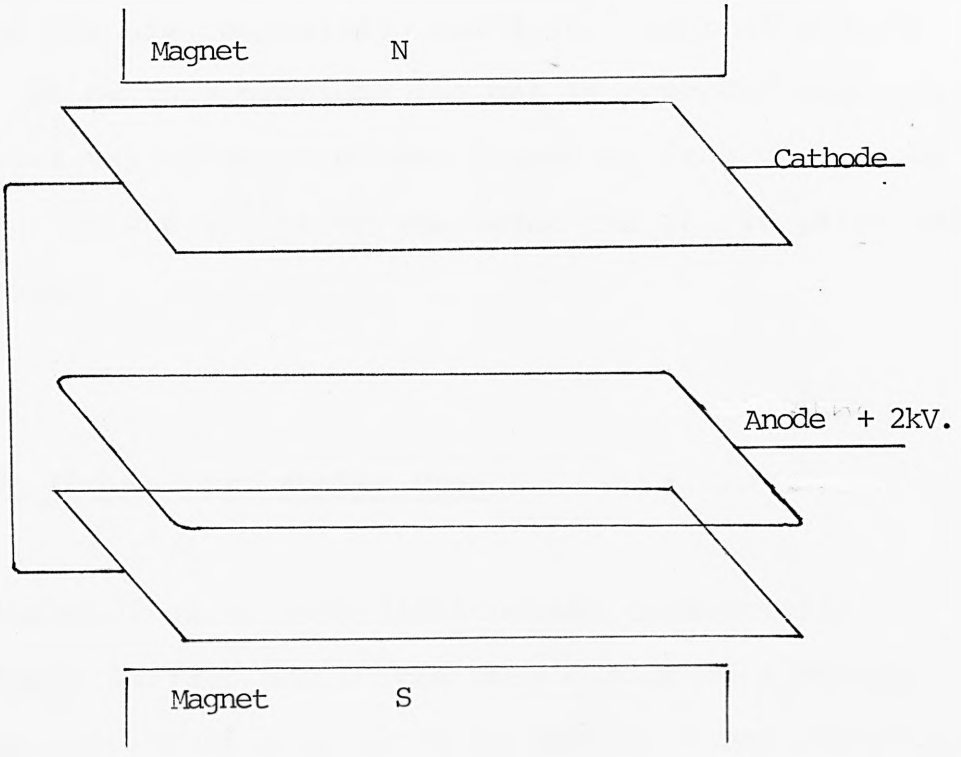

Figure 2.1.5. The Penning Gauge.

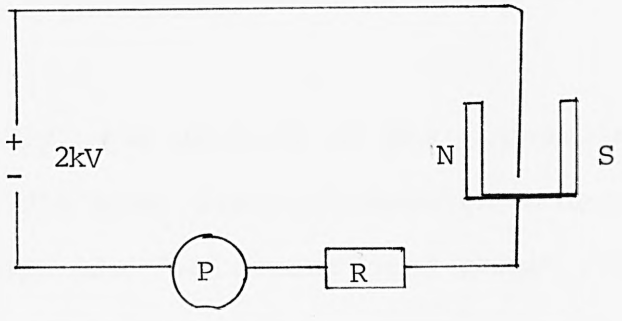

Figure 2.1.6. Circuit to measure pressure.
P = milliammeter calibrated in pressure units.

be interpreted with this fact in mind. For an unbaked system the gas composition above 10^{-3} torr is usually air. Below this pressure the gas is composed principally of water vapour and hydrogen desorbing from the vessel walls. Around 10^{-5} torr and below the gas is principally hydrogen.

2.1.3 The Turbomolecular Pump

The turbomolecular pump first became commercially available in 1948 and is the only design of a purely mechanical vacuum pump which is able to reach pressures of less than 7.5×10^{-11} torr without using cold traps or oil traps. Its unique design does not allow back-streaming of lubricating oil, because of this it gives an ultraclean hydrocarbon-free vacuum and is thus ideally suited to the manufacture of contamination-free tunnel junctions.

Historically, the origins of the turbomolecular pump began in 1918 when Gaede introduced a new type of vacuum pump, the "molecular drag pump" (108). In this device the gas molecules are pumped by their frequent collisions with a moving solid wall. The principle of the Gaede was fairly simple. Particles after colliding with a moving surface obtain in addition to their own thermal velocity, a velocity component in the direction

of the moving surface. The superposition of these molecules determines the final velocity of the leaving particle. In its simplest form, Gaede's molecular pump consisted of a high speed rotor in a housing (Figure 2.1.7). When gas or vapour molecules hit the rotor, the rotor's impulse is transmitted to the particles giving them a component of velocity in the direction of rotor movement. Providing a suitable geometry is chosen, the non-destructive motion of the molecules can be changed into a directive motion, this achieving a pumping action. Gaede's pump, although theoretically sound and practicably realisable to an extent, suffered from one major drawback in that the distance between the rotor and the outside walls was only of the order of 10^{-1} to 10^{-2} mm which involved extremely careful engineering. As a result, baking out the pump was difficult,since too great a temperature would cause the rotor to expand and seize. Also the pump was easily jammed by any small dust or grit particles becoming trapped between the rotor and housing. For these reasons, the Gaede pump never became commercially available. (The theory of the Gaede pump which is the basis of the turbomolecular pump can be found in a recent review (110).) It was not until 1957 that the turbomolecular pump in its present form was invented by Becker (111).

The turbomolecular pump consists of a high speed rotor in a fixed stator housing. The rotor has a number of

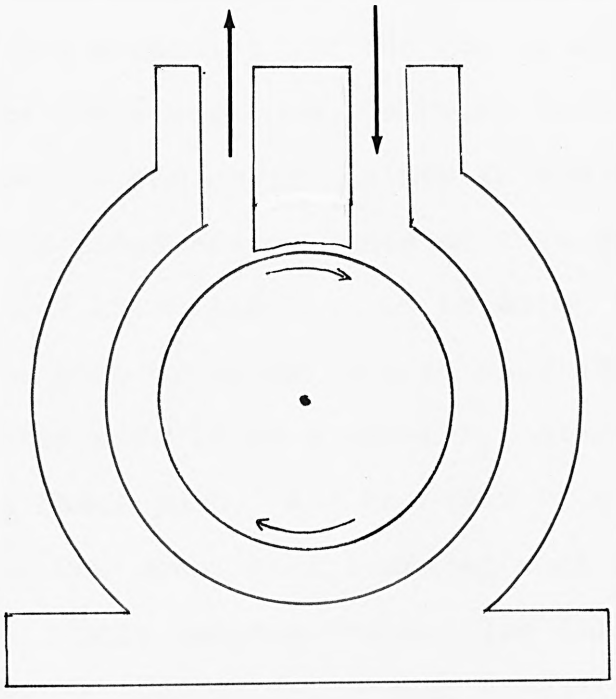

Figure 2.1.7. The Molecular Drag Pump by Gaede. (Reference 111.)

slotted discs (typically 20) between which slotted stator rings (which are part of the housing) are fitted. The slots in the rotor are of the opposite pitch to the stator discs. (Figure 2.1.8). The pumping action is achieved as a result of the relative velocities between the gas molecules and the moving and stationary slotted discs and rings when the rotor is at its normal operating speed. The oblique slots in the rotor discs and the stator rings are designed so that gas molecules are accelerated along the axis of rotation from the centre of the pump outwards to both ends (109). Each channel of each disc is an elementary molecular pump similar to a Gaede pump. All channels of each disc work in parallel. One rotor disc combined with one stator ring forms a single pumping stage. The turbomolecular pump consists of several individual pumping stages connected in series; each stage having been formed from many elemental molecular pumps connected in parallel. The discs on the high vacuum side of the pump (in the middle) have a larger number of slots which are at a steep angle, where as the slots on the discs on the fore-vacuum side (the ends of the rotor) are fewer and of a shallower angle. The discs on the high vacuum side have a faster pumping speed and smaller compression ratio compared with the fore-vacuum side discs which have a low pumping speed and high compression ratio. (The large number of elemental molecular pumps means that the gap between the rotor and the stator can be as large

Diagram of pump (after p.87) removed for copyright reasons

as 1 mm this allowing the pump to be baked out without any expansion problems). Both ends of the rotor are connected via an internal channel to an outlet which is connected to a rotary backing pump. The rotor runs on two bearings fitted on either end of the shaft. The bearings are lubricated via a wick from an oil reservoir. Since the bearings are in the region of fore-vacuum (downstream from the high vacuum region) no lubricating oil can reach the high vacuum centre of the pump and thus no backstreaming can occur. This is one of the major advantages of a turbomolecular pump over a conventional oil-diffusion pump. The turbo pump gives an ultra-clean vacuum without the need of a coldtrap or the risk of hydrocarbon contamination from backstreaming.

2.1.4 Characteristics of Turbomolecular Pumps

(1) Compression Ratio k

The theoretical compression ratio (neglecting return losses through the pump and leakages) is the ratio of the pressure at the outlet to the pressure at the inlet and is given by:-

$$k_{max} \cong \exp\ (-\sqrt{M}\ U.g) \qquad (2.1\text{-}1)$$

where g = geometrical constant

u = circumferential speed of the rotor

m = molecular weight of the gas being pumped

Within the range of molecular flow k is independent of pressure, however, k ultimately depends on the design of the rotor discs and leakages. There are two types of disc design, open and closed. In the closed disc structure (Figure 2.1.9A) there is no direct path through the disc. This is termed an optically opaque disc. Whereas in the open disc structure (Figure 2.1.9B) the molecules are able to pass directly through the disc. Pumps employing an optically opaque disc structure have a high compression ratio and faster pumping speed (109, 111). Leakages occur when molecules return through the pump against the pumping direction to the high vacuum side. This can happen more for a pump employing an open disc structure. Leakages also occur around the perimeter of the rotor discs and the inner stator surfaces, therefore this gap is kept as small as possible. As a result of these considerations, the actual compression ratio is much more complex than equation (2.1-1) (110).

The compression ratio as a function of molecular weight is plotted in Figure (2.1.10).

2. Pumping Speed s

The maximum pumping speed is a product of the pump's geometry g, and the circumferential speed U.

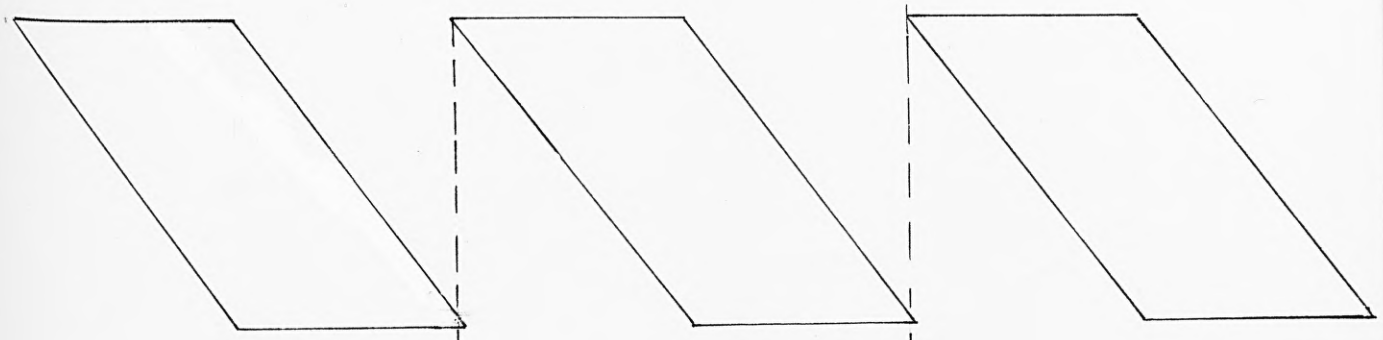

Figure 2.1.9A. Closed Disc Structure.

Figure 2.1.9B. Open Disc Structure. (Reference 111).

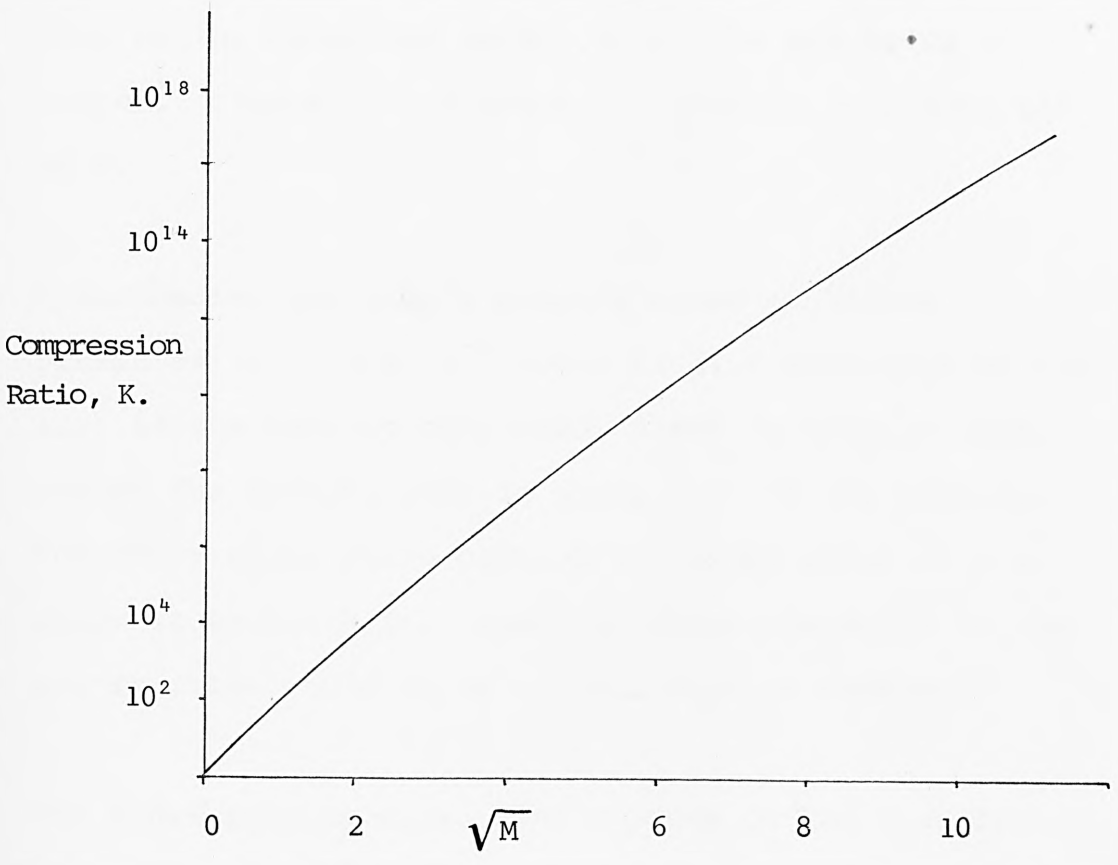

Figure 2.1.10. Compression Ratio as a function of Molecular weight, M.

$S \cong U.g$ (2.1-2)

It should be noted that the pumping speed is independent of pressure below approximately 10^{-3} torr, and independent of the molecular weight,M, of the gas being pumped. Figure 2.1.11 shows S plotted as a function of M.

A turbomolecular pump's pumping speed at higher pressures ($\geq 0.76 \times 10^{-2}$ torr) is also dependent on the size of the backing pump used, since in this pressure region the backing pump is doing most of the pumping. The electronics which control the rotor speed do not allow it to reach full speed at these pressures as the air friction would cause the bearings to overheat.

The final pumping speed also depends on the cleanliness of the system. In order to reach the ultimate pressure as quickly as possible, the turbomolecular pump can be heated (or "baked out") in order to remove any adsorbed vapour - principally water - from the rotor and stator blades. The pump is baked out whilst it is operating, consequently, the rotor blades will only reach bakeout temperature after about 4 hours;the only heat reaching them is by radiation. Bakeout periods are typically 10 to 20 hours.

The turbomolecular pump used on this vacuum system is a pfieffer TPU270 and has a pumping speed of 270 litres

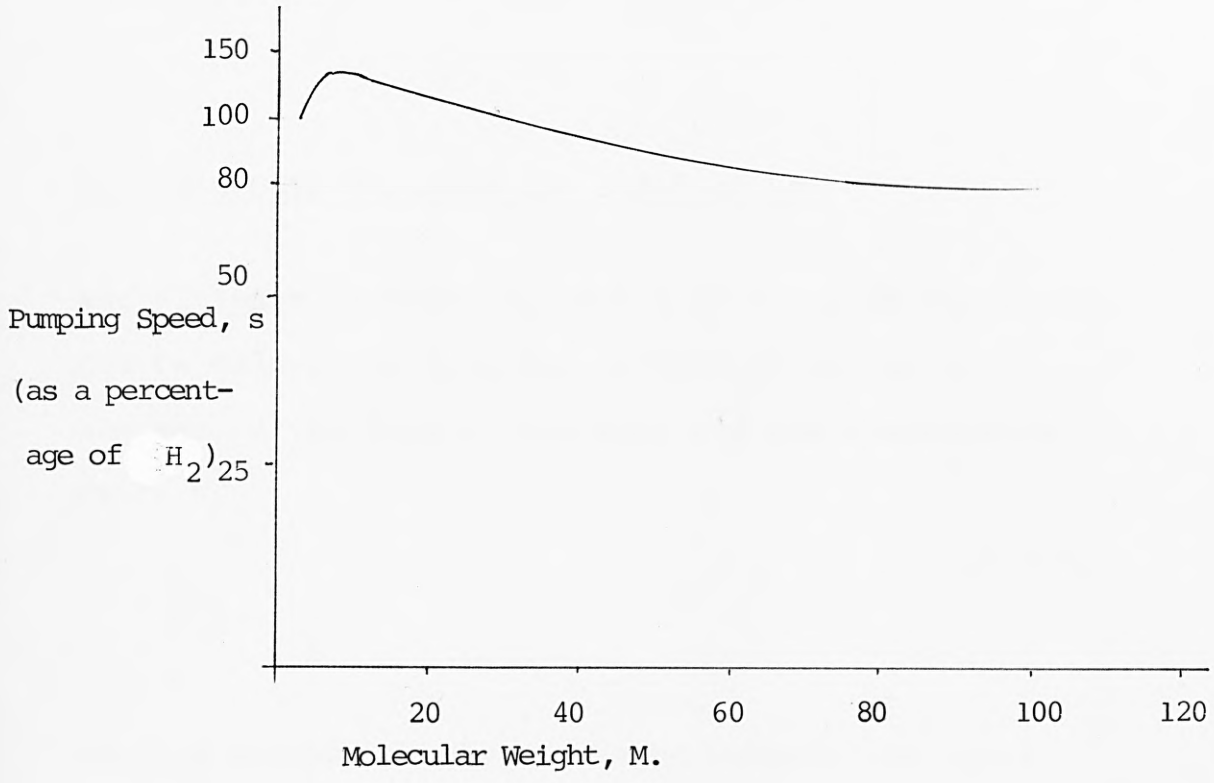

Figure 2.1.11. Pumping speed as a function of molecular weight. (Reference 111).

per second. However, turbomolecular pumps are commercially available with pumping speeds ranging from 16 litres sec^{-1} (111) to 6,500 litres sec^{-1} (114).

3. Ultimate Pressure and Residual Gas

The ultimate pressure P_f that a vacuum pump can attain can be calculated from the partial pressure, p, of the gas on the fore vacuum side and the compression ratio K.

$$P_f = \frac{p}{k} \qquad (2.1\text{-}3)$$

Since K depends on the gas being pumped, the total ultimate pressure has to be calculated for the partial pressures of each gas present using equation 2.1-3 above, and the results summed to obtain P_f.

The increase of K with molecular weight, M, is the reason for the "clean" vacuum (i.e. uncontaminated by oil vapours and hydrocarbons from the backing pump and rotor bearings) produced by the turbomolecular pump. Oil vapours are not able to reach the high vacuum side of the pump from the fore vacuum region whilst the pump is running. The compression ratio with oil vapour of Mass 100 is approximately 10^{16}:1. With an oil vapour partial pressure of 7.5×10^{-4} torr on the fore-vacuum side,

the oil partial pressure on the high vacuum side cannot exceed 7.5×10^{-20} torr. Hence, the vacuum produced is free from hydrocarbon contamination. For hydrogen the compression ratio is $\cong 10^3$ due to its low molecular mass and hence hydrogen is the dominant residual gas. Figure 2.1.12 shows the residual gas mass spectrum at a pressure of 1.5×10^{-10} torr. The peaks at masses 17 and 18, due to HO^+ and H_2O^+, can be reduced by baking out, so that the hydrogen fraction increases to >95%. The two peaks at heavy masses are the double and triply ionised states of the metal vapour of the rhenium cathode of the mass spectrometer used (a Balzers model QMG 311).

The fact that the residual gas remaining in a turbo-molecular pump is mainly hydrogen can be deduced as follows. The partial pressure of hydrogen on the fore-vacuum side is about 3.75×10^{-7} torr. The compression ratio for hydrogen is $\cong 10^3$, hence, the partial pressure of hydrogen on the high vacuum side is:-

$$P_{H_2} = \frac{3.75 \times 10^{-7}}{10^3}$$

$$= 3.75 \times 10^{-10} \text{ torr} \qquad (2.1\text{-}4)$$

which is about the same as the ultimate pressure which can be expectedfrom a turbomolecular pump.

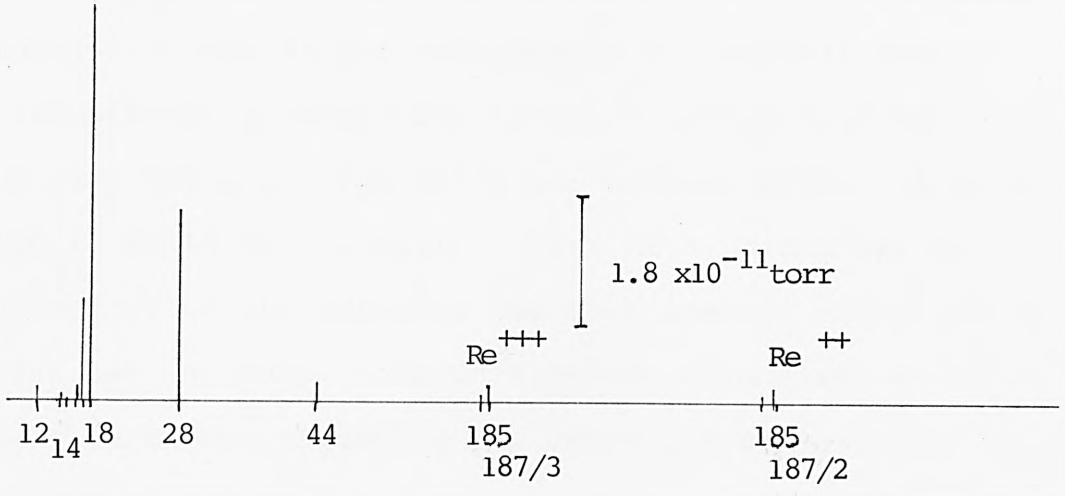

Figure 2.1.12. Mass specrtum of residual gas at 3.5 x 10^{-10}torr.(111)

H_2 : 52%

H_2O : 32%

CO_1N_2 : 12%

CO_2 : 2%

CH_4 : 0.4%

4. Drive Electronics

The TPU 270 turbomolecular pump operates at a rotor speed of 60,000 r.p.m. (1000 Hz). In order to accurately maintain this speed, sophisticated drive electronics are necessary. The TCP 270 uses a brushless d.c. motor controlled by Hall effect probes. This method of control also allows the rotor to reach full speed in a controlled manner: the pump is not designed to run at full speed at atmospheric pressure due to gas friction causing excessive heating. The drive electronics allow the rotor speed to build up gradually. Fast revolutions are only achieved after the pressure has been lowered sufficiently by the backing pump. The driving motor consists of a 2 pole permanent magnet on the rotor and two excitor windings on the stator. Within the stator windings on a printed circuit board are two Hall effect probes located at the correct angle to detect the magnetic field from the rotor poles. A constant current is fed to the Hall probes which give out a signal which is dependent on the position of the rotor poles with respect to the stator windings. These signals, after amplification and conversion, are used to control power transistors which supply power to the excitor windings. Power is applied to the excitor winding whose magnetic field is vertical to the field of the permanent magnet on the rotor. The resulting torque accelerates the rotor. As the speed increases, the inductive resistance

of the stator windings becomes significant and results in reduced power input. To compensate for this a regulator circuit gives an automatic increase in excitor winding voltage as the frequency increases. A maximum preset voltage determines the maximum speed of the rotor.

Power transistors are used to control the stator voltage rather than thyristors, as thyristors introduce large voltage spikes onto the mains supply which can interfere with electrical equipment.

The hydrocarbon-free vacuum created may become contaminated with oil vapours from the bearings and backing pump when the turbo pump is stopped. To prevent this, the compression stages of the pump are vented with dry oxygen-free nitrogen. The entering gas is evenly distributed to the fore-vacuum and high vacuum side simultaneously thus preventing any hydrocarbon backstreaming.

5. Safety Aspects and Maintenance

The T PU 270 is fitted with several protection devices. The first is a fine mesh splinter shield which prevents debris from being sucked into the pump and damaging it. This reduces the pumping speed by about 15% to 230 litres per second. There is also a vent control unit which in the case of a mains supply failure auto-

matically shuts off the turbo and backing pump and opens the venting valve. The unit will not allow the pump to restart until it has been manually reset. The other safety device is a pressure sensor which shuts off power to the pumps and vents the system if the pressure on the high vacuum side remains at greater than 10^{-1} torr for a few seconds whilst the rotor is running at full speed. Again, this has to be manually reset.

The exhaust gases from the rotary pump are plumbed out of the building via 2 inch diameter plastic piping, thus keeping the laboratory air free from exhaust gas and preventing further contamination of the chamber when it is exposed to air.

The turbomolecular pump used in this system requires very little maintenance and has given trouble free service for over three years. The only maintenance involved is changing the bearing oil every 6 months or 5000 hours. This operation is extremely easy and takes about 20 minutes. After 20,000 hours running the main bearings and oil seals have to be changed. This operation requires no special equipment or re-balancing of the rotor and can be accomplished in about 6 hours (113).

Table 2.1 lists some technical details of the TPU 270 turbomolecular pump used on the vacuum system described here.

Table 2.1 Technical details of the Pfieffer TPU 270 turbomolecular pump. (112).

Volume flow rate for:	nitrogen	270 l/s
	helium	330 l/s
	hydrogen	280 l/s
Compression ratio for:	nitrogen	3×10^{9}
	helium	5×10^{4}
	hydrogen	2.5×10^{3}
Ultimate pressure		7.5×10^{-12} torr
Rotor speed		60000 r.p.m.
Run-up time		3 minutes

2.1.5 General maintenance of the Vacuum system

The lowest pressure attainable ultimately depends on the presence of any leaks in the system. There are two types of leaks real and virtual. True leaks are caused by gas entering the system through a hole or faulty joint, virtual leaks are due to the de-gassing of various materials within the vacuum system. Both types of leaks can be extremely time consuming and difficult to find, however, if the vacuum system is carefully maintained they can be kept to a minimum.

True leaks are most easily detected by spraying acetone (a so called "probe gas") around the suspect joint and noting any pressure change. This crude yet effective method of detection will only work for leaks which are above the pressure gauges: any leaks in between the gauges and the pump will not register. Other more elaborate leak detectors using mass spectrometers are discussed elsewhere(106), however, because of the simplicity of the turbomolecular pump based system it has not been necessary to resort to such drastic time consuming leak detection methods. Potentially the major source of real leaks is the viton 'L' section seal since this is moved every time the chamber is let up to atmospheric pressure. However, by ensuring that the baseplate and viton base are free from any dust and metal particles, the seal is trouble free. Occasionally, the 'L' ring became scratched. The scratches

were removed with metal polish and cleaned with acetone.

Virtual leaks caused by the degassing of materials in the chamber can be minimised by careful choice of construction materials. Wherever possible constructions within the chamber were either screwed together or silver soldered as soft solder contains a large percentage of tin which has a low vapour pressure and will continuously evaporate under vacuum. Soldered electrical joints were made using a special In/Sn content solder.

The principal source of virtual leaks was caused by water vapour desorbing from the vessel's walls after the chamber had been exposed to the atmosphere. For this reason, the chamber was always kept evacuated, vented to dry nitrogen, and only kept at atmospheric pressure for the minimum of time.

Whilst working on the chamber, grease deposits from finger prints were thought to be a possible contamination hazard; nylon gloves were originally worn to prevent this. However, in practice, providing the operators' hands were clean, no contamination (manifesting as a reduction in pumping speed or in large hydrocarbon peaks on the tunnel spectrum) was detected.

After the chamber had been loaded and evacuated to better than 10^{-5} torr a 15 minute, 750 volt, 20ma

discharge in an oxygen atmosphere at a pressure of 7×10^{-2} torr was used to oxidise any remaining organic contamination and to clean the junction substrate thus providing an ultra-clean vacuum for junction preparation.

The only maintenance of the vacuum system required was the replacement of the evaporation sources and the cleaning of the evaporation slits which eventually became blocked with metal. The tungsten basket used for aluminium evaporation was replaced after every 6 evaporations. Continual use of the same basket resulted in tungsten-aluminium alloy forming and being evaporated on the junction. The molybdenum boat used for lead evaporation was replaced only if it became damaged. After every 20 or 30 evaporations, the collimating slits were cleaned with a razor blade and re-adjusted to a width of $1mm$ if necessary. After about 50 evaporations the entire evaporation unit was removed and the excess deposited metal cleaned from the masks.

Finally, if more than 10 junctions were made in one day the turbomolecular pump was baked out overnight.

2.2 CHOICE OF A JUNCTION SUBSTRATE

The vast majority of all tunnel junctions are fabricated on either a glass or silica substrate. However, using a

fragile support material does pose a number of problems.

(1) An elaborate chemical cleaning and de-greasing procedure is necessary to prepare the substrate for electrode deposition.

(2) Electrical contact between the electrodes and the rest of the electronics is difficult. This usually rquires a third vacuum deposition of indium contact terminals. These pads are then attached to a series of wires which connect to the rest of the electronics by pressure contacts. The contacts can give rise to a contact resistance which must be taken into account by the electronics. (See section 2.5)

(3) At liquid helium temperatures the pressure contacts may contract and lift off the electrical contact.

(4) If the junction is lowered too fast into the helium the slide may crack breaking the junction.

In view of these problems, it was decided to use an alternative method of junction support based on a glass fibre printed circuit board. This would offer the following advantages:-

(1) No elaborate clean-up procedure is necessary: the high voltage plasma discharge used for cleaning the vacuum chamber prior to junction preparation is adequate.

(2) The electrodes are deposited directly onto the glass fibre surface in such a way that the ends are connected to copper contacts. Electrical connections can then be soldered to these contacts, eliminating contact resistance problems and the need for a third metal deposition.

(3) The copper terminals and soldered joints are mechanically and electrically sound at cryogenic temperatures.

(4) The circuit board is strong enough to withstand severe thermal shock without breaking.

The first printed circuit board substrate designed by Shott (106) is shown in Figure 2.2.1. This design suffered from two faults. Firstly, the copper tracks are not wide enough and may add significantly to the lead resistance. Secondly, the joints between the aluminium electrode and the copper track kept breaking and had to be repaired with silver conductive paint (Electrodag). (No such problems were encountered with the lead electrode) To remedy these faults a new printed circuit board was designed (Figure 2.2.2)

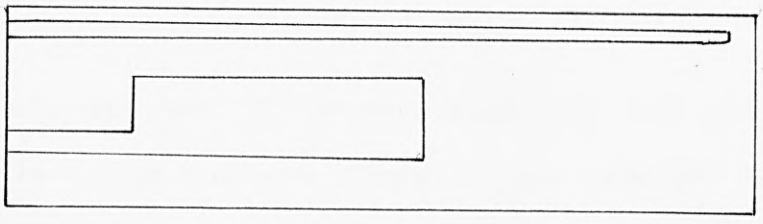

Figure 2.2.1. Original printed circuit board substrate.

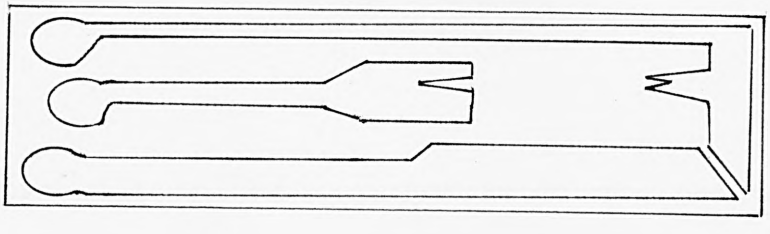

Figure 2.2.2. Redesigned substrate.

The main improvements to the design are as follows:-

(1) The width of the copper tracks have been considerably widened, thus contributing much less to lead resistance.

(2) There are two 'V' shaped contacts for the aluminium electrode. The V shape gives a much greater area of contact between the copper and aluminium and therefore less chance of faulty connection.

(3) The three circular ends of the copper tracks serve two purposes. Firstly, to facilitate easy soldering of the electrical connections. Secondly, the terminals connect with electrical contacts in the vacuum chamber. This allows the integrity of the aluminium electrode and the resistance of the junction to be monitored whilst it is in the vacuum chamber.

The first step in the manufacture of the printed circuit boards was to produce a four times enlarged master artwork with the areas which ultimately became copper tracks marked in black. The artwork was was photographed using Kodak "Kodalith" which is a high contrast film which yields only a black and white image with no grey tones. After retouching,the negative was reduced to the final substrate size (66 x 12 mm) and multiply printed onto a 5"x4" piece of Kodalith sheet film. This

formed the final master positive. To produce the printed circuit boards, the master positive was placed with its emulsion side in contact with a piece of copper-clad printed circuit board which had been coated in a positive photoresist, and exposed to an ultra-violet light for about 2½ minutes. The circuit board was then developed in a weak sodium hydroxide solution for about 1 minute to remove the areas of photoresist which were exposed to the U.V. The board was then rinsed in water and etched in a solution of ferric chloride at room temperature until all the excess copper had been removed (about 4 hours). Finally the board was rinsed with acetone to remove the photoresist which had been covering the copper tracks whilst in the etchant.

[A later electron microscope investigation revealed that if the ferric chloride was too hot, severe under etching of the 35μm thick copper tracks occured. This under etching was a contributory cause to the failure of the aluminium electrode to make proper contact with the track].

The new design of p.c.b. substrate has reduced the breakages in the aluminium strip from 20% to less than 0.5%. (The printed circuit board with the evaporated electrodes is shown in photograph No. 3)

2.3 CRYOGENICS

In order to reduce thermal broadening to an acceptable level, tunnelling experiments are performed with the junction immersed in liquid helium at 4.2K.

A satisfactory description of the cryogenic equipment used is given by Ivar Giaever:

"To do a tunnelling experiment at superconducting temperatures, one first of all needs two Dewars, one inside the other. A Dewar is nothing else than a large coffee jug. The outer Dewar is filled with liquid nitrogen or air. Liquid nitrogen boils at 77K and, at least in the United States, it is cheaper than milk. The inner Dewar is filled with liquid helium. Liquid helium boils at 4.2K at atmospheric pressure and costs about the same as cheap cognac and probably lasts about as long too!"

(Chapter 19,
Reference 118)

Liquid He had to be purchased from an outside supplier (B.O.C.) and was shipped in a 17 litre double walled Dewar. The most economical way to use the helium was to lower the junction into the storage Dewar rather than pump the liquid to another experimental Dewar. The neck on the Dewar has a diameter of about 20mm which restricted

the maximum width of the junction substrate and probe assembly to about 15mm (see photograph 3). The probe assembly, used for holding the junction consisted of a low thermal capacity strip of glass fibre circuit board with four broad copper tracks (two per side) etched on it. The junction was soldered onto two tracks at the lower end of the probe by two thick copper wires. (The other two tracks were connected to a temperature sensing diode). Electrical connections to the probe assembly were made via a high quality locking connector with gold plated contacts.

A cotton wool plug was placed around the neck which prevented air and water vapour from entering the Dewar, solidifying in the narrow neck and blocking it. The outer Dewar was filled with liquid N_2 at the end of every working day. With care, one Dewar of liquid Helium would last about nine days, enough to run about 120 junctions.

2.3.1 Temperature Measurement

Whilst it was possible to detect whether the junction was below 7.5K by the presence of superconducting gap structure in the tunnel spectrum, it was also useful to know whether the junction was in liquid Helium at 4.2K or just in cold vapour between 4.2 and 7.5K. In order to answer this question, a simple temperature sensor based on a silicon alloy junction diode was constructed. This gave a positive indication if the junction was in liquid Helium or not.

The circuit diagram for the temperature probe is shown in Figure 2.3.1. Applying a voltage across the sensing diode D1 sets a current flowing in the circuit R1, D1. The voltage at X will vary depending on this current. Since the diode's current-voltage characteristic varies with temperature, the voltage at X will change as the diode is cooled in liquid helium. The voltage at X is applied to the signal inputs of the comparators. (Basically, a comparator compares an imput voltage with a reference voltage and changes its output state when the input voltage becomes greater than or equal to the reference voltage). Comparator A is adjusted by means of RVA (which sets the reference voltage) so that its output is logic O when D1 is at 298K and when it is just above liquid helium, and logic 1 when D1 is immersed in liquid helium. Comparator B is adjusted by means of RVB so that its output is logic 1 when D1 is immersed in nitrogen and helium and logic 0 otherwise. The logic outputs from the two comparators are used to drive two 74 low power Shottky series logic I.C.'s which operate three coloured light emitting diode (D2 to D4) such that the colour to the diode lit indicates the temperature of the sensing Diode, D1, thus -

D_2	Red	298K	(Power on)
D_3	Yellow	$T \geqq 5K$	(Not in Helium)
D_4	Green	$T \leqq 4.2K$	

The sensing diode was connected to the end of the probe assembly and situated just above the junction (See photograph 3).

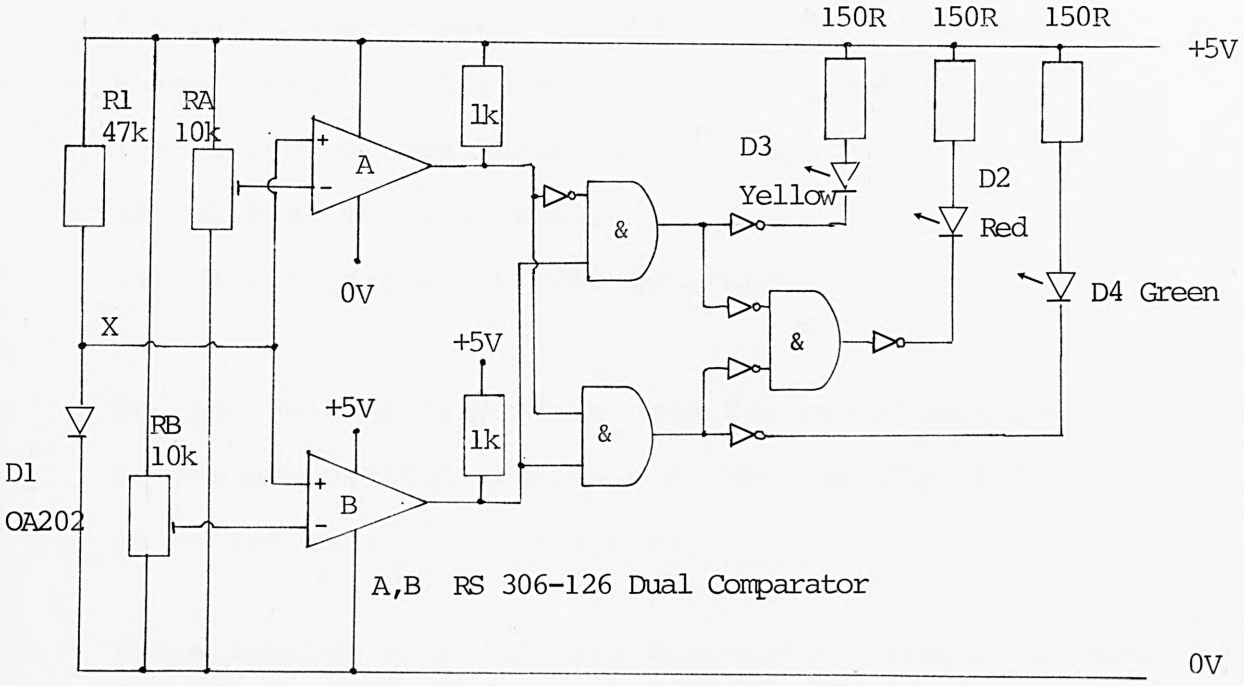

Figure 2.3.1. Circuit diagram of temperature probe.

2.4 POWER SUPPLY

The power supply used for this project consists of three sections and is shown in photograph 1.

(1) A low voltage, high current supply

(2) A high voltage supply

(3) A Radiofrequency (RF) generator.

The low voltage supply was used for resistance heating of the evaporation sources. It was capable of delivering up to 100 amps at eight volts.

The aluminium electrode was evaporated using a current of 40 amps for 10 seconds, and the lead electrode was evaporated using a current of 25 amps for 2 minutes.

The high voltage supply was capable of delivering a maximum of 1kV at 500mA. For the clean-up oxidation a power of 575V at 60mA for a period of 15 minutes was used. For oxidation of the aluminium electrode, 375 volts at 1mA was needed. The current and time parameters of the oxidation discharge are extremely critical in obtaining the currect thickness of oxide and are discussed in Chapter 3. The H.T. supply output was controlled by a solidstate programmable timer which allowed the user to select the duration of the H.T. discharge form 0.1 seconds to 100 minutes in 0.1 second steps.

The Rf. heater, originally designed for an Rf evaporation source, was not used in this project.

2.5 ELECTRONICS

2.5.1. The Basic Detection Circuit

The basic requirements and theory discussed in Chapter 1 can now be put in more practical terms. Although the straightforward circuit outlined in Section 1.6 and Figure 1.6.2 will detect second harmonic signals, it does suffer from several difficulties which give the circuit an inherently low resolution. Since the junctions studied are only weakly non-linear, the deviation from linearity and hence the signal of interest comprises of only an extremely small percentage (0.1 to 0.5%) of the total signal across the junction. Hence, after amplification and detection, most of the lock-in amplifier's output signal must be bucked out, or offset, in order to display the small signal of interest. This raises two problems. Firstly, the high gains required cannot always be realised because of the limited dynamic range of the lockin amplifier. Secondly, large significant errors may be introduced into the output as a result of gain variations and instabilities in the offset voltage. These two problems can be overcome by offsetting most of the signal prior to amplification. One way of

achieving this is to use an a.c. Wheatstone bridge with the tunnel junction incorporated as one of its arms. This circuit has the extra advantage that it can be tuned to reject the fundamental frequency, ω, when second harmonic measurements are being performed. The fundamental frequency is cancelled out when the bridge is balanced. The second harmonic component is unaffected as the tunnel junction is the only non-linear element in the bridge. However, there is one major drawback in using the conventional Wheatstone bridge circuit. When performing measurements on low resistance junctions, the lead resistance may become comparable to the junction resistance itself (especially if the leads are in a non-superconducting state). Also, this form of bridge requires the use of high modulation voltage signals (220μV r.m.s.) when measuring d^2V/dI^2. At cryogenic temperatures such voltage levels produce serious modulation-voltage broadening.

The basic bridge configuration is shown in Figure 2.5.1. The tunnel junction has been incorporated as one arm of the bridge R_J. The bridge is balanced by R_3 so that $R_3 \cong R_J$. The inductance L_1 and the resistance R_1 are large enough so that a.c. shunting of the d.c. bias supply (or junction) is negligable. Similarly, R_2 is large enough so that shunting by the d.c. supply is also small. Finally, the values of R are chosen such that $R >> R_J$ and R_3. In the bias region of interest (0-500mV) the

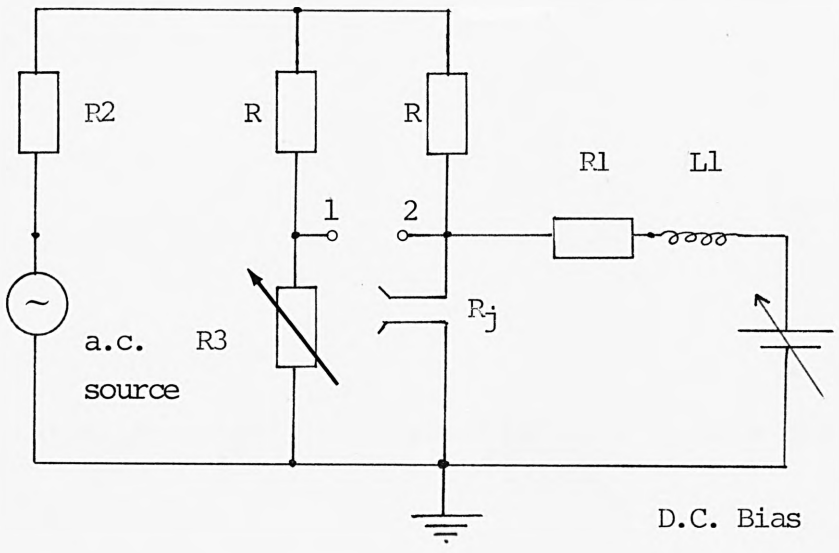

Figure 2.5.1. Basic two terminal bridge configuration.

tunnel junction is only weakly non-linear, and since R is large, the current in the two arms of the bridge is about the same, and is given by:-

(2.5-1)

$$I_o = \delta \cos \omega t$$

Then,

(2.5-2)

$$V_1 \cong R_3 \ \delta \cos \omega t$$

(2.5-3)

$$V_2 \cong I_o R_3 + \left[\frac{dV}{dI}\right]_{I_o} \delta \cos\omega t + \frac{1}{4}\left[\frac{d^2V}{dI^2}\right]_{I_o} \delta^2 (1+\cos 2\omega t) + \ldots$$

where Io is the d.c. bias flowing in the junction (see equation 1.6-5)

(This assumes the bridge is balanced i.e. $R_3 \cong R_J$).

The potential difference across the junction as points 1 and 2, $V_{1\,2}$, has compenents of the fundamental frequency ω, and of the second harmonic 2ω. (Plus higher order terms which are neglected.) Thus:-

(2.5-4)

$$V_{1\,2}(\omega) = \delta \cos\omega t \left(R_3 - \left[\frac{dV}{dI}\right]_{I_o} \right)$$

(2.5-5)

$$V_{1\,2}(2\omega) = \frac{1}{4} \delta \cos 2\omega t \left[\frac{d^2V}{dI^2}\right]_{I_o}$$

It is possible to obtain from these two voltages the dynamic tunnel resistance, $R_t = dV/dI$ and its first derivative $dR/dI = d^2V/dI^2$. When the bridge is balanced it allows the small variation in dV/dI to be measured rather than dV/dI itself, hence the gain stability and dynamic range problems of the lock-in amplifier are circumvented.

In most cases the experimentalist is interested in $\sigma = (dV/dI)n/(dV/dI)s$, this measurement involves measuring the derivative of the current in both the normal and superconducting states. A problem then arises when using thin film and/or superconducting electrodes. The leads will have zero resistance when the electrodes are superconducting and an appreciable resistance (of the order of several ohms) when the electrodes are normal. If this variation in lead resistance is not accounted for then significant errors are introduced into the values of σ.

One way to account for these problems is to use a four terminal bridge configuration shown in Figure 2.5.2 (44, 45). In this circuit, any change in the current lead resistance (r_1 and r_4) is negligable compared with the magnitude of R, and hence the current remains effectively constant when the leads are in the normal and superconducting state. One of the disadvantages of this circuit is that resistances much larger than R_J

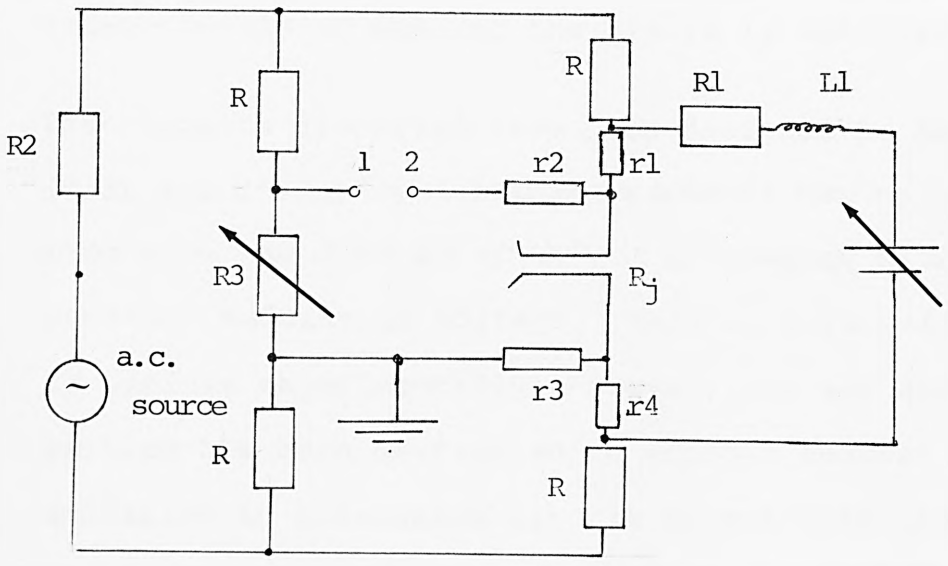

Figure 2.5.2. Four terminal bridge configuration (45).

are required in the bridge. Hebard and Shumate (104) have modified the circuit in order to use lower resistance values in the arms of the bridge (Figure 2.5.3). They claim the output voltage V_{12}, is proportional to changes in conducance over a large dynamic range, independently of whether the bridge is balanced or not.

The circuits discussed have been designed to measure dV/dI and d^2V/dI^2 by maintaining a constant current I_0. In order to measure dI/dV and dI^2/dV^2, it is nesessary to maintain a constant modulation voltage. This is more difficult to perform experimentally, however, one way around the problem has been devised which employs another lock-in amplifier in a feedback circuit to maintain the modulation signal at a constant voltage. The dynamic conductance, σ, and its first derivative are derived directly without any mathematical manipulation (104). The circuit was not considered for construction for this project since its cost, mainly that of two lock-in amplifiers is prohibitively expensive, and from a chemical viewpoint, the derivatives dV/dI and d^2V/dI^2 are perfectly adequate (see section 1.6 paragraph 2).

Before deciding on whether to construct a two terminal or four terminal device, the following points were considered:

The main disadvantage of two terminal devices is that they do not account for changes in the lead resistance especially when measuring σ_S/σ_N. Secondly, they need

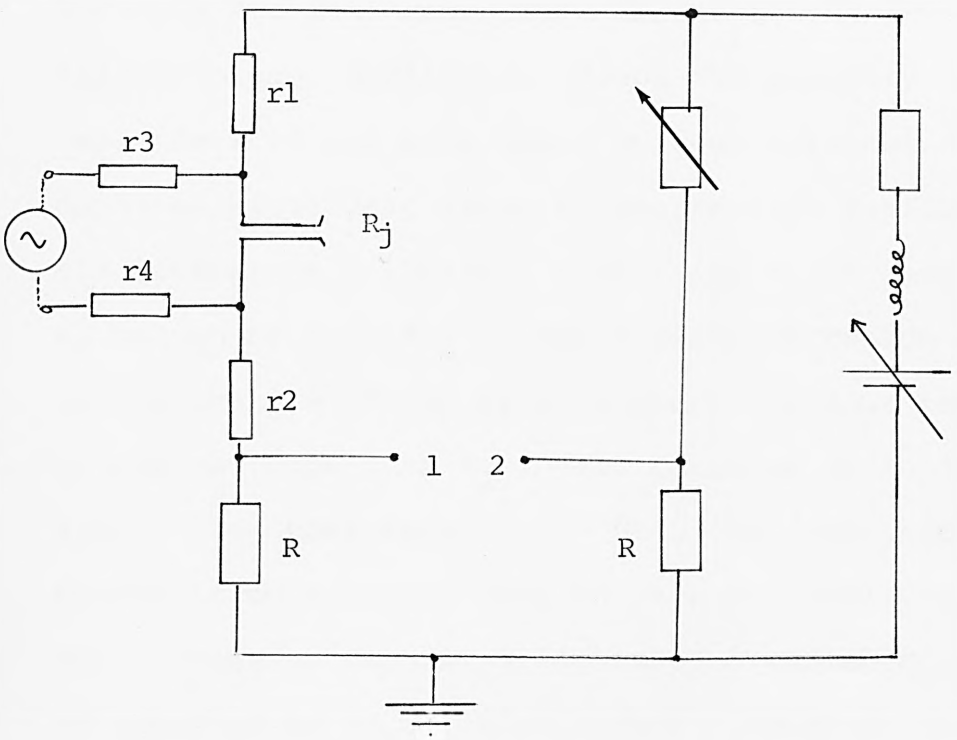

Figure 2.5.3. Modified four terminal bridge of Hebard and Schumate (104).

to use higher modulation voltage amplitudes and thus even at 4.2K some modulation voltage broadening may result. Conversely, a four terminal bridge configuration accounts for lead resistance and uses much lower modulation voltage amplitues. Since the majority of research work has been based on four terminal devices, detailed electronic circuits are readily available in the literature. Finally, when using a two terminal bridge R_J has to be within a narrow resistance region defined by the parameters of the circuit whereas a four terminal bridge can cope with R_J in the range of 1Ω to $10^4\Omega$ (104). It therefore seems that the four terminal bridge is much better than the two terminal version, and indeed, as far as physicists are concerned, there is no question as to which is better. However, for the chemist the choice is not so obvious. First, the spectroscopist is, in general, not remotely concerned about the difference in conductance between the normal and superconducting states, but more in measuring the vibrational peak positions and their relative intensities. The change in lead resistance is therefore of no concern. However, the lead resistance itself is still a problem, however, it can be minimised by remembering that in an Aluminium-Aluminium oxide lead junction at 4.2K the lead (Pb) electrode is superconducting and of zero resistance; and by using marginally broader and shorter aluminium and lead (Pb) electrodes, and also by employing large cross-section copper conductors as connecting wires.

Secondly, because of the low modulation voltage employed, four terminal bridge networks use a separate pre-amplifier before signal detection by the lock-in. This serves to amplify the signal from the junction plus all the noise as well. The lock-in is therefore presented with a much noisier imput that without the pre-amplifier. Conversely, if larger modulation voltage levels are used, a pre-amplifier becomes unnecessary. There is thus a trade-off between signal-to-noise ratio and resolution; it is easily possible to obtain a good spectrum using a slightly larger modulation voltage and no pre-amplifier.

Finally, the apparent problem of being unable to cope with a large dynamic range of R_J values with a two terminal bridge is in actuality non-existent, providing meticulous experimental procedures in junction preparation are observed, it is easily possible to constantly fabricate junctions with a resistance in the range 800 to 1,500 ohms.

It was therefore decided to design a two terminal bridge configuration and associated power supply. The circuit shown and described below was developed by Field and Shott (106).

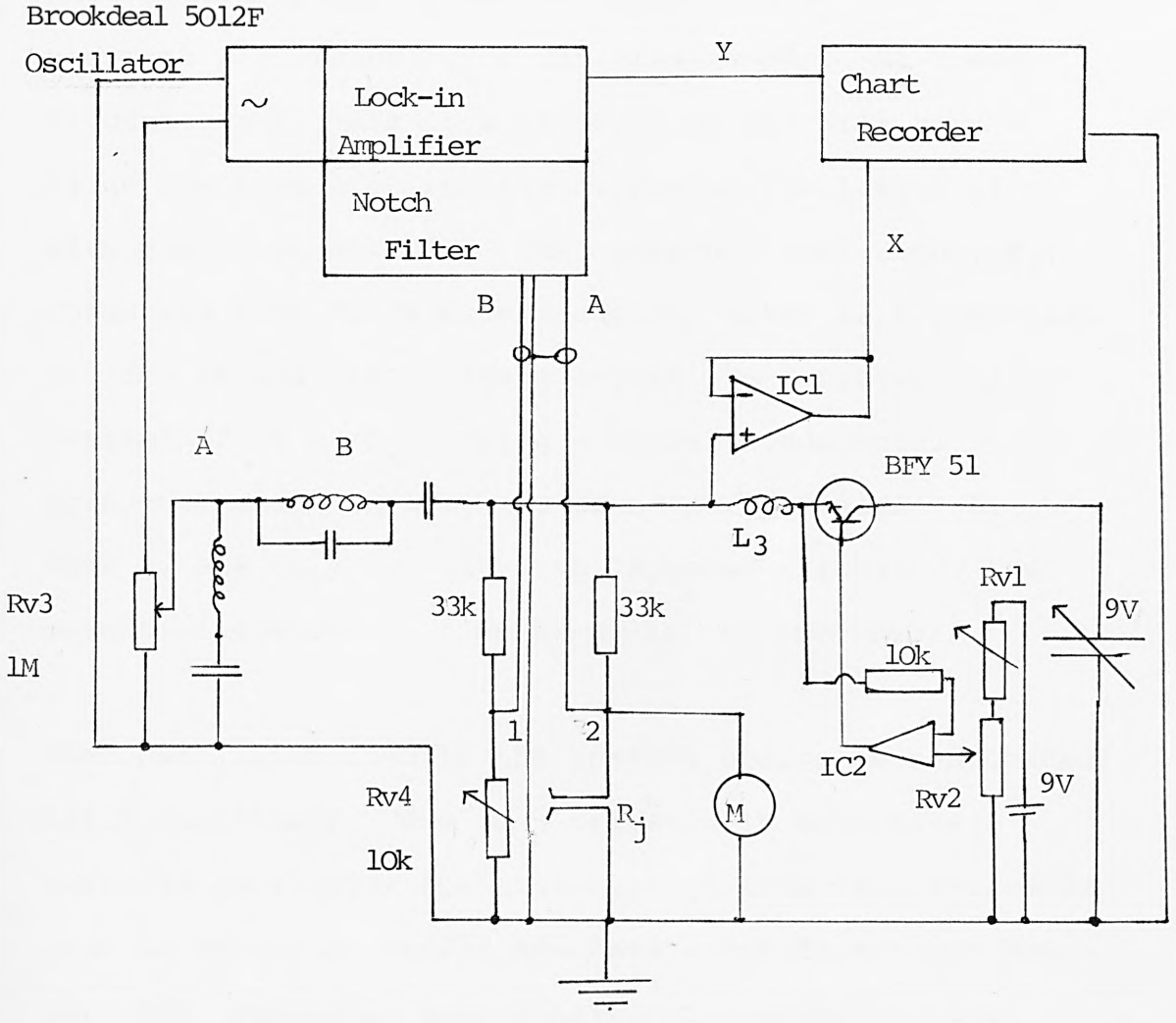

Figure 2.5.4. Circuit diagram of bridge network and bias supply.

(After Field and Shott 55).

M Monitor oscilloscope.

Figure 2.5.4 shows the bridge and bias voltage circuit diagram. It was originally decided to operate at a fundamental frequency of 5kHz. (The main reason for such a high frequency was the construction of L_3 which prevents a.c. shunting of the bias supply. At lower frequencies L_3 must be a large value and will have a large physical d.c. resistance due to the length of wire needed to make it. Thus internal resistance, R_i, which was 670Ω for a 6.5H inductor, acted as a potential divider in that the voltage across the junction was determined by R_J/R_i. Using a higher fundamental frequency means that L_3 has to be much smaller. At 5kHz R_i was only 8Ω, and with improved circuitry, the potential divider problem was circumvented).

The oscillator used in the present design is a Brookdeal 5012F oscillator. The main criteria in selecting a suitable oscillator for this type of detection system is that it should be stable and have a low distortion output with negligible second harmonic component. The frequency stability of the 5012F is 0.1%/°C, its total harmonic distortion is 0.05% and the second harmonic content of the output is 0.005%. The 5012F oscillator is used in conjunction with a Brookdeal 9503 lock-in amplifier which contains its own internal frequency doubler which provides a 2ω reference signal for second harmonic measurements. In order to minimise distortion of the oscillator from any second harmonic generated in

the junction itself, the oscillator is connected to the bridge via a tuned filter network. The R.C. network B has a high impedence to 10kHz, thus preventing any second harmonic returning to the oscillator by rejection. The second filter network, A, provides a low impedence for 10kHz allowing any 2ω to get through B to pass to earth. (This network will also filter out any of the second harmonic generated by the oscillator itself).

The d.c. bias supply is provided by a ten turn potentiometer RV_2. The wiper of RV_2 is connected to a small geared motor. By selecting various gear combinations a scan time of 1 to 80 minutes could be achieved. RV_1 represents a series of switchable resistors which govern the voltage scan range. The following ranges are available: 0-500mV, 0-1.1V, 0-2.2V, 0-4.4V and 0-6.6 volts. The d.c. bias circuit is able to supply stable bias voltages into resistances as low as 1Ω. This is achieved by applying a positive voltage to the collector of Q_1. By varying the voltage at the base of Q_1 the output transistor is also varied. The voltage applied to the base of Q_1 is the ramp voltage from RV_2. Before this voltage is applied to Q_1 it is fed into IC2 which acts as a differential comparator which compares the ramp voltage generated via RV_2 with the output voltage, and operates Q_1 to ensure these are identical. As well as being applied to the junction, the bias

voltage is also applied to the x-axis of a Bryans model 26000 chart recorder via IC1, which acts as a voltage follower. This prevents noise generated by the chart recorder feeding back into the bridge network.

The output of the bridge is taken to the lock-in amplifier via a Brookdeal 5011F active filter. When operated in the notch mode and tuned to 5kHz, it filters out most of the remaining fundamental modulation frequency prior to detection and amplification of the second harmonic component. Using this arrangement, it is unnecessary to use a separate pre-amplifier.

2.5.2 Electrical Noise

The major problems with setting up sensitive electronic equipment of this nature is the electrical noise. Since the signal levels being measured by the equipment are of the order of microvolts or less, most forms of electrical discharge will cause interference.

The primary source of noise was from the 240V mains supply. If the supply was examined on an oscilloscope small 750 volt high voltage spikes of about one micro-second duration could be seen. These are caused by the

operation of electrical equipment such as thyristors, thermostats and electric motors. There are three possible solutions to alleviate this interference.

(1) Fitting suppressors to all the equipment causing interference.

(2) Installing a mains filter on the spectrometer.

(3) Using a separate mains supply.

Clearly, option (1) is impractical. Fitting a mains filter is the best solution; although at the time of construction the necessary filter was unavailable. Finally, a small electric generator was purchased which uses a three phase electric motor to drive a 240 volt generator.

The second form of electrical interference is airborne and due primarily to spark plugs in car engines, electrical discharges and atmospherics. To eliminate airborne interference all the electrical equipment was housed in an electrically screened room.

One of the biggest electrical problems in building the spectrometer was earthing. For the same reasons as above, it was impractical to use the mains earth. Any attempt to earth the Faraday cage and spectrometer to the mains earth resulted in more electrical noise being

picked up from the earth. A recently installed copper water pipe was found not to be connected to any of the existing earth points within the building and was therefore suitable for use as a quiet earth. The Faraday cage was thus connected to the water pipe using a length of copper lightning conductor. The next problem was to isolate all the electrical equipment from the mains earth and connect it to the quiet earth at one point in the Faraday cage. This process immediately gives rise to another type of problem, namely, earth loops. An alternating magnetic field such as that from a transformer can induce a current in a loop of wire (Figure 2.5.5). The stray magnetic field from, for example, an oscilloscope transformer, intersects one earth on a screened cable inducing a small current which can circulate in the wire because of the second earth connection. To stop this problem, interconnecting pieces of equipment were arranged to convey a signal by one path only; that path consisting of a single wire and an earth in the form of a coaxially screened lead. The mains earths on all the equipment were all connected to a single earthing point in the Faraday cage. A minor problem was the chart recorder. When earthed to the Faraday cage, it injected electrical noise from its power supply onto the quiet earth. The problem was solved by earthing the chart recorder to the normal mains earth: the signal imputs to the recorder went through voltage followers to prevent noise being injected into the electronics.

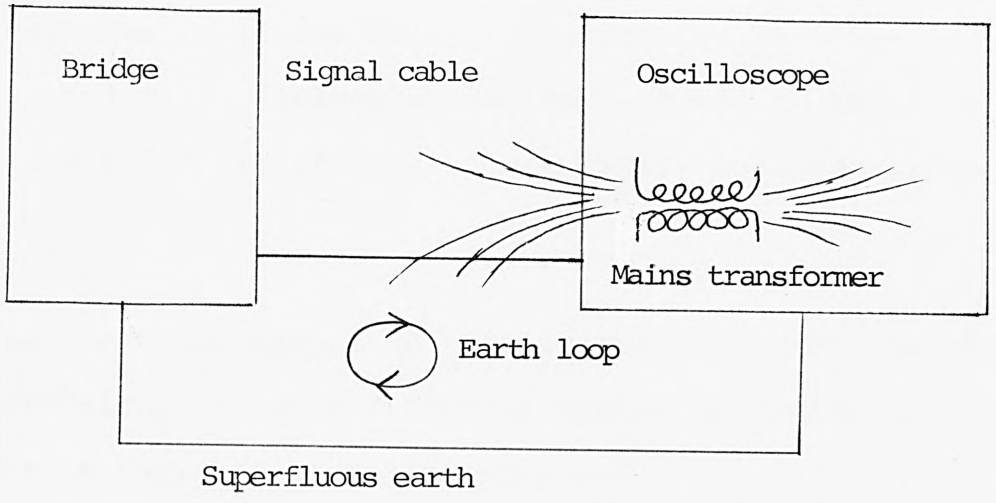

Figure 2.5.5. Earth loop caused by stray induced currents.

The final source of electrical noise is generated by the equipment itself and is basically thermal in nature. Random thermal motions of free electrons in conductors gives rise to minute current fluctuations which cause random noise. Secondly, the thermal excitation of electrons across p-n junctions in semiconductors also gives rise to random noise. (The problem is worse in semiconductor devices where the band-gap is small (e.g. Silicon) and electrons are more easily excited across it).

These problems cannot be totally solved,but by use of short signal wires and careful choice of semi-conductor devices they can be minimised.

2.5.3 The Lock-in Amplifier

A lock-in amplfier is basically a detector which only gives an output signal when the input signal is synchronous with an (internal) reference signal. Its rôle and principle of operation in the second harmonic detection system can now be explained more fully. Figure 2.5.6 is a block diagram of the Brookdeal 9503 lock-in amplifier.

(1) A.C. Amplifier

The a.c. amplifier has five functions:-

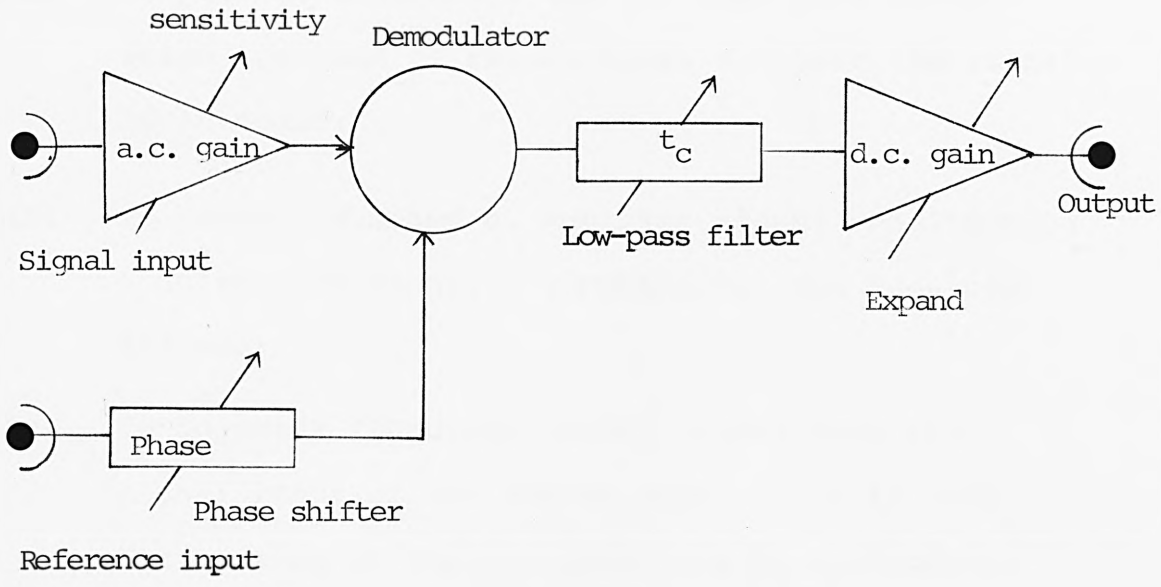

Figure 2.5.6. Block diagram of the Brookdeal 9503 Lock-in amplifier. (Reference 107).

(i) To provide gain or attenuation of the input signal, providing the correct signal level to the phase demodulator. The gain/attenuation is provided by the sensitivity switch;

(ii) To provide switchable low and high pass filters which are used to reduce noise not near the signal of interest;

(iii) To provide a means of applying signal conditioning modules such as noise suppressors and tuneable filters;

(iv) To inject a "function check" signal into the signal input of the demodulator. This is used for setting up the amplifier and fault finding;

(v) To provide a true differential high impedence interface at the signal imput.

The two outputs from the bridge in Figure 2.5-4 are applied to the A and B imputs on the a.c. amplifier which is set in a differential mode and giving the difference of the two imputs (A-B) as its output. This signal is then filtered by the 5011F active notch filter to remove any 5kHz fundamental frequency if second harmonic measurements are being made.

(2) The Reference Channel

The reference channel generates a symmetrical square wave which drives the reference imput of the demodulator.

This wave form is either the same frequency as the reference trigger imput or twice its frequency. The phase of the square wave can be accurately adjusted. The four main components of the reference channel are:-

(i) An isolation switch allowing the input to be floated with respect to ground. This switch is used to minimise earth loops discussed above.

(ii) A frequency doubler which is used when second harmonic measurements are made.

(iii) A precision phase shifter allowing the phase of the reference signal to be shifted by up to 360° with respect to the imput signal.

The Brookdeal 5012F sinewave oscillator is internally connected to the reference input. Thus as well as providing the modulation signal for the bridge network, the oscillator also provides the reference signal to drive the demodulator.

(3) The Demodulator

The demodulator us a linear gating circuit which is switched by the reference input waveform. The demodulator is able to cope with noise signals several million times greater than any error signals generated by the gating action or by subsequent d.c. amplification circuits. Thus, only signals which are in phase with

the reference gating waveform will give a d.c. output from the demodulator. These signals may be many orders of magnitude smaller than the noise level without the offset errors becoming significant.

(4) Low Pass Filter

The d.c. output from the demodulator is switched into a low pass filter which provides the main noise attenuation by means of a time constant control. Basically, the lock-in amplifier is a frequency selective voltmeter whose centre frequency is the same as the reference frequency applied to it. The bandwidth of this frequency (which is independent of frequency) depends only on the time constant of the low pass filter. The longer the time constant, the longer the system takes to respond but the smaller the bandwidth and the less noise there is. The noise bandwidth is given by (107).

(2.5-6)

$$\Delta f_{en} = \frac{1}{4T} \text{ Hz}$$

where T is the time constant in seconds

The output noise is thus determined by the time constant setting. After passing through the low pass filter, the output is routed to the d.c. amplifier.

(5) D.C. Amplifier

The d.c. amplifier provides a switchable gain of x1 or x10 and a zero-offset control. In addition, the d.c. amplifier incorporates an output smoothing filter whose purpose is to filter out low frequency ripples in the output. These low frequency ripples can be due to either a beat frequency occuring between the reference signal, or an interference signal, or just because modulation frequency of the experiment is low. There are two settings of the output smoothing filter. "Fast" is used when the ripples are 10Hz or greater, and "slow" for ripples of about 3Hz or less. Using the output smoothing filter does not significantly alter the response time of the d.c. amplifier.

The final output of the lock-in, which swings from -10 to +10 volts, can be monitored on a built-in centre-zero analogue meter (±10 volts corresponding to full-scale-deflection).

The lock-in amplifier can be operated in one of two modes which alter the distribution of a.c. gain and d.c. gain within the amplifier, thus optimising its performance under a wide range of operating conditions.

The overall sensitivity of the amplifier is proportional to the product of a.c. gain and d.c. gain. This value is kept constant when switching between the two operational modes, this preserving the overall sensitivity.

In the "Hi-Stab" or high stability mode, the d.c. gain of the demodulator is set to its lowest value and compensated for by additional a.c. gain in the signal channel. In this mode, the output stability of the demodulator is at a maximum; and the setting is therefore suitable for precise measurement of a.c. signals.

In the "Hi-Res" (high dynamic reserve) mode, the demodulator gain is switched to its maximum value which results in some deterioration of its d.c. output stability. The a.c. signal gain is reduced by a corresponding amount, thus making the best use of the overload capability (dynamic reserve) of the demodulator. This mode of operation is used for extracting signals from a noisy environment, a situation in which the reduced output stability is not a significant factor.

Table 2.2 illustrates the effect of the two modes on output stability and dynamic reserve.

The basic procedure for setting up the lock-in amplifier and bridge network is now described:

Table 2.2 Output zero stability and dynamic reserve figures for the Brookdeal 9503 lock-in amplifier(107)

Output Stability (ppm/^{o}C)

Mode	Output(x1)	Expand(x10)
Hi-Stab	10	100
Hi-res	100	1000

Dynamic reserve

(Demodulator overload capability)dB

Mode	Output(x1)	Expand(x10)
Hi-Stab	30	50
Hi-res	50	70

After setting up the fundamental frequency on the 5012F oscillator, the high and low pass filters are set to reject frequencies away from the frequency of interest. (For a second harmonic of 10kHz the settings would be: High pass 1kHz; low pass maximum). The 5011F active filter is set in notch mode and adjusted to reject the fundamental frequency, (a procedure described in the lock-in instruction manual). Next RV_3 (Figure 2.5-4) is adjusted to give a suitable a.c. modulation voltage amplitude, (typically 4mV peak to peak) which is measured on an oscilloscope. With the sensitivity setting on the lock-in at 1mV, RV_4 is adjusted to balance the bridge. (The balance point is reached when the lock-in meter registers zero). Now a small bias voltage (about 120mV) is applied to the bridge and the lock-in adjusted to detect the second harmonic signal which is a measure of the inelastic tunnelling current. This is achieved by activating the lock-in's internal frequency doubler (a button marked "2f") and adjusting the sensitivity to a maximum (usually 1μV). The phase of the reference signal is now adjusted to exactly coincide with the phase of the imput signal by means of the external phase controls. When the two signals are in phase the d.c. output from the demodulator is zero (Figure 2.5-7(a)). Next the phase of the reference signal is shifted by 90° with respect to the input signal. (The waveforms are now said to be in quadrature) and the d.c. output from the demodulator is now at a

maximum (Figure 2.5-7(b)). The zero-offset control is adjusted to give an on-scale deflection and the time constant of the low pass filter is selected. Choice of the time constant depends on two variables: the amount of noise which is to be attenuated and scan speed of the d.c. bias voltage. If a short scan speed has been selected (5 minutes, for example), then an optimum time constant would be one which just attenuates the noise yet allows the system to respond to changes in the second harmonic voltage. Obviously, a time constant of 100 seconds for a 5 minute scan is too large: by the time the lock-in output has responded to the second harmonic, the scan will be half completed. A more suitable time constant would be 300 milliseconds or less.

The bias voltage is now returned to zero, the gear mechanism engaged to RV_2 and activated thus scanning the bias voltage through a pre-determined range (usually 0-600mV). The bias voltage is applied to the X axis of the chart recorder giving a linear plot of bias voltage with distance. As the energy range is scanned by the bias voltage, changes in conductance (and hence the measure of inelastic tunnelling) are detected by the lock-in whose output is connected by the Y-axis of the recorder. The final result is an inelastic electron tunnelling spectrum of intensity (Y) against bias voltage (X).

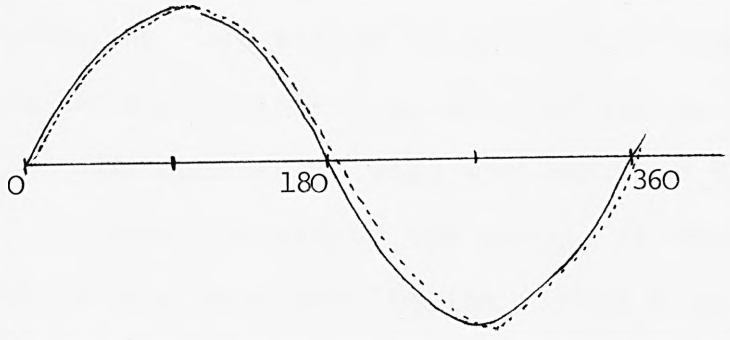

Figure 2.5.7a. Signals in phase producing zero demodulator output.

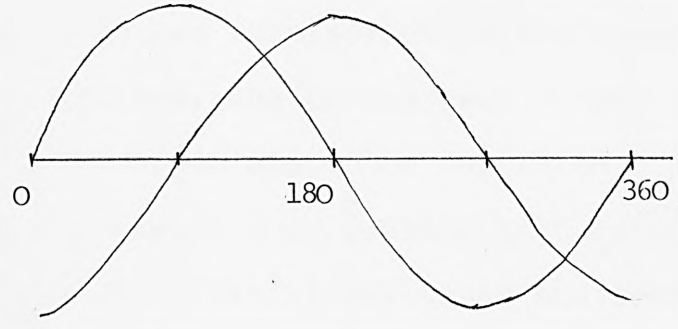

Figure 2.5.7b. Signals in quadrature producing maximum demodulator output.

CHAPTER 3. PRELIMINARY RESULTS

3.1 A REVIEW OF DOPING METHODS

Originally Jaklevic and Lambe (32) introduced the organic molecules they wished to study onto the oxide layer by exposing the oxide to an organic vapour in the sample preparation chamber. This was achieved by breaking a small glass tube containing the sample in the chamber. This method was used for liquids with a high vapour pressure e.g. acetic acid, propionic acid, methanol, ethanol and water. For substances with a lower vapour pressure (e.g. cyanoacetic acid) the sample was evaporated from a resistively heated boat. After exposure to the vapour at a pressure of $\sim 10^{-2}$ to 10^{-1} torr for five minutes, during which time a small percentage of the molecules would become chemisorbed to the oxide, the rest just being physisorbed, the chamber was pumped down to about 10^{-6} torr and the upper electrode deposited. Although this method of doping yields good quality high resolution spectra, it is only really useful for gases and samples with low vapour pressures and has several disadvantages.

(i) Since sample vapour pressure is a sensitive function of chamber pressure it is difficult to control exposure, especially with high molecular weight samples.

(ii) Cross contamination from back streaming hydro carbon pump oils is difficult to prevent.

(iii) The method is limited to molecules that vaporise without decomposing.

In addition to these problems Jaklevic and Lambe were only able to produce successful spectra of acids and alcohols which formed strong (chemisorbed) bonds with the oxide surface and produced a stable adlayer. They were unable to produce detectable spectra of acetone, benzene, and chloroform; presumably because these species only physisorbed to the oxide surface and were mostly pumped off before evaporation of the upper electrode.

Later Simonsen and Coleman (119,120) improved on the original vapour doping technique using a carefully temperature-controlled evaporation source and a separate doping chamber to minimise contamination.

Another method of doping was developed by Hansma and Coleman (121,122) and is applicable to liquids and solutions of organic compounds. After the formation of the oxide the half-completed junction is removed from the vacuum system and placed on a spinner (similar to the sort used for spreading photoresist on circuit boards) and a drop of the liquid sample placed on the oxide. The substrate is then spun to remove any excess liquid, and replaced in the vacuum chamber for deposition of the upper electrode. Using this method it is possible to dope with most liquid samples and solutions of organics.

The two principal solvents used by Hansma and Coleman are water and benzene: they claim that these solvents give no detectable spectra. However we have produced assignable spectra of benzene by spin doping and hence the principal peaks detected must be accounted for when a spectrum using benzene as a solvent is analysed. It is also possible to use other organic solvents such as methanol and cyclohexane, however these also give detectable solvent spectra. Using this method it is possible to exercise great control over doping parameters by variation of the solution concentration and its contact time on the oxide before removal by the spinner. In addition only one drop of sample is required. However the method does suffer from the possible risk of contamination by exposing the undoped junction to the atmosphere.

The advantages of spin doping over vapour doping for temperature sensitive molecules are illustrated below.

Figure 3.1.1 is the vapour doped spectrum of phenylalanine. Figure 3.1.2 is the spin doped spectrum of the same compound. Although the same peaks are present in both spectra, the resolution is clearly superior in the spin-doped spectrum thus allowing more peaks to be identified.

Another method of doping juctions originated by Skarlatos and his co-workers(123), is to dip the oxidised aluminium strip into an aqueous solution of the organic molecules.

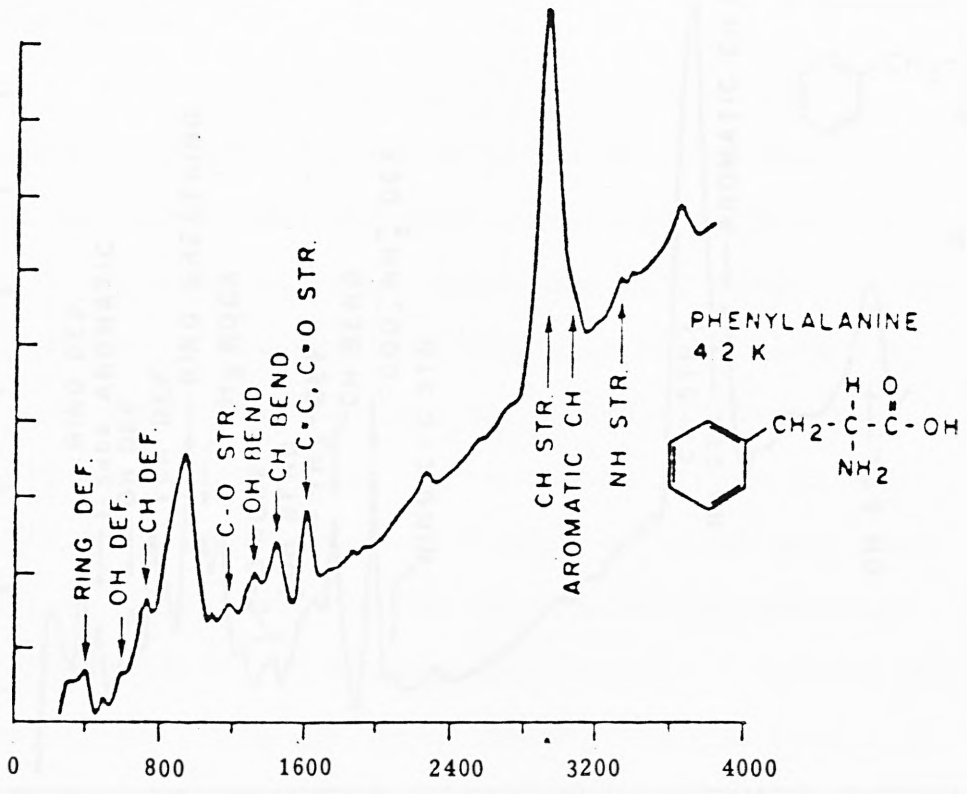

Figure 3.1.1. Vapour doped spectrum of phenylalanine.(Reference 47)

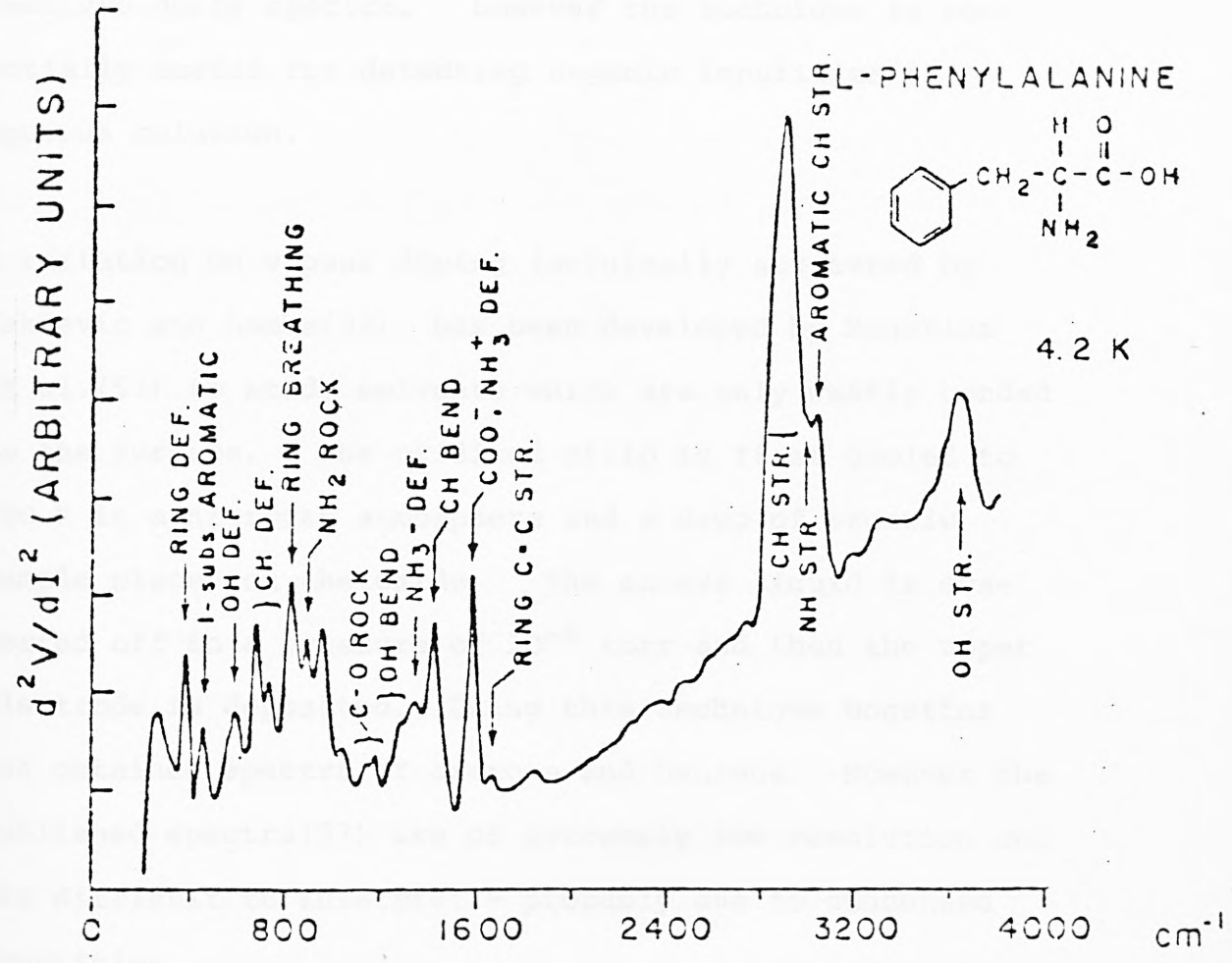

Figure 3.1.2. Spin doped sprctrum of phenylalanine.Note the improved resolution of the spin doped spectrum compared with the vapour doped spectrum in Figure 3.1.1. (Reference 47).

However as Figure 3.1.1 shows this method yields poorly resolved noisy spectra. However the technique is potentially useful for detecting organic impurities in aqueous solution.

A variation on vapour doping (originally suggested by Jaklevic and Lambe(32), has been developed by Bogatina et al.(57) to study solvents which are only weakly bonded to the surface. The oxidised strip is first cooled to 200 K in a nitrogen atmosphere and a drop of organic sample placed on the oxide. The excess liquid is evaported off to a pressure of 10^{-6} torr and then the upper electrode is deposited. Using this technique Bogatina has obtained spectra of acetone and benzene. However the published spectra(57) are of extremely low resolution and are difficult to interpret - probably due to condensed impurities.

It was partly because of this lack of high resolution spectra of weakly bonded surface species that the electrode penetration doping technique (described below) was developed.

The above methods of doping the junction all require the molecules to be introduced halfway through the junction preparation process. Apart from the possibility of introducing contamination these methods do not lend themselves to ease of use; it is not possible to sample a vapour physically far removed from the junction preparation chamber thus making it

experimentally inconvenient to use I.E.T.S. as a pollution monitor. The alternative is to prepare undoped junctions which can be stored in a dry nitrogen atmosphere or in vacuum sealed containers, and to externally dope them as required. There are two methods of externally doping junctions the first termed infusion doping is due to Jaklevic and Gaerttner(124) and the second, electrode penetration doping was developed as part of the work presented in this thesis.

Infusion doping is achieved by placing a completed junction above a solution of an organic sample in water in a closed vessel. The resistance of the junction is monitored and the junction is removed when a value of about 5 KΩ is reached. The rate of resistance change and hence the doping rate is proportional to the relative humidity. At 95% relative humidity a resistance change of 0.1 Ω to 10^3Ω takes about five minutes; at 70% relative humidity the same resistance change takes several hours, and below about 50% relative humidity the resistance remains constant and no doping occurs. Using this technique it is possible to dope junctions with polar molecules: acids, bases, and solvents and with large molecules such as napthol.

Jaklevic and Gaerttner performed masking experiments to deduce whether doping occurred predominantly through the lead electrode or at the edges of the junction.

Different areas of the junction were masked with Apiezon type L vacuum grease. The masked junctions were then infusion doped with a solution of the organic sample in water. After doping the grease was removed by rinsing the junction several times with benzene, and the tunnelling spectrum then produced. As a result of this work Jaklevic and Gaerttner concluded that doping takes place predominantly through the lead electrode, rather than from the edges.

There are two shortcomings to these experiments:

(i) The use of a hydrocarbon grease as a masking agent;

(ii) The removal of the grease with benzene.

Inelastic Electron Tunnelling Spectroscopy is extremely sensitive to hydrocarbon contamination, and it is quite probable that the vacuum grease would take part in competitive doping of the junction. Similarly, washing the junction in benzene should cause some doping of the oxide by the benzene.

Despite exposure to vacuum grease and benzene, Jaklevic and Gaerttner do not mention the presence of any hydrocarbon contamination in their results. (The tunnelling spectra of these experiments are not given in the relevant

paper either(124). The apparent absence of contamination suggests the interpretation of these results should be treated with caution. The technique is advantageous in that completed junctions can be stored until needed and used to sample vapours and gases without the need to use a vacuum system after doping; consequently the I.E.T.S. can be used for pollution, monitoring and remote sampling.

Another doping technique developed as part of this research is electrode penetration doping. It is by far the simplest of all the doping techniques discussed and it has the advantage that it uses completed junctions. Quite simply, a drop of the organic sample to be doped (or a weak solution of it in an organic solvent or water) is placed on the top of the completed junction whose resistance is continuously monitored using a low power ohmmeter. After an induction period of two or three minutes the resistance rises quite quickly at a rate of about 2 Ω per second. When about twice the optimum tunnel resistance is reached, the excess liquid is removed with a warm-air blower. The resistance then drops by about 50%. This technique is simple yet has advantages over the other doping methods in that it has been possible to obtain high resolution spectra of volatile solvents (e.g. benzene cyclohexane, acetone and diethyl ether), of large molecules such as paraquot and bis-pyridine cobalt dichloride. The possible mechanisms of electrode penetration doping are discussed after the results of an electron microscope investigation have been presented in Section 3.4.

Throughout this work only two doping methods were used spin doping(122,123) and electrode penetration doping.

3.2 OBTAINING THE CORRECT OXIDE THICKNESS FOR TUNNELLING

In order to obtain a thin uniform insulating barrier suitable for tunnelling, the aluminium electrode must be oxidised using a plasma discharge in a controlled manner. The following parameters were found to be crucial in this process.

1) The geometry of the chamber and the position of the oxidation ring carrying the high voltage
2) Purity of oxygen
3) Pressure of oxygen
4) Discharge current
5) Length of discharge (oxidation time)
6) Doping time

The geometry of the vacuum chamber and the position of the oxidation ring were not altered once the correct oxidation time had been found. High purity oxygen (99.999%) was used for the oxidation. The remaining factors were all kept constant, except for the oxidation time which was varied to obtain the correct oxide thickness. After several weeks of experimentation the pressure of oxygen was standardised to 7×10^{-2} torr and the discharge current was kept to $1(\pm 0.05)$mA, at a discharge voltage of $\simeq$375V. (The oxidation voltage was much less critical than the oxidation current). The doping time was standardised to 5 seconds followed by 40 seconds spinning time. However with samples that were

difficult to dope (e.g. α-chloro-p-xylene) the doping time was varied from 0.5 to 15 seconds in order to obtain a good result.

The optimum junction resistance for the equipment used in this project was 1 KΩ, and although adequate spectra could be produced from junctions in the resistance range 80 Ω to 5 KΩ, and junctions with a 1(±0.2) KΩ resistance gave the best results. In order to obtain the optimum junction resistance spin doped benzaldehyde junctions were made with oxidation times varying from 30 seconds to 80 seconds. Several junctions (usually four) were made at each oxidation time in order to ensure repeatable results. Occasionally a junction would have an anomalously high or low resistance, high resistances were probably caused by the junction becoming contaminated with dust or grit, and low resistances-usually a dead short between the electrodes - were probably due to incomplete oxide formation. Figure 3.2.1 shows how the oxide thickness is reflected in the I.E.T. spectrum. Eventually, an oxidation time of 70(±0.5) seconds was found to give reproducible tunnel junction resistances of approximately 1 KΩ and yield good spectra when the oxide was doped with benzaldehyde. However the optimum oxidation time varied by ±7% depending on the sample to be doped.

The effect of a small change in oxidation time (up to 1%) was not reflected in the junction resistance, but was more

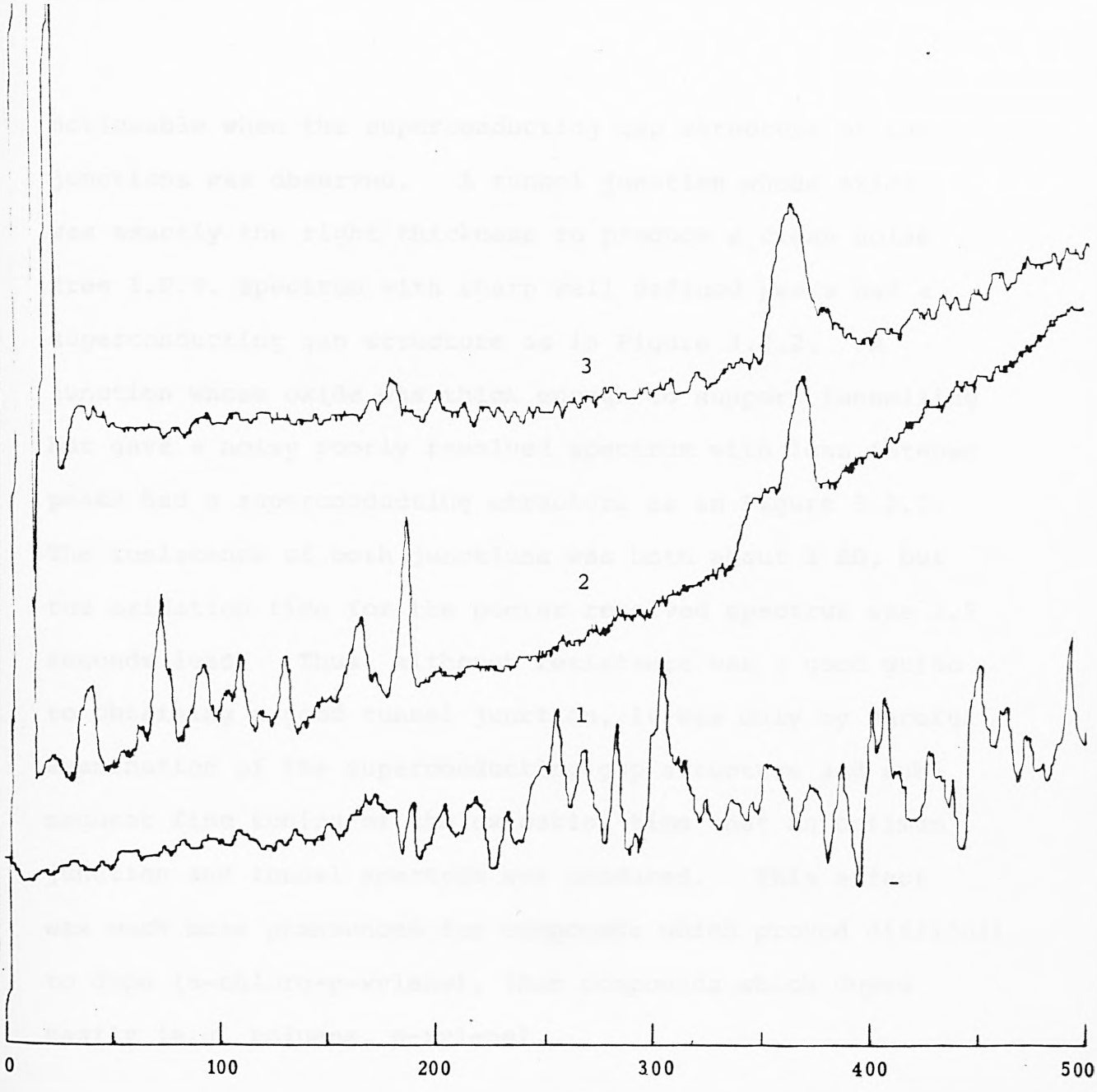

Figure 3.2.1. Result of different oxide thicknesses on tunnelling spectra at 4.2 k.

Trace 1: Oxide too thin. The superconducting gap is not present and instabilities are occuring at low bias voltages. (T_{ox} 65 seconds).

Trace 2: The oxide is the optimum thickness to support tunnelling. (Benzaldehyde, spectrum no. 303627. T_{ox} 70 seconds).

Trace 3: Oxide too thick. The superconducting structure is present but the peaks are poorly resolved. (T_{ox} 75 seconds).

(T_{ox} = oxidation time.)

noticeable when the superconducting gap structure of the junctions was observed. A tunnel junction whose oxide was exactly the right thickness to produce a clean noise free I.E.T. spectrum with sharp well defined peaks had a superconducting gap structure as in Figure 3.2.2. A junction whose oxide was thick enough to support tunnelling but gave a noisy poorly resolved spectrum with less intense peaks had a superconducting structure as in Figure 3.2.3. The resistance of both junctions was both about 1 KΩ, but the oxidation time for the poorer resolved spectrum was 1.5 seconds less. Thus, although resistance was a good guide to obtaining a good tunnel junction, it was only by careful examination of the superconducting gap structure and subsequent fine tuning of the oxidation time that an optimum junction and tunnel spectrum was produced. This effect was much more pronounced for compounds which proved difficult to dope (α-chloro-p-xylene), than compounds which doped easily (e.g. toluene, p-xylene).

An interesting phenomenon that occurred about 10% of the time, principally in thin junctions was noise. A junction would produce an I.E.T. spectrum which would be fairly noise free except for one region which would be noisy. This noise was not random in nature but systematic and time independent. Figure 3.2.4 shows two spectra of the same junction one taken 17 hours after the other, the noise which starts at about 300mV is clearly non-random in nature. The noise could be removed by a technique termed "boosting". The bias voltage was

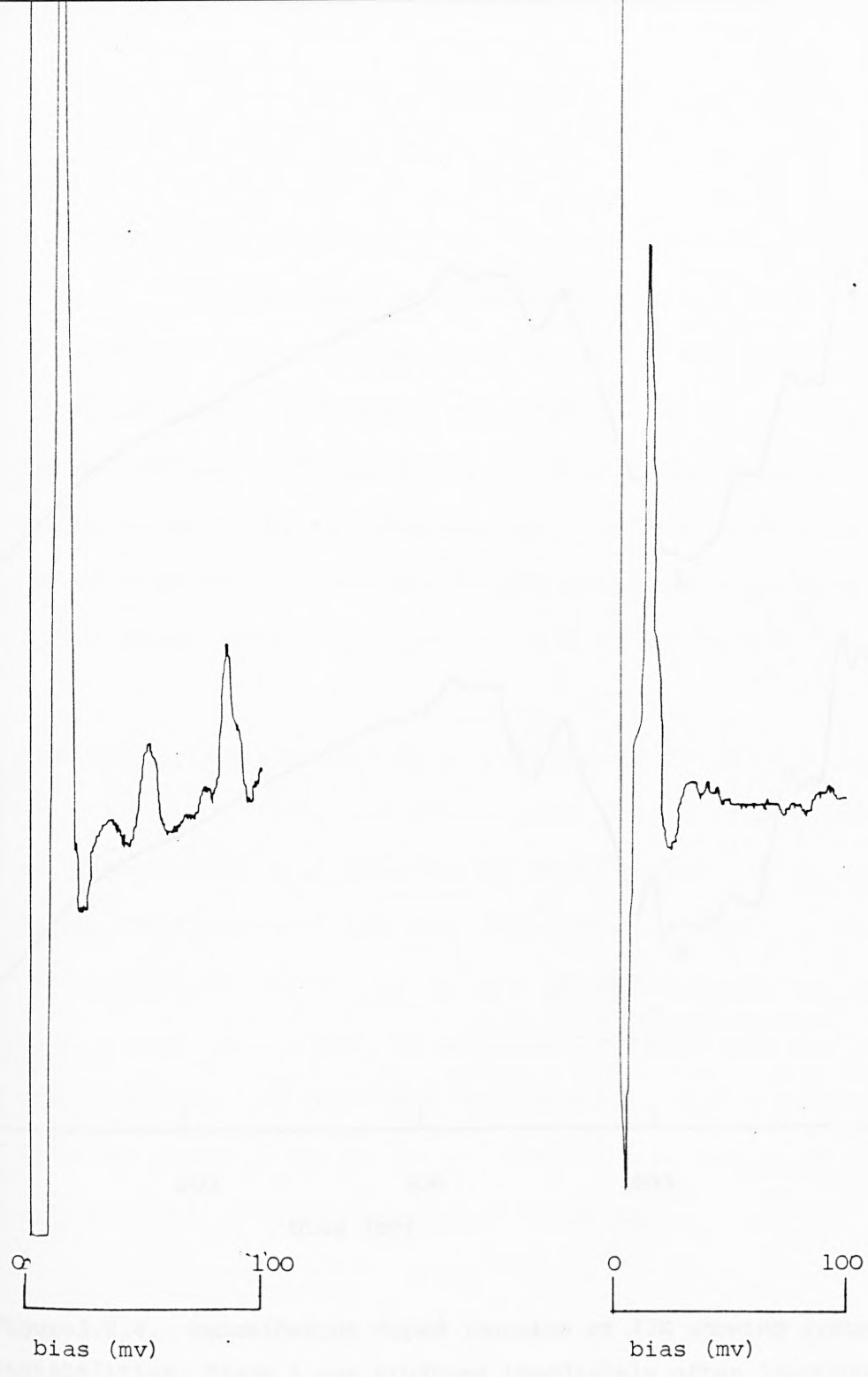

Figure 3.2.2 (left). Tunnel junction with optimum oxide thickness. Note the large superconducting structure. (Oxidation time: 70.5 secs.)

Figure 3.2.3 (right). Tunnel junction with very slightly too thin oxide . The superconducting structure is still present, but is much weaker. (Oxidation time: 69 secs.)
Both samples are α-chloro-p-xylene.

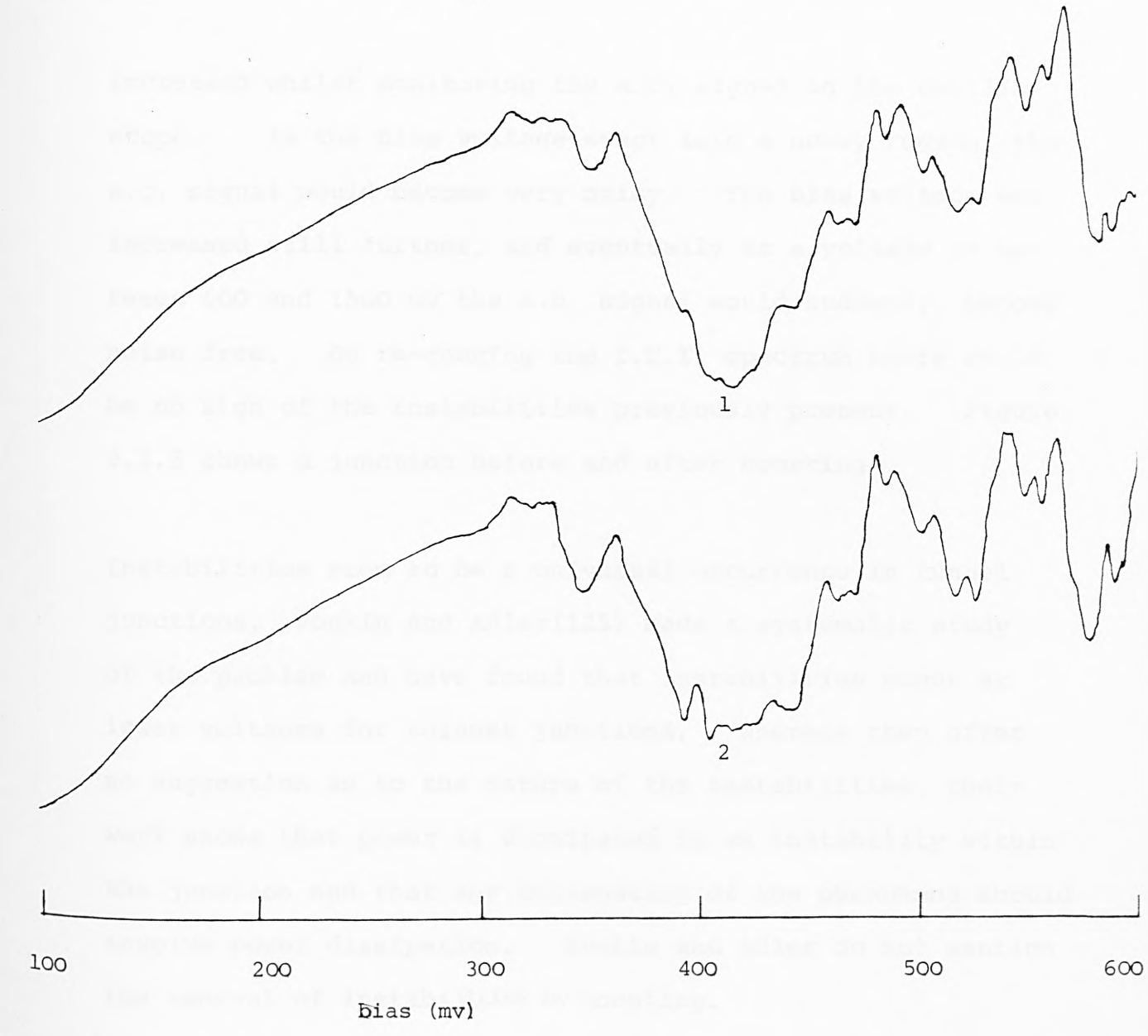

Figure3.2.4. Benzaldehyde doped junction at 77K showing systematic instabilities. Trace 1 was produced immediately after junction fabrication; Trace 2 was produced 17 hours later. (Scan time 6 minutes, time constant 10 seconds.)

increased whilst monitoring the a.c. signal on the oscilloscope. As the bias voltage swept into a noisy region, the a.c. signal would become very noisy. The bias voltage was increased still further, and eventually at a voltage of between 600 and 1500 mV the a.c. signal would suddenly become noise free. On re-running the I.E.T. spectrum there would be no sign of the instabilities previously present. Figure 3.2.5 shows a junction before and after boosting.

Instabilities seem to be a universal occurrence in tunnel junctions. Konkin and Adler(125) made a systematic study of the problem and have found that instabilities occur at lower voltages for thinner junctions. Whereas they offer no suggestion as to the nature of the instabilities, their work shows that power is dissipated in an instability within the junction and that any explanation of the phenomena should involve power dissipation. Konkin and Adler do not mention the removal of instabilities by boosting.

Two suggestions are now proposed to explain instabilities and boosting:

1) Some form of adsorbate rearrangement is occurring.

2) A physical change in the structure of the insulator occurs on boosting.

A discussion of these proposals is left until the results of

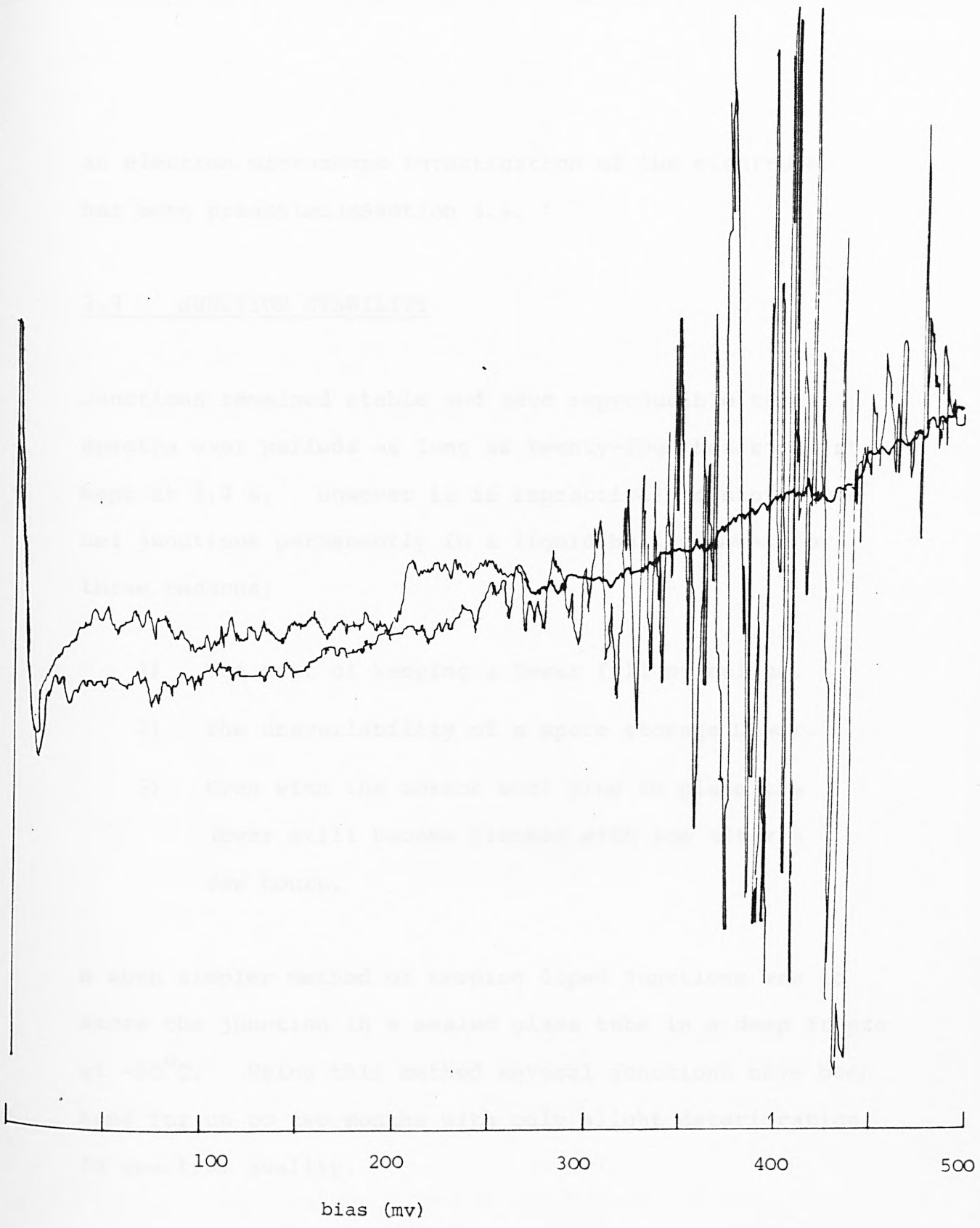

Figure 3.2.5. Junction after and before boosting showing removal of instabilities.

an electron microscope investigation of the electrodes has been presented in Section 3.4.

3.3 JUNCTION STABILITY

Junctions remained stable and gave reproducible tunnel spectra over periods as long as twenty-four hours whilst kept at 4.2 K. However it is impractical to store tunnel junctions permanently in a liquid helium Dewar for three reasons:

1) The cost of keeping a Dewar full of helium.

2) The unavailability of a spare storage Dewar.

3) Even with the cotton wool plug in place the Dewar still became blocked with ice after a few hours.

A much simpler method of keeping doped junctions was to store the junction in a sealed glass tube in a deep freeze at $-50^{\circ}C$. Using this method several junctions have been kept for up to two months with only slight deterioration in spectrum quality.

Figure 3.3.1 is the spectrum of tert-butyl benzene. Trace 1 was taken immediately after junction fabrication, trace 2 was made under identical operating conditions ten days later; the junction having been stored in a deep freeze. The only degradation is the broadening of some of the peaks, and a

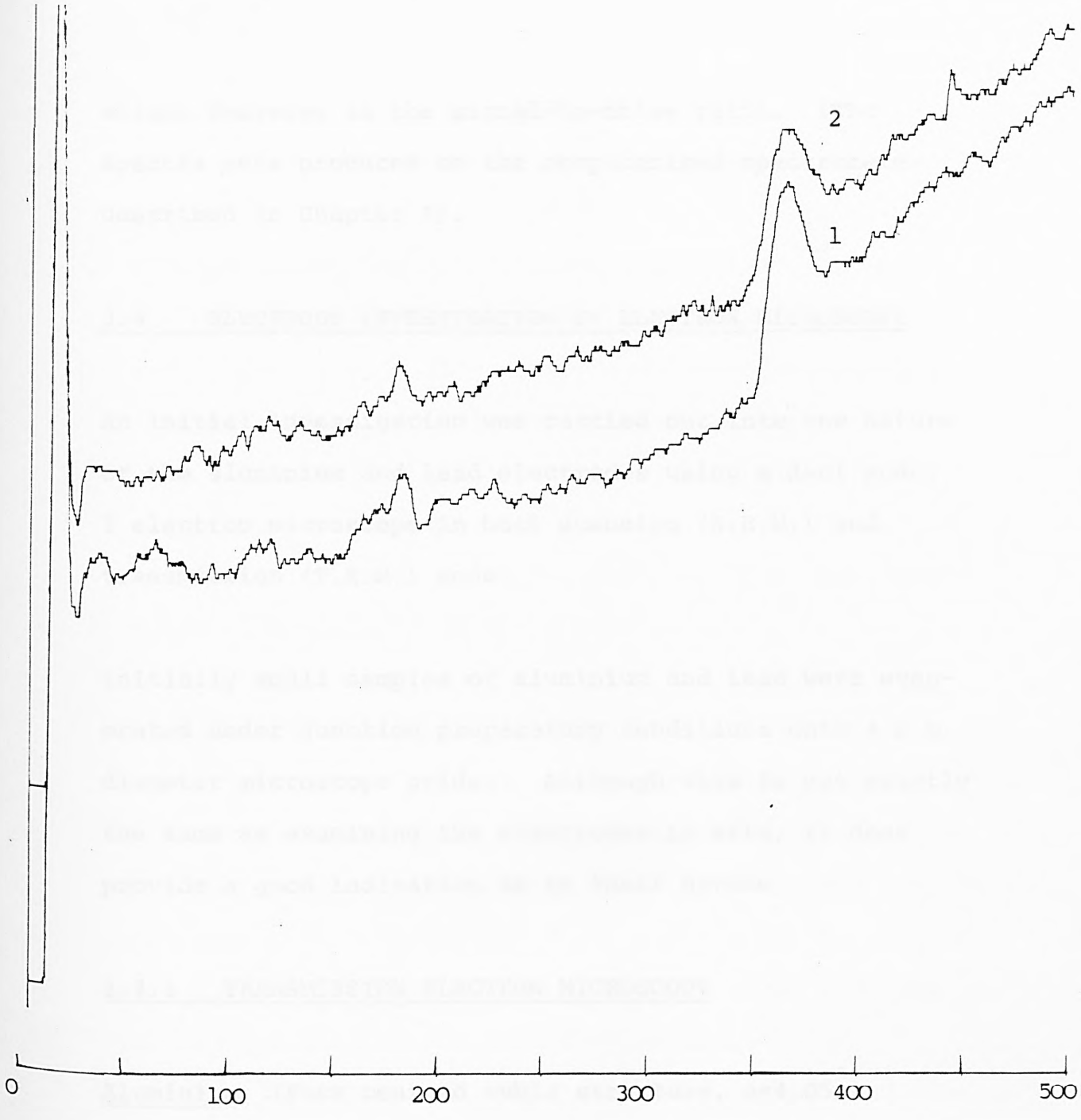

Figure 3.3.1. Trace 1 (no.311523) was produced immediately after the junction was fabricated, Trace 2 (no. 313524) is the same junction after ten days storage.

slight decrease in the signal-to-noise ratio. (The spectra were produced on the computerised spectrometer described in Chapter 4).

3.4 ELECTRODE INVESTIGATION BY ELECTRON MICROSCOPY

An initial investigation was carried out into the nature of the aluminium and lead electrodes using a Jeol model 3 electron microscope in both scanning (S.E.M.) and transmission (T.E.M.) mode.

Initially small samples of aluminium and lead were evaporated under junction preparatory conditions onto 4 m.m. diameter microscope grids. Although this is not exactly the same as examining the electrodes in situ, it does provide a good indication as to their nature.

3.4.1 TRANSMISSION ELECTRON MICROSCOPY

Aluminium (Face centred cubic structure, a=4.05$\mathring{A}$)

T.E.M. of the aluminium revealed a continuous crystalline film with the crystallite size ranging from 0.3μm in the medium and low density regions to 0.6μm in the thickest area examinable. The crystallite structure was essentially the same in all thickness regions of the aluminium (Photographs: 5, 6 and 7).

(There were no signs of any electron beam damage to the

sample. If local heating had occurred it may have annealed the aluminium changing its crystal structure).

The electron diffraction patterns showed that the aluminium was to some extent oriented on a preferred crystal plane. When considering electron diffraction phenomena it is easier to deal with the reciprocal lattice of the crystal structure in question, then each lattice point in fourier space corresponds to a spot on the diffraction pattern. Each lattice point (or diffraction spot) then represents a plane of atoms in real space.

The reciprocal lattice of aluminium (which is a face centred cubic structure) is a body centred cubic (b.c.c.) lattice(126). Thus when interpreting the electron diffraction pattern of aluminium, a body centred cubic lattice model was used. Photograph 8 was taken with the sample perpendicular to the electron beam. It shows a series of continuous diffraction rings of differing intensities. The first few have been assigned to the following crystallographic planes.

(111) innermost, (200), (220), (113), (222)

The intensities of the rings are in approximately the same ratio as for the X-ray diffraction data on aluminium. Furthermore, the relative intensities of the (111), (200) and (220) arcs as estimated from the reciprocal lattice model (on the

basis of the lattice points intersecting the Ewald's sphere, which for electron diffraction phenomena approximates to a plane surface), are in agreement with the observed intensities:

$$I\ (220) > I\ (111) > I\ (200)$$

The electron diffraction pattern becomes more interesting when the sample is tilted in the electron beam. Photograph 9 was taken with the sample titled 25^{o}. Some of the rings now show distinct signs of arcing which indicates there is some degree of preferred orientation in the sample. Distinct arcing has occurred on the (111) and (220) rings. This suggests the orientation is occurring on the (111) close-packed plane. If the b.c.c. lattice model is examined there can be seen a group of lattice points (which are equivalent to a group of planes in real space) which contain the (111) and some (220) points which are all in the same plane. (Figure 3.4.1. In order to verify that the preferred orientation is on the (111) plane, tilting the specimen through an optimum angle will make the arcs appear with their greatest intensity. The optimum angle is the angle between the (111) and (220) crystal planes, which is 35.26^{o} (from $\underline{a}.\underline{b} = [\underline{a}][\underline{b}] \cos\theta$). Thus, tilting the specimen through this angle will bring the reciprocal lattice "plane" shown in Figure 3.4.1 into the optimum Bragg condition for electron diffraction. Photograph 10 is the electron diffraction pattern taken with the

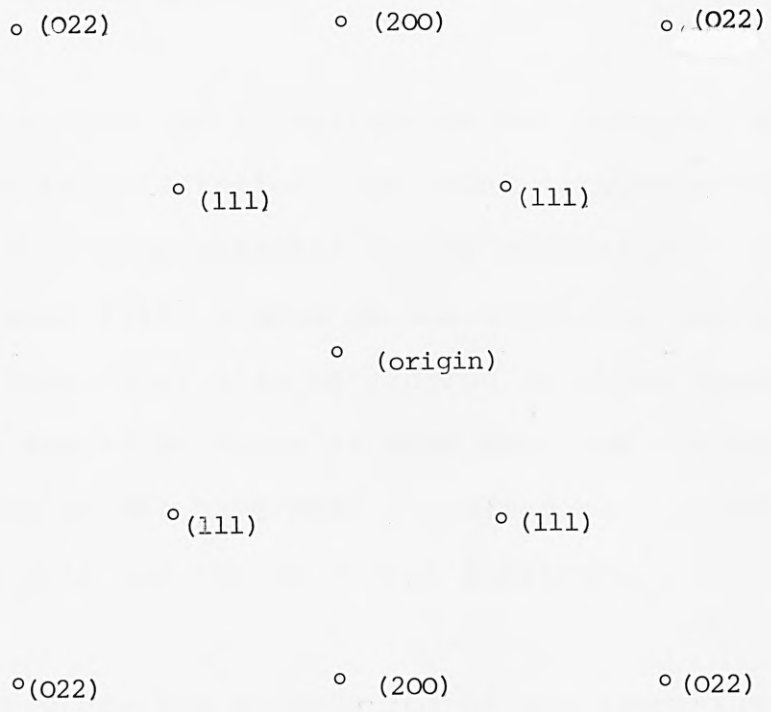

Figure 3.4.1. F.C.C. lattice in reciprocal space. Labelled points represent planes of atoms in real space.

sample tilted at 35.25°. The arcing is now much more pronounced on the (111), (220) and (200) rings. (The faint arcing on the (113) ring is because the (113) lattice points are equivalent to the (111) lattice points on an adjacent layer). At first it is surprising to see arcing on the (200) ring, but on examination of the reciprocal lattice model it can be seen that there is a plane that contains the (111) and (220) as well as the (200) lattice points.

So far the microscope investigation has revealed signs of a preferred orientation, the atoms forming a close packed (111) planes parallel to the substrate. Assuming there are some (111) planes on the aluminium surface, then the oxide layer must also be ordered in these regions. However it should be borne in mind that the aluminium samples investigated so far have been deposited on a carbon covered microscope grid and not on a real substrate.

In order to study the orientation of the aluminium on a printed circuit board it is necessary to resort to a technique known as reflection electron diffraction. These experiments were performed in a Siemen's transmission electron microscope whose sample holder had been modified to allow a large degree of lateral movement and accommodate a larger specimen. The experimental arrangement for reflection electron diffraction is shown in Figure 3.4.2. A small piece of printed circuit board with an aluminium

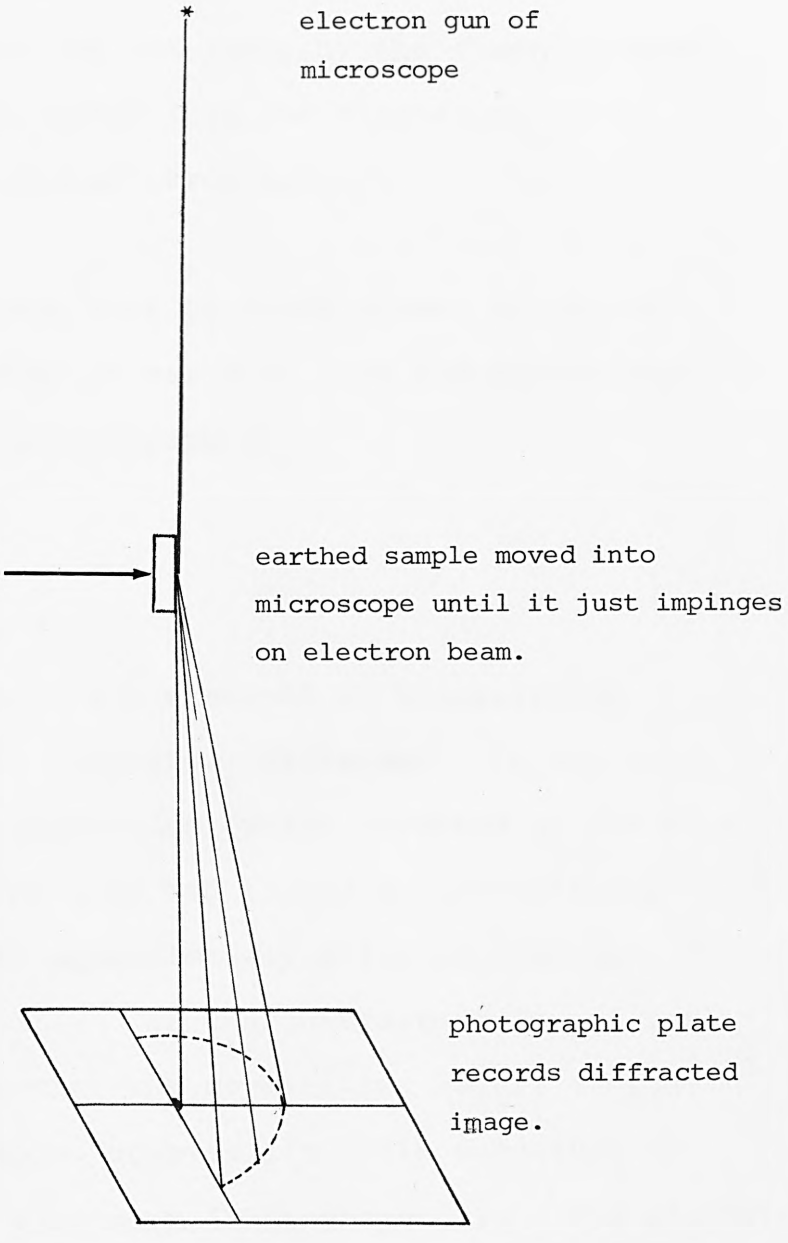

Figure 3.4.2. Experimental arrangement for reflection electron diffraction using a transmission electron microscope with a modified sample holder.

electrode deposited on it was mounted in the sample holder using conductive silver paint (Silverdag). |The sample had to be earthed to prevent charge build-up and subsequent degradation of the image by the electron beam|. The circuit board was moved into the microscope until it just impinged on the electron beam.

The diffraction pattern thus produced showed arcing on the (111) ring, however it was much less pronounced than for the tem. sample (Photograph 11).

Lead

When the lead electrode was examined in transmission mode the results were completely different. In the thinnest region of lead deposition (which occurred at the edge of the electrode), the lead had formed a discontinuous film of small islands approximately 0.1μm in diameter. (Photographs 12 and 13). In the thickest region of the electrode (in the centre) the crystalline nature of the lead is clearly visible, however its grain structure is much finer than the aluminium (Photograph 14). The electron diffraction pattern showed no signs of a preferred crystallographic orientation, even when the specimen was tilted.

The most interesting structure observed was in the medium thickness region. Photograph 15 was taken in between the thinnest and thickest areas. The islands originally

present have linked together to form a semicontinuous film with large pores in between. (White areas in photograph). Measurements reveal that these pores are approximately 0.1 x 0.6μm in size. In a thicker region (Photograph 16) the pores are still visible and of approximately the same dimensions. (The blurred appearance of the photograph is due to the sample thickness - not camera movement).

3.4.2 SCANNING ELECTRON MICROSCOPY

S.E.M. photographs were taken of the aluminium and lead electrodes deposited on the substrate.

Photograph 17 shows the surface of the aluminium after deposition on the printed circuit board. The surface is extremely rough with only a few smooth areas visible. If this is compared with a similar aluminium deposition on glass (Photograph 18) the difference in surface roughness is immediately obvious.

The lead electrode (Photograph 19) which was deposited on top of an aluminium electrode on a printed circuit board, reveals a similar surface to the aluminium electrode by itself (Photograph 16). The rough nature of both electrodes when on a printed circuit board substrate immediately prompted a closer examination of the circuit board surface.

3.4.3 SUBSTRATE EXAMINATION

Small samples of the printed circuit board were examined using scanning electron microscopy. The samples had to be gold coated in order to prevent charge build up on the insulator. The coating was only about 50Å thick and thin enough to mimic the substrate exactly. [As opposed to a 2000Å thick aluminium deposition which would tend to blanket the surface and conceal some of its finer structure]. Photograph 20 (a stero pair) reveals large pits in the surface these are estimated to be about 10μm deep. There are also very sharp jagged ridges on the edge of the pits.

3.5 JUNCTION STRUCTURE: INTERPRETATION OF OBSERVED PHENOMENA

It is now possible to build up a picture of the junction and interpret the results of electrode penetration doping, instabilities and boosting on this basis.

3.5.1 MACROSCOPIC STRUCTURES

The electron micrographs suggest several types of junction all of which are rough in nature. The electrode roughness being entirely due to the substrate. The principal macroscopic feature is not however due to the substrate surface roughness but to the lead evaporation: which reveals the porous structure of the lead electrode. Figure 3.5.1

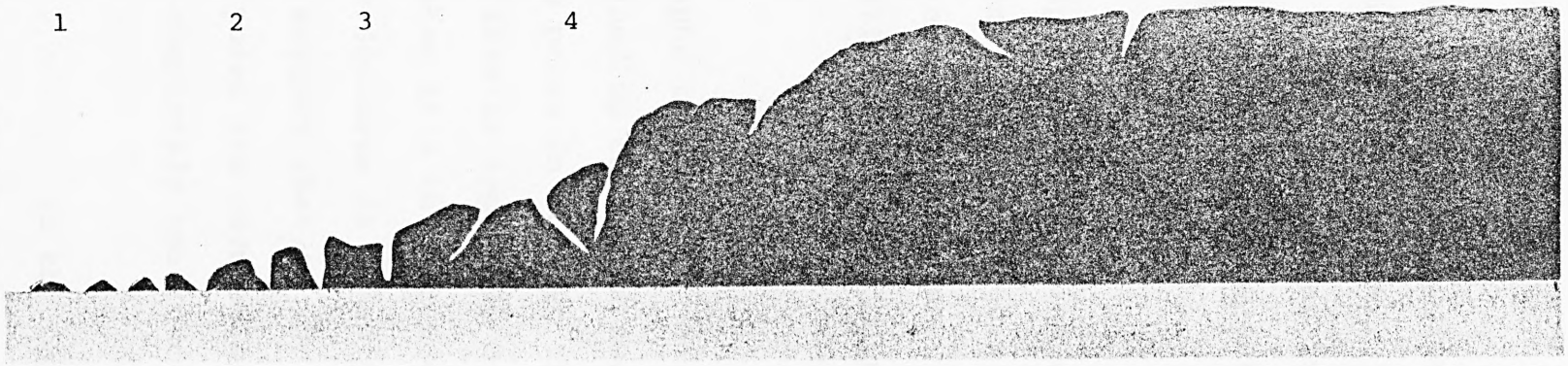

Figure 3.5.1. Proposed macroscopic structure of lead electrode. Region 1: Discontinuous film of small lead islands. Region 2: Islands are now coalescing. Region 3: Semicontinuous film. Region 4: Continuous film. (Not to scale.)

shows the large scale proposed cross section of the lead electrode. The four regions suggested by the microscope investigation are as follows:

Region 1 (Photograph 12) This region is a discontinuous film consisting of small lead islands approximately 0.1μm in diameter on an insulating alumina substrate. This region does not take part in the tunnelling process.

Region 2 (Photograph 13) The islands are now coalescing and forming small continuous regions of electrode approximately 0.4μm in size. As yet the film is still discontinuous and no conduction occurs through this region.

Region 3 (Photographs 15 and 16) Most of the islands have now joined up to form a semi-continuous film(127) with large pores in between the conducting region. The pores size is typically 0.5μm x 0.1μm. Photograph 15 was taken in a thinner region than Photograph 16. The decrease in density as the thickness increases suggest that as the lead becomes thicker more of the pores are covered over, the film eventually becoming completely continuous.

Region 4 In the centre of the electrode the film is completely continuous and

crystalline there is no evidence of any pore structure. The crystallite size varies from 0.2μm to 0.7μm. This Region (and Region 3) are the conductive regions of the electrode which participate in the metal-insulator-superconductor tunnelling process.

3.5.2 ELECTRODE PENETRATION DOPING

The large scale pore structure explains electrode penetration doping (and Jaklevic and Gaerttner's infusion doping(124)). The electrode structure allows molecules to penetrate (via capillary action) the upper electrode and adsorb onto the oxide surface. Such a doping mechanism also explains why it is possible to reversibly dope extremely volatile solvents such as ether. A comparison of spin doped and penetration doped spectra is given at the end of this section.

3.5.3 MICROSCOPIC STRUCTURE, INSTABILITY AND BOOSTING

On a larger magnification the surface roughness of the substrate becomes significant. A cross-section of a small area of junction is shown in Figure 3.5.2. The rough surface of the substrate is now evident and when the electrodes are deposited on this surface they imitiate its contours. The substrate cross-section in Figure 3.5.2 is quite accurate when the S.E.M. photographs (numbers 17, 19 and 20) are examined.

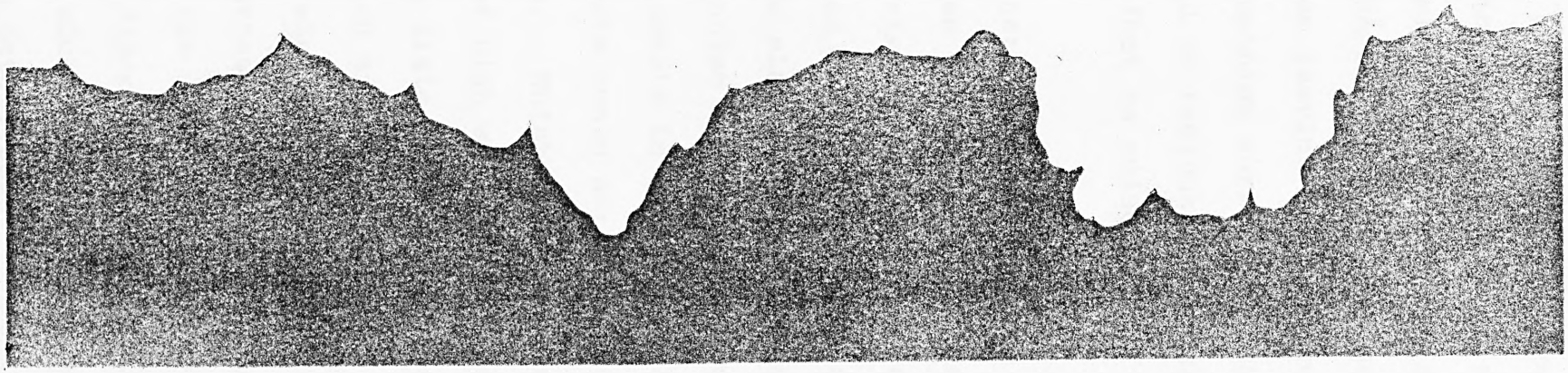

Figure 3.5.2. Cross-section of printed circuit board substrate. (Approximate scale: 2.5 cm = 10 μm.)

An even closer examination of the substrate reveals small sharp ridges protruding from its surface for several microns. The aluminium electrode has an estimated thickness of 2000Å or 0.2μm(34) and may not completely cover the surface leaving exposed areas of substrate. The uneven aluminium surface and consequent uneven oxide layer may lead to regions of differing conductivity which could manifest as noise in an I.E.T. spectrum.

A much more credible explanation of the surface structure which explains instabilities and boosting is the presence of metallic bridges, occurring between the two electrodes. Small filaments of aluminium formed during the deposition process would short the two electrodes providing a more favourable conduction mechanism between the electrodes. The formation of metal filaments is quite plausible. Points on the rough substrate could act as a starting point for metallic bridges. Whiskers have been observed to grow under conditions of high supersaturation without the need for more than one dislocation. On such a rough surface even the areas which are (111) oriented crystal planes will not be completely dislocation free and could thus act as nucleation centres. Herring and Galt(128) have observed whiskers of tin with a diameter of ∿1μm, and R.W. de Bois(128) has discovered nickel whiskers with diameters of ∿0.1μm: such dimensions are comparable with the scale of junction detail being considered.

The presence of metallic bridges explains boosting and instabilities in slightly thin tunnel junctions. The noise and slight degradation of the spectrum could be due to competitive conduction process through the oxide and the bridges. The non-zero resistance of the bridges would also fit in with the suggestions of Jaklevic and Gaerttner(124) who state that instabilities involved a power of dissipation law within the junction. It would be interesting to see if the instabilities disappear below 1.140 K when aluminium becomes a superconductor. Finally boosting and the subsequent removal of noise from the junction can be explained as the resistive heating and subsequent destruction of the metallic bridges. On the basis of the information available, a cross-section of the junction is as shown in Figure 3.5.3.

If the rough substrate is ultimately providing nucleation for whisker formation, then using a smoother substrate should reduce the number of instabilities and occurrences of boosting. In a series of toluene-doped I.E.T.S. junctions produced on a pyrex substrate the number of occurences of instabilities and boosting was less than $\sim$1%, compared with $\sim$20% for a printed circuit board substrate.

It is not proposed that tunnelling and metallic bridges are the sole conduction mechanism occurring in a junction: only that they are the principal conduction mechanism. Tunnelling via impurity traps and ionic conduction mechanisms

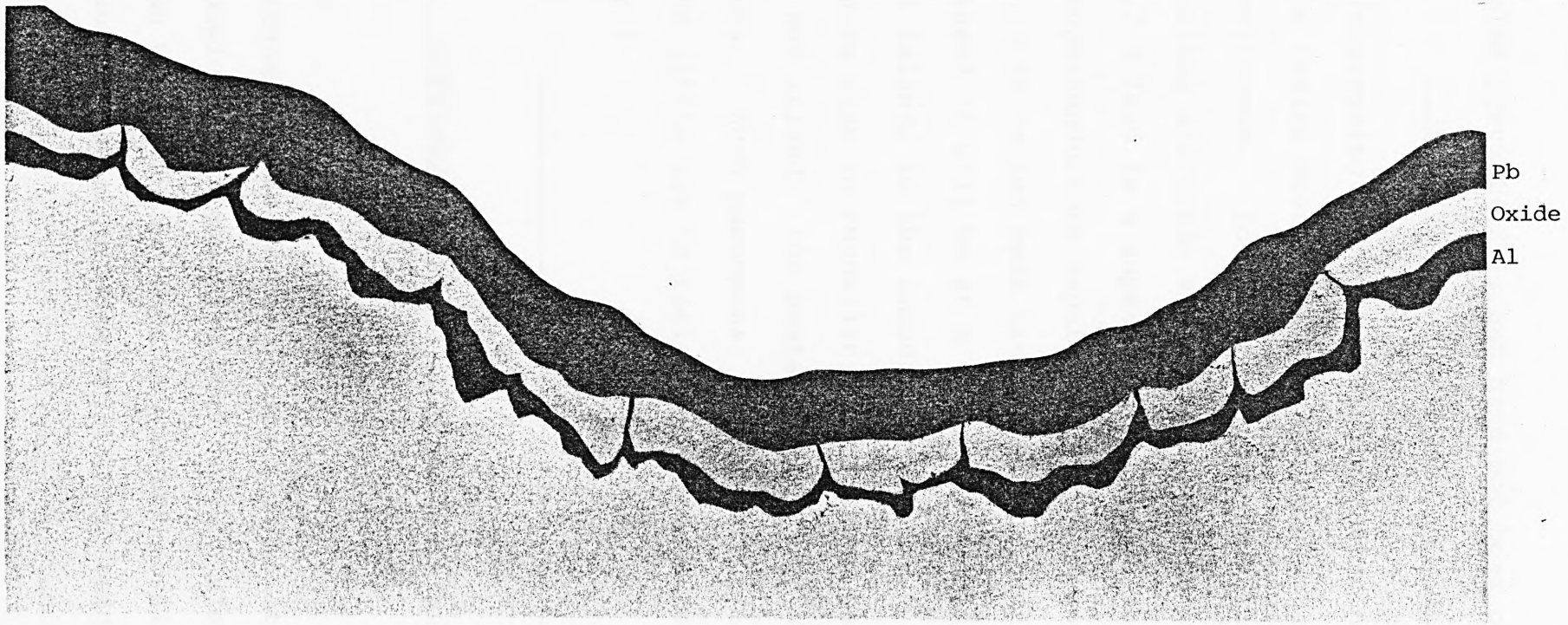

Figure 3.5.3. Proposed cross-section of junction showing metallic bridges between the electrodes. (Approximate scale: 10 cm = 10 μm.)

may also prevail(129); but have not been observed here).

(An interesting phenomena worth speculating on may occur in the region where the lead electrode starts to become discontinuous. In this region there will be the main conducting electrode and small insulated lead islands. At 4.2 K lead is a superconductor, thus there will be two superconductors separated by a thin region of insulator, a so called weak link. If now the lead electrode is biased it will be at a different potential from the small islands in the immediate vicinity. Such a situation may give rise to tunnelling of electron pairs between electrode and island: the basis for the A.C. and D.C. Josephson effects. Such phenomena, if they occur in tunnel junctions are of little use to inelastic electron tunnelling spectroscopy.)

3.6 COMPARISON OF SPIN AND ELECTRODE PENETRATION DOPING TECHNIQUES

Unfortunately, no direct in depth comparative study of the two doping techniques has been made. Electrode penetration doping was used only when it was not possible to spin dope a compound; either because of its high reactivity or because of the impracticability of returning the junction to the vacuum chamber after doping. Electrode penetration doping when

used as a "reserve" doping technique produces reasonable results. Figure 3.6.1 trace 1 is the spin-doped spectrum of benzene, and trace 2 is the same compound penetration doped. The signal-to-noise ratio in the 500 cm^{-1} to 1500 cm^{-1} on trace 1 is ∿6dB and a lot worse for many peaks, whereas for the same energy region in trace 2 the signal-to-noise ratio is ∿15dB. It is interesting to note there is very little shift in peak position for these two spectra.

When the spectrum of a compound that has spun doped well is compared with a penetration doped spectrum, the results are more interesting. The only spectra available for this comparison were;

benzene - penetration doped (as in Figure 3.6.1, trace 2)

benzene : toluene (10:1) - penetration doped (courtesy of Mr. D.M. Lewis)

toluene - spin doped

All three spectra are shown in Figure 3.6.2. The five principal differences between the spin and penetration doped spectra are:

1. The presence of Al-OH stretch at ∿3600 cm^{-1} in the penetration doped spectra;

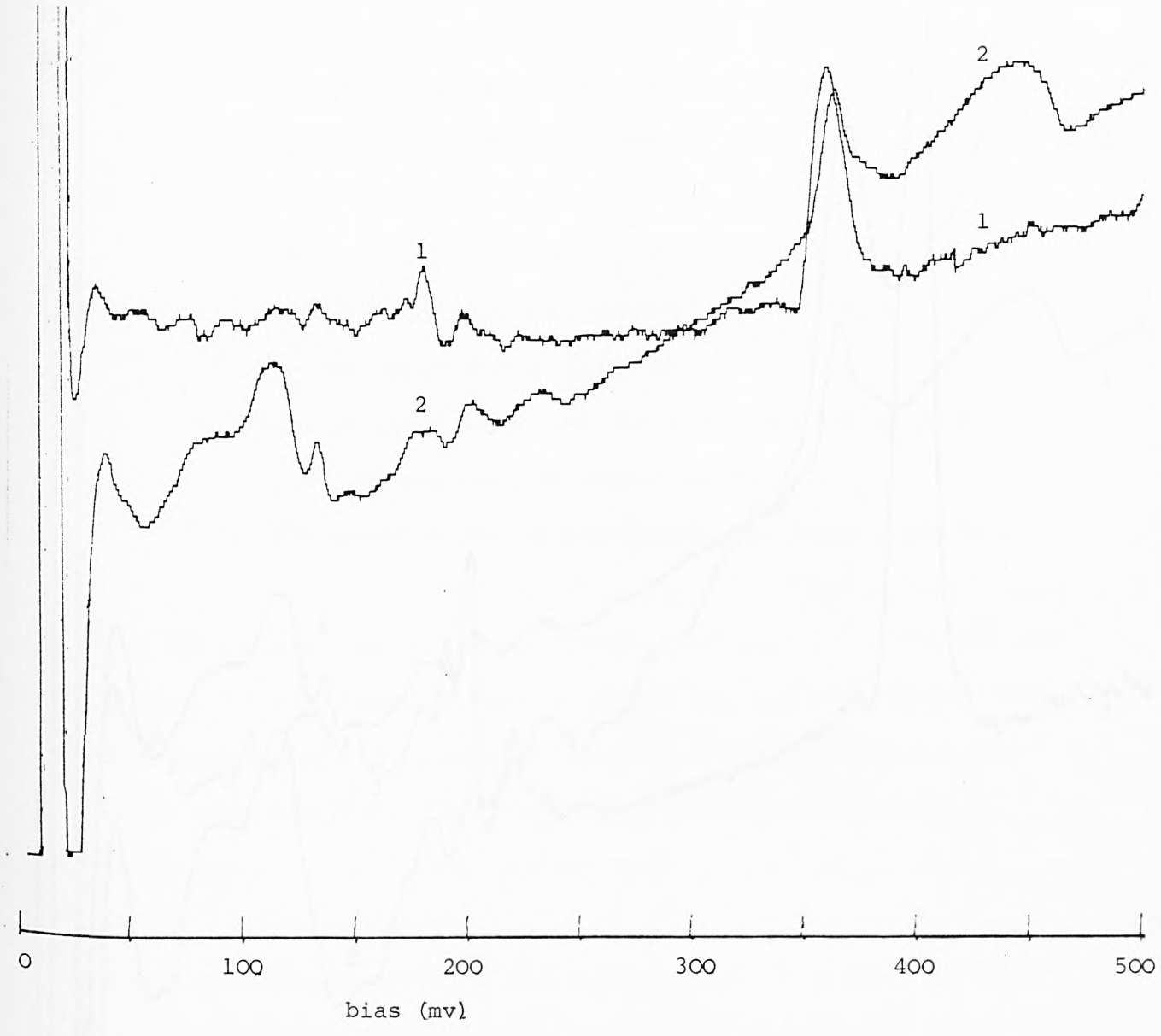

Figure 3.6.1. Comparison of spin-doped and penetration-doped benzene. Trace 1. Spin-doped (No. 415119)
Trace 2. Penetration-doped. (No. 335679).
(Spectrum 415119 courtesy of Mr. A. Fairfoull.)

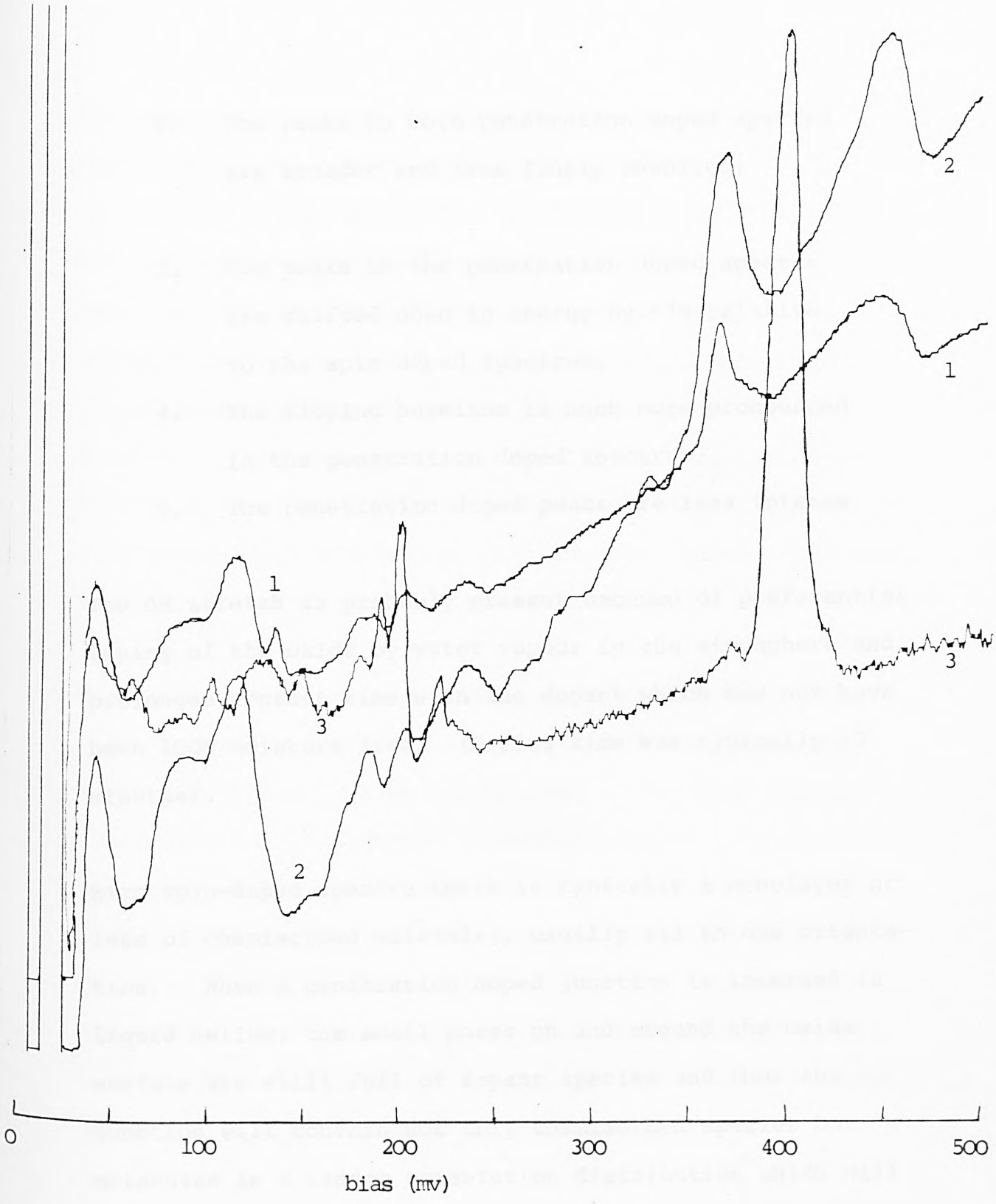

Figure 3.6.2. Comparison of penetration-doped spectra and spin-doped spectra.
Trace 1: Benzene, penetration-doped (no. 335679)
Trace 2: Benzene/Toluene (10:1), penetration-doped (no.602563)
Trace 3: Toluene, spin-doped (no.316584)

2. The peaks in both penetration doped spectra are broader and less finely resolved;

3. The peaks in the penetration doped spectra are shifted down in energy by ∿7% relative to the spin doped spectrum;

4. The sloping baseline is much more pronounced in the penetration doped spectrum;

5. The penetration doped peaks are less intense.

The OH stretch is probably present because of preferential doping of the oxide by water vapour in the atmosphere and prolonged contact time with the dopant which may not have been 100% moisture free. (Doping time was typically 15 minutes).

With spin-doped spectra there is typically a monolayer or less of chemisorbed molecules, usually all in one orientation. When a penetration doped junction is immersed in liquid helium, the small pores on and around the oxide surface are still full of dopant species and thus the junction will contain not only chemisorbed species but molecules in a random orientation distribution which will result in broader peaks. Since the molecules are in a larger number of different orientations the upper electrode effect (discussed in Section 1.12) will be more pronounced, thus giving a noticeable shift of peaks to lower energies. The C-H stretch has shifted from 3156 cm^{-1} in

the spin doped spectrum to 2900 cm^{-1} in the penetration-doped spectra, a change of 8%. Whereas the b_1 vibration at 998 cm^{-1} in the spin-doped spectrum has shifted to 984 cm^{-1} in the penetration-doped spectrum a change of less than two percent. (This b_1 vibration which occurs at 900 cm^{-1} in the infra-red at 77 K, is associated with the out of plane bending of the ring hydrogens and the ring torsion). The observed shifts and their subsequent decrease at lower wavenumbers is exemplary of the upper electrode effect previously only observed between different upper electrodes. (See Section 1.12.1).

The sloping baseline and less intense peaks of the penetration-doped spectra can be explained on the basis of surface coverage. If we assume that in the penetration-doped junction, the dopant (although present in excess in the pores of the electrode), has not formed a complete adsorbed monolayer on the oxide surface, then the peaks will be less intense as there is less inelastic tunnelling: consequently the ratio of inelastic conductance to elastic conductance (equation 1.4-15, page 22, etc.) will decrease resulting in a more pronounced sloping baseline.

Finally, penetration-doped spectra have been produced of polluted river water, phenol in water(130), and volatile anhydrous solvents. (A spectrum of diethyl ether was produced but only at 77 K: its consequent low resolution due to thermal broadening makes its inclusion trivial).

The success of penetration-doping compared with infusion doping, especially with samples such as benzene and ether, can only be attributed to the roughness of the substrate used for penetration doping studies. However these results are of a preliminary nature only and further investigation of substrate roughness in general is required before these results can be fully justified.

In conclusion, electrode penetration doping is a useful technique, especially in situations where the doping of a completed junction is a necessity, such as remote sampling. Provided the exaggerated top electrode perturbations are taken into account, (which fortunately in the fingerprint region of the spectrum are only a few per cent), I.E.T.S. absorption peaks can be correlated with infra-red and Raman spectra. However due to the multitude of molecular orientations present and the corresponding negation of the orientational selection rules, the utmost care should be exercised when proposing the geometry of the adlayer: data should be compared with spin-doped I.E.T. spectra of similar compounds wherever possible.

CHAPTER 4. COMPUTERISATION

Experimentally, it has been demonstrated that when running noisy junctions, increasing the time constant of the lock-in amplifier above ∿10 seconds does little to remove the low frequency noise fluctuations present; consequently it is not possible to obtain a high signal-to-noise (s/n) ratio and hence a good clearly resolved spectrum. However summing a series of short scans will reduce the low frequency fluctuations present. Before reviewing the various computerised systems which achieve this, it is worthwhile analysing the nature of the noise and how it can be reduced by multiple scanning.

4.1 ANALYSIS OF NOISE

The noise present in tunnel junctions can be broadly classified into two categories:

1) Random, shot noise. This noise is present even in "quiet" junctions when a low amplitude modulation voltage is used. (Its origins were discussed in Section 2.5.2). In this case increasing t_c, the lock-in time constant, will improve the s/n ratio; since the detector bandwidth, $\Delta\Omega \sim 1/t_c$, is reduced. (In fact $\Delta\Omega = 1/4t_c$.(107). Figure 4.1.1 shows the effect of increasing t_c in reducing shot noise.

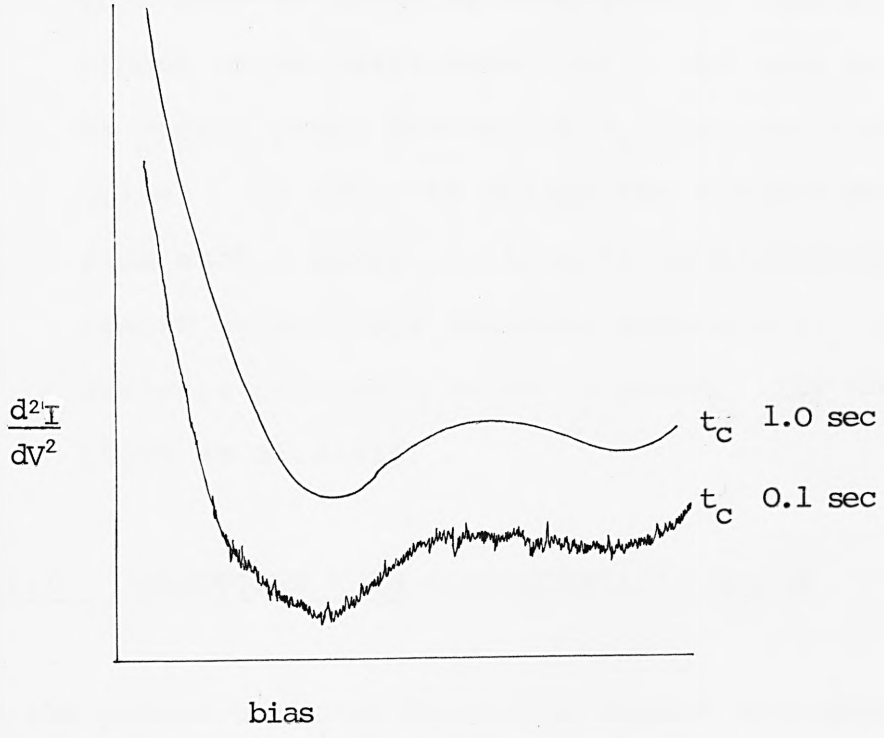

4.1.1 The effect of increasing lock-in time constant t_c on reducing Shot noise

2. Instabilities. Apart from the systematic instabilities as discussed in 3.2, random instabilities also occur in noisy tunnel junctions. This form of noise is much greater than shot noise: random noise peaks appear with the same intensity as tunnel peaks increasing t_c does not remove the noise. In order to obtain the optimum spectrum from such a noisy junction it is necessary to resort to multiple scanning techniques. (The analysis presented below is essentially due to Léger et al.(131).

4.1.1 JUNCTIONS WITH CHARACTERISTIC NOISE

In the second-harmonic detection system discussed in Chapter 1, a d.c. voltage, Vo, and a small a.c. voltage $V\omega \cos \omega t$, are applied to a junction and the resulting current I(V(t)) is studied.

$$V(t) = Vo + V\omega \cos \omega t \qquad (4.1\text{-}1)$$

(where $Vo >> V\omega$)

is applied to the sample and the second derivative d^2I/dV^2, is obtained from the lock-in amplifier, which is tuned to a frequency 2ω. Superficially, characteristic noise can be accounted for by superimposing it on to the detected signal. Expanding 4.1-1 with respect to $V\omega/Vo$ gives:

$$I(t) = Io + I\omega \cos \omega t + I_{2\omega} \cos 2\,\omega t + .. + n(t) \qquad (4.1\text{-}2)$$

where n(t) is the noise function, and

$$Io = I(Vo) + \frac{V\omega^2}{4} \left.\frac{d^2I}{dV^2}\right|_{Vo}$$

$$I\omega = V\omega \left.\frac{dI}{dV}\right|_{Vo}$$

$$I_{2\omega} = \frac{V\omega^2}{4} \left.\frac{d^2I}{dV^2}\right|_{Vo}$$

Thus the lock-in amplifier when tuned to a frequency 2ω with time constant t_c, detects the component of $I_{2\omega(t)}$ at $\Omega=0$ with a bandwidth $\Delta\Omega \sim 1/t_c$, and a component of n(t) at $\Omega=2\omega$ with the same bandwidth (see Figure 4.1.2).

In such a model the quadratic mean value of the noise is given by:

$$\overline{n^2} = g.(2\omega.)\frac{1}{t_c} \qquad (4.1\text{-}3)$$

where $g(\Omega)$ is the noise spectral density function. This function has a white part (i.e. a part consisting of a wide frequency spectrum whose amplitude is independent

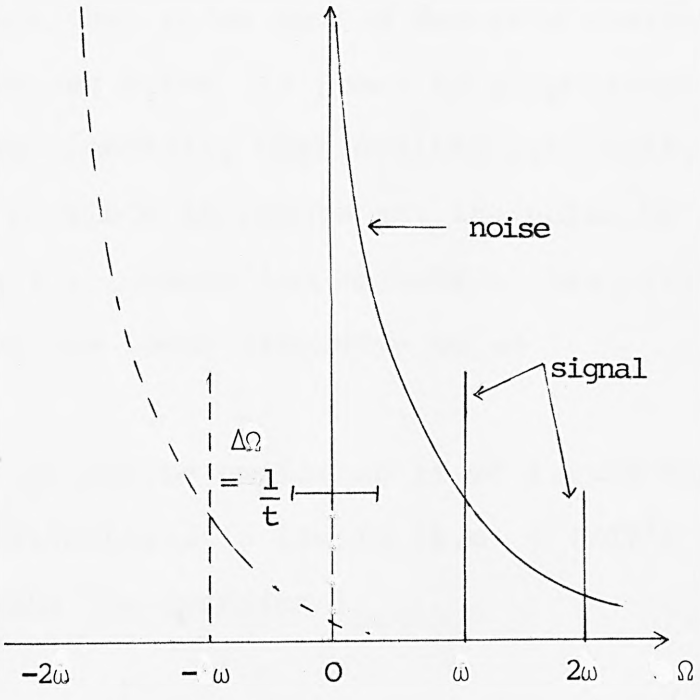

before synchronous detection

after synchronous detection

4.1.2 Diagram of the synchronous detection action on the noise and signal spectral densities as represented by eq.(4.1-2) After the frequencies shift, the lock-in detects signal in a bandwidth $\Delta\Omega = 1/t$ around $\Omega = 0$. For simplicity, only initially positive frequencies are represented. Note that, in this model for noise, the detection seems to be free from the low frequency peak in the noise spectral density.
(After Reference 131)

of Ω) and a 1/f part which is large only at low frequencies. When using synchronous detection at $2\omega \simeq 36$ KHz the lock-in is primarily sensitive to a value of a g at high frequencies where the 1/f component is negligible. This implies that noise should decrease continuously as t_c is increased since its power is proportional to $1/t_c$. However experimentally when dealing with noisy junctions it is not possible to remove all the noise by continually increasing t_c. Above $\sim$10 seconds t_c has little effect in removing the lower frequency noise.

The situation can be explained if we assume that the junction characteristic itself (i.e. d^2I/dV^2) is inherently noisy. Thus the function $I_{2\omega(t)}$

$$I2\omega(t) = \frac{V\omega^2}{4} \frac{d^2I}{dV^2}. \; Vo(t) \qquad (4.1\text{-}4)$$

is time dependent for two reasons. Firstly, the bias voltage Vo(t) is varying slowly with time, and secondly because junction characteristic d^2I/dV^2 also fluctuates in time. [The junction characteristic of a noisy junction can be seen to fluctuate if the bias voltage is kept constant and the lock-in output monitored on a voltmeter].

We assume that:

$$\frac{d^2I}{dV^2} = S(t) + N(t) \qquad (4.1\text{-}5)$$

where S(t) is the signal and N(t) is the characteristic noise. Again we assume that the spectral density $G(\Omega)$ of N(t) is composed of a white part and a 1/f part. Thus when the lock-in detector is set to detect the junction characteristic it is unable to avoid detecting the 1/f part of $G(\Omega)$ centred at $\Omega = 0$. The principal difference between characteristic noise and the characteristic signal is that for a fixed voltage the junction characteristic (due to tunnelling) will be constant and reproducible whereas the noise will occur at random. Thus averaging several scans will remove the characteristic noise leaving only the signal of interest.

4.1.2 CALCULATION OF THE CHARACTERISTIC NOISE FOR THE AVERAGE OF SEVERAL SCANS

The noise can now be calculated for two types of experiment:

(1) One scan lasting $\Theta_1 = T$

(2) n scans ($10 \leqslant n \leqslant 1000$) each of duration $\Theta_2 = T/n$.

(Where Θ is the scan time and T is the total scan time $60s \leqslant T \leqslant 3600s$)).

The optimum time constant t_c (which will be calculated

later) is a fraction ($\alpha \sim 10^{-2}$), of the scan time. Hence:

$$\left.\begin{aligned} t_1 &= \alpha\, \Theta_1 \\ t_2 &= \alpha\, \Theta_2 \end{aligned}\right\} \qquad (4.1\text{-}6)$$

We consider two extreme cases for the noise spectral density:

$$\left.\begin{aligned} &\text{for white noise} && G(\Omega) = a \\ &\text{for } 1/f \text{ noise} && G(\Omega) = b/\Omega \end{aligned}\right\} \qquad (4.1\text{-}7)$$

(When dealing with the $1/f$ noise we have to introduce a minimum frequency, or low frequency cut off, below which no $1/f$ noise is present. This value is arbitrarily chosen as $1/\Theta$, and its exact value is not critical).

For $1/f$ characteristic noise, the signal and noise are calculated as shown in Figure 4.1.3. For one sweep we obtain:

$$\left.\begin{aligned} \overline{N_1^2} &= \int_{1/T}^{1/\alpha T} \frac{b}{\Omega}\, d\Omega = b \ln \frac{1}{\alpha} \\ S_1^2 &= S^2 \end{aligned}\right\} \qquad (4.1\text{-}8)$$

4.1.3 Integration of $G(\Omega)$ giving the characteristic noise for two experiments (1 and 2), with a 1/f spectrum. The low frequency cut-offs are assumed to be the inverses of the sweep times (θ_1 and θ_2), and the high frequency cut-offs are the inverses of the lock-in time constants (t_1 and t_2). Note that, in this model, because of the low frequency divergence of $G(\Omega)$ the noise values are the same for a short sweep (1) and for a long one (2). On the contrary, an averaging procedure of n sweeps will reduce the noise as n.

After Reference 131.

For the sum of the n scans we obtain:-

$$\left.\begin{aligned} \overline{N_2^2} &= n. \int_{n/T}^{n/\alpha T} \frac{b}{\Omega}\, d\Omega = n.b.\ \ln \frac{1}{\alpha} \\ S_2^2 &= n^2\, S^2 \end{aligned}\right\} \qquad (4.1\text{-}9)$$

(since quadratic values for noise are added during the sum of scans. From 4.1-8 and 4.1-9 we obtain the signal-to-noise ratio:-

$$\frac{S_2^2/\overline{N_2^2}}{S_1^2/\overline{N_1^2}} = n \qquad (4.1\text{-}10)$$

i.e. the s/n ratio increases, in power, as the number of scans, n, is increased.

For white noise we similarly obtain:

$$\overline{N_1^2} = \frac{a}{T}\left(\frac{1}{\alpha} - 1\right) \quad \text{and}$$

$$\overline{N_2^2} = \frac{n.na}{T}\left(\frac{1}{\alpha} - 1\right)$$

hence:

$$\frac{S_2^2/\overline{N_2^2}}{S_1^2/\overline{N_1^2}} = 1 \qquad (4.1\text{-}11)$$

With white noise the s/n ratio is independent of the number of scans, n.

Equations (4.1-10 and 4.1-11) are the two extremes, and the exact result will depend on the form of $G(\Omega)$. However because $G(\Omega)$ contains a large 1/f component, (typically the low frequency component is of the order of 0.5 to 2 Hz), it does seem worthwhile to average a large number of scans.

Since the white part of $G(\Omega)$ is independent of frequency, it can be included either in n(t), equation (4.1-2), or in N(t) equation (4.1-5). Then, providing we ignore the 1/f component of the characteristic noise $G(\Omega)$, we obtain the expected result that it is equivalent to scan once with a time constant t_c, or to scan n times with a time constant t_c/n.

This is the basis for the reason why the s/n ratio is not improved when t_c is increased above $\sim$10 seconds. This value of the t_c probably corresponds to the frequency below which the 1/f component of $G(\Omega)$ becomes significant, and hence equation (4.1-8) demonstrates the non-dependence of the s/n ratio on t_c or T.

In conclusion, we see that increasing the time constant of the lock-in amplifier above a certain value will not eliminate low frequency characteristic noise, however signal averaging will eliminate this sort of noise.

4.1.3 CALCULATION OF OPTIMUM VALUE OF SCAN TIME (θ) AND TIME CONSTANT (t_c)

Scan time, θ: Since the s/n ratio increases with n, the number of plots (equation 4.1-10) the optimum scan time should be as short as possible for a given total scan time T, however there are limitations:

(1) Limitations due to modulation frequency ω (Figure 4.1.4) if the peaks are to be resolved when their full-width-half-maximum (f.w.h.m.) is 1% of the maximum bias voltage, i.e.

$$\Delta V/V_{max} = 0.01$$

then during a scan of duration θ the output of the lock-inwill be a function of time Y(t) with peaks of width:

$$\Delta\theta/\theta = 0.01$$

Assuming the curves approximate to a gaussian shape, then the Fourier transform of Y(t) will be a gaussian curve of f.w.h.m. $\Delta\Omega$ (we are now in frequency domain) where:

$$\Delta\Omega = \frac{4}{\Delta\theta}$$

Thus in order to preserve sufficient information when

(a)

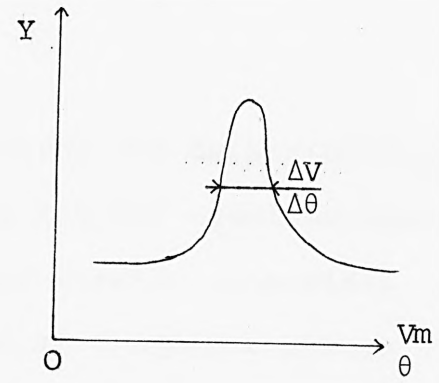

(b)

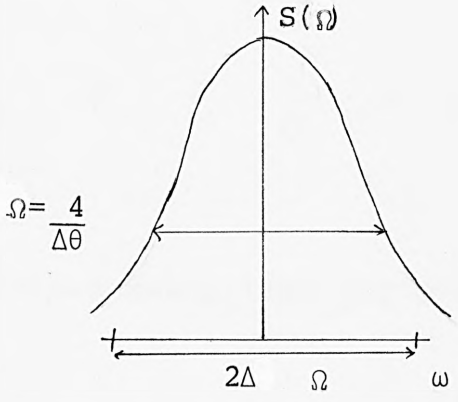

(c)

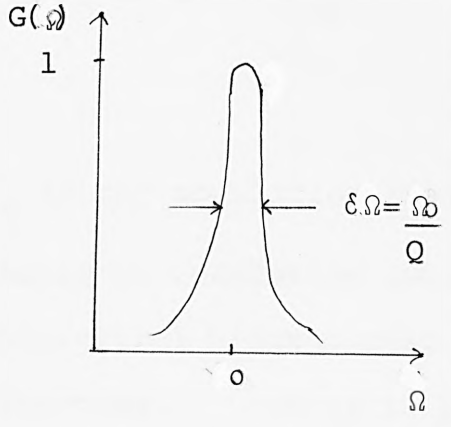

4.1.4 (a) Example of the time dependence of the lock-in output Y during one sweep. The characteristic is supposed to have a peak, whose width is $\Delta\theta$, a fraction of the total sweep time θ.

(b) Fourier analysis of Y(t). The peak in Y(t) is assumed to be a Gaussian and therefore gives another gaussian for $S(\Omega)$. Widths are defined at $e^{-\frac{1}{2}}$ of the full heights.

(c) Frequency response $G(\Omega)$ of detection filters. Signals are preserved in a bandwidth $\delta\Omega$. In order to realise a good restitution of the original signal, we need $\delta\Omega \gtrsim 2\Delta$. This will lead to a limitation for the shortest sweep time θ compatible with good resolution of characteristic structures.

Y(t) passes through the detection filter (the lock-in amplifier), the Fourier spectrum should be continued in a band $\delta\Omega$ about twice this width. Thus for atuned filter centred at frequency ω with a quality factor, Q we have:

$$\delta\Omega = \frac{\omega}{Q} = 2.\frac{4}{\Delta\Theta}$$

hence the minimum sweep time for $Q \sim 10$ is

$$\Theta = \frac{1000}{f_o.}$$

where f_o is the modulation frequency ($=\omega/2\Pi$).

Thus on the basis of resolution considerations alone, there is a theoretical minimum scan time for f_o= 18 KHz of 55.6 milliseconds. However in practical terms the electronics must be capable of storing data at this rate.

(2) Limitations due to electronics. In a computerised system the time taken to execute one instruction depends on an internal clock frequency. The faster the frequency the faster the C.P.U. can execute instructions. For our particular microcomputer, based on a Motorola 6502 microprocessor chip the oscillator runs, at $\sim 1 \times 10^6$Hz. However this is not the maximum rate that data could be

received and processed, since many separate instructions have to be executed in order to store one data value.The maximum rate at which the computerised spectrometer described in section 4.3, can process data is 39 milliseconds per point. Thus when scanning 0-500 millivolts, the minimum scan times are:

1000 data points : 0.65 minutes (≡39 seconds)

2000 data points : 1.3 minutes (≡78 seconds)

4000 data points : 2.6 minutes (≡156 seconds)

Time Constant, t_c: calculation of α.

The optimum time constant is determined by the sweep time. The largest value of α ($t_c = \alpha\theta$) will give the best s/n ratio as determined by equation (4.1-9). However there is a restriction imposed by the lock-in response time. The rise time (the time taken for a signal to increase from 10% to 90% of its final value) of a 6dB per octave low pass filter, is $2.2t_c$, thus in order to resolve peaks of width $\Delta V/V_{max} = 0.01$ the optimum time constant is:

$$t_c \simeq \frac{\theta}{200} = \alpha \simeq \frac{1}{200}$$

Thus for a scan time of 600 seconds ($\theta = 600$) the optimum time constant is 3 seconds, for a scan time of 39 seconds (or 0.65 minutes), the fastest scan speed available on

the system used here, the optimum time constant is

$$\frac{39}{200} = 0.195 \text{ seconds}$$

(the nearest available setting is in fact 300 milliseconds).

A list of scan times and optimum time constants is given in Table 4.1.

Thus for the computerised system built for this research project, the deciding factor in selecting the optimum time constant and minimum scan speed is the response time of the computer, which results in a minimum scan time of 39 seconds per scan.

4.2 REVIEW OF MULTIPLE SCAN SPECTROMETERS

This review is concerned only with I.E.T. spectrometers which are capable of running several scans and averaging the results, thus improving the resolution and s/n ratio. The following spectrometer systems, although representing significant advances in tunnelling spectroscopy are principally single scan instruments and have therefore not been included.

1. The digital system of Oxley, Reynolds et al.(132)

Table 4.1. Scan times (θ) to use for the available time constant settings (t_c). (Based on a rise time of 2.2 t_c for a 6 dB/octave low-pass filter.)

t_c (seconds)	θ (seconds)
0.10	20 *
0.30	60
1.00	200 (3.3 minutes)
3.00	600 (10 minutes)
10.00	2000 (33.3 minutes)
30.00	6000 (1.67 hours) *

* scan times shorter than 39 seconds and longer than 60 minutes are at present outside the scope of the spectrometer. These limits can be altered by modifying the software.

2) The differential bridge network of Colley and Hansma(133).

3) The Computerised System of Hipps and Mazur(134).

The above systems (with the exception of (2)) have essentially used a normal analogue spectrometer, and digitized the output from the lock-in amplifier. The resultant digital signal is then processed using a mini computer. These systems merely facilitate ease of data handling : there is no improvement in s/n ratio. Hansma's differential bridge(133) simultaneously runs a doped junction and a blank junction and subtracts one from the other by analogue means.

There are as yet only three multiple scan systems in operation:

1) A Multichannel Analyser-based system by Léger(131).

2) A minicomputer-based system by Dargis(135)

3) The microprocessor-based system constructed for this project.

4.2.1 MULTICHANNEL ANALYSER SYSTEM

The M.C.A.-based spectrometer developed by Léger et al.(131) is shown in Figure 4.2.1. It is essentially an adaption

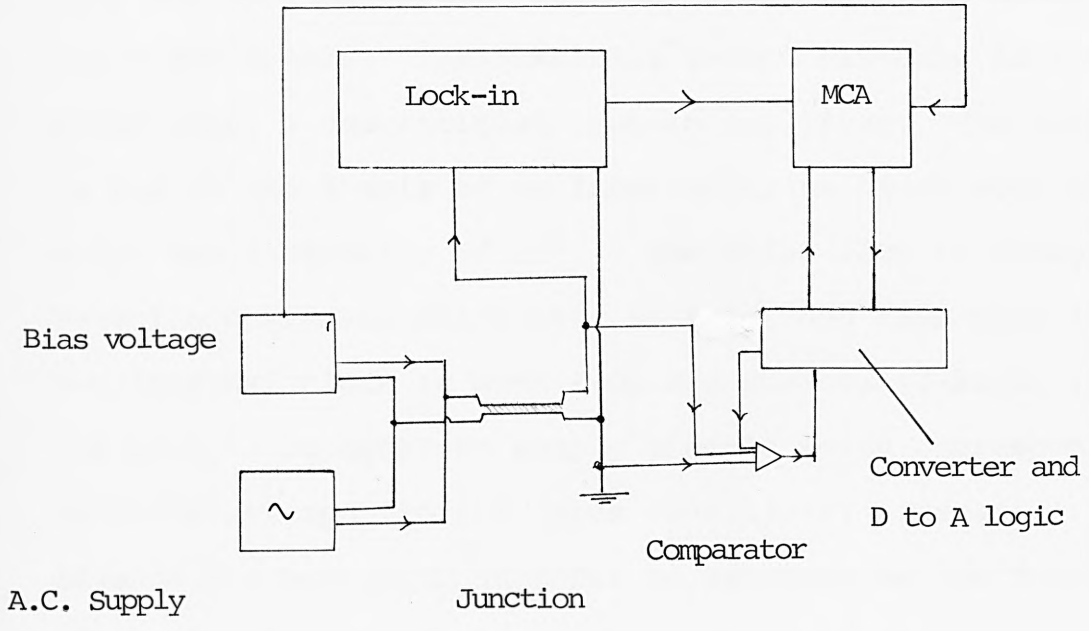

Figure 4.2.1. Multi Channel Analyser (MCA)-based spectrometer system of Leger (131).

of an analogue spectrometer by the addition of a multi-channel analyser (M.C.A.). Although at first this idea may be crude, the system is elegant in its simplicity: the only extra digital equipment needed is the address advance logic used to drive the M.C.A. which replaces its own internal clock. The ramp voltage (d.c. bias) and the a.c. modulation voltage are generated conventionally and applied to the junction. (Four terminal measurements are used). The resulting second harmonic is detected using a conventional lock-in amplifier. The output is fed to the Y axis of an Intertechnique Didac 4000 M.C.A. which has a capacity of 10^6. The Didac 4000 is designed to collect signals which vary in time, and thus uses its own internal clock to move from one channel (X-axis) to the next. In order to sample signals which correspond to different applied d.c. bias conditions, a separate advance has been built in order to synchronise the X-axis of the M.C.A. with the ramp voltage.

4.2.2 MINICOMPUTER-BASED SYSTEM

The minicomputer-based spectrometer developed by Dargis(135) uses a P.D.P. 11/20 minicomputer to generate the d.c. bias supply and store first derivative measurements. Figure 4.2.2 shows the block diagram of the system. The P.D.P. 11 computer generates an analogue ramp voltage via a 12-bit digital-to-analogue converter. The ramp voltage is fed (via an opto-isolator which isolates the computer ground from the spectro-

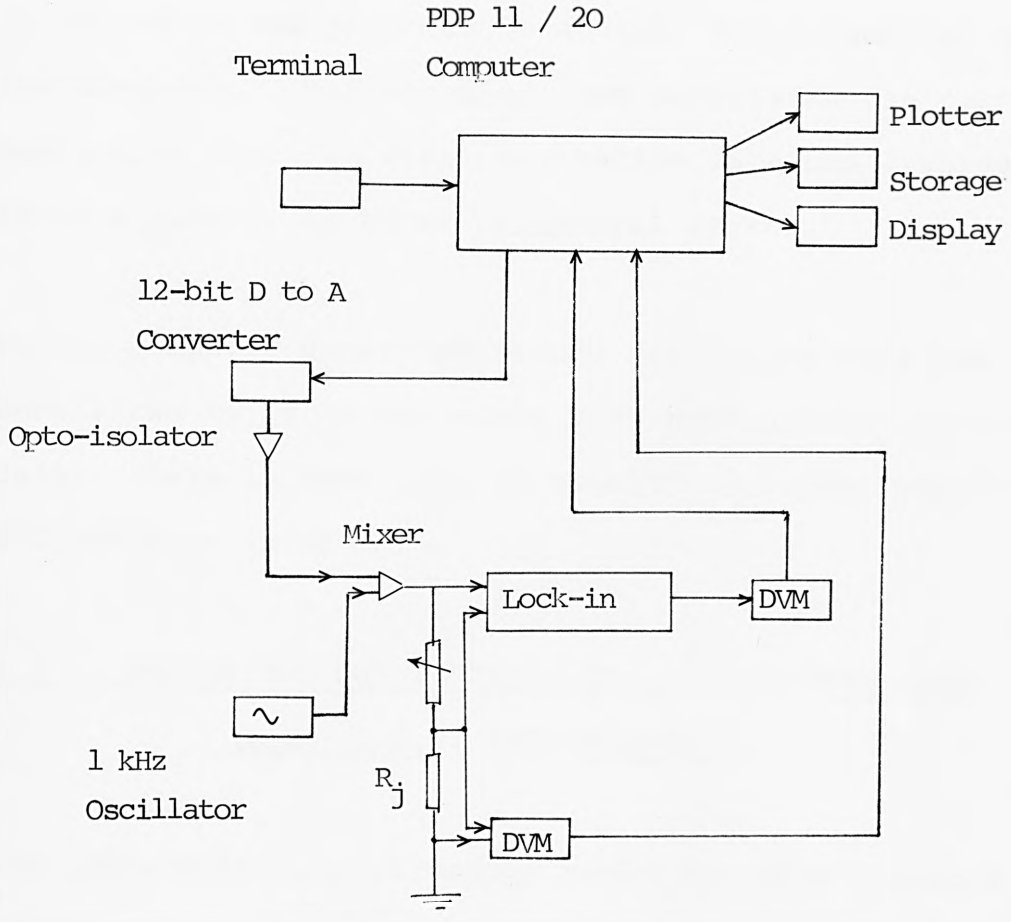

Figure 4.2.2. Mini computer-based system of Dargis (135)

meter ground) into a mixer where it is mixed with a conventionally-generated sinewave. The resultant signal is fed to the junction where a lock-in amplifer used to detect the FIRST derivative. The output from the lock-in is then digitized using a digital voltmeter (D.V.M.) and fed into the computer. The X axis voltage is sensed at the junction by another D.V.M. and fed into the computer. The computer then calculates the second derivative from the first derivative data and displays it on a plotter or other peripheral device.

Whilst computer generated second derivative data has been shown to be in agreement with harmonically detected data; there is some loss in sensitivity when computing d^2I/dV^2 from dI/dV data.

4.3 DESIGN AND CONSTRUCTION OF A MICROPROCESSOR-BASED I.E.T. SPECTROMETER

The computerised spectrometer built for this research combines the advantages of the multichannel analyser system of Léger et al.(131) with the more accurate and flexible control capabilities offered by a computer controlled system.

A block diagram of the spectrometer is shown in Figure 4.3.1. A Pet 3032 microprocessor is used to control the spectrometer via a 16 way data bias. The spectro-

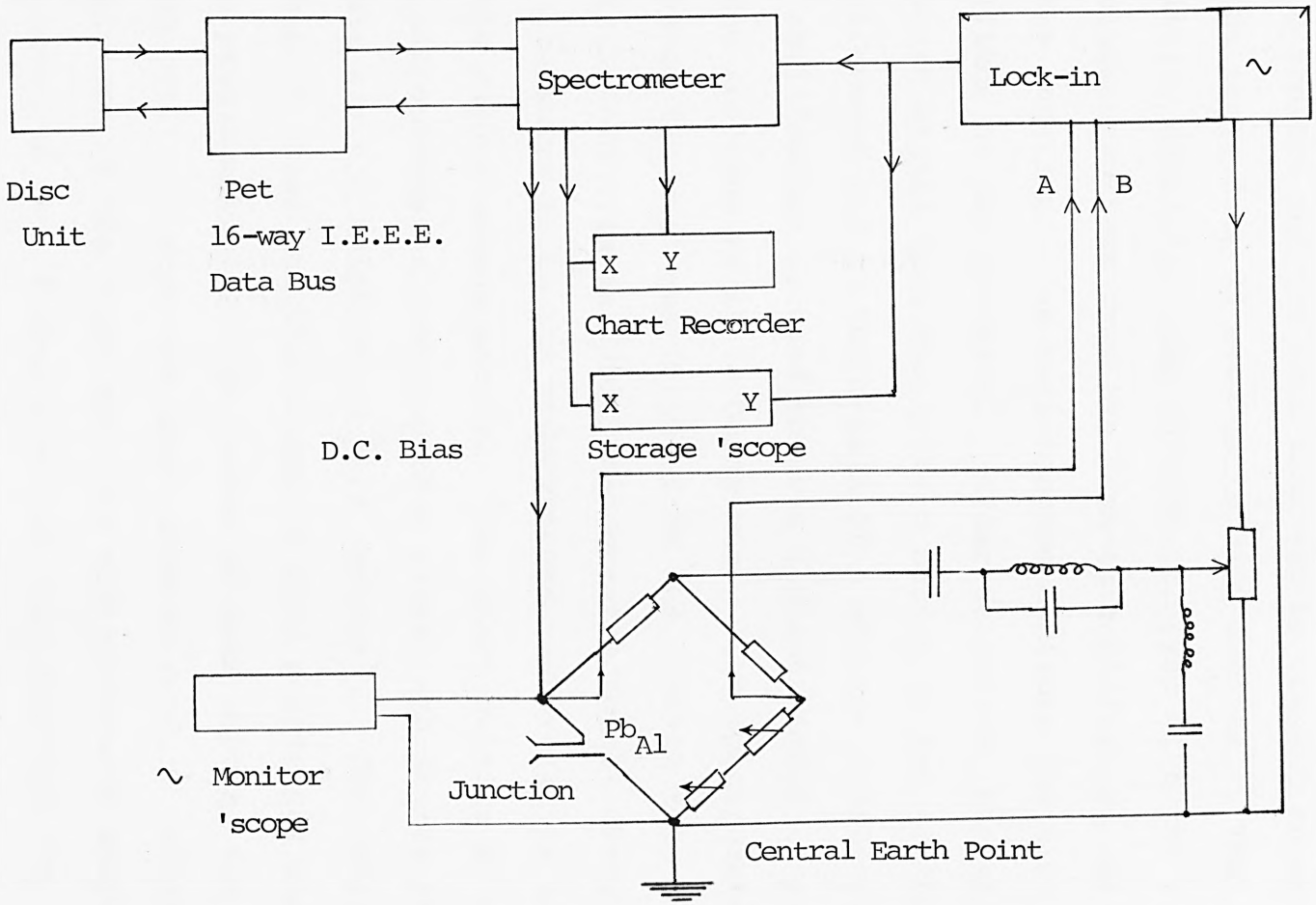

Figure 4.3.1. Block diagram of computerised spectrometer.

meter generates a d.c. ramp voltage using a 12-bit digital-to-analogue (D.to A) converter. The maximum d.c. voltage and scan speed are programmable; with the present software two scan ranges are available (0-500mV and 0-5volts) and the scan time can be present anywhere in the range from 39 seconds to 3600 seconds. The digitally generated ramp voltage is mixed with the a.c. modulation voltage from the lock-in amplifer and applied to the junction. An oscilloscope monitors the a.c. amplitude at the junction. After detection, the second harmonic signal from the lock-in output is fed to the spectrometer and to the Y-axis of a storage oscilloscope. The oscilloscope is used to give a quick visual record of the spectrum as it is being run. The spectrometer converts the analogue output from the lock-in into a digital form (via an 8-bit analogue-to-digital converter) and transmits it to the microprocessor where it is stored in the random access memory. [The exact details of how the microprocessor averages this signal and stores the result are not relevant in this section]. The total number of scans and the number of data points per scan are also programmable. (The number of data points, for a 0-500 millivolt scan are 1000, 2000 or 4000.). After completion of the final scan the microprocessor stores the spectrum on a floppy disc and then displays the resultant spectrum on a chart recorder.

4.3.1 INSTALLATION AND MODIFICATIONS

Several teething problems became apparent during the first few days operation. Firstly the spectrometer was very susceptible to electrical interference, which would immediately cause the d.c. ramp voltage to rise to +5 volts damaging the junction in the process; secondly if the junction shorted out, (thus shorting the ramp voltage to ground) the output transistor became overloaded and was destroyed. Finally if the junction shorted out or went open circuit during a large number of scans, the computer would carry on sampling the lock-in output even though there was no signal present. This resulted in the microprocessor averaging any recorded part of the spectrum to zero.

There were several sources of electrical interference. The biggest problem was the 240 volt power supply. Originally this was derived from a three-phase electric generator. However this supply proved to be too unstable to operate the microprocessor and so the entire spectrometer was powered from the main supply which was filtered to remove most of the interference. (The filter network used is shown in Figure 4.3.2).

The transformer of the spectrometer's own power supply which was housed in the same box as the spectrometer also interfered with the logic circuitry. The power supply

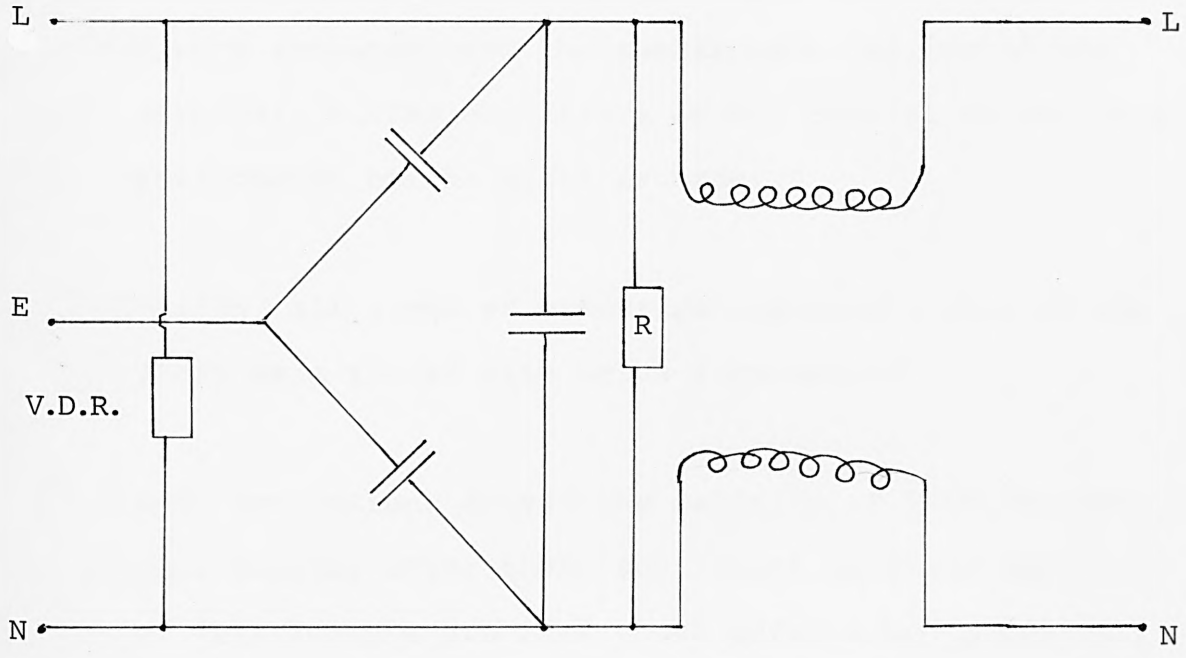

240V Mains (unfiltered)

Filtered Mains
(10A max.)

Figure 4.3.2. Mains filter network. The V.D.R. (Voltage Dependent Resistor) is to supress voltage transients. The case is earthed.

was rehoused in a separate box which removed this interference source.

A third source of noise was generated by the chart recorder which injected noise onto the filtered mains supply and into the spectrometer via the X and Y axis connectors. In order to remove this interference, the chart recorder was connected to the unfiltered mains supply and the X and Y inputs were isolated from the spectrometer by installing two unity-gain buffer amplifiers on the coaxial output from the spectrometer to the chart recorder.

In addition, all items of electrical equipment used in the laboratory were fitted with mains suppressors.

The above precautions solved the majority of interference problems, however after their subsequent solution several smaller interference problems,whose effects had previously been masked, now became significant.

The first of these problems was caused by the clock of the microprocessor interfering with the lock-in amplifier, causing its demodulator to overload. The problems was solved by having two separately filtered mains supplies. One was used to power the microprocessor and disc drive, the other was used to power the lock-in amplifier and oscilloscopes. (Figure 4.3.3).

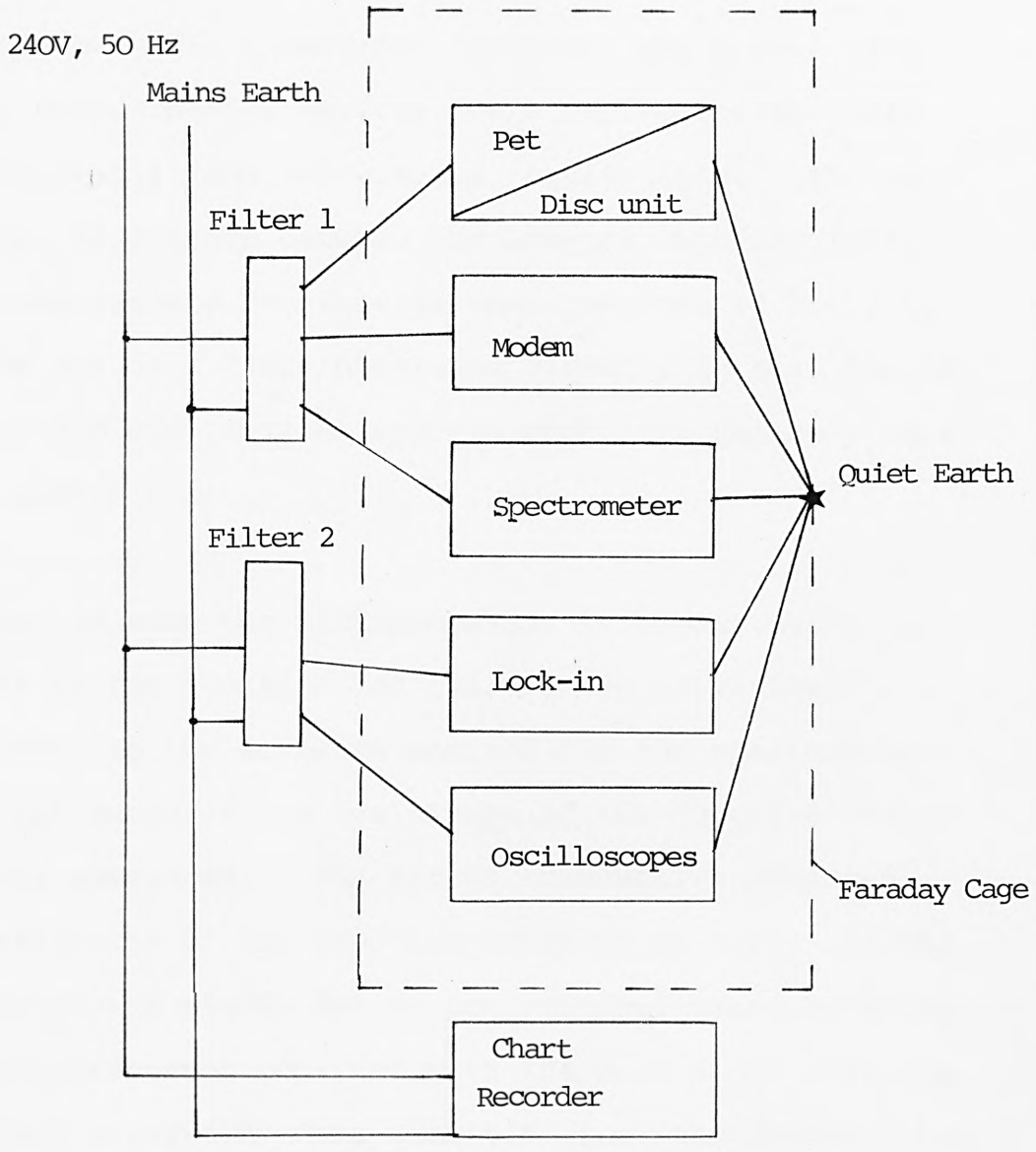

Figure 4.3.3. Mains earthing and power distribution system to avoid interference. Cases of filters and chart recorder are connected to mains earth.

Finally in a successful attempt to reduce the inherent noise susceptibility within the spectrometer itself, most of the logic integrated circuits, which were originally standard 7400 devices, were replaced with their pin compatible 74LS and C.M.O.S. equivalents. The only relevant difference between the Low-pow Shottley (LS), the Complementary Metal-Oxide Semiconductor (C.M.O.S.), and the standard 7400 integrated circuits is that the LS and the C.M.O.S. devices operate much more reliably in a noisy environment.

In order to stop the microprocessor from continuing to operate if the junction had failed, two subroutines were added to the software controlling the spectrometer. The first measured the resistance of the junction before scanning commenced. The second subroutine measured the resistance of the junction after every scan. If the resistance was within 50% of the original measured value the microprocessor contined with the next scan. If the value had changed by more than 50% (i.e. the junction had shorted out or had gone open circuit) the microprocessor transferred the scans already stored in its memory to a floppy disc and reported the junction failure to the operator by printing a message on the microprocessor's display screen.

(The destruction of the d.c. output transistor when a dead short occurred was alleviated by redesigning the

d.c. output stage and incorporating a more powerful output transistor).

4.3.2 SOFTWARE

The spectrometer is controlled by a programme called I.E.T.S. This programme is written in BASIC to provide a high-level interface between the microprocessor and the operator; however the programme codes for controlling the spectrometer hardware (e.g. incrementing the bias voltage at the correct rate, making sure the digitised signal from the lock-in was routed to the correct part of the RAM etc.) were written in machine code and accessed from the main I.E.T.S. programme. A simplfied flowchart of the programme is shown in Figure4.3.4. The programme is capable of either running a series of scans and storing the result or re-plotting a spectrum which has been previously stored on a floppy disc. One feature of the I.E.T.S. programme is the junction failure check. At the beginning of the programme the spectrometer measures the junction resistance at a given bias voltage. After each scan the resistance is measured again and compared with the initial value. If the value has changed by more than 50% it is assumed that the junction has broken or shorted out. The programme halts, stores the data so far gathered and informs the operator of a possible junction failure. The spectrometer also draws a calibration scale along the lower edge of the spectrum.

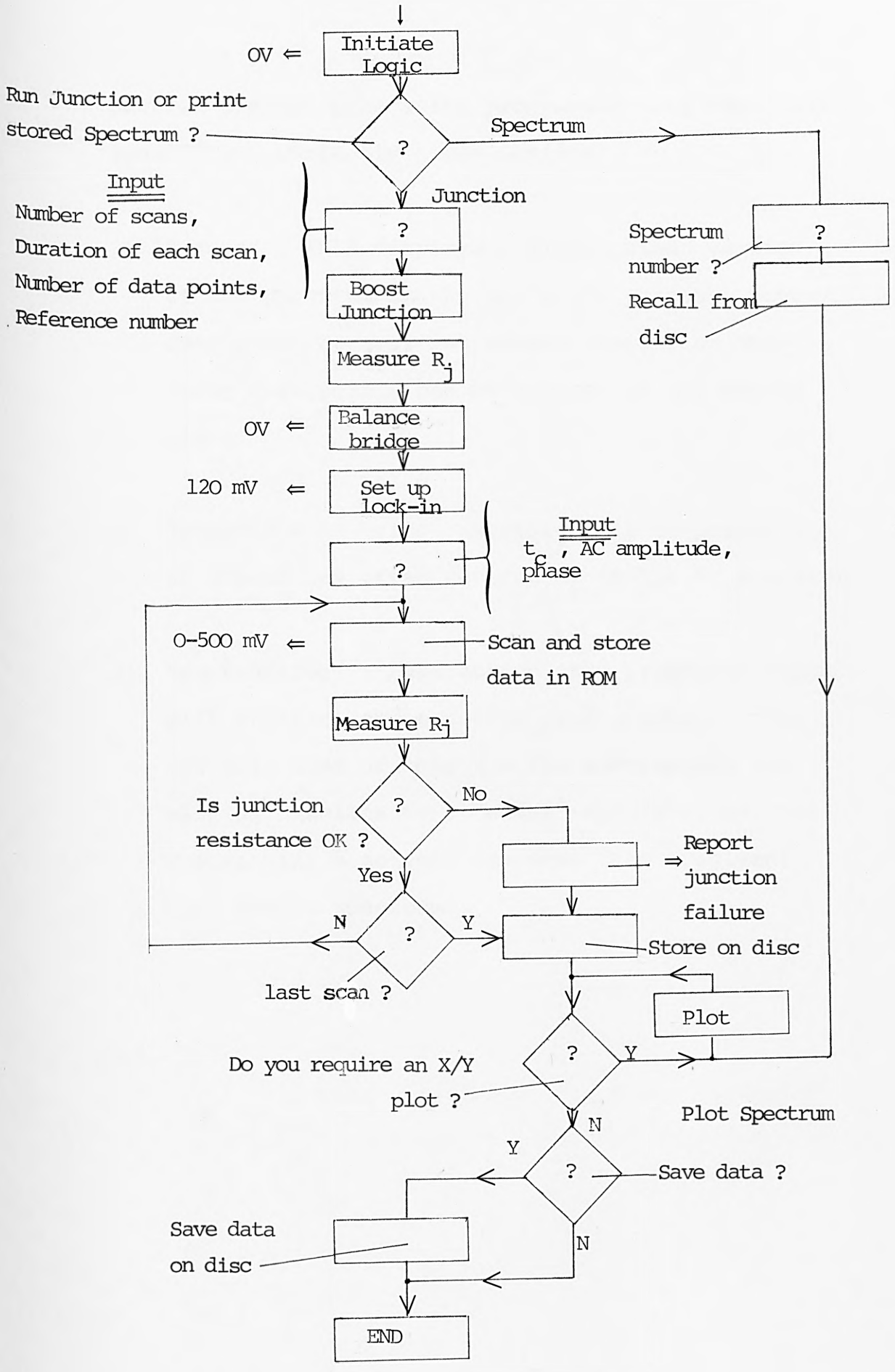

Figure 4.3.4. Simplified flowchart of IETS programme.

Several spectra processing programmes have been written(137). Currently these include:

1) "Graph" : This displays a miniaturised version of the spectrum on the Pet's VDU screen. However due to the present low screen resolution only forty data points can be plotted in one screen width.

2) "Expansion" : Using "expansion" it is possible to expand any given section of an I.E.T. spectrum.

3) "Subtraction" : Subtraction is a programme which will subtract one spectrum from another. The two main uses of this are for subtracting the sloping baseline or a "blank" spectrum, and for subtracting a solvent spectrum from a solvent plus sample spectrum.

4.4 PET/HONEYWELL INTERFACE

When generating such a large quantity of information several shortcomings of a small microprocessor become evident:

1) Storage Space: the present 5.1/4" diameter floppy discs can only store five 4000 point spectra per side;

2) Speed : when executing large programmes such subtraction of one spectrum from another, the execution time was of the order of ten minutes or longer.

If spectra could be stored on the University's Honeywell 6080 mainframe computer, there would be several advantages:

1) Almost unlimited storage space;

2) Significantly quicker data processing time;

3) The availability of the NAG software library (which contains programmes for least squares fit, integration and fast Fourier transforms etc.);

4) The availability of a large number of peripheral devices such as digitizing tablets and high resolution graph plotters.

There are several methods of transferring an I.E.T. spectrum into the Honeywell computer:

1) Manually, i.e. type in the required information. For a 4000 point spectrum this would be too laborious;

2) Transfer the information to punched tape and read the tape into the computer. Again this method would take too long;

3) Interface the Pet directly with the Honeywell.

Of the three options available, interfacing the two computers seemed the most advantageous and convenient solution.

Fortunately, several Pet/Honeywell interface units were already operating in conjunction with the Honeywell computer at the University-College of Wales, Aberystwyth. After consultation with [redacted], the Senior Programming Advisor and designer of the interface unit at Aberystwyth, it was thought feasible that the interface unit would operate with The City University's Honeywell after some minor software modifications. The only problem was the connection of the interface with the computer. The Chemistry Department at The City University is separated from the main computer unit by a main road and it is physically (and bureaucratically)impossible

to run any electrical connections between the two buildings. The only alternative was to use the computer's dial-in telephone lines and connect the spectrometer to the Honeywell via the telephone network. This involved the use of a modem and a circuit to convert the data into a suitable form for transmission.

4.4.1 CURRENT LOOP - RS 232C CONVERTER

There are two accepted methods for transmitting serial data along a twisted pair cable, 20mA current loop and RS 232.

The 20mA current loop was originally used for operating relays in teletype terminals. Essentially, the current loop works thus: a receiver contains a current detector and is connected by two wires to the transmitter which contains a switch which can be either open or closed. When current flows in the loop the detector registers logic '1', when no current is flowing, the detector registers logic '0'. The current source may reside in either the receiver or the transmitter. The unit containing the current source is termed "active" and the unit not containing the current source is termed "passive". In order to function correctly, each transmitter and receiver must contain one active and one passive element. (See Figure 4.4.1).

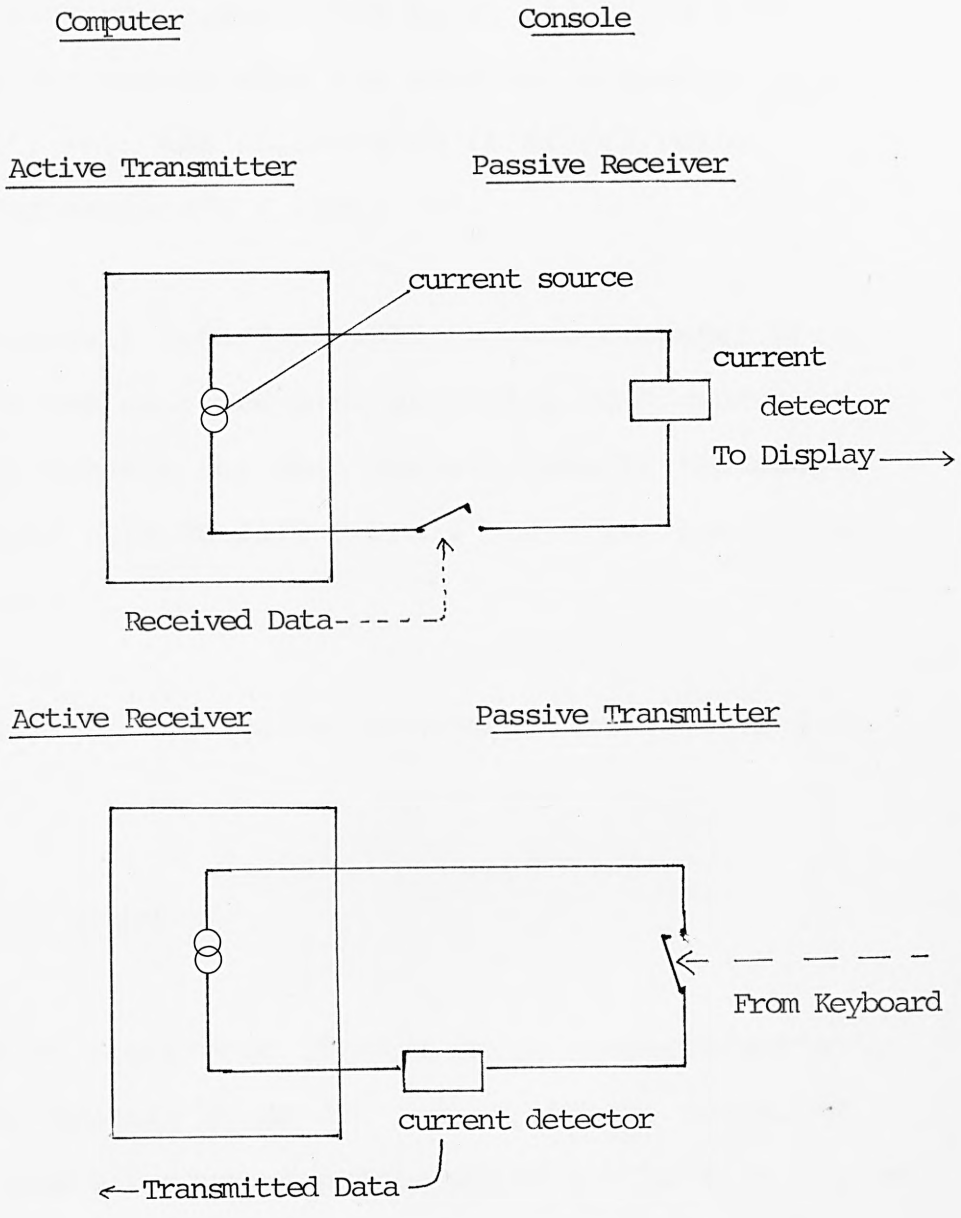

Figure 4.4.1. The 20 mA Current-loop

The RS 232C communication standard uses a ±12 volt system. When the signal wire is at +12 volts with respect to the ground wire the receiver registers a logic '1', when the signal wire is at -12 volts, the receiver registers a logic '0'.

The Pet/Honeywell interface built by the Computer Unit, Aberystwyth was supplied with an active 20mA connector. In order to connect the 20mA current loop to the modem which accepts only RS 232C a small converter had to be constructed.

Figure 4.4.2 is the circuit diagram of the 20mA-RS 232C converter.

4.4.2 THE MODEM

A modem is an electronic circuit which converts serially coded data, usually in RS 232 format, into a series of different audio frequency pulses which can be transmitted via a normal telephone line. The original modem used to connect the Pet to the telephone network utilised an audio transmitter and receiver over which the telephone headset was placed. The transmission of data from the modem to the telephone relied upon good acoustic coupling between the transceiver and the headset. Unfortunately in the noisy environment of a research laboratory, the acoustic link, although soundproofed, was subjected to some audio

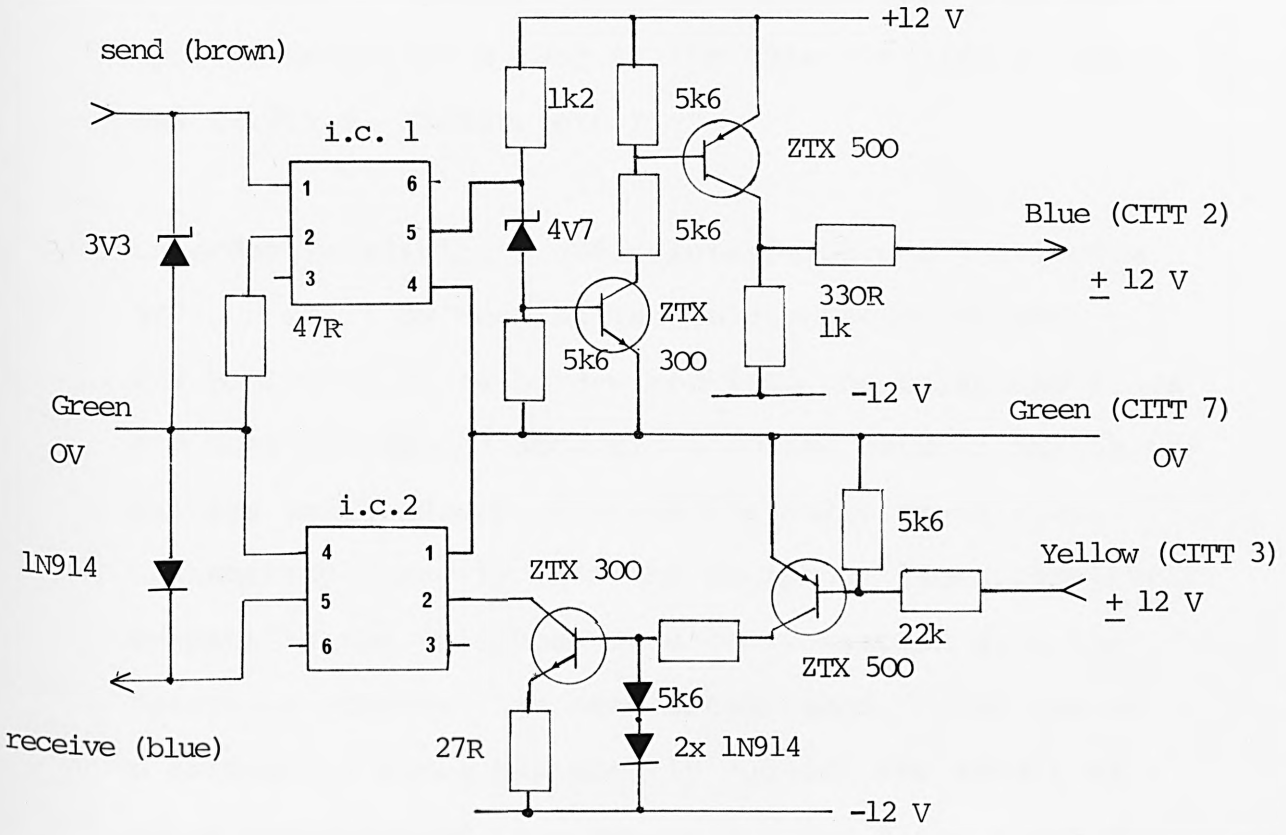

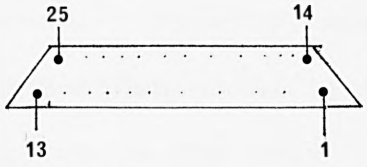

Pin numbering of CITT connector

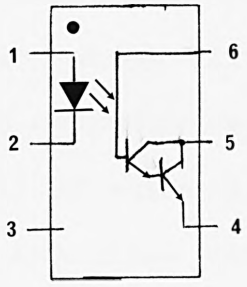

i.c. 1, i.c.2 Darlington Opto-isolators
(RS 307 963)

Figure 4.4.2. 20 mA / RS 232C converter.

interference causing erroneous data to be transmitted (or received) to the computer.

The result of spurious data in the spectra, made the spectra unuseable by any of the data handling programmes (I.E.T.S. EXPAND, etc.).

In order to eliminate audio interference a "Minimodem 3C" built by Modular Technology and purchased. The Minimodem 3C is hard-wired into the telephone lines and does not use an acoustic coupling between the transceivers and headset; instead the audio signals are transmitted directly onto the telephone lines, completely by-passing the telephone once communication with the mainframe computer has been established. The use of a hard-wired modem has greatly reduced the amount of noise incorporated in a spectrum The final block diagram of the Pet/Honeywell interface is shown in Figure 4.4.3. Two features should be noted. Firstly, the colour-coded wiring of the telephone-modem connection is critical. The above configuration is the only permutation which allows operation of the telephones, type 3750 computerised facilities (automatic storage and recall of numbers, re-routing of incoming calls etc.). Any other combination whilst allowing full operation of the modem and telephone, disables these special features. Secondly, the organisation of the Honeywell's "dial-in" telephone lines is similar to

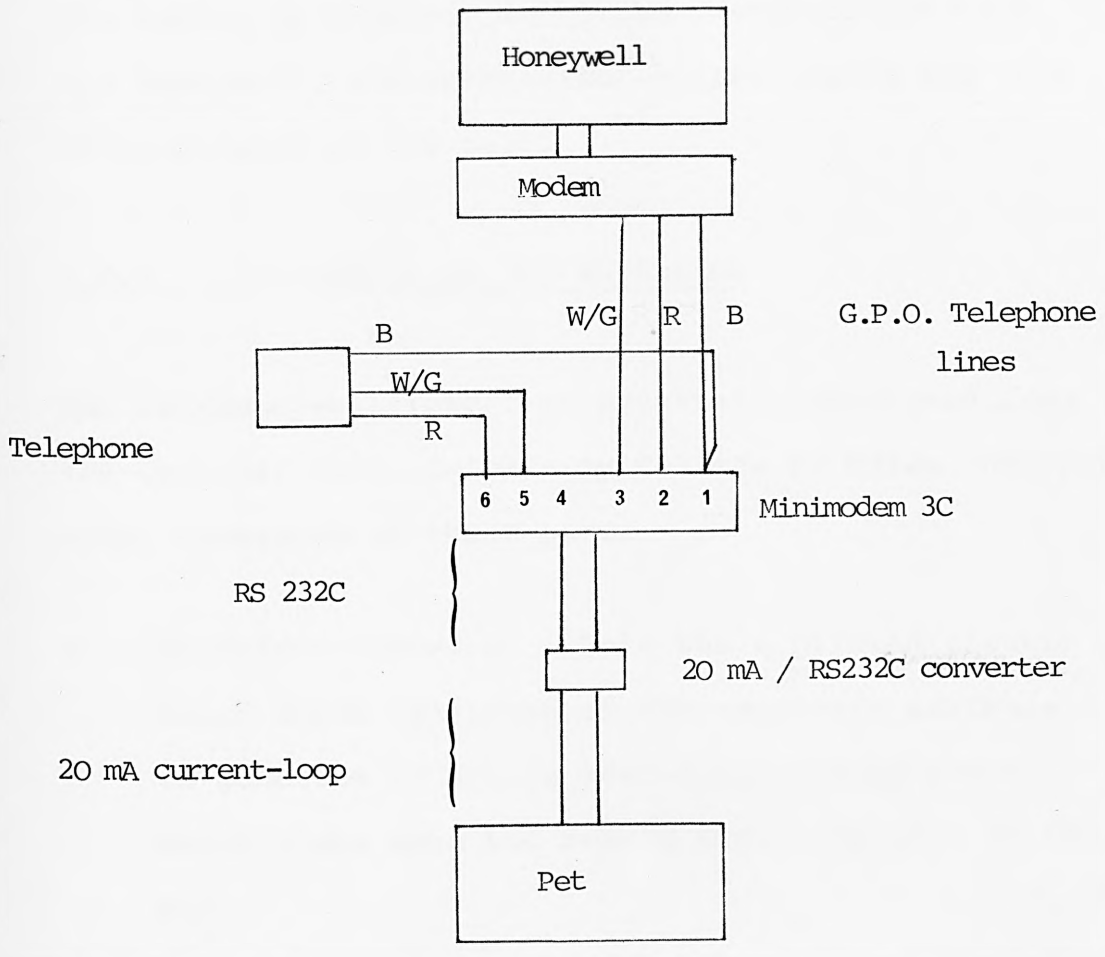

Figure 4.4.3. Final block diagram of the Pet / Honeywell interface.

Colour Code - B Blue

R Red

W/G Green/White (2 wires)

the modem link at the Pet end, except that the Honeywell's modem automatically answers the telephone when the number is dialled, initiates communication with the Honeywell, and automatically disconnects the line on completion of the call.

4.4.3 OPERATION OF THE INTERFACE

The Pet/Honeywell interface eventually purchased from the Computer Unit, University College of Wales, Aberystwyth, consisted of three parts:

1) Interface hardware. This was a printed circuit board which consisted of the necessary hardware to generate an active 20mA current-loop output, which plugs into the memory expansion port of the Pet.

2) Interface control software. The programme necessary to make the Pet behave as a computer terminal was contained in a PROM. (programmable-read -only-memory) which fitted into one of the spare ROM (read-only-memory) sockets in the Pet.

3) Honeywell software. The Pet will act as a computer terminal without the Honeywell software, however the addition of this software enables

the Honeywell to transfer data files directly to and from the Pet's disc unit. The software was supplied as a computer listing which had to be manually typed into the Honeywell.

The installation of the interface was straightforward, and once the software was put on the Honeywell, the system worked perfectly. To operate the interface, the Honeywell's dial-in line is called and the mini-modem connected. The operator then types the command

SYS 41047

into the Pet. (This causes the Pet to start executing the programme beginning at address 41047, which is the location of the PROM containing the Pet software). The screen then clears, and the normal Honeywell time-sharing-system log-on sequence appears. The Pet can then be used as a normal computer terminal. The main memory of the Pet remains undisturbed by the operation of the interface, and thus a programme already stored in the Pet can be run once the Pet is returned to normal operation.

The following features are available: (136)

Character Set

i) The characters ` { and } are not available

on the Pet keyboard but can be generated by typing shift /@, shift /[and shift /]. They are displayed on the Pet screen as a reversed @, a reversed [and a reversed].

ii) Control. There is no control key on the Pet instead, the RVS key is used. This is pressed and released before the desired control character is pressed, e.g. to type control/C (≡ ETX or end of transmission in ASCII code), RVS is typed and released, and then the key c is typed.

iii) Break. There is no break key on the Pet, instead the RUN/STOP key is used.

iv) The backspace character. The backspace character is used on the Honeywell to delete one or more characters on the current line. On the interface both backspace and DEL are used for this purpose and have the effect of transmitting a backspace to the Honeywell and echoing a backspace on the screen so that the line is corrected visually as well as on the Honeywell. [This was one of the software modifications for The City University's Honeywell 6080: the Honeywell at Aberystwyth uses the @ character

for the same purpose].

v) The ASCII characters GS (group separator) control/ and RS(record separator) control/ are used for special purposes on the Pet and must not be used.

Linelength

The screen on the Pet is only 40 characters wide and the interface will simply continue displaying on the next line (wrap around) if this linelength is exceeded. The maximum linelength under TSS (the Honeywell time-sharing-system) is 160 characters.

Communicating With the Interface Control Software

It is possible to communicate with the interface control software by transmitting control/P, which must be executed by typing:

RVS then releasing the key and typing P.

The Pet then responds with the command prompt:

type pet command or? for help.

Then one of the commands as follows should be typed.

Help System

Typing? lists a menu of facilities available with the relevant commands highlighted in reverse field.

Baud Rate Selection

The interface can be set to any of the line speeds of the Honeywell by typing r, the operator is then shown a list of available baud rates. Unfortunately the maximum baud rate that can be used over the Honeywell's dial-in lines is 300 baud. (The maximum for the interface is 9600), consequently it takes about fifteen minutes to transfer a 4000 point spectrum. The only way to circumvent this problem is to have a direct wire link between the Honeywell and interface. (The default baud rate is 300).

Printing Control Characters

Typing a (for allow) makes the interface print all the control characters received as reverse field ASCII characters. Normal printing can be reinstated by typing s (for suppress).

Keyboard Lock

Typing l (for lock) in reponse to the command prompt

locks the keyboard in uppercase characters. Normal printing is resumed if the character u (for unlock) is typed.

Repeat

If a single key is kept depressed the character will repeat. Typing d in response to a command prompt, disables the repeat software; typing e enables it to proceed.

Changing Mode

To return to terminal mode the character t is typed.
To return to basic mode the character b is typed.
When returning to basic mode the terminal is not disconnected and can be reinstated by typing the SYS 41047 command.

File Transmission

The most important feature of the interface is the transmission of files to and from the Pet's dual disc drive. This programme is only suitable for ASCII files, (which is the format the I.E.T. spectra are stored in), the programmes written for the Pet and stored on the disc drive will not transfer as runnable programmes as they are stored in a non-standard format in the disc drive.

Pet to Honeywell File Transmission

Having entered the Pet terminal programme by typing the SYS 41047 instruction and logging on to the Honeywell in the normal manner, files can be transmitted to the Honeywell by typing the command:

frompet

the Honeywell then responds with

filename?

The filename of the file to be created on the Honeywell is then typed in. Prefixing the filename with a solidus(/) will make the file permanent. The two instructions can be combined thus:

frompet/filename

The Honeywell then responds with

pet file?

in reply, the name of the file to be transmitted is typed. The filename may be optionally prefixed by a drivenumber and separated by a colon : from the file name. This drive number (which refers to the

drive which contains the file) and the filename must be enclosed in quotes. The filename can have a maximum of 14 characters.

If the type of file is not specified (e.g. prg representing a programme file, or seq representing a sequential file), the file is assumed to be sequential. The Pet then initialises the discs in the disc drive and transmits the file to the Honeywell listing it on the screen as it does so. At the end of the file the Pet displays the message;

end of file

and after a short delay, the Honeywell displays the message:

Transfer complete - wait
Number of characters transferred = n

where n is the number of characters. Thus to transfer the I.E.T. spectrum 335679 which is penetration-doped benzene, the following commands would be used:

```
frompet
file? / benzene
petfile? "0:␣ 335679, seq"
          ¦
        ¦
335679  where:0 - drive zero (optional);
```

```
      28                    └──┘  = space. All I.E.T. spectra
      75                    are stored with a space before
    0.22564                 the index number
      ¦
      ¦                     seq = sequential file (optional)
```

the contents of the file
are listed on the screen
beginning with the file
number.

```
      ¦
      ¦
      ¦
```

end of file

Transfer complete - wait

Number of characters transferred = 3715

Honeywell to Pet File Transmission

To send a file from the Honeywell to the Pet the command

topet

is typed. The Honeywell prompts with the question:

file?

the Honeywell file which is to be transferred is typed in. The Honeywell then asks:

pet file?

The name of the Pet file is then typed in. This name MUST be enclosed in quotes and be preceded by a drive number. The filename itself can have a maximum of 12 characters. To transfer the benzene spectrum from the Honeywell to the Pet the procedure is:

```
topet

file?  benzene

petfile?  "1 : benzene"
    ¦
    ¦
    ¦
file is listed as it is transferred
    ¦
    ¦
    ¦
end of file.
```

The list of commands for the Pet/Honeywell interface are summarised in Table 4.2.

Table 4.2 Summary of

Pet/Honeywell commands

SYS 41047	initiates control of interface
BREAK	use RUN/STOP key
CONTROL	use RVS key
`	type shift/@
{	type shift/[
{	type shift/]

To communicate with the interface control software

Type RVS then P (=control/P) then the relevant Pet command or ?. After typing ? the following menu of facilities becomes available:

r	selects baud rate
a	(allow) prints control characters in reverse field ASCII
S	(suppress) suppresses control characters
l	(lock) locks keyboard in uppercase characters
u	(unlock)
d	disables character repeat
e	enables character repeat
t	returns to terminal mode
b	returns to BASIC mode (Honeywell is not disconnected)

4.5 EXAMPLES OF MULTI-SCANNED JUNCTIONS

Figure 4.5.1 shows the I.E.T. spectra of benzaldehyde at 77 K. All three traces were recorded under the following conditions:

Scantime : 2 minutes each scan
Number of data points : 2000;
Time constant 300 milliseconds
a.c. amplitude : 6 millivolts (peak-to-peak)
Junction resistance; 615Ω

the number of scans per spectrum are:

Spectrum 1 : 1 scan
Spectrum 2 : 4 scans
Spectrum 3 : 8 scans

Figure 4.5.2 shows two I.E.T. spectra of para-xylene at 4.2 K. Both spectra were recorded under the following conditions:

Scan time: 3 minutes each scan
Number of data points: 4000
Time constant : 30 milliseconds
a.c. amplitude : 6 mV (p.p.)
Junction resistances: 1.3 KΩ

the number of scans per spectrum are:

Spectrum 1 : 1 scan

Spectrum 2 : 10 scans

The reduction of noise in both figures is self-evident.

It should be stressed that the junctions used for these examples were exceptionally noisy: and in no way are they representative of I.E.T. spectra in general.

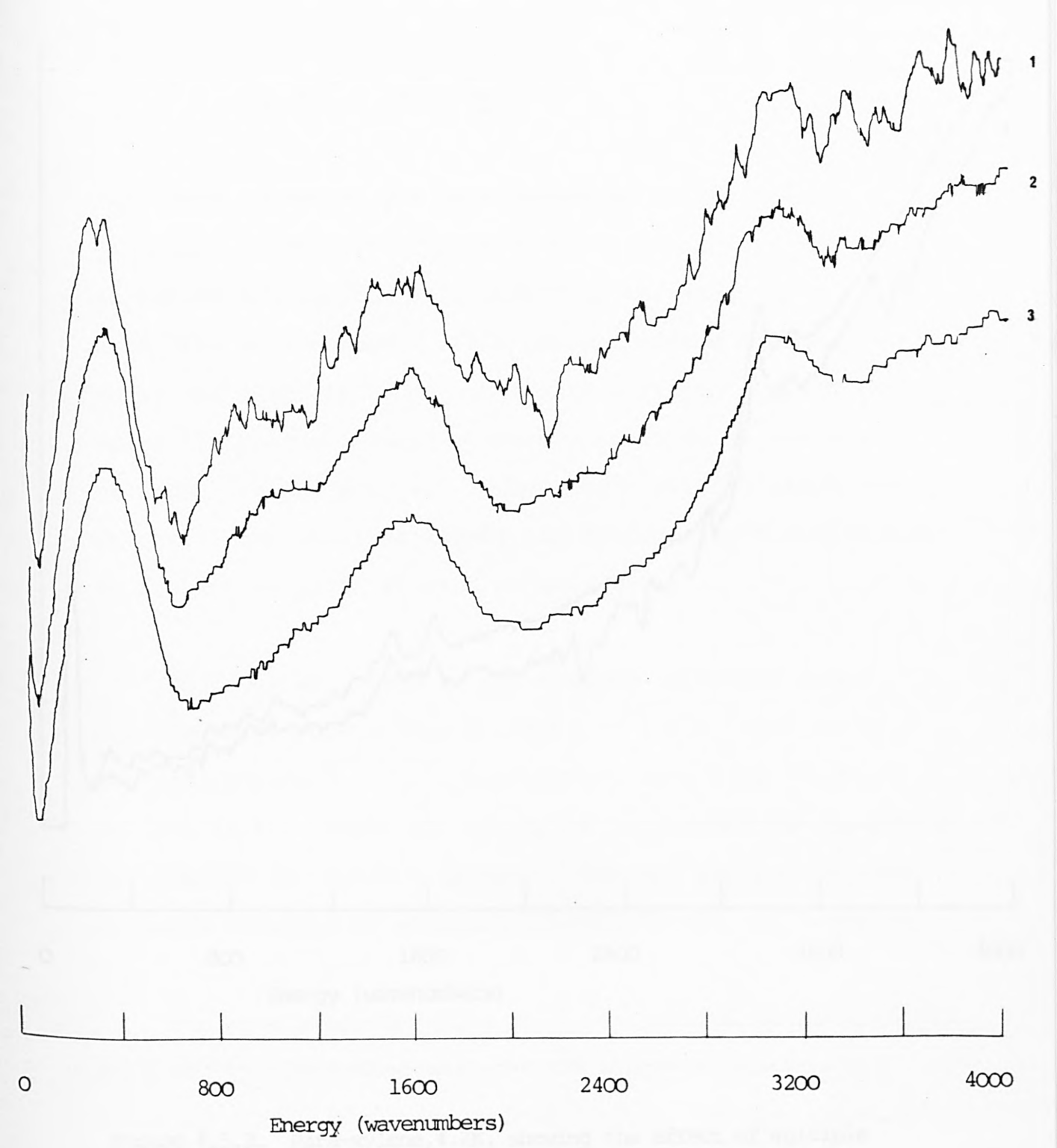

Figure4.5.1. Benzaldehyde, 77K, showing the effect of multiple scans. 1. 1 scan.
2. 4 scans.
3. 8 scans.

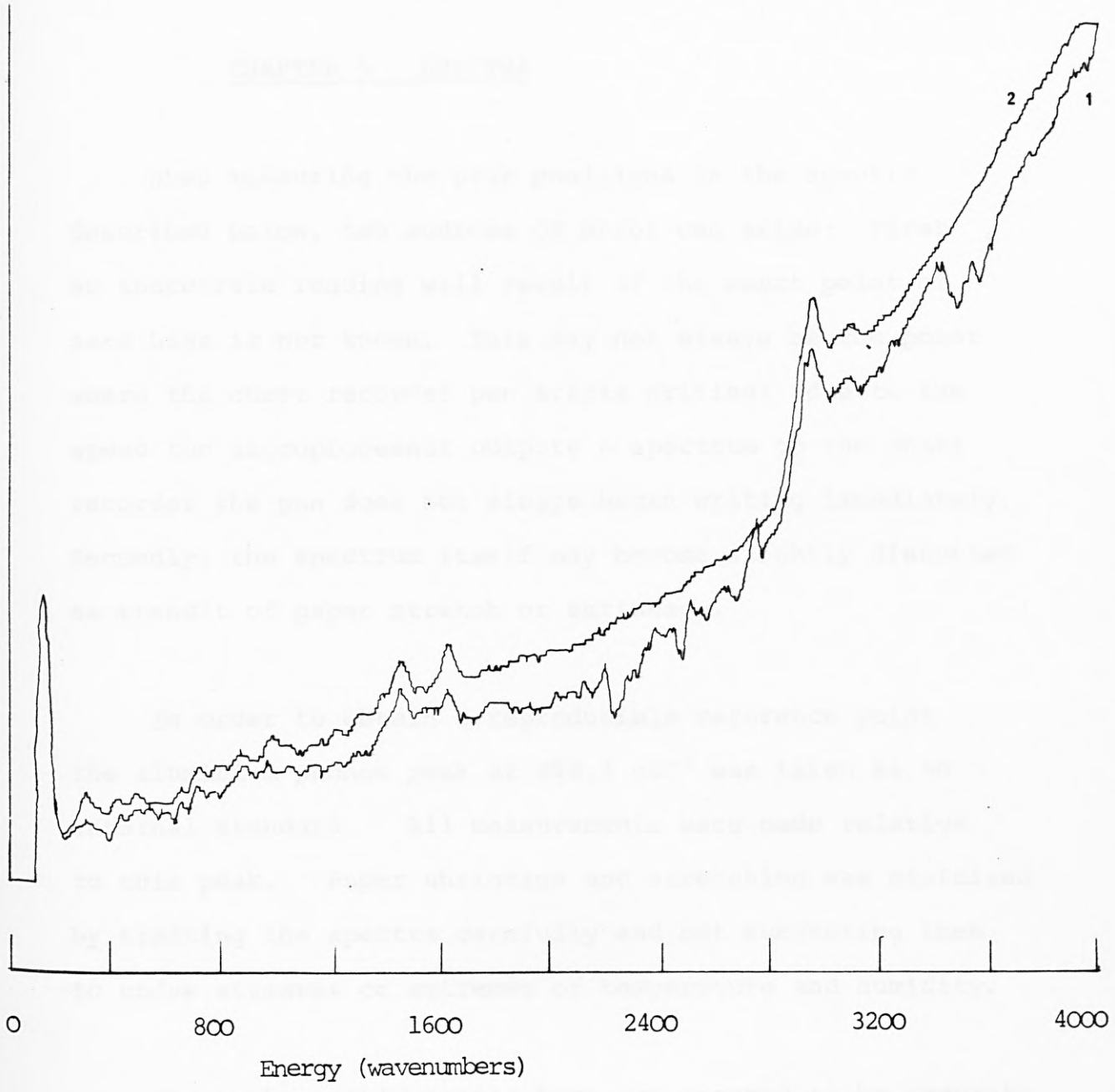

Figure 4.5.2. Para-xylene,4.2K, showing the effect of multiple scans. 1. 1 scan
2. 10 scans.

CHAPTER 5 SPECTRA

When measuring the peak positions in the spectra described below, two sources of error can arise: First, an inaccurate reading will result if the exact point of zero bias is not known. This may not always be the point where the chart recorder pen starts writing: due to the speed the microprocessor outputs a spectrum to the chart recorder the pen does not always begin writing immediately. Secondly, the spectrum itself may become slightly distorted as a result of paper stretch or shrinkage.

In order to obtain a reproducible reference point the aluminium phonon peak at 298.4 cm^{-1} was taken as an internal standard. All measurements were made relative to this peak. Paper shrinkage and stretching was minimised by treating the spectra carefully and not subjecting them to undue stresses or extremes of temperature and humidity.

The peak positions given here are assumed to be accurate to 16 cm^{-1}. This is equivalent to a linear measurement error of ±1mm. (However, in the future, the peak positions will be taken direct from the digitised form of the spectra which are stored on floppy disc. Numerically differentiating the data will result in peak mamima occurring as zero crossing points on a straight line, (see Figure 5.1.1). Unfortunately this peak maximum programme was not available at the time of writing.

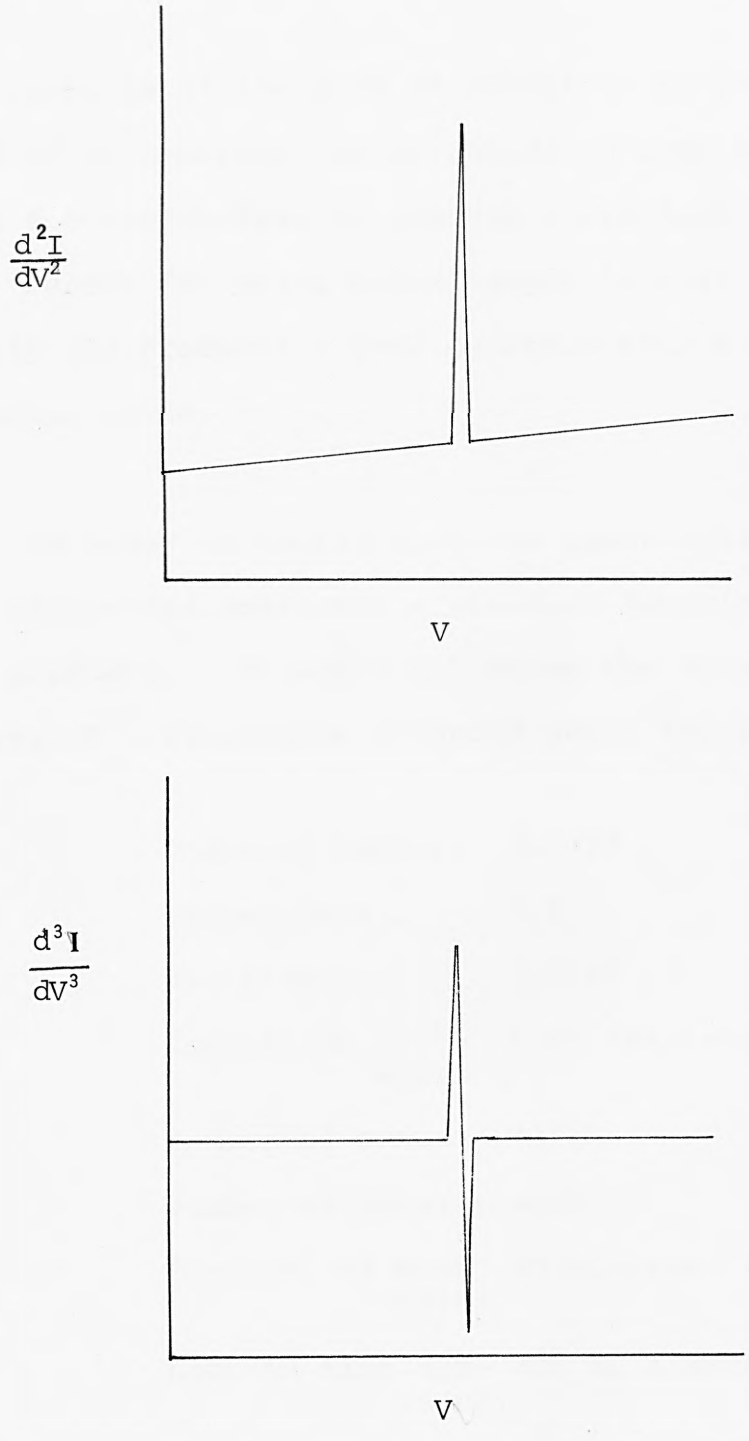

Figure 5.1.1 Second and third derivative plots of an idealised tunnel spectrum.

5.1 BENZALDEHYDE

Inspite of its ease of oxidation to produce benzoic acid as an impurity, benzaldehyde is used by most tunnelling spectroscopists to produce a standard spectrum. The main reason for using benzaldehyde is that it dopes very easily and produced a good spectrum with a high signal-to-noise ratio.

In order to verify that the spectrometer was working and calibrated correctly a standard benzaldehyde spectrum was produced. Figure 5.1.2 shows the spin doped spectrum of analaR benzaldehyde produced under the following conditions:

Spectrum number:	303627
Temperature:	4.2 K
Resistance:	1.8 kΩ
Modulation voltage:	6 mV (peak-to-peak)
Number of scans:	4
Number of samples:	4000
Duration of each scan:	10 minutes
Lock-in time constant:	300 milliseconds

The positions of the principal peaks and their probable assignments are given in Table 5.1. The assignments have been correlated with the work of Kuipner(69) who has published infared and Raman spectra of benzaldehyde, benzaldehyde

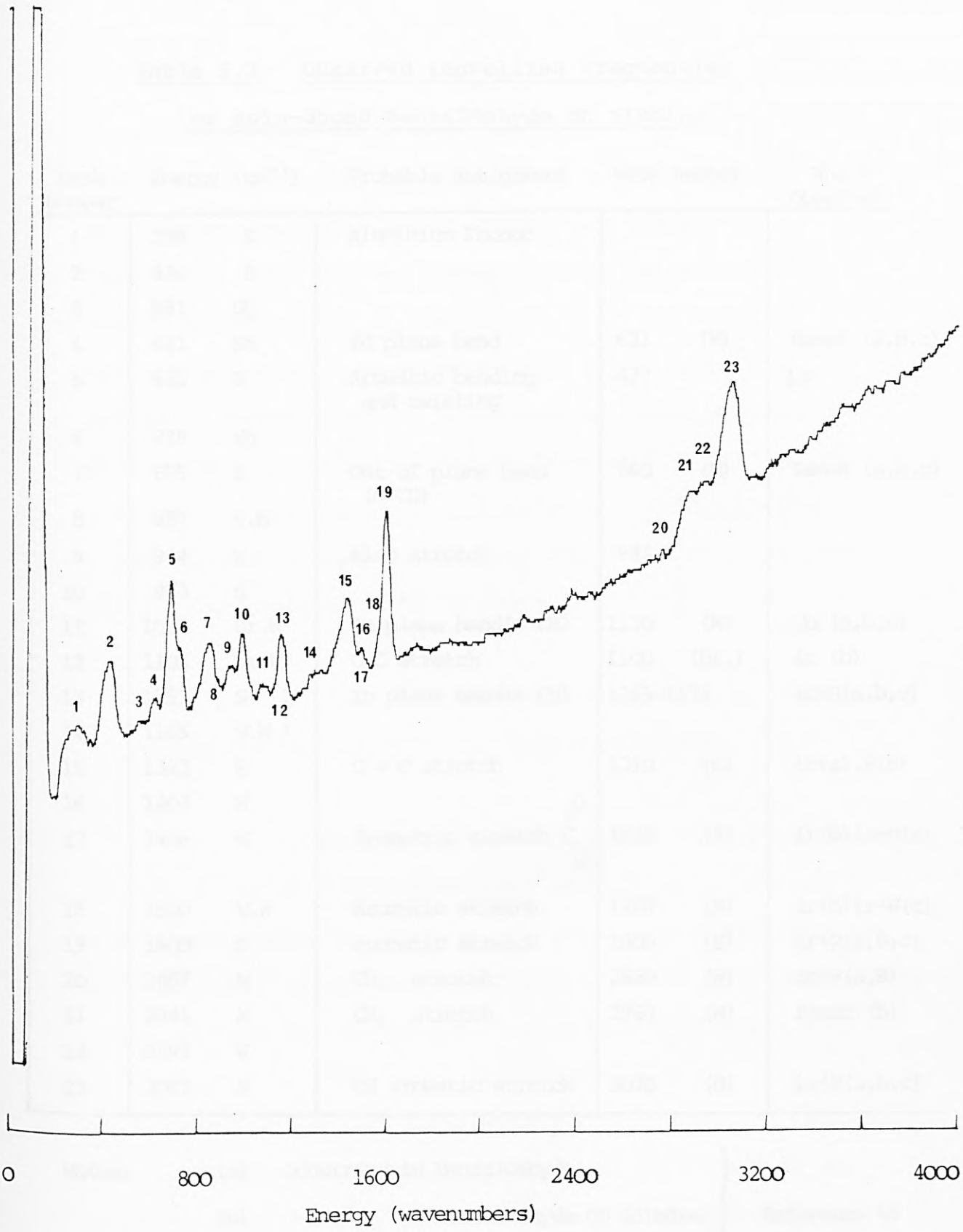

Figure 5.1.2. Benzaldehyde. Spectrum303627.
Numbering indicates approximate peak position only.

Table 5.1 Observed tunnelling frequencies

of spin-doped Benzaldehyde on alumina

Peak Number	Energy (cm^{-1})		Probable assignment	Wave number		Where observed
1	298	S	Aluminium Phonon			
2	436	S				
3	581	Sh				
4	621	Sh	In plane bend	621	(M)	Raman (a,b,c)
5	686	S	Aromatic bending and twisting	677		i.r
6	726	Sh				
7	855	S	Out of plane bend (= CH)	860	(M)	Raman (a,b,c)
8	887	V.W				
9	944	W	Al-O stretch	944		
10	973	S				
11	1065	Br.W	In plane bend(= CH)	1170	(W)	ir (a,b,c)
12	1105	Br.W)	C-O stretch	1100	(Br.)	ir (b)
13	1153	S)	In plane bend(= CH)	1165-1174		ir+R(a,b,c)
14	1165	V.W)				
15	1323	S	C = O stretch	1310	(S)	ir(a),R(b)
16	1403	W				
17	1436	M	Symmetric stretch C^{O}_{O}	1435	(S)	ir(b)ir+R(c)
18	1500	V.W	Aromatic stretch	1495	(M)	ir(b)ir+R(c)
19	1600	S	Aromatic stretch	1600	(S)	ir+R(a,b,c)
20	2887	M	CH_2 stretch	2850	(W)	ir+R(a,B)
21	2941	M	CH_2 stretch	2960	(W)	Raman (b)
22	2992	W				
23	3057	S	CH aromatic stretch	3070	(S)	ir+R(a,b,c)

Notes: (a) occurring in Benzaldehyde

(b) " " Benzaldehyde on alumina } Reference 69

(c) " " Aluminium benzoate

Intensities: S : strong; M : medium; W : weak;

VW : very weak; Br : broad; Sh : shoulder.

on alumina and of aluminium benzoate. In general the inelastic tunnelling peak positions are in agreement with Kuipner's work, however there are several differences: In previous tunnel spectra of benzaldehyde on alumina(55), the asymmetric C-O stretch (1560 cm^{-1}) and the symmetric C-O stretch (1435 cm^{-1}) have been absent. However in the benzaldehyde spectrum presented here, there is a strong peak at 1436 cm^{-1} which has been assigned to the symmetric C-O stretch. Additionally there is a very weak shoulder at 1570 cm^{-1} which is probably due to the asymmetric C-O stretch.

The C=O stretch, present in benzaldehyde at 1700 cm^{-1} is completely absent from the tunnel spectrum.

The C-H stretch associated with aryl aldehydes present in the infrared spectrum at 2815 cm^{-1} is not observed in the tunnel spectrum, however the small broad peak centred at $\sim$2887 cm^{-1}, which is attributed to $\nu(-CH_2)$ in benzyaldehyde (69), may contain a contribution from the aldehyde group.

Finally, the C=O stretch in the infrared spectrum of benzaldehyde and the Raman spectrum of benzaldehyde on alumina at 1310 cm^{-1}, is shifted to 1298.5 cm^{-1} in the tunnel spectrum due a weakened bond.

The above tunnel spectrum is in general agreement with the tunnel spectrum of benzaldehyde on alumina by Field and Shott(55), and consequently supports their

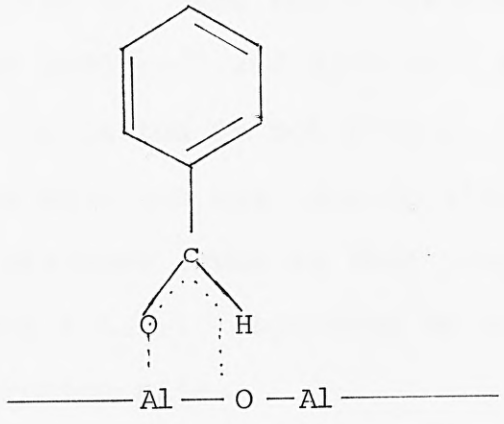

Figure 5.1.3. Proposed orientation of benzaldehyde on alumina. (After Field and Shott (55).)

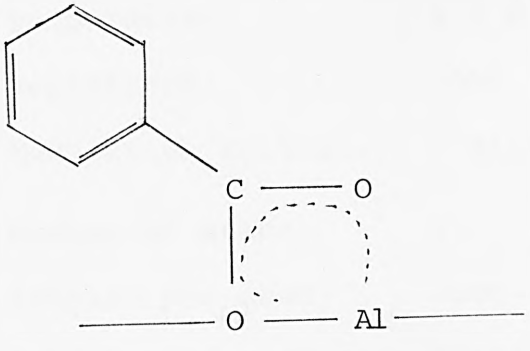

Figure 5.1.4. Proposed orientation of benzaldehyde on alumina. (After Simonsen (122).)

proposed orientation of benzaldehyde on alumina (Figure 5.1.3). However, the presence of the C-O stretch at 1436 cm^{-1} and the broadening of other peaks in the 1080 cm^{-1} and 2900 cm^{-1} ranges, suggest that this orientation is not unique, and that the benzaldehyde molecule may take up alternative preferred orientations (such as that proposed by Simonsen, (122), Figure 5.1.4.), depending on the exact nature of the adsorption site.

5.2 TOLUENE

The spin-doped spectrum of toluene is shown in Figure 5.2.1 and was made under the following conditions:

Spectrum number:	314584
Temperature:	4.2 K
Resistance:	700Ω
Modulation voltage:	7 millivolts (peak-to-peak)
Number of scans:	4
Samples per scan:	4000
Duration of each scan:	10 minutes
Time constant:	100 ms.

(Toluene spin-doped easier than benzaldehyde)

The principal peak positions are listed in Table 5.2 and are correlated with the infrared spectra of liquid toluene at 298 K and the infrared spectrum of toluene at

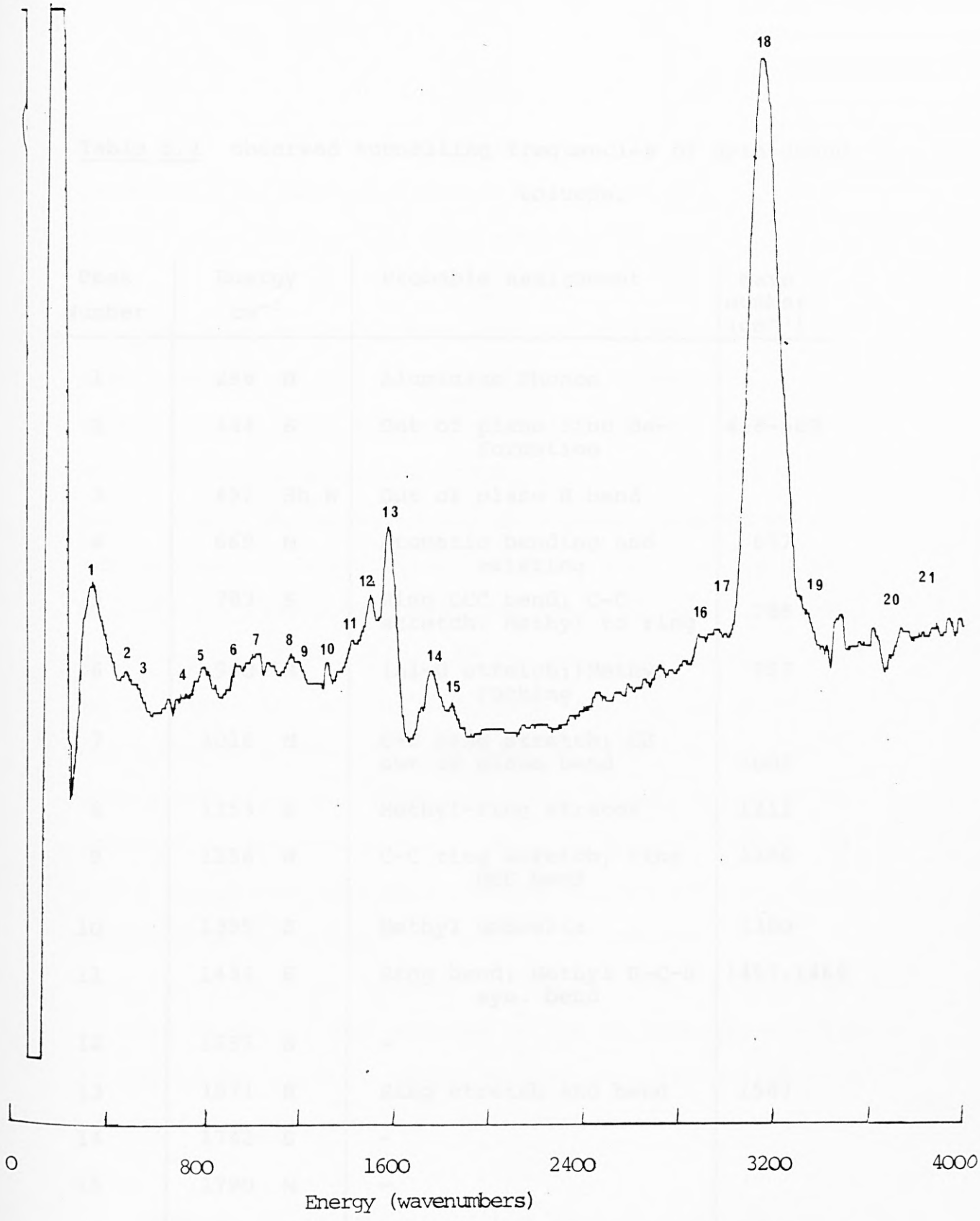

Figure 5.2.1. Toluene. Spectrum 314584.

Table 5.2 observed tunnelling frequencies of spin-doped toluene.

Peak Number	Energy cm^{-1}		Probable Assignment	Wave number (cm^{-1})
1	298	S	Aluminium Phonon	
2	444	S	Out of plane ring deformation	418-560
3	492	Sh.W	Out of plane H bend	
4	669	M	Aromatic bending and twisting	677
5	783	S	Ring CCC bend; C-C stretch: Methyl to ring	788
6	960	M	(Al-O stretch;)Methyl rocking	967
7	1016	M	C-C ring stretch; CH out of plane bend	1005
8	1153	S	Methyl-ring stretch	1211
9	1258	W	C-C ring stretch; ring HCC bend	1286
10	1395	S	Methyl umbrella	1380
11	1484	S	Ring bend; Methyl H-C-H sym. bend	1497,1468
12	1555	S	-	
13	1571	S	Ring stretch and bend	1587
14	1742	S	-	
15	1790	M	-	
16	2936	M	Methyl symmetric stretch	2900
17	3045	Sh	Ring CH stretch	
18	3129	S	Ring CH stretch	
19	3315	W	-	
20	3742	W	-	
21	3888	W	-	

77 K(138). From the available data it is not possible to deduce if toluene adsorbs onto alumina with a unique orientation for the following reasons:

The peak in the tunnel spectrum at 1395 cm^{-1} has been assigned as the methyl symmetric deformation, or umbrella-mode which occurs in the infrared at $\sim$1380 cm^{-1}. The presence of this mode completely rules out the orientation where the methyl group of toluene is adsorbed on the alumina surface (Figure 5.2.2). This idea is also backed-up by the presence of the symmetric methyl stretch occurring at $\sim$2940 cm^{-1}. If the molecule was orientated as in Figure 5.2.2, then this mode ought to be absent. One possible orientation is shown in Figure 5.2.3. In this orientation any vibration modes involving the H-C-H movement of the methyl group would be absent, indeed the H-C-H asymmetric bend which occurs at 1455 cm^{-1} in the infrared is not present in the I.E.T. spectra. The methyl rocking mode (present in the infrared at $\sim$1040 cm^{-1}) is also absent. The shifting of the CH stretch to $\sim$3129 cm^{-1} in the tunnel spectrum would also support the orientation suggested in Figure 5.2.3.

However it is quite possible that this is not the only orientation since the CH stretching region from 2900 cm^{-1} to 3350 cm^{-1} contains several small broad peaks and shoulders whose exact assignment is difficult to interpret, additionally the methyl umbrella at 1395 cm^{-1} also supports the suggestion

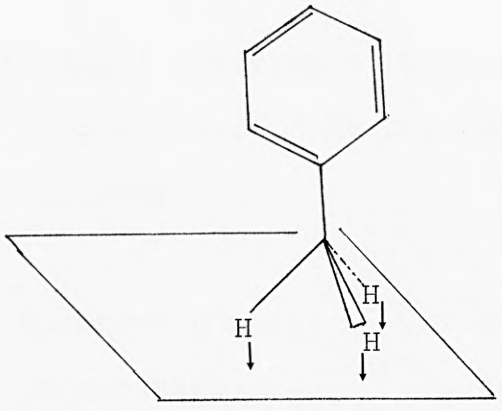

Figure 5.2.2. Possible orientation of toluene on alumina.

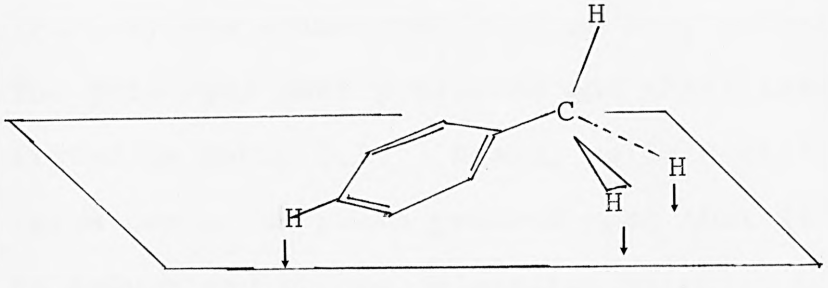

Figure 5.2.3. Proposed orientation of toluene on alumina.

that there is more than one orientation present.

5.3 P-XYLENE

The spin-doped spectrum of para-xylene on alumina is shown in Figure 5.3.1. It was recorded under the following conditions:

Spectrum number:	320493
Temperature:	4.2 K
Resistance:	660Ω
Modulation voltage:	4mV (peak-to-peak)
Number of scans;	8
Samples per scan;	4000
Duration of each scan:	3 minutes
Time constant:	30 milliseconds

(Para-xylene spin-doped just as easy as toluene).
The principal peak positions and their assignments are listed in Table 5.3. Again, as in Section 5.2 the large number of peaks present mean that it is not possible to deduce any unique orientated geometry of the adsorbate on the alumina surface. One possibility is shown in Figure 5.3.2, with one methyl group chemisorbed on the surface. This would account for the present of the methyl umbrella mode at 1395 cm^{-1}, in the presence of the ring modes) and all the symmetric and asymmetric methyl vibrations. However when this structure is considered with reference to

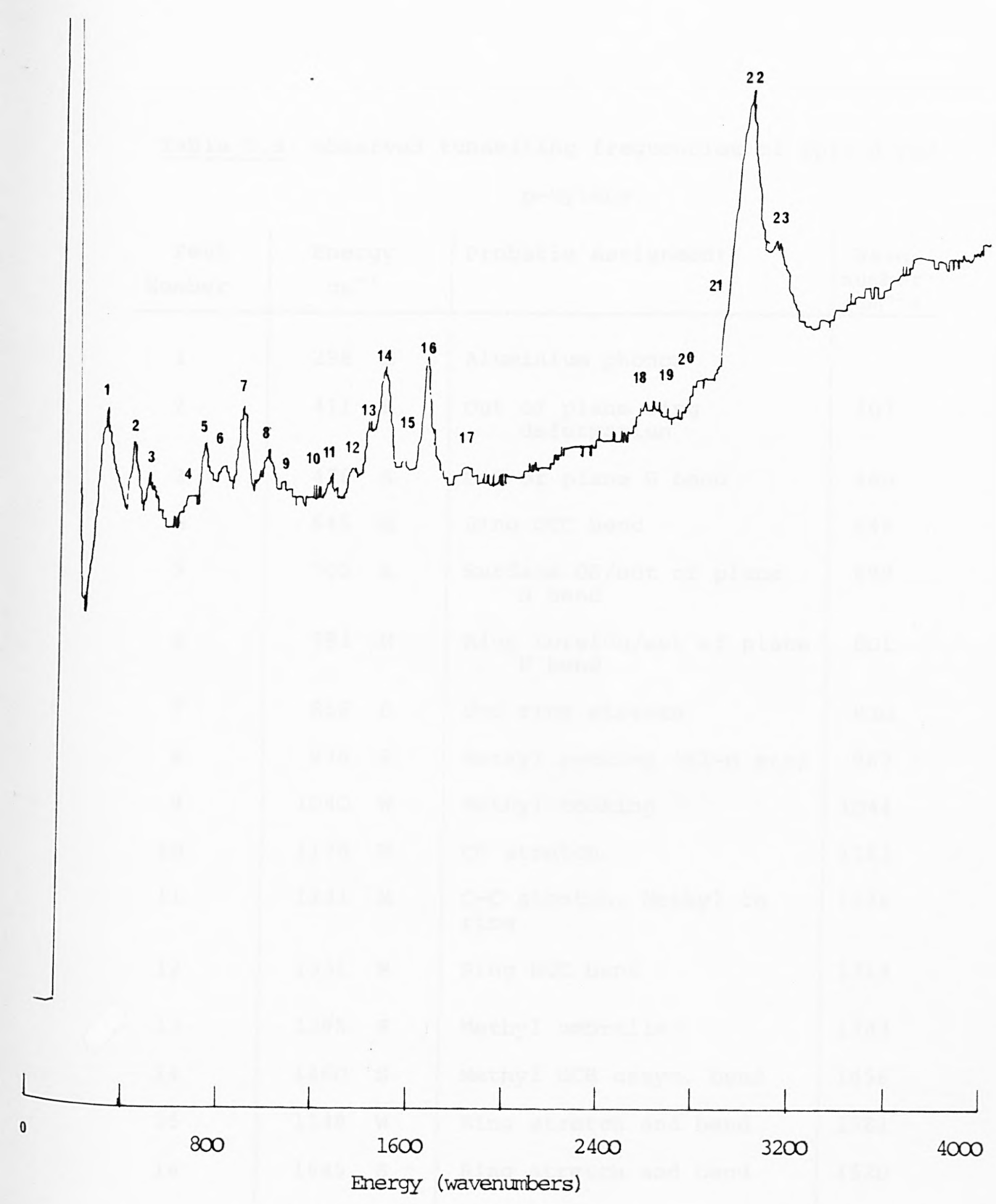

Figure 5.3.1. Para-xylene. Spectrum 320493.

Table 5.3 observed tunnelling frequencies of spin-doped p-xylene

Peak Number	Energy cm^{-1}		Probable Assignment	Wave number (cm^{-1})
1	298	S	Aluminium phonon	
2	411	S	Out of plane ring deformation	407
3	476	S	Out of plane H bend	460
4	645	M	Ring CCC bend	646
5	702	S	Surface OH/out of plane H bend	699
6	791	M	Ring torsion/out of plane H bend	801
7	866	S	C-C ring stretch	830
8	976	S	Methyl rocking (Al-O str)	967
9	1040	W	Methyl rocking	1044
10	1178	W	CC stretch	1183
11	1231	M	C-C stretch: Methyl to ring	1226
12	1331	M	Ring HCC bend	1314
13	1395	S	Methyl umbrella	1383
14	1460	S	Methyl HCH assym. bend	1456
15	1549	W	Ring stretch and bend	1581
16	1645	S	Ring stretch and bend	1620
17	1815	W	-	
18	2573	W	-	
19	2621	W	-	
20	2775	W	-	
21	2928	Sh.W	Methyl CH stretch	∿2900
22	3000	S	Methyl CH stretch	3000
23	3089	W	Aromatic stretch occurs as small peak on shoulder of 3000 cm^{-1} absorption	

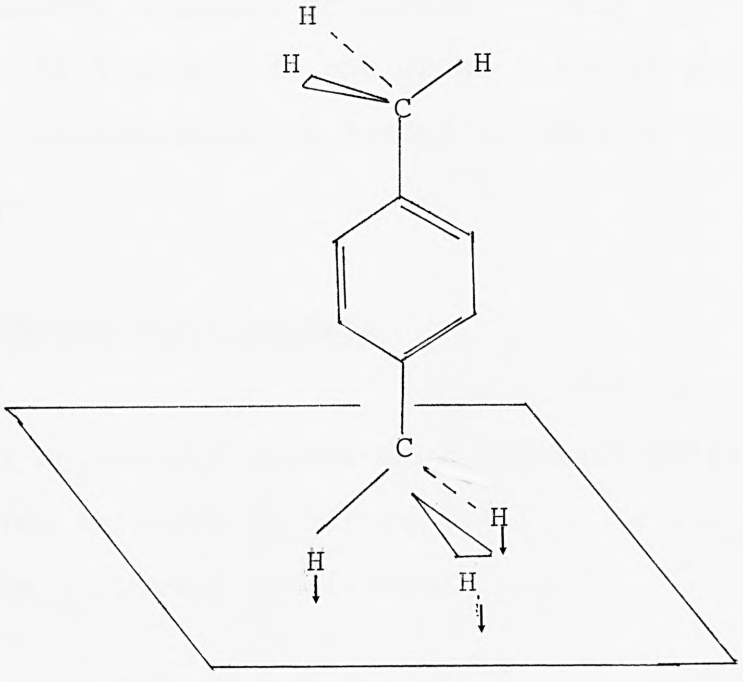

Figure 5.3.2. Proposed orientation of p-xylene on alumina.

the toluene spectrum -which also exhibits a strong absorption at 1395 cm^{-1} - its shortcomings are obvious: if the orientation is as shown in Figure 5.3.2, then it is quite reasonable to suppose that toluene would adopt a similar orientation. This directly contradicts the suggestion that the 1395 cm^{-1} peak is due to the methyl umbrella vibration. This contradiction suggests that more than one orientation is present. Further investigation is needed to resolve this question.

5.4 TERTIARY-BUTYL BENZENE

The spin-doped spectrum of tertiary butyl benzene on alumina is shown in Figure 5.4.1. It was recorded under the following conditions:

Spectrum number:	341534
Temperature:	4.2 K
Resistance:	850Ω
Modulation voltage:	6mV (peak-to-peak)
Number of scans:	4
Samples per scan:	4000
Duration of each scan:	30 minutes
Time constant:	1 second

(The compound was spin-doped neat).

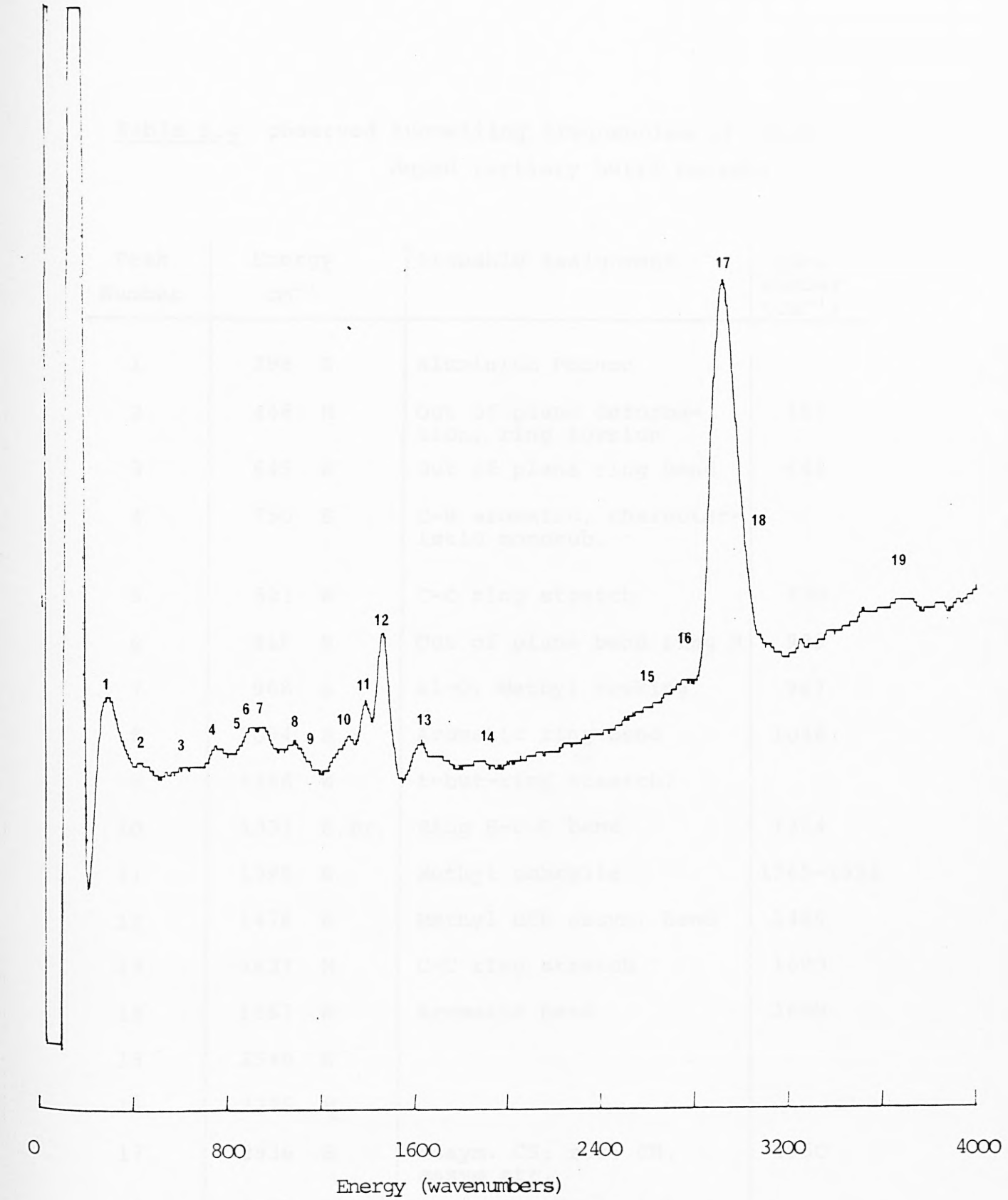

Figure 5.4.1. Tertiary-butyl benzene. Spectrum 341534.

Table 5.4 observed tunnelling frequencies of spin-doped tertiary butyl benzene.

Peak Number	Energy cm^{-1}		Probable Assignment	Wave number (cm^{-1})
1	298	S	Aluminium Phonon	
2	448	M	Out of plane deformation, ring torsion	467
3	645	W	Out of plane ring bend	646
4	750	S	C-H aromatic, characteristic monosub.	
5	823	W	C-C ring stretch	830
6	916	S	Out of plane bend ring H	936
7	968	S	Al-O, Methyl rocking	967
8	1094	S	Aromatic ring bend	1048
9	1158	W	t-but-ring stretch?	
10	1331	S.Br.	Ring H-C C bend	1314
11	1399	S	Methyl umbrella	1365-1391
12	1476	S	Methyl HCH assym. bend	1455
13	1637	M	C-C ring stretch	1620
14	1887	W	Aromatic bend	1850
15	2549	W		
16	2775	M		
17	2936	S	Assym. CH_2 str; CH_3 assym str.	2960
18	3097	W.Sh.	Aromatic CH stretch	
19	3710	V.W.	Surface OH str.	

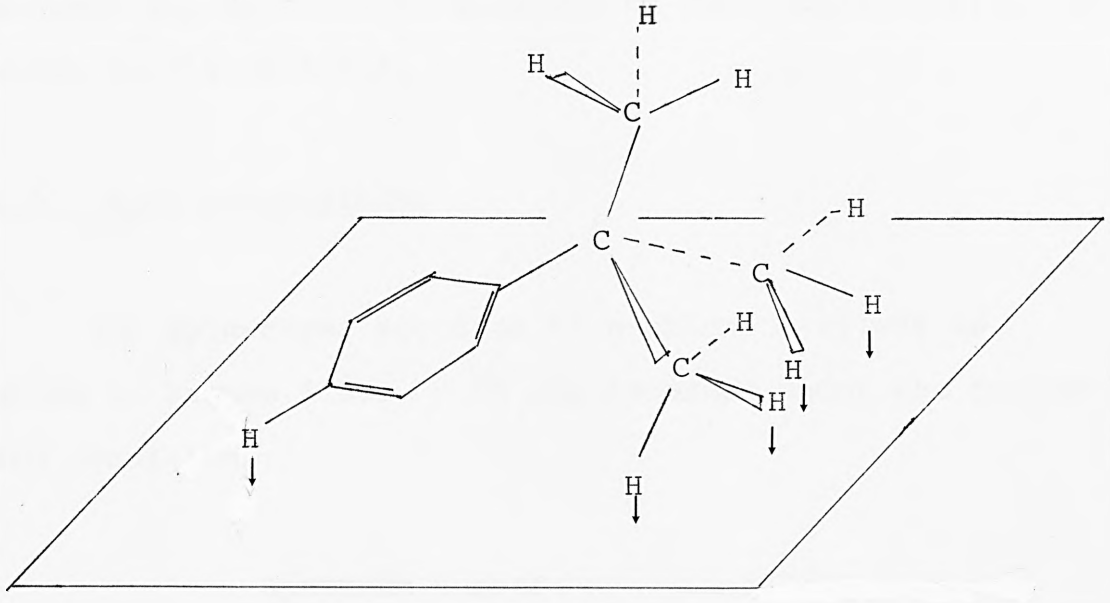

Figure 5.4.2. Proposed orientation of t-(butyl)- benzene on alumina.

The principal peaks and assignments are listed in Table 5.4. One major absence is the skeletal vibrations of the tertiary butyl group occurring at $\sim$1255 cm^{-1} in the infrared spectrum. The presence of the methyl umbrella mode at 1399 cm^{-1} and the asymmetric stretch at 2936 cm^{-1} suggest the molecule is oriented on the alumina surface as shown in Figure 5.4.2.

5.5 α-CHLORO-P-XYLENE

The spin-doped spectrum of α-chloro p-xylene is shown in Figure 5.5.1. It was recorded under the following conditions:

Spectrum number:	330506
Temperature:	4.2 K
Resistance:	951Ω
Modulation voltage:	4mV (peak-to-peak)
Number of scans:	4
Samples per scan:	4000
Duration of each scan:	10 minutes
Time constant:	10 milliseconds

α-chloro-p-xylene was extremely difficult to dope. Spin doping with neat α-chloro-p-yxylene resulted in junctions which always had zero resistance. It was assumed that the compound had attacked the alumina, removing the insulating layer. Weak solutions of α-chloro-p-xylene in benzene

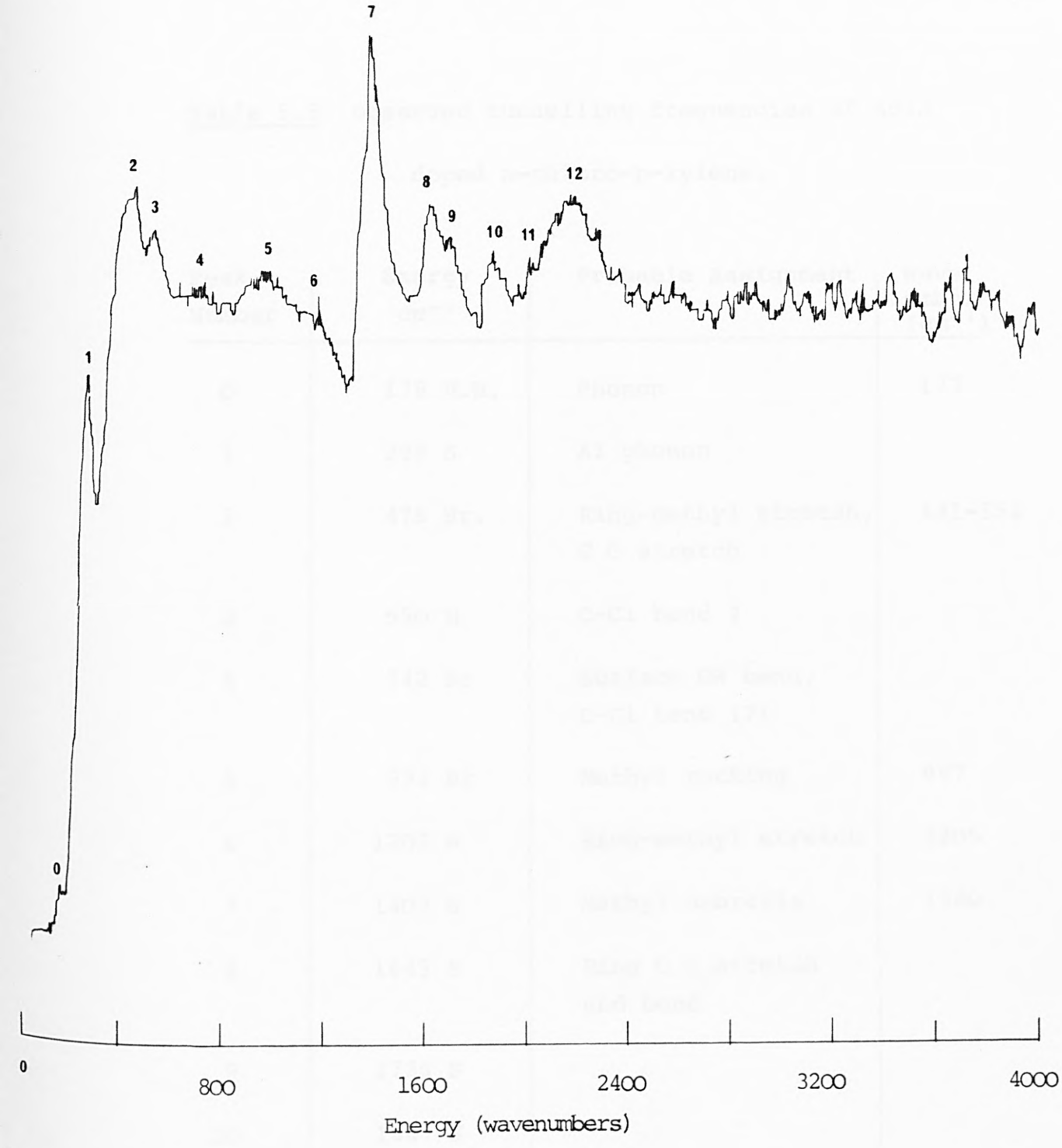

Figure 5.5.1. Alphachloro para-xylene. Spectrum 330506.

Table 5.5 observed tunnelling frequencies of spin doped α-chloro-p-xylene.

Peak Number	Energy cm^{-1}	Probable Assignment	Wave number (cm^{-1})
0	178 V.W.	Phonon	177
1	298 S	Al phonon	
2	476 Br.	Ring-methyl stretch, C C stretch	441-552
3	550 M	C-Cl bend ?	
4	742 Br	Surface OH bend, C-Cl bend (?)	
5	992 Br	Methyl rocking	967
6	1202 W	Ring-methyl stretch	1205
7	1403 S	Methyl umbrella	1380
8	1645 S	Ring C C stretch and bend	
9	1726 S		
10	1887 S		
11	2032 W		
12	2194 Br.		

would spin dope providing the solution was not too strong. The spectrum in Figure 5.5.1 was doped with a 20% (by volume) solution of α-chloro-p-xylene in analar benzene. The principal peaks (below ∿2200 cm^{-1}) are listed in Table 5.5. The difficulty in doping is due entirely to the $-CH_2Cl$ group since para xylene spin-doped very easily (Section 5.3) and neat α-chloro-p-xylene destroyed the alumina insulator. This evidence suggests the $-CH_2Cl$ group is reacting with the alumina: fortunately when diluted with benzene, the effect is reduced permitting an I.E.T. spectrum to be produced. The band at ∿548 cm^{-1} is probably due to the C-Cl stretch; however it is not possible to observe an aluminium-chlorine stretch, which would occur in the 150 to 300 cm^{-1} region as this region is obscured by the aluminium phonon at ∿298 cm^{-1}.

The presence of the methyl umbrella mode at ∿1403 cm^{-1} suggests the molecule is oriented with the CH_2Cl group chemisorbed on the surface and the methyl group free to vibrate as shown in Figure 5.5.2. The results in Sections 5.3 and 5.2 have suggested that there may be several orientations for one given adsorbate species; however in the case of α-chloro-p-xylene where previous doping attempts using the undiluted sample have shown it to be highly reactive towards the form of aluminium oxide used in tunnel junctions, strongly suggest the $-CH_2Cl$ end of the molecule is chemisorbed to the insulator (even in the slightly dilute

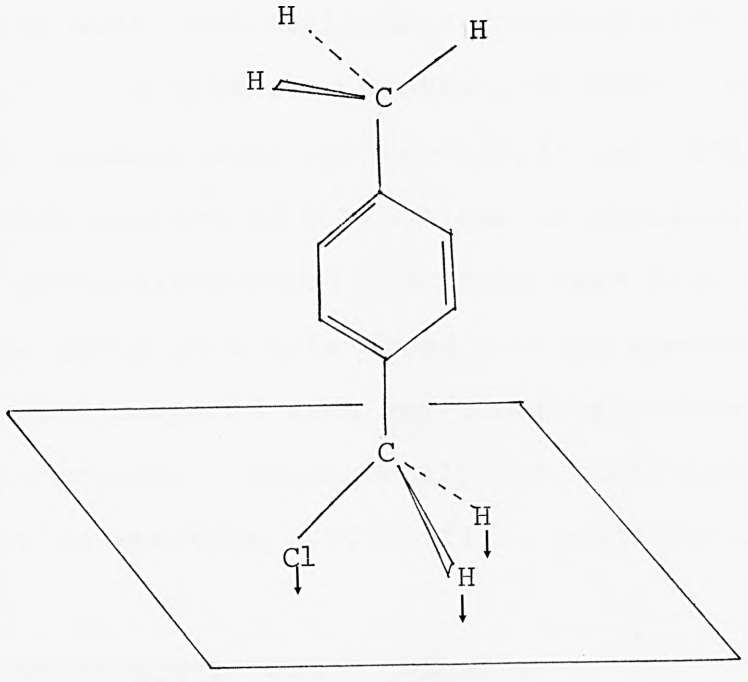

Figure 5.5.2. Proposed orienataion of α-chloro-p-xylene on alumina.

form used to produce Figure 5.5.1). Furthermore, the presence of the band at ∿1403 cm^{-1}, and the ring modes suggest that the majority of the molecules must be oriented as in Figure 5.5.2 with the molecular plane perpendicular to the surface of the oxide. (Any contributions to the spectrum from the solvent (benzene) will be extremely weak, and negligible compared with the peaks due to α-chloro-p-xylene. Contrary to most other workers belief that benzene does not dope(32,47),we have found that suitable spectra of benzene can be obtained from spin-doped and penetration-doped junctions (see Figure 3.6.1) however the peaks in a spin-doped benzene spectrum are extremely weak compared with any other spin-doped spectra of other compounds. Consequently the contribution of the solvent to spectrum 5.5.1 will be negligible).

5.6 P-(TERTIARYBUTYL)BENZYL CHLORIDE

The spin-doped spectrum of para(tertiary butyl) benzyl chloride on alumina is shown in Figure 5.6.1. It was recorded under the following conditions:

Spectrum number:	311545
Temperature:	4.2 K
Resistance:	1.3kΩ
Modulation voltage:	6 millivolts (peak-to-peak)
Number of scans:	4

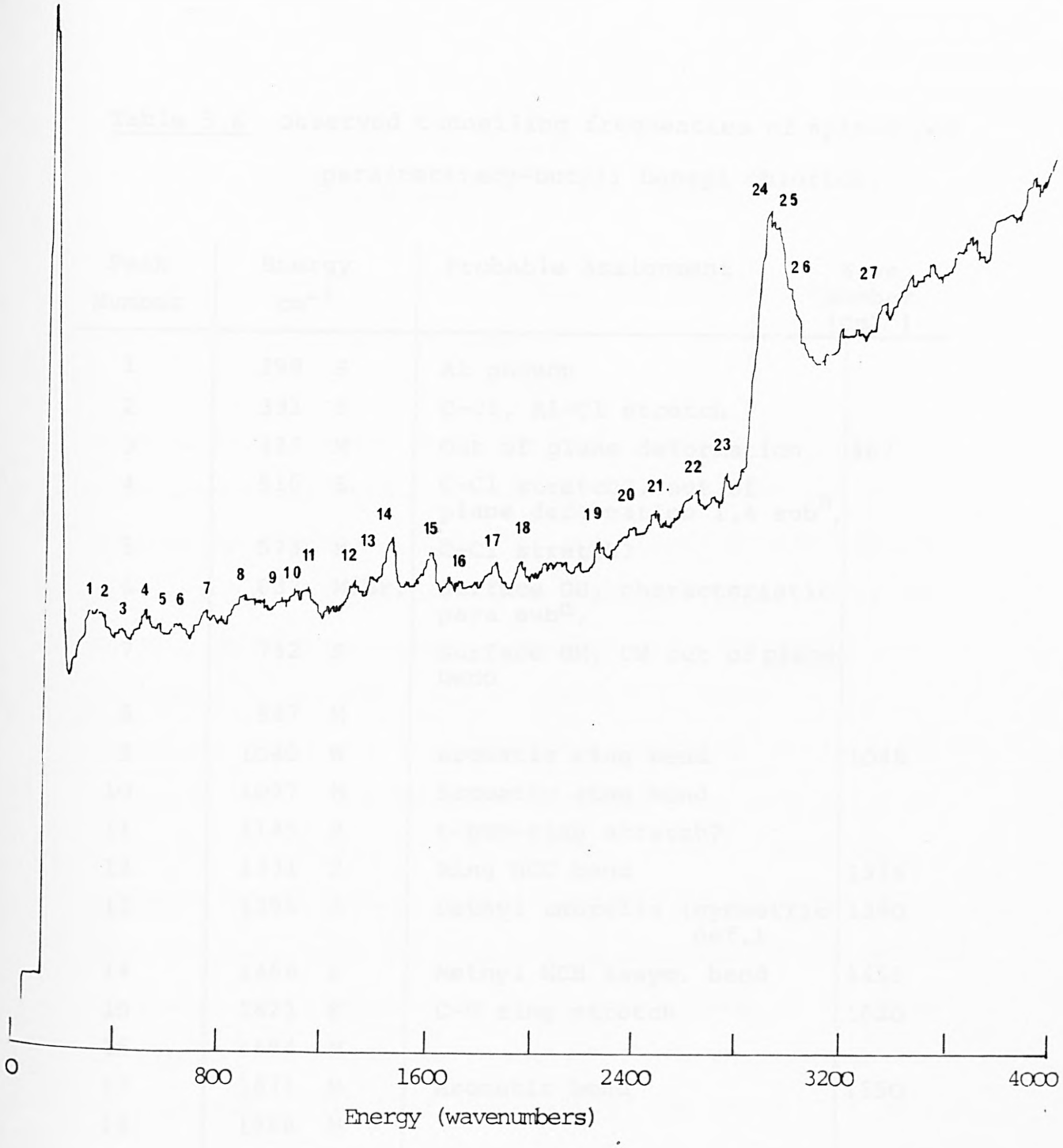

Figure 5.6.1. Para (tertiary-butyl) benzylchloride
Spectrum 311545

Table 5.6 observed tunnelling frequencies of spin-doped para(tertiary-butyl) benzyl chloride.

Peak Number	Energy cm^{-1}		Probable Assignment	Wave number (cm^{-1})
1	298	S	Al phonon	
2	331	S	C-Cl, Al-Cl stretch ?	
3	427	M	Out of plane deformation	467
4	516	S	C-Cl stretch?, out of plane deformation 1,4 sub^n,	
5	573	M	C-Cl stretch?	
6	637	M.Br.	Surface OH, characteristic para sub^n,	
7	742	S	Surface OH, CH out of plane bend	
8	887	M		
9	1040	W	Aromatic ring bend	1048
10	1097	M	Aromatic ring bend	
11	1145	S	t-but-ring stretch?	
12	1331	S	Ring HCC bend	1314
13	1395	S	Methyl umbrella (symmetric def.)	1380
14	1468	S	Methyl HCH assym. bend	1455
15	1621	S	C-C ring stretch	1620
16	1694	M		
17	1871	M	Aromatic bend	1850
18	1968	M		
19	2274	W		
20	2395	W		
21	2492	M		
22	2694	W		
23	2766	M		
24	2904	S	C-H stretch	2900
25	2944	S	Aromatic CH stretch	
26	3000	Sh	Aromatic CH stretch	
27	3339			

Duration of each scan: 4 minutes

Time constant: 100 milliseconds

(para-(tertiary butyl) benzyl chloride was also difficult to dope).

Spin doping with the neat compound resulted in junctions with zero resistance. It was only possible to produce spin-doped spectra by diluting the compound with benzene. Figure 5.6.1 was produced from a 5% (by volume) solution. As with α-chloro-p-xylene, (Section 5.5) the difficulty in doping is probably due to the $-CH_2Cl$ group. The principal peaks and their probable assignments are listed in Table 5.6. The skeletal tertiary butyl vibration at $\sim$1255 cm^{-1} is again notably absent; together with the presence of the methyl umbrella vibration at $\sim$1395 cm^{-1}, this suggests that the molecule is oriented on the surface in a similar fashion to tertiary butyl benzene, as shown in Figure 5.6.2 with the reactive $-CH_2Cl$ chemisorbed on the surface. The weak intensity of the peaks (due to the necessity to dilute the dopant) means that it is not possible to unambiguously identify all the peaks. However one interesting feature is the broadening of the aluminium phonon. This peak can be resolved into two peaks of equal intensity one the aluminium phonon (298 cm^{-1}) and the other at $\sim$331 cm^{-1}. This peak, which is not observed in any other spectra reported here, is probably due to the aluminium-chlorine stretch, and thus supports the orientation suggested in Figure 5.6.2.

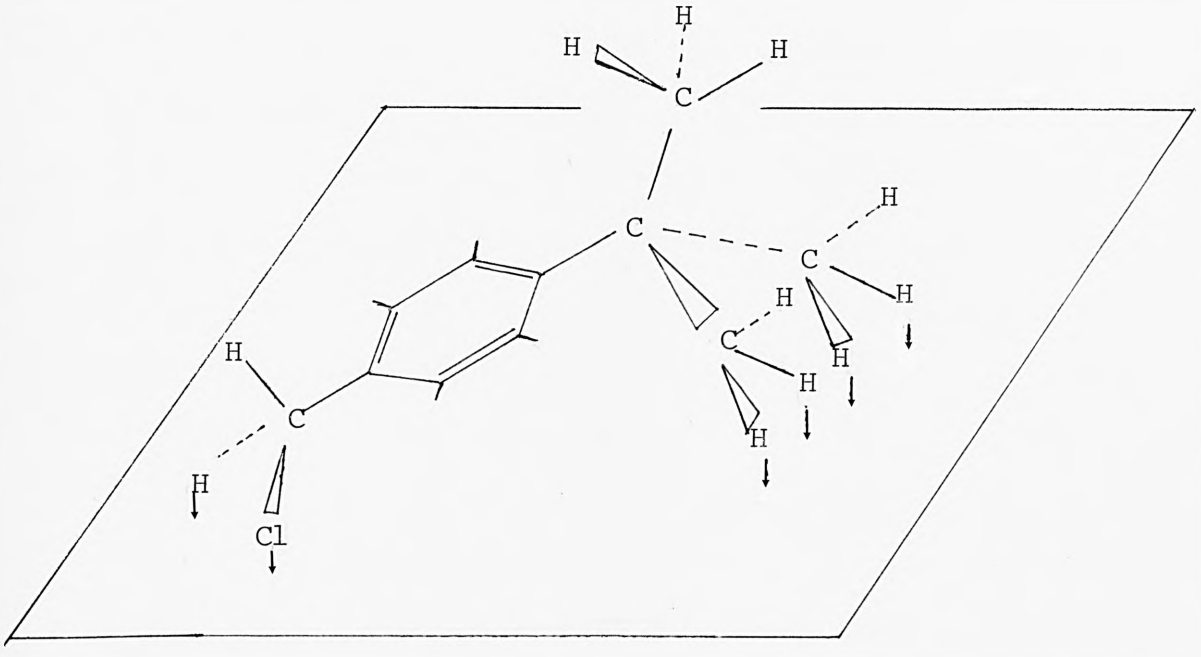

Figure 5.6.2. Proposed orienataion of p-(t-butyl) benzylchloride on alumina.

5.7 SUMMARY OF SECTIONS 5.1 TO 5.6

Several general features common to all of the tunnelling spectra reported in Sections 5.1 to 5.6 are now evident. Firstly the extreme weakness of surface OH bends at 605 cm^{-1} and 726 cm^{-1} and their combination and overtone bands at 1331 cm^{-1} and 1855 cm^{-1}; secondly, the almost total absence of the broad surface OH stretch at $\sim$3600 cm^{-1}. These absences in this work (or at the most, very weak absorptions), are attributed to the way in which the oxide layer is grown using pure, dry oxygen and a plasma discharge - this differs from the insulator growth techniques of some other workers which involves oxidation in wet air.

The difficulty in obtaining spectra of more reactive compounds (Sections 5.4 and 5.5) due to their reaction and subsequent removal of the oxide layer means that I.E.T.S. cannot be used for sampling and analysis of such compounds unless they are in a diluted form or a more chemically inert tunnelling insulator is employed.

Finally, the inability to draw definite conclusions concerning the geometry of an adsorbate molecule is almost certainly due to rough and uncharacterised nature of the substrate used in these experiments. This is only a disadvantage in that it is not always possible to deduce the surface orientation of complex molecules; Orientation problems could be resolved with corroborative evidence from

surface infrared and surface-enhanced Raman spectroscopy (S.E.R.S.). The advantagein using a rough substrate is that a large number of vibrational modes will be present (due to several orientations being present at once): hence making identification of an unknown compound easier.

5.8 BENZENE

The penetration-doped spectrum of analar benzene on alumina is shown in Figure 5.8.1. It was recorded under the following conditions:

Spectrum number:	335679
Temperature:	4.2 K
Resistance:	600Ω
Modulation voltage:	10 millivolts (peak-to peak)
Number of scans:	4
Samples per scan:	4000
Duration of each scan:	15 minutes
Time constant:	1 second

Although benzene would spin dope, it did not give very intense peaks. The only other tunnel spectrum of benzene by Bogatina(57) is not sufficiently resolved to permit detailed vibrational analysis. The spectrum reported here is the first high resolution tunnelling spectrum of benzene. The principal peaks and their vibrational assignments are given in Table 5.8.1. The presence of

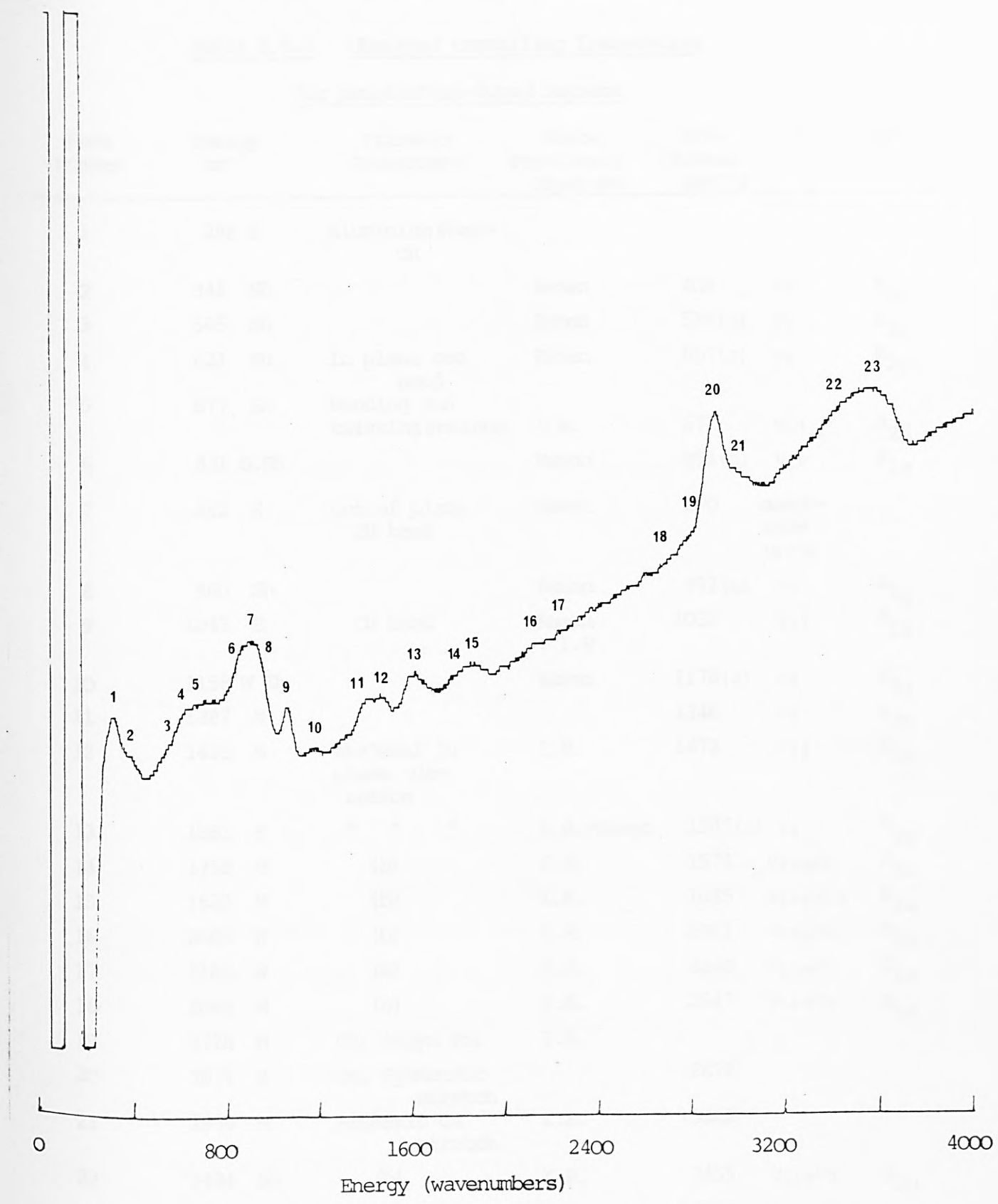

Figure 5.8.1. Penetration-doped benzene. Spectrum 335679.

Table 5.8.1 Observed tunnelling frequencies for penetration-doped benzene

Peak number	Energy cm^{-1}	Probable Assignment	Where Previously Observed	Wave Number (cm^{-1})	νi	D_6h
1	298 S	Aluminium Phonon				
2	348 Sh		Raman	404	ν_6	E_{2u}
3	565 Sh		Raman	578(a)	ν_6	E_{2g}
4	621 Sh	In plane ccc bend	Raman	607(a)	ν_6	E_{2g}
5	677 Sh	bending and twisting motions	I.R.	677	ν_{11}	A_{2u}
6	831 S.Sh		Raman	856(a)	ν_{10}	E_{1g}
7	882 S	out of plane CH bend	Raman	860	resonance $\nu_9+\nu_5$	
8	960 Sh		Raman	992(a)	ν_1	A_{1g}
9	1045 S	CH bend	Raman + I.R	1038	ν_{18}	E_{1u}
10	1158 W Sh		Raman	1178(a)	ν_9	E_{2g}
11	1387 M			1346	ν_3	A_{2g}
12	1428 M	skeletal in plane vibration	I.R.	1472	ν_{19}	E_{1u}
13	1581 S	" " "	I.R.+Raman	1587(a)	ν_8	E_{2g}
14	1758 M	(b)	I.R.	1574	$\nu_{15}+\nu_6$	E_{1u}
15	1839 M	(b)	I.R.	1825	$\nu_{17}+\nu_{19}$	E_{1u}
16	2065 W	(b)	I.R.	2011	$\nu_{16}+\nu_8$	A_{2u}
17	2162 W	(b)	I.R.	2210	$\nu_{18}+\nu_9$	E_{1u}
18	2662 M	(b)	I.R.	2647	$\nu_{19}+\nu_9$	E_{1u}
19	2775 W	CH_2 Assym str	I.R.			
20	2871 S	CH_3 Symmetric stretch		2872		
21	2984 M	Aromatic CH stretch	I.R.	∿3028		
22	3484 Sh	(b)	I.R.	3455	$\nu_{16}+\nu_7$	A_{2u}
23	3581 Br	Surface OH stretch	I.R.	∿3600		

S : strong; M : medium; W : weak; Sh : shoulder; Br : broad.

(a) Benzene crystal 4.2 K, reference 143.

(b) Predicted in theoretical work: see Table 5.8.2. Information in such row is theoretical.

Infra-red and Raman data (apart from (a) above) from References 139,140,141,142.

most of the vibrational modes again suggests the molecule is in more than one orientation. This supports the theories concerning the mechanisms of penetration doping discussed in Section 3.5. However in order to verify these assumptions the frequencies in Table 5.8.1 are correlated with the theoretical work of Bogatina(58). Bogatina has calculated the active tunnelling frequencies that will be present for two types of molecular orientation. One with the molecularplane parallel to the insulator, the other with the molecular plane perpendicular to the insulator surface. The fact that vibrations uniquely characteristic to either a perpendicular vibration mode (indicated by an entry in column 3, Table 5.8.2) or a parallel vibration mode (indicated by an entry in column 2, Table 5.8.2) are both present implies that both orientations are present on the insulator surface (see Figure 5.8.2). The apparent discrepancy between the experimental values and the theoretical values are accounted for by measurement error: some peaks in Figure 5.8.1 overlap with other vibrational modes preventing accurate determination of frequency. Additionally some peaks are too weak to measure their frequency with the desired accuracy. Finally Bogatina's theoretical results (which are given in Table 5.8.3) are extremely variable in intensity: (for example the intensities of the 1406 cm^{-1} and the 2624 cm^{-1} vibrations are 300 times lower than that of the 292 cm^{-1} vibration). The large intensity variation in the theoretical results would account for the absence of some of the weaker theoretically calculated modes

Table 5.8.2 *Correlation of experimentally obtained benzene vibrational frequencies with the theoretical values calculated by Bogatina(58)*

1. I.E.T.S. (cm^{-1})	2. *Molecular Plane parallel to the insulator surface* Frequency	Symmetry Type	Energy (cm^{-1})	Where previously observed	3. *Molecular Plane perpendicular to the insulator surface* Frequency	Symmetry Type	Energy (cm^{-1})	Where previously observed
348								
565								
621					ν_6	E_{2g}	607	Raman
677	ν_{11} (+lattice (twisting (vibrations)	A_{2u}	687	i.r.				
831	?	?	818	i.r.				
882								
960	ν_1	A_{1g}	992	Raman	ν_1	A_{1g}	992	Raman
1045					ν_{18}	E_{1u}	1038	i.r.
1158					ν_9	E_{2g}	1178	Raman
1387	$2\nu_4$	A_{1g}	1406	Raman	$2\nu_4$	A_{1g}	1406	Raman
1428					ν_{19}	E_{1u}	1478	i.r.
1581					ν_8	E_{2g}	1587	Raman
1758	($\nu_2 + \nu_4$	A_{2u}	1713	i.r.)	$\nu_{15} + \nu_6$	E_{1u}	1754	i.r.
1839	($\nu_8 + \nu_{10}$	A_{2u}	1877	i.r.)	$\nu_{17} + \nu_{10}$	E_{1u}	1825	i.r.
2065	$\nu_{12}+\nu_5$ and $\nu_{16}+\nu_8$	A_{2u}	2011	i.r.				
2162					$\nu_{18} + \nu_9$	E_{1u}	2210	i.r.
2662					$\nu_{19} + \nu_9$	E_{1u}	2647	i.r.
2775					$\nu_3 + \nu_{19}$	E_{1u}	2816	i.r.
2871					$\nu_{14} + \nu_8$	E_{1u}	2907	i.r.
2984	$2\nu_{19}$	A_{1g}	2970	Raman	$2\nu_{14}$	A_{1g}	2970	Raman
3484	$\nu_{16} + \nu_7$	A_{2u}	3455	i.r.				
3581					$\nu_{20} + \nu_6$	E_{1g}	3630 & 3688	i.r.

Table 5.8.3 Dependence of the active frequencies in the tunnel spectrum (calculated/ on the orientation of the C_6H_6 molecule in the barrier (After Bogatina,(58))

C_6H_6 plane parallel to the metal-dielectric interface				*C_6H_6 plane perpendicular to the metal-dielectric interface*			
Frequency	Symmetry Type	Energy cm^{-1}	Where previously observed	Frequency	Symmetry Type	Energy cm^{-1}	Where previously observed
ν_{11} and twisting vibrations of lattice	A_{2u}	687	I.R.	ν_6	E_g^+	607	Raman
				ν_1	A_{1g}	992	Raman
		769					
		788	I.R.	ν_{18}	E_u^-	1038	I.R.
		818					
ν_1	A_{1g}	992	Raman	$\nu_{16}+\nu_4$	$E_{\bar{u}}$	1108	I.R
$3\nu_{16}$	A_{2u}	1220	I.R.	ν_9	E_g^+	1178	Raman
$2\nu_6$	A_{1g}	1212	Nowhere	$\nu_{16}+\nu_{10}$	E_u^-	1249	I.R
$2\nu_4$	A_{1g}	1406	Raman	$\nu_{16}+\nu_5$	$E_{\bar{u}}$	1405	I.R.
$2\nu_{10}$	A_{1g}	1708	Nowhere	$2\nu_4$	A_{1g}	1406	Raman
$\nu_2+\nu_4$	A_{2u}	1713	I.R.	ν_{19}	E_u^-	1478	I.R
$\nu_8+\nu_{10}$	A_{2u}	1877	I.R.	$\nu_{11}+\nu_{10}$	$E_{\bar{u}}$	1551	I.R
$\nu_{12}+\nu_5$ / $\nu_{16}+\nu_8$	A_{2u}	2011	I.R.	ν_8	E_g^+	1587	Raman
				$\nu_1+\nu_6$	E_g^+	1606	Raman
$2\nu_9$	A_{1g}	2356	Nowhere	$\nu_{12}+\nu_6$	E_u^-	1618	I.R
$\nu_{19}+\nu_{10}$	A_{2u}	2347	I.R.	$\nu_{18}+\nu_6$	$E_{\bar{u}}$	1645	I.R
$2\nu_{14}$	A_{1g}	2624	Raman	$\nu_{17}+\nu_4$	E_u^-	1680	I.R
$2\nu_{19}$	A_{1g}	2970	Raman	$\nu_{15}+\nu_6$	$E_{\bar{u}}$	1754	I.R
ν_2	A_{1g}	3062	Raman	$\nu_{17}+\nu_{10}$	$E_{\bar{u}}$	1825	
$\nu_{16}+\nu_7$	A_{2u}	3455	I.R.	-	-	1839	I.R
$\nu_{20}+\nu_{10}$	A_{2u}	3935	I.R.	-	-	1850	
				$\nu_{17}+\nu_5$	E_u^-	1959	I.R
				$\nu_{18}+\nu_9$	$E_{\bar{u}}$	2210	I.R
				$\nu_{15}+\nu_9$	E^-	2323	I.R
				$\nu_{18}+\nu_3$	$E_{\bar{u}}$	2382	I.R
				$\nu_{12}+\nu_8$	$E_{\bar{u}}$	2608	I.R
				$2\nu_{14}$	A_{1g}	2624	Raman
				$\nu_{19}+\nu_9$	$E_{\bar{u}}$	2647	I.R
				$\nu_3+\nu_{19}$	E^-	2816	I.R
				$\nu_{14}+\nu_8$	$E_{\bar{u}}$	2907	I.R
				$2\nu_{14}$	A_{1g}	2970	Raman
				ν_{20}+resonance / $\nu_{19}+\nu_8$	E^-	3030 / 3085	I.R.
				ν_2	A_{1g}	3062	Raman
				$\nu_{20}+\nu_{16}$	E^-	3630 / 3688	I.R.

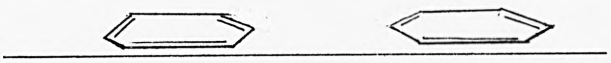

Molecular plane parallel to surface.

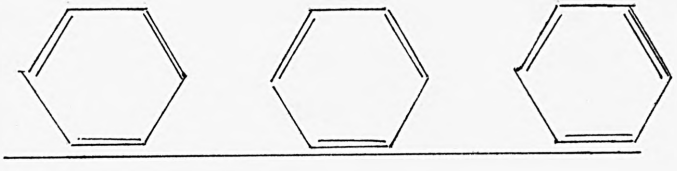

Molecular plane perpendicular to surface.

Figure 5.8.2. The two orientations of benzene used by Bogatina to calculate the theoretical frequencies in table 5.8.3.

Table 5.8.4 Comparison of benzene frequencies obtained by tunnelling spectroscopy (I.E.T.S.) and surface-enhanced Raman spectroscopy (SERS) (after Reference 144)

ν_i	I.E.T.S.	liquid	SERS	D_{6h}
1	960(a)	992	982	A_{1g}
2	c,d	3059	3062	A_{1g}
3	1387	1346	b	A_{2g}
4	c	703	b	b_{2g}
5	b	989	c	b_{2g}
6	621	606	605	e_{2g}
7	c,d	3046	3047	e_{2g}
8	1581	1596	1587	e_{2g}
9	1158	1178	1177	e_{2g}
10	831	849	864	e_{1g}
11	677	670	697	A_{2u}
12	b	1008	b	b_{1u}
13	c,d	3062	c	b_{1u}
14	c	1309	1311	b_{2u}
15	1158	1149	1149	b_{2u}
16	348	404	397	e_{2u}
17	a	966	c	e_{2u}
18	1045	1036	1032	e_{1u}
19	1428	1479	1473	e_{1u}
20	c,d	3073	c	e_{1u}

Notes:

(a) 960 cm^{-1} in I.E.T.S. overlaps with ν_1, ν_5 and ν_{17} however since ν_5 and ν_{17} are absent from the surface Raman spectrum, the 960 cm^{-1} band in the I.E.T.S. has been assigned to the ν_1 vibration at 982 cm^{-1} in the surface Raman spectrum. (This assignment is also in theoretical agreement with Bogatina(58)).

(b) Modes absent in surface spectra.

(c) Possible overlap with other modes prevents the determination of the presence or absence of this mode.

(d) I.E.T.S. results only: the broad C-H band extends from $\sim$2825 cm^{-1} to $\sim$3100 cm^{-1}, with its maxima at $\sim$2896 cm^{-1}. It is not possible to deduce individual frequencies within this region.

(e) This table gives fundamental frequencies only: combination and overtone bands (many of which are present in the original tunnelling spectrum) are not given here.

from the tunnel spectrum.

Finally, the experimental results have been correlated with the surface-enhanced Raman spectrum (S.E.R.S.) of benzene adsorbed on silver by Moskovits and DiLella(144) in Table 5.8.4. The results obtained from the tunnel spectrum and those obtained from S.E.R.S. are in agreement well within experimental error. The comparison in Table 5.8.4. does show that some frequencies which are present in the Raman spectrum are not present in the tunnel spectrum (e.g. ν_2, ν_7, ν_{13} and ν_{20}). Their apparent absence is accounted for by the fact that the modes are either too weak to observe in I.E.T.S. and/or their overlap with other modes prevents their observation.

5.9 BIS-PYRIDINE COBALT DICHLORIDE, $Co(py)_2Cl_2$.

$Co(py)_2Cl_2$, where py stands for pyridine, is known to exist in two forms(145) a tetrahedral monomer which is blue incolour (Figure 5.9.1a) and an octahedral polymer which is lilac in colour (Figure 5.9.1b). Solutions of the largely octahedral polymeric solid were made up in benzene, water, ethanol and dimethyl formamide. Only the benzene and water solutions produced suitable junctions for running I.E.T. spectra: the ethanol solution gave very weak peaks and the dimethyl formamide solution produced a very noisy spectrum with instability above $\sim$2000 cm^{-1}.

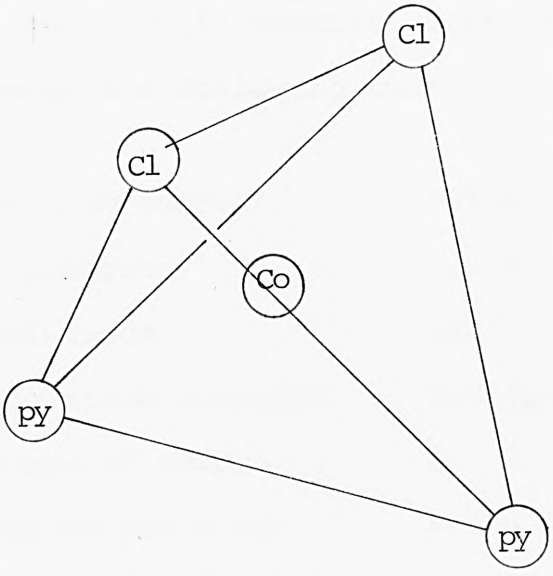

Figure 5.9.1a. $Co(py)_2Cl_2$ tetrahedral monomer.

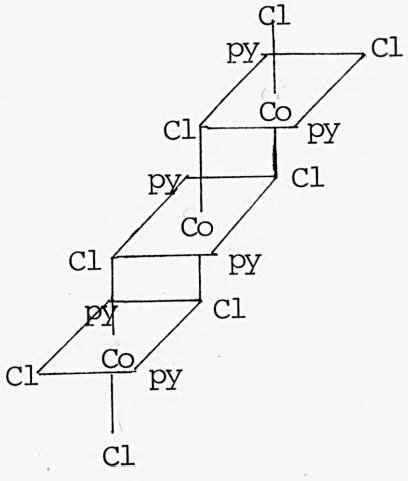

Figure 5.9.1b. $Co(py)_2Cl_2$ octahedral polymer.
(After Nyholm reference 145).

The penetration-doped spectrum of $Co(py)_2Cl_2$ in benzene, a blue solution, is shown in Figure 5.9.2. It was recorded under the following conditions:

Spectrum number:	335681
Temperature:	4.2 K
Resistance:	1kΩ
Modulation voltage:	8mV (peak-to-peak)
Number of scans:	1
Samples per scan:	4000
Scan duration:	60 minutes
Time constant:	10 seconds

(Several shorter duration multiscan spectra were also produced; (e.g. 4 x 20 minutes, 4 x 10 minutes) however in all cases it was not possible to remove the noise which was present above $\sim$2400 cm^{-1}. Later attempts to remove the noise by boosting irreparably damaged the junction. Spectrum 335681 is the most clearly resolved of the spectra produced).

The spin-doped spectrum of $Co(py)_2Cl_2$ in water (a pink solution) is shown in Figure 5.9.3. It was recorded under the following conditions:

Spectrum number:	374671
Temperature:	4.2 K
Resistance:	2.2kΩ

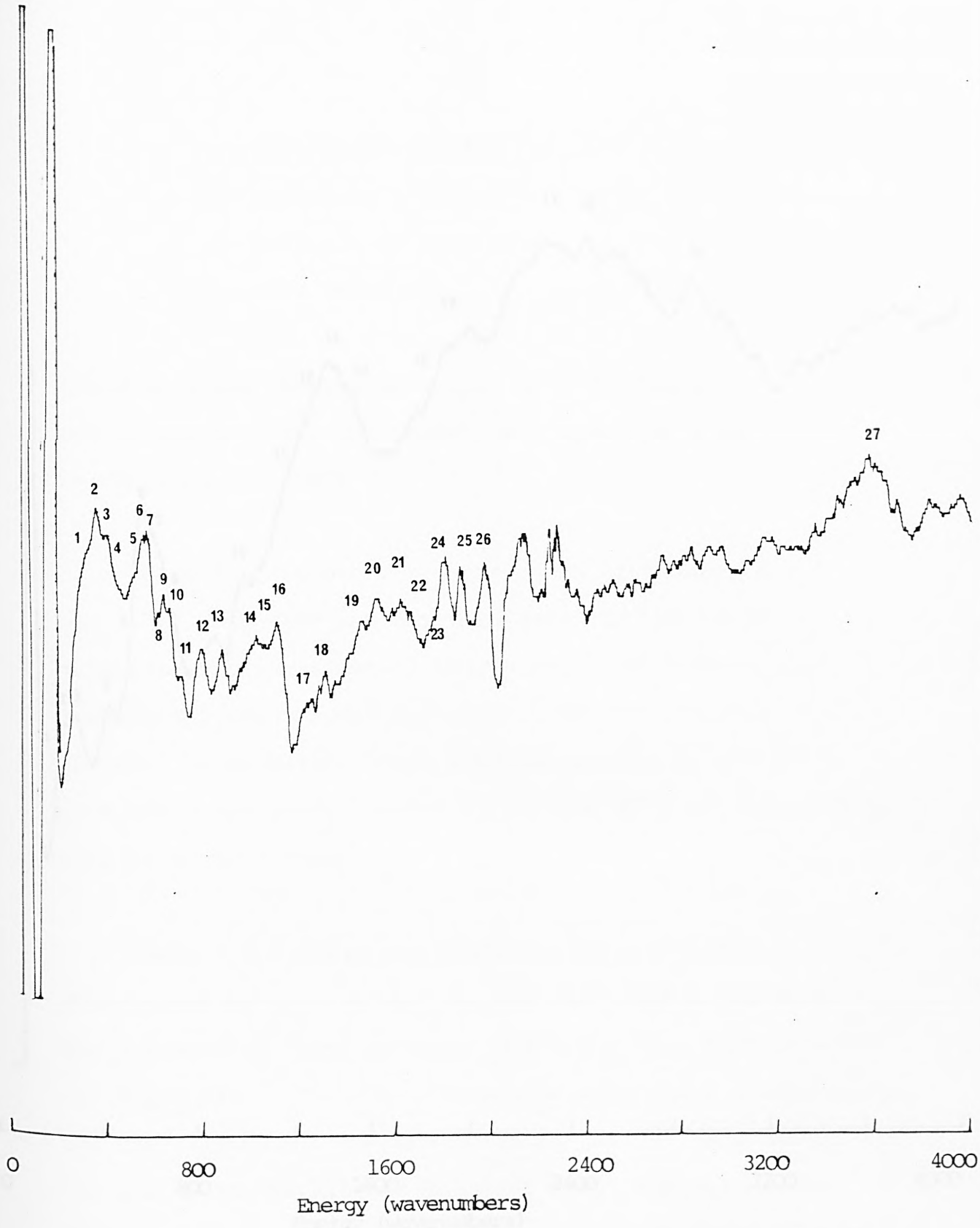

Figure 5.9.2. Bis pyridine cobalt dichloride (solvent: benzene)
Spectrum 335681

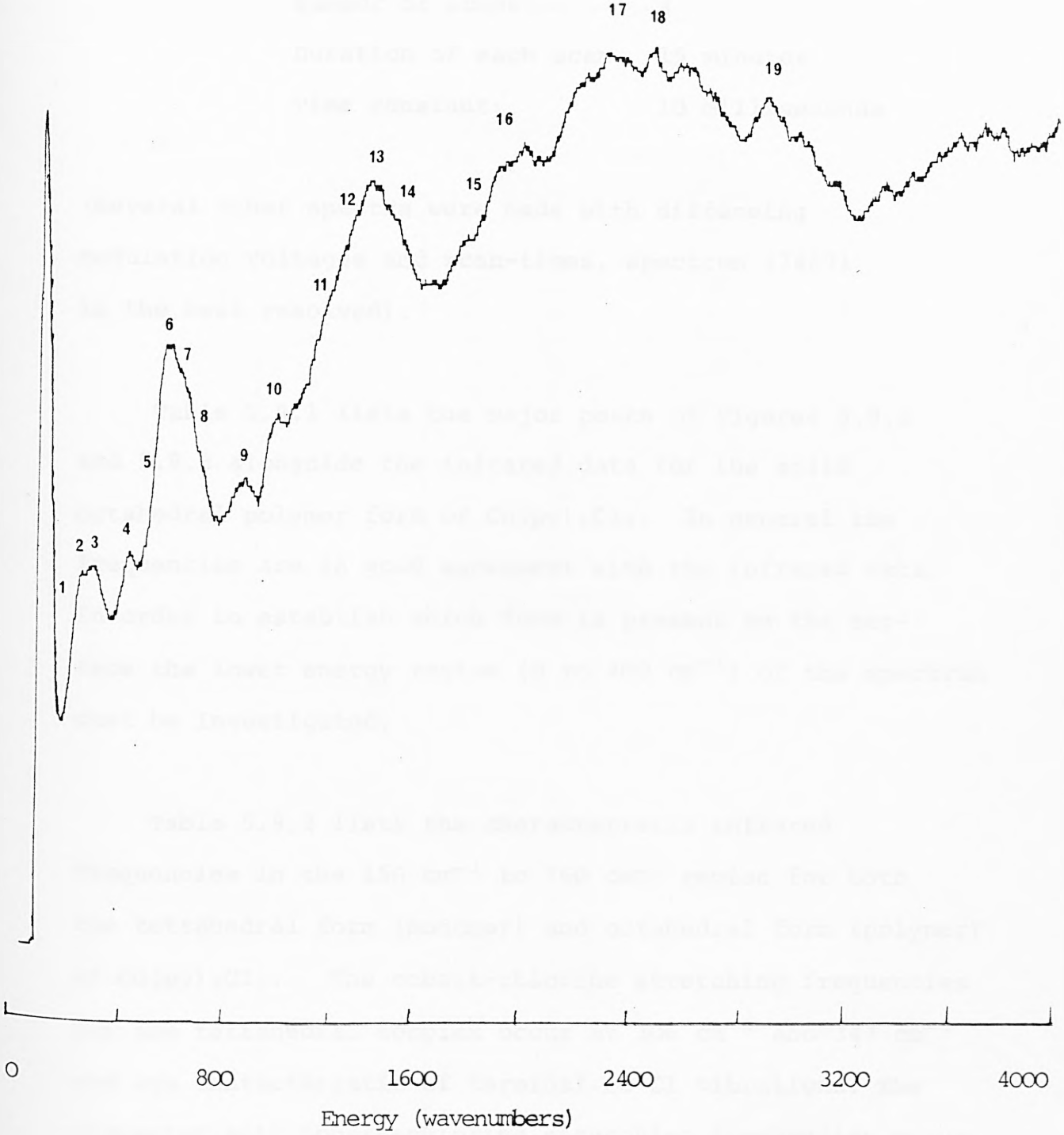

Figure 5.9.3. Bis pyridine cobalt dichloride (solvent: water) Spectrum 374671.

Modulation voltage:	9mV (peak-to-peak)
Number of scans:	4
Duration of each scan:	15 minutes
Time constant:	10 milliseconds

(Several other spectra were made with differeing modulation voltages and scan-times, spectrum 374671 is the best resolved).

Table 5.9.1 lists the major peaks of Figures 5.9.2 and 5.9.3 alongside the infrared data for the solid octahedral polymer form of $Co(py)_2Cl_2$. In general the frequencies are in good agreement with the infrared data. In order to establish which form is present on the surface the lower energy region (0 to 400 cm^{-1}) of the spectrum must be investigated.

Table 5.9.2 lists the characteristic infrared frequencies in the 150 cm^{-1} to 360 cm^{-1} region for both the tetrahedral form (monomer) and octahedral form (polymer) of $Co(py)_2Cl_2$. The cobalt-chlorine stretching frequencies for the tetrahedral complex occur at 306 cm^{-1} and 347 cm^{-1} and are characteristic of terminal Co-Cl vibrations. The characteristic cobalt-chlorine stretching frequencies occur much lower than these values in the octahedral complex. This is due to the chlorine atom forming a bond between two cobalt atoms. The cobalt-chlorine "bridging frequencies"

Table 5.9.1 Comparison of observed tunnelling frequencies with infrared data for $Co(py)_2Cl_2$

I.R. octahedral form		I.E.T.S. Figure 5.9.2. (335681)		Figure 5.9.3 (374671)		
				274	M	
		300	Sh	298	M	
		342	S	323	Sh	
		379	Sh			
442	S	427	Sh	436	S	
		508	Sh	516	Sh	
		548	S			
		565	S			
		605	Sh	592	S.Br	
		629	Sh			
642	S	653	Sh	661	Sh	
690	S.Br	700	S	710	Sh	
		782	S			
880	M	{871	S	887	Br	
		{879	Sh			
960	M.W	952	Sh			
1016	M	1016	S	1008	M	
1042	M					
1070	W.Sh.W					
1085	M	1097	S			
1160	M			1150	Sh	
1222	S					
1244	M	1242	M	1242	Sh	
		1300	W			
1365	M			1363	S	
1445	M.Br	1452	M	1468	Sh	
1490	S	1516	M			
1576	Sh	1565	M			
1600	S.Br	1613	M			
1645	M	1657	W			
		1799	S	1792	Sh	
		1871	M	1855	W	
1900	W	1968	W			
2010						
2350	Br.W			2290	Br	
				2452		Region noisy in
3010	W			3000	M	tunnel spectra
3050	W					
3070	W					
3115	W			3140	M	
		3580	Br.W			

Table 5.9.2 Characteristic infrared frequencies of $Co(py)_2Cl_2$ in the 150 cm^{-1} to 360 cm^{-1} region (165)

Monomeric (tetrahedral) form

Energy (cm^{-1})		
144	S	
190	S	
225	M	
253	S	
306	S	ν(Co-Cl) terminal
347	S	ν(Co-Cl) terminal
422	S	pyridine
642	S	pyridine

Polymeric (octahedral) form

Energy (cm^{-1})		
174	S	ν(Co-Cl) bridging
186	S	ν(Co-Cl) bridging
225	S	
235	S	
243	S	

occur at 174 cm^{-1} and 186 cm^{-1}.

The 0-1000 cm^{-1} regions of Figures 5.9.2 and 5.9.3. have been expanded and are shown in Figures 5.9.4 and 5.9.5 respectively. Before comparing the expanded spectra with the infrared data two points should be noted.

(i) Modulation-voltage broadening will become significant when comparing two peaks of similar frequencies. If the peaks are close enough, they will broaden into one peak.

(ii) There are a large number of phonon peaks also occurring in the 0-300 cm^{-1} region their presence may mask some of the weaker bis-pyridine-cobalt dichloride vibrational frequencies. A list of phonons for an aluminium-aluminium oxide-lead junction are listed in Table 5.9.3.

The principal peaks of the expanded $Co(py)_2Cl_2$ spectra (Figures 5.9.4 and 5.9.5) and their probable assignments are presented in Table 5.9.4. However because of the close proximity of phonon peaks to the majority of the adsorption peaks of the complex (for example the phonon at 177 cm^{-1} and the Co-Cl bridging frequency of the octahedral complex at 174 cm^{-1}) unambiguous identification is not possible

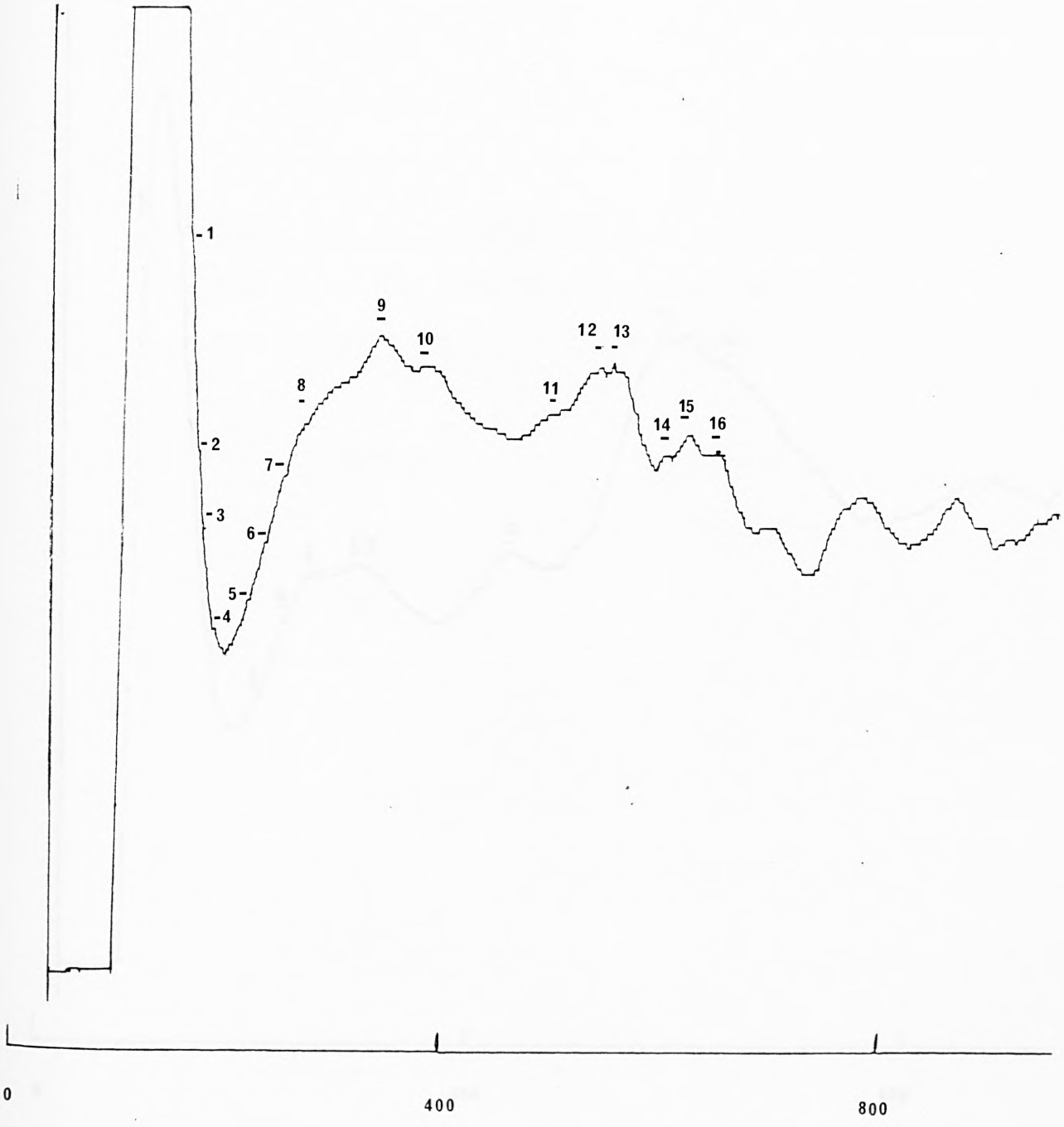

Figure 5.9.4. Spectrum 335681. Bis pyridine cobalt dichloride in benzene. (Expanded in x-direction.)

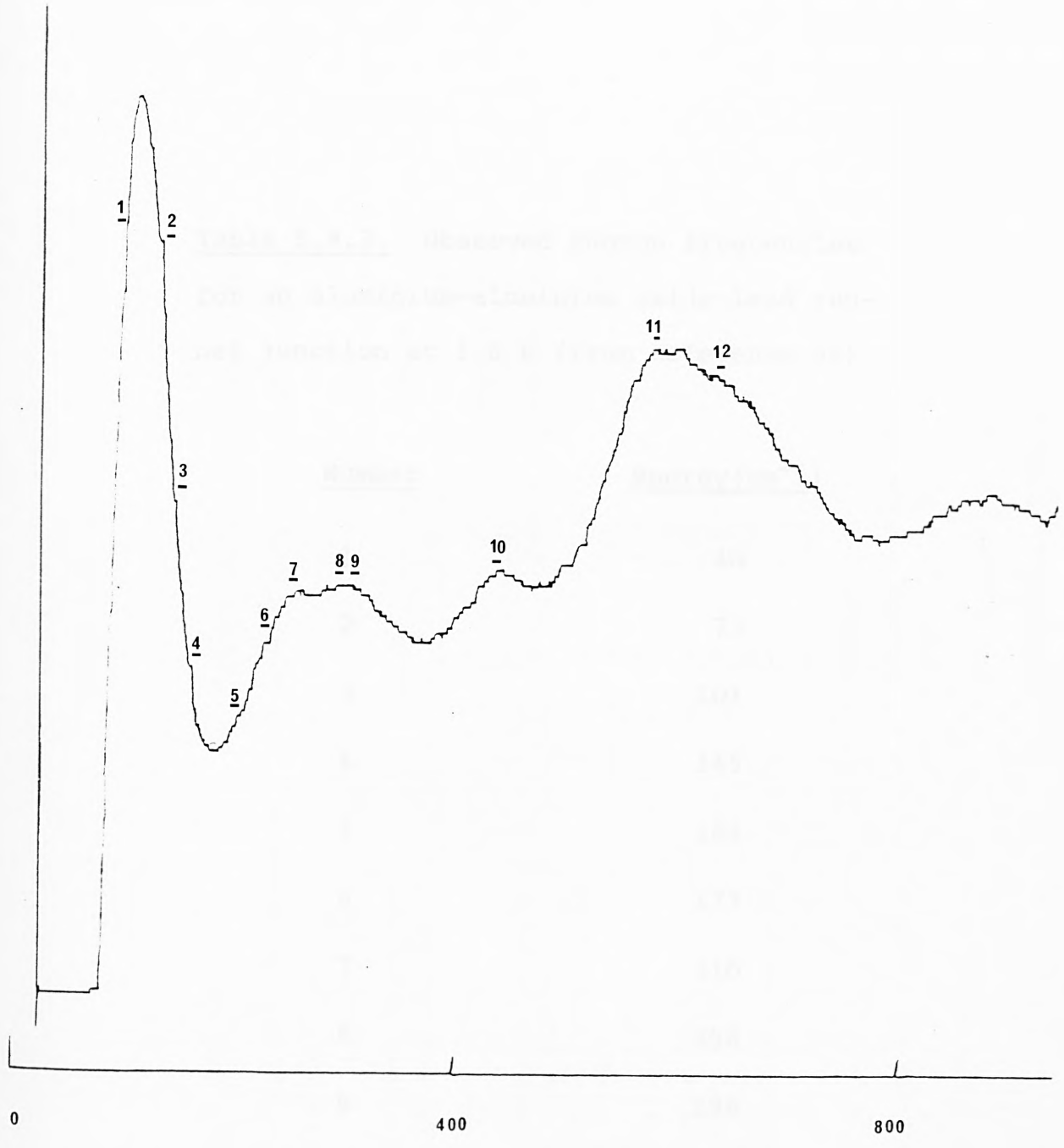

Figure 5.9.5. Spectrum 374671. Bis pyridine cobalt dichloride in water. (Expanded in x-direction.)

Table 5.9.3. Observed Phonon frequencies for an aluminium-aluminium oxide-lead tunnel junction at 1.6 K (from Reference 64)

Number	Energy(cm^{-1})
1	40
2	73
3	101
4	145
5	161
6	177
7	210
8	258
9	298

Table 5.9.4 Principal peaks of the two expanded spectra shown in Figures 5.9.4 and 5.9.5.

Figure 5.9.4 Spectrum 335681

Penetration-doped $Co(py)_2Cl_2$ (in benzene solution)

Peak	Energy (cm^{-1})	Probable Assignment (energy in cm^{-1})
1	161	Phonon (161)
2	168	?
3	174	ν(Co-Cl)b.Oh.(174) Phonon (177)
4	182	ν(co-Cl)b.Oh.(186)
5	190	td. (190)
6	222	Oh, td(225)
7	237	td (235)
8	254	Phonon (258) Phonon (298) Oh (243)
9	347	ν(Co-Cl)t, td (347)
10	382	
11	500	
12	536	
13	552	
14	600	Surface OH (605)
15	616	
16	644	pyridine (642)

Figure 5.9.5 Spectrum 374671

Spin-doped $Co(py)_2Cl_2$ (in water solution)

Peak	Energy (cm^{-1})	Probable Assignment (energy in cm^{-1})
1	97	Phonon (101)
2	129	?
3	145	Phonon (145) td (144)
4	158	Phonon (161)
5	202	Phonon (210)
6	226	Oh, td (225)
7	248	Oh (243)
8	296	Phonon (298)
9	300	ν(Co-Cl)t, td (306)
10	432	pyridine (422)
11	580	
12	628	pyridine (642)

Notes:

Oh: vibration characteristic of octahedral complex

ν(Co-Cl)b: Bridging cobalt-chlorine frequency

td: vibration characteristic of tetrahedral complex

ν(Co-Cl)t: terminal cobalt-chlorine frequency

for most peaks. Fortunately there are four absorptions which are sufficiently removed from phonon peaks to be more positively identified. These are:-

1. 306 cm^{-1} a cobalt-chlorine terminal frequency of the tetrahedral complex;

2. 347 cm^{-1} also a cobalt-chlorine terminal frequency of the tetrahedral complex;

3. 235 cm^{-1}
4. 243 cm^{-1}

} Characteristic frequencies of the octahedral complex

However, the 347 cm^{-1} and 243 cm^{-1} are both present in spectrum 335681 (Figure 5.9.4, Table 5.9.4), and the 306 cm^{-1} and 243 cm^{-1} absorptions are both present in spectrum 374671 (Figure 5.9.5, Table 5.9.4). From the data available it is only possible to conclude that the tetrahedral monomeric form and the octahedral polymeric form of $Co(py)_2Cl_2$ are present in both spectra.

There are several ways to produce clearer spectra in order to resolve the ambiguity as to the surface species present on the alumina surface:

(1) Repeat the experiment using a much lower modulation voltage. This will significantly reduce modulation-voltage broadening;

(2) Repeat the experiment at a lower temperature in order to reduce thermal broadening. By pumping liquid helium it is possible to reach a temperature of 1.1 K.

(3) Utilizing a different metal-insulator system (e.g. Mg-MgO-Mg) whose phonon peaks occur at different energies from the aluminium-lead electrode system. This would remove some of the ambiguities concerning peak identification.

(4) Subtracting a "blank" undoped spectrum from the sample spectrum would remove the background slope and most of the phonon effects.

(5) Repeating the experiment using a smoother substrate (e.g. glass or silica). This would reduce the peak broadening caused by several orientations being simultaneously present on the surface as a result of the rough substrate.

These improvements are necessary not only to obtain better spectra of the cobalt complex but also to obtain high resolution spectra of the 0-300 cm^{-1} energy region in general. This region contains many potentially important vibrational

frequencies such as metal-halogen; metal-oxygen and metal-sulphides. Accurate determination of frequencies within this region is especially important when considering metal-carbonyl and metal cluster compounds, and their rôle in heterogeneous catalysis. The 0-300 cm^{-1} region is chemically important and has up until now been neglected by tunnelling spectroscopists because of the phonon problem.

Unfortunately it was not possible to implement the above experiments in the time available: they have been mentioned here as suggestions for future work.

CHAPTER 6 ANTI-STOKES' ELECTRON TUNNELLING (A.S.E.T.)

The concept of anti-Stokes' electron tunnelling was developed in order to circumvent the natural shortcomings of inelastic tunnelling spectroscopy, namely its energy range which is limited by the dielectric breakdown of the insulator at approximately 2.2 volts (18,000 cm^{-1}). With the new technique proposed in this Chapter it ought to be possible to study higher energy (>18,000 cm^{-1}) vibrational and electronically excited states of adsorbed species without any dielectric breakdown problem.

Essentially the technique aims to interact tunnelling electrons with adsorbate species which have been selectively excited by an external (laser) light source, and to measure the gain in energy of the tunnelling electron as a result of the excited state-electron interaction.

6.1 INTRODUCTION

Inelastic electron tunnelling spectroscopy deals exclusively with a Stokes' process in which a tunnelling electron gives up a quantum of energy to the ground vibrational state of an adsorbed molecule. However, equation 17, (Appendix) shows that the opposite, anti-Stokes' process (where an adsorbed species in an excited vibrational and/or electronic state gives a quantum of energy to the tunnelling electron), will also occur. The Stokes' process is however

favoured in I.E.T.S. because tunnelling experiments take place at 4.2 K or lower in order to reduce thermal broadening effects. At such temperatures nearly all the adsorbed molecules will be in their ground vibrational state consequently only the Stokes' process will operate.

However consider what will happen if the electron interacts with a molecule in an excited state and gains energy. We would expect to see extra structure in the I-V characteristic caused by the electrons increased energy.

(The idea is similar to photosensitive tunnelling and inelastic resonant(two-step) tunnelling processes (146, 147, 148, 149, 150). In photosensitive tunnelling (146, 150) a change in the I-V characteristic of a gold-doped gallium arsenide tunnel diode occurs when the junction is illuminated with light of an energy greater than or equal to the bandgap energy. (See Figure 6.1.1).

The extra conduction being due to the excitation of the gold atoms by the incident radiation).

The idea proposed here is to use a form of anti-Stokes' (inelastic) electron tunnelling in the hope of being able to study the higher vibrational and electronic states of adsorbate species which would not be possible to study by normal inelastic electron tunnelling spectro-

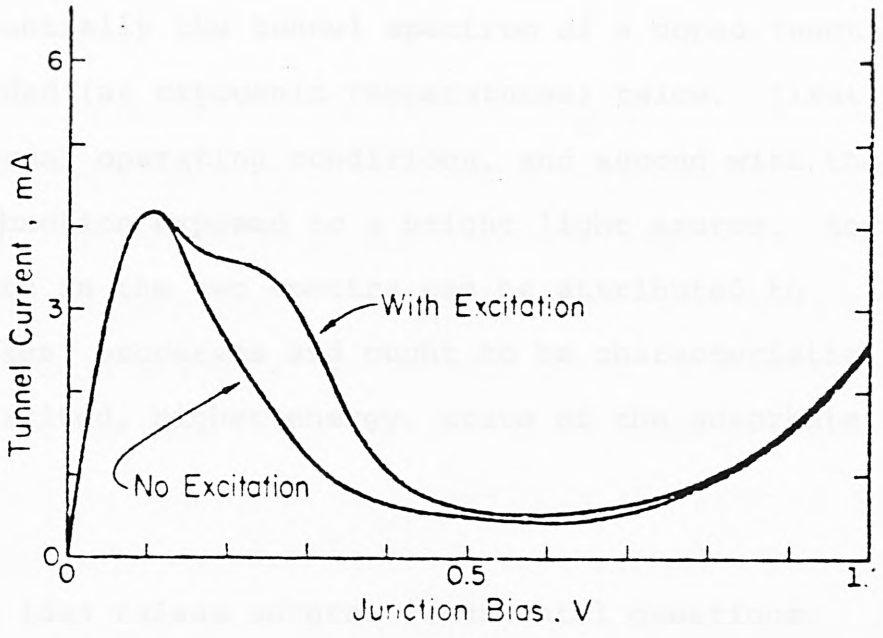

Figure 6.1.1. I-Vcharacteristic of a GaAs tunnel diode at 77K. Lower curve labelled 'no excitation' shows characteristic obtained by sweeping bias from 0 to 1 volt. Upper characteristic is obtained by sweeping bias voltage whilst irradiating the junction with band-gap or higher radiation. (After reference 146).

scopy due to the dielectric breakdown of the insulator at ≃2.2 volts (18,000 cm^{-1}).

Essentially the tunnel spectrum of a doped junction is recorded (at cryogenic temperatures) twice. First under normal operating conditions, and second with the tunnel junction exposed to a bright light source. Any difference in the two spectra can be attributed to anti-Stokes' processes and ought to be characteristic of the excited, higher energy, state of the adsorbate species.

The idea raises several fundamental questions:

1. Will the incident radiation react with the adsorbed molecular species in the tunnel junctions, (or even with the insulator itself)?

2. Assuming the incident radiation will excite the adsorbate, will the surface adsorbate concentration be great enough to yield an observable result?

3. What will the lifetime of the excited states be?

4. If the lifetime of the excited state is short, will the intensity of the incident radiation

be sufficient to maintain enough molecules in an excited state to participate in an electron-molecule interaction?

References 146 to 150 inclusive support the idea that incident light will interact with a tunnel junction and that the magnitude of such an interaction is large enough to be observed. Holonyak et al.(146) have reported the lifetime of the excited state of gold atom impurities in GaAs tunnel diodes is at least one hour. Although this situation is not exactly the same as for the experiment proposed here, it does suggest that the excited lifetime will be appreciable.(Similar conclusions can be drawn from the uncertainty principle which can be stated in the form:

$$(\text{linewidth, W}) \times (\text{lifetime}) \simeq \hbar$$

from which it can be seen that the lifetime of the state will be large if its width is small. When deriving the expression for the linewidth due to thermal and modulation voltage broadening, all workers assume the natural linewidth to be negligible(32, 47) which suggests that the lifetime will be appreciable).

6.2 EXPERIMENTAL CONSIDERATIONS

There are two major experimental requirements:

1. The tunnel junction must have a suitably translucent upper (or lower) electrode in order to allow the incident radiation to reach the adsorbate.

2. The junction must be housed in a cryostat assembly with viewing ports which are transparent to the wavelength of exciting radiation being used.

6.2.1 THE TRANSLUCENT UPPER ELECTRODE

Tsang and Kirtley have reported the use of a translucent silver upper electrode in Aluminium-Aluminium oxide-Silver tunnel junctions for studying anomalous surface enhanced molecular Raman scattering (151, 152). (It is worth noting that Tsang and Kirtley obtained strong surface enhanced Raman spectra (S.E.R.S) from the tunnel junction: this answers questions 1 and 2 in Section 6.1:- that incident radiation will interact with the adsorbed species; and an absorption effect is observable (by S.E.R.S.). Strangely enough, whilst the two papers (151 and 152) present results from S.E.R.S and L.E.I.T. (light emission from inelastic tunnelling) no mention is made of any anti-Stokes' electron tunnelling (A.S.E.T.) pbenomena). The upper electrode used by Tsang and Kirtley was 20 to 30 nanometers thick with a reported transmittance of 0.4 to 0.5.

Attempts to evaporate translucent conductive silver electrodes on glass substrates by carefully controlling the evaporation process were successful, however tunnel junctions made with translucent silver upper electrodes all had zero resistance. The same was true for experiment with gold as a top electrode. The only difference in fabrication procedure between the junctions used for the work here and those of Tsang and Kirtley(151), was that Tsang and Kirtley cooled the junction down to 77 K before depositing the upper electrode. It was not possible to accomplish this using the vacuum system described earlier (Section 2.1.1), which was probably the reason for junction failure.

As a last resort, lead was used for the translucent upper electrode. Eventually evaporating conditions were standardised enough to allow a 60% success rate. Photograph 21 shows a translucent electrode alongside a normal thickness electrode (the electrodes were photographed on graph paper with 1 mm squares). The resistance of a typical electrode was of the order of several tens of ohms: however since it was intended to use the junction at 4.2 K, the upper electrode would be in a superconducting state with zero resistance.

The first tunnel junctions with a translucent upper electrode were spin-doped with p-xylene and had resistances in the range 500 to 5000 ohms. The junctions were made on

20 mm square glass microscope slides for three reasons:

(1) In order to fit into the cryostat (described below).

(2) So the final transmittance of the upper electrode could be qualitatively controlled during deposition in a visual manner. (this would not have been necessary except that the control of the resistance heated evaporation source was very crude and did not lend itself to quantitative control.

(3) Thin films deposited on the printed circuit board substrate were found to be discontinuous due to the rough surface.

Electrical connections for the two electrodes were painted onto the glass slide prior to junction fabrication with conductive silver paint ("Electrodag").

6.2.2 THE CRYOSTAT

A cross-section of the cryostat assembly is shown in Figure 6.2.1 and 6.2.2. The sample holder is made from copper. The spring clips which hold the junction in place are made of phosphor bronze and also serve to make two electrical connections to the junction. When

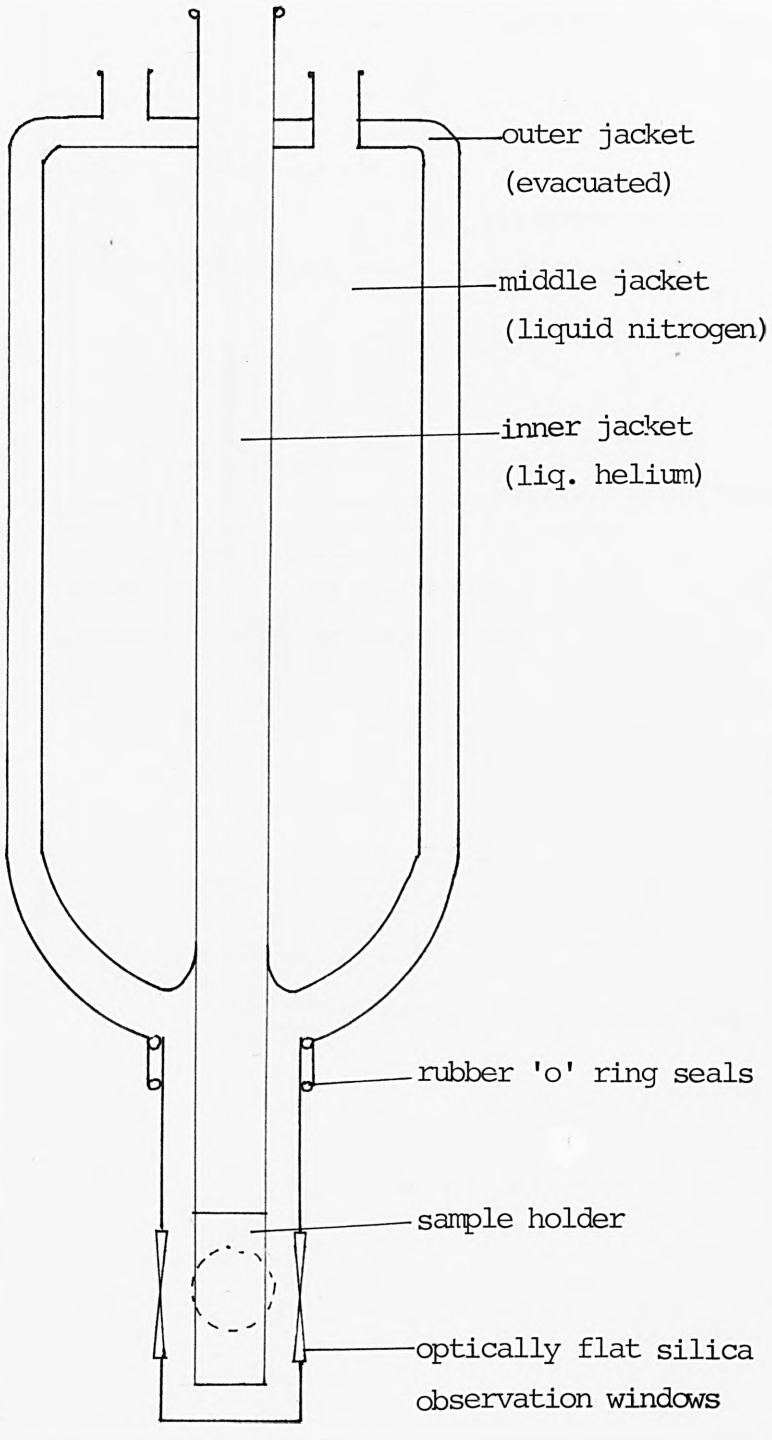

Figure 6.2.1. Cross-section of the cryostat assembly used for a.s.e.t. experiments.

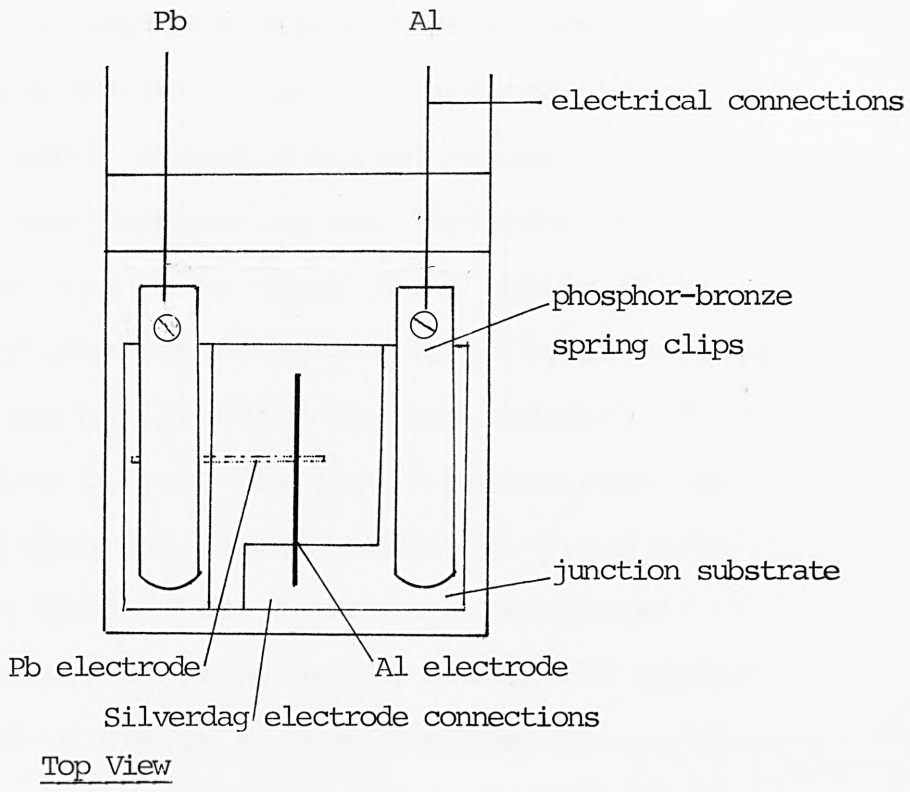

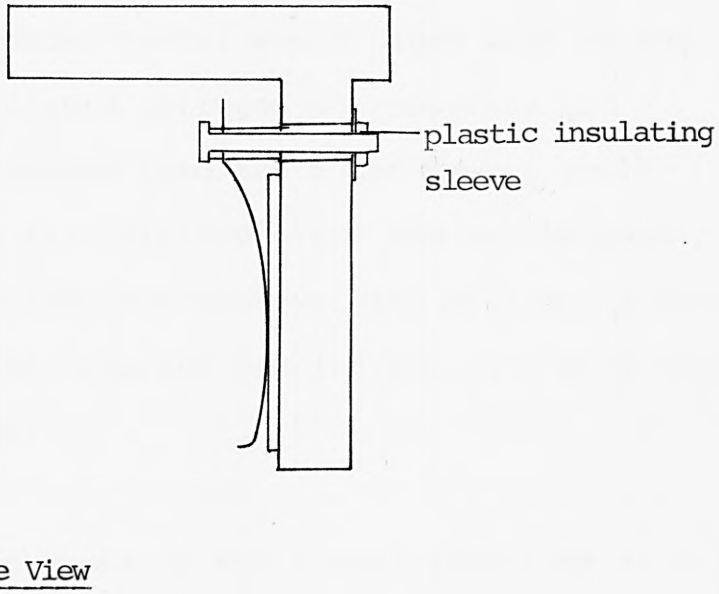

Figure 6.2.2. Close-up of sample holder.

the outer shield (which contains four silica windows) is in place and the outer jacket evacuated the cryostat becomes essentially a double-walled vacuum flask. Originally it was intended to run junctions at liquid helium temperatures: the inner jacket being filled with liquid helium, the outer one with liquid nitrogen. However this was not possible for two reasons: Firstly, it was difficult to pump the liquid helium from the storage dewar into the cryostat without an ice plug forming at the base of the inner cryostat jacket. Secondly at temperatures below ∿70 Kelvin the rubber 'O' rings used to create an airtight seal on the observations windows would contract and leak. This caused the vacuum in the outer jacket to deteriorate as air was sucked into it. This had two results: the resulting warming up of the outer jacket would cause some of the helium vapour and liquid nitrogen to evaporate and secondly, the air sucked into the outer jacket would condense making it more difficult for the vacuum pump to remove. Re-sealing the windows with silicone rubber produced the same disasterous results but at a much lower temperature (∿45 K).

Any further attempts to run tunnel junctions at 4.2 K in the cryostat had to be called off due to the unsuitability of the equipment. Therefore the tunnel spectra had to be run at 77K: the cryostat worked perfectly well at this temperature. Even so, some effect ought to be visible at

77 K, since several impurity-assisted tunnelling experiments were successfully performed at this temperature(146, 148).

6.3 RESULTS

Originally the final aim was to use a tuneable light source, select one bias voltage at which a conductance change could be observed, and then sweep the frequency of the light source and observe how the conductance changed as a function of the wavelength of the incident radiation. The purpose of varying the incident radiations frequency was to selectively excite different vibrational states of the adsorbate species. However before this could be implemented a conductance change had to be observed.

The light source first used was a high intensity quartz-iodine lamp focused on the junction through one of the viewports in the cryostat.

Figure 6.3.1 shows one of the first results from the cryostat. The spectra were all recorded under the following conditions:

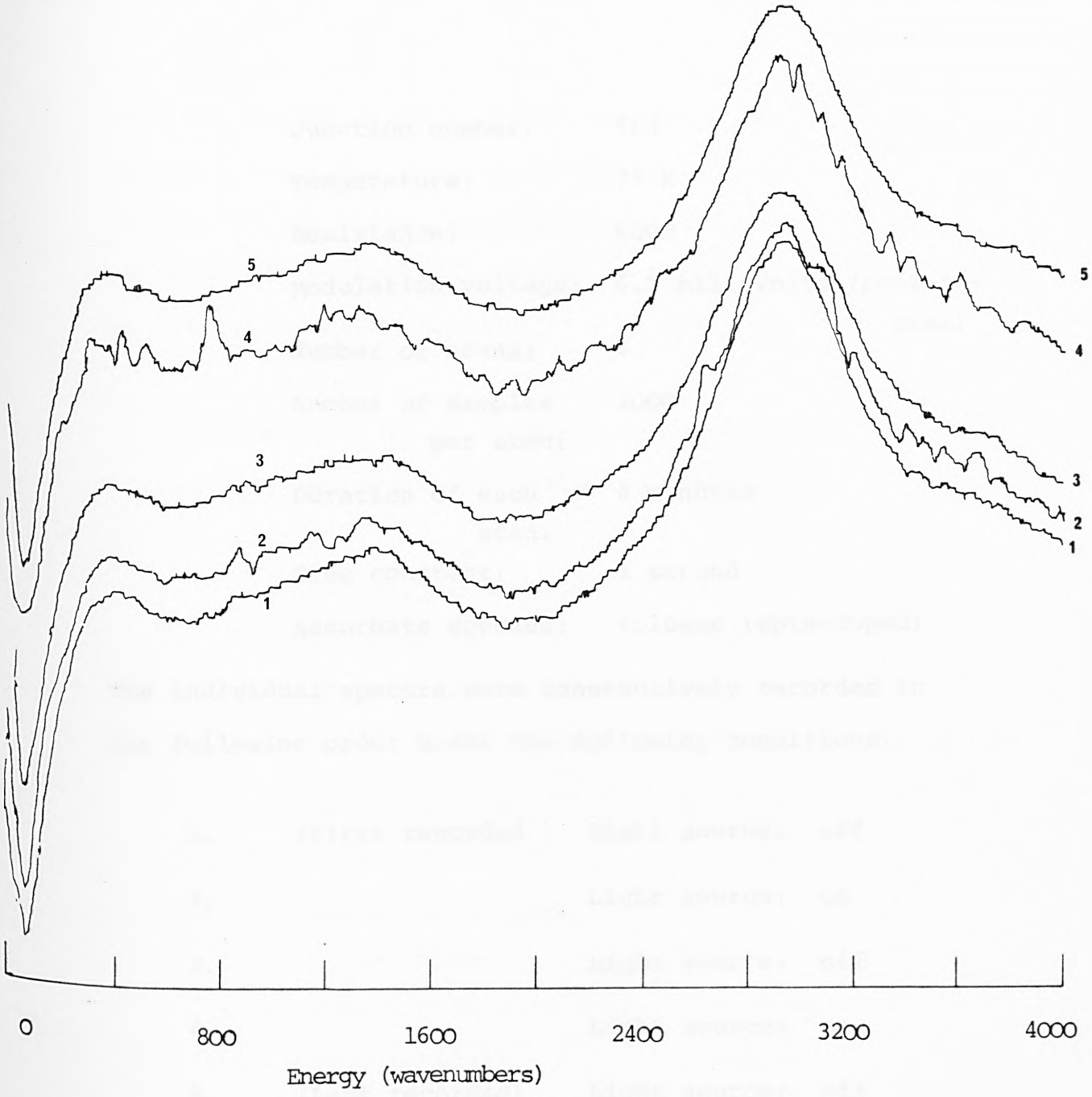

Figure 6.3.1. Tunnelling spectrum of toluene at 77K. Traces 1,3 & 5 are obtained with no excitation, traces 2 & 4 are obtained by irradiating the junction with light.

Junction number:	565
Temperature:	77 K
Resistance:	600Ω
Modulation voltage:	6.5 millivolts (peak-to-peak)
Number of scans:	4
Number of samples per scan:	2000
Duration of each scan:	4 minutes
Time constant:	1 second
Adsorbate species:	toluene (spin-doped)

The individual spectra were consecutively recorded in the following order under the following conditions:

1.	(First recorded)	Light source: off
2.		Light source: on
3.		Light source: off
4.		Light source: on
5.	(Last recorded)	Light source: off

The most obvious difference between the two sorts of spectra is that those recorded with the light source on seem much "noisier" and extra structure is visible at $\sim$800 cm^{-1}, 2600 cm^{-1} and from 3000 to 4000 cm^{-1}. This structure is not visible in any of the spectra recorded with the light off. The time between removing the light source at the end of one recording and the

next (non-irradiated) spectrum was approximately five minutes; since the noise and extra structure are not visible in the following, non-irradiated, spectrum the lifetime of any excited species in the junction must be less than five minutes.

Figure 6.3.2 is a repeat of the above experiment. It was recorded under the following conditions:

Junction number:	562
Temperature:	77 K
Resistance:	800Ω
Modulation voltage:	6 millivolts (peak-to-peak)
Number of scans (per spectrum):	4
Number of samples per scan:	2000
Duration of each scan:	5 minutes
Time constant:	1 second
Absorbate species:	toluene (spin-doped)

(1)	(Recorded first)	Light source	off
(2)		Light source	on
(3)		Light source	off
(4)		Light source	on
(5)	(Recorded last)	Light source	off

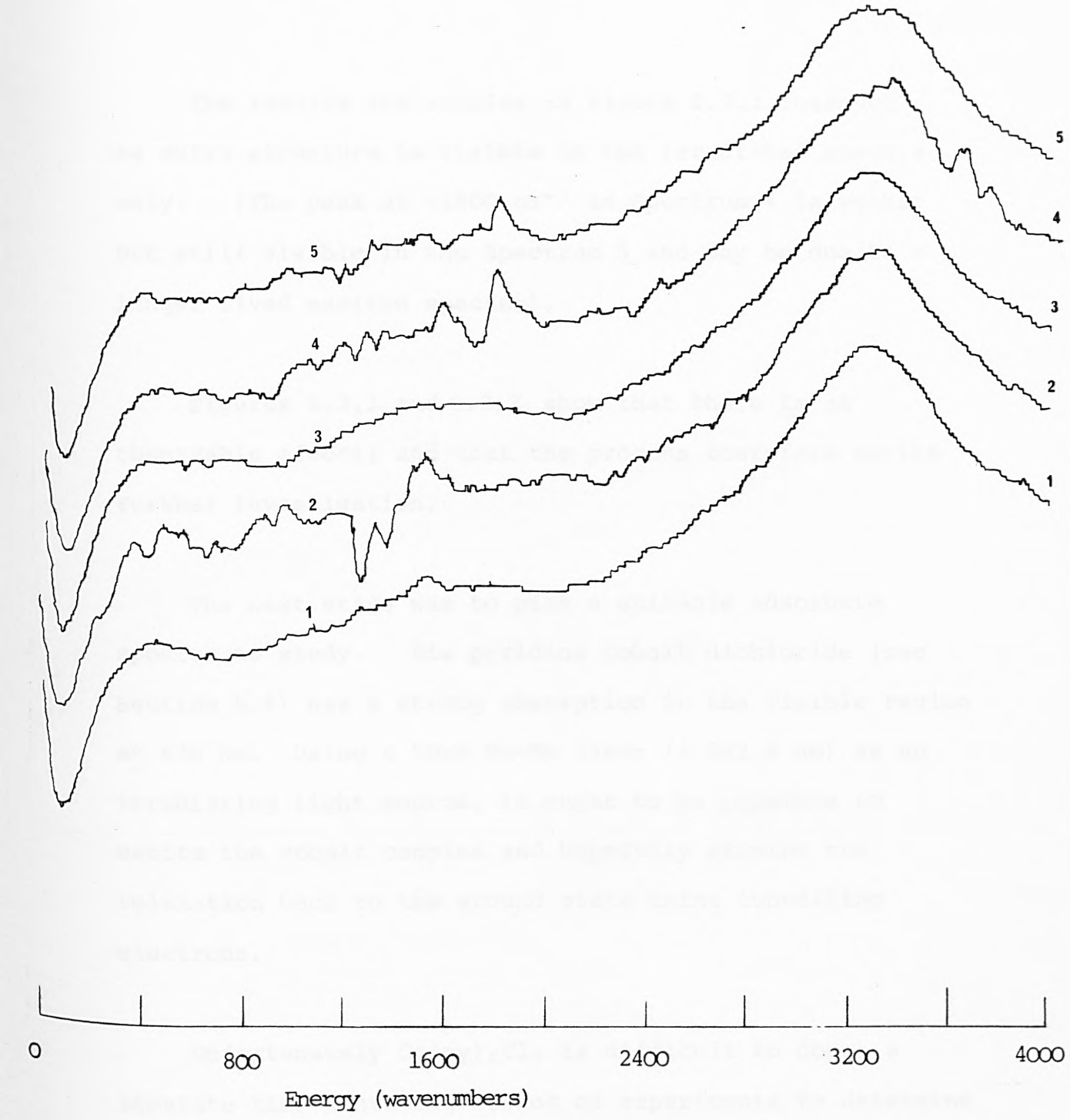

Figure 6.3.2. Tunnelling spectrum of toluene at 77K showing the reproducibility of the effect shown in Figure 6.3.1.

The results are similar to Figure 6.3.1 inasmuch as extra structure is visible in the irradiated spectra only. (The peak at $\sim$1800 cm^{-1} in Spectrum 4 is weaker but still visible in the Spectrum 5 and may be due to a longer lived excited species).

Figures 6.3.1 and 6.3.2. show that there is an observable effect; and that the process therefore merits further investigation.

The next stage was to pick a suitable adsorbate species to study. Bis pyridine cobalt dichloride (see Section 5.9) has a strong absorption in the visible region at 630 nm. Using a 50mW He-Ne laser (λ 632.8 nm) as an irradiating light source, it ought to be possible to excite the cobalt complex and hopefully examine the relaxation back to the ground state using tunnelling electrons.

Unfortunately $Co(py)_2Cl_2$ is difficult to dope; a separate time consuming series of experiments to determine the correct doping parameters had to be carried out before any further A.S.E.T. experiments could be conducted. (The results of the doping experiments are given in Section 5.9).

One of the early A.S.E.T. results using a penetration-doped solution of bis pyridine cobalt dichloride in benzene is shown in Figure 6.3.3. It was recorded under the follow-

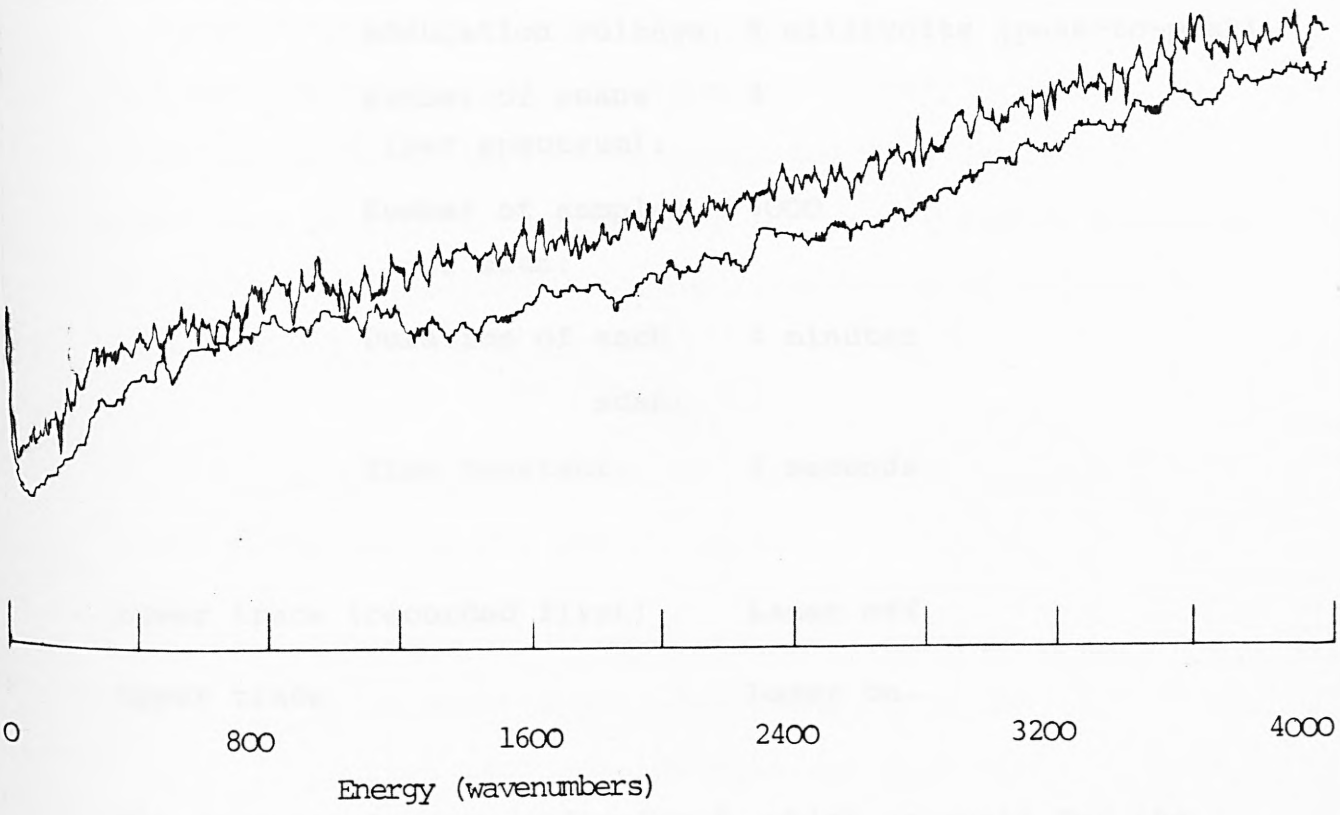

Figure 6.3.3. Tunneling spectrum of $Co(py)_2Cl_2$ in dilute solution.
Upper trace: laser on
Lower trace: laser off.

ing conditions:-

Junction number:	679
Temperature:	77 K
Resistance:	4.3kΩ
Modulation voltage:	8 millivolts (peak-to-peak)
Number of scans (per spectrum):	4
Number of samples per scan:	4000
Duration of each scan:	4 minutes
Time constant:	3 seconds

Lower trace (recorded first)	Laser off.
Upper trace	Laser on.

The junction is very under-doped, which accounts for the very small peaks in the lower spectrum. The only observable effect upon irradiating the sample is a very marked increase in noise: no extra peaks are observed however since there is very little of the cobalt complex adsorbed on the surface to be excited, this is not surprising.

However, the presence of excess noise generated in the irradiated junction is closely connected with the tunnelling mechanisms that are operating(149), and can

be associated with tunnelling via an excited state of the adsorbate species.

6.4 CONCLUSION

Unfortunately no more time was available to pursue the anti-Stokes' tunnelling experiments any further. However the preliminary results presented in Section 6.3 do show that an effect is occurring and that a deeper in-depth investigation(starting with the irradiation of $Co(py)_2Cl_2$) is essential.

Two major modifications to the existing equipment would prove useful for future work:

(1) a better evaporation source to enable translucent upper electrodes to be deposited with greater ease and reproducibility. (This could be achieved by fitting a shutter in between the evaporation source and collimating slit).

(2) use of a more efficient cryostat to enable spectra to be run at liquid helium temperatures.

Additionally, a tuneable laser source would be useful for selectively exciting an adsorbate species at a given

frequency. (This would also allow the surface Raman spectra to be taken simultaneously and compared with the anti-Stokes' electron tunnelling spectra).

I hope that the ideas and results presented in this Chapter will provoke discussion and stimulate new work.

CHAPTER 7 FUTURE WORK AND CONCLUSION

7.1 FUTURE WORK

Inelastic Electron Tunnelling Spectroscopy is still a relatively recent discovery: the scope for future work is therefore almost boundless. However there are several areas in which the technique is currently developing.

Theory: The theories presented in Chapter 1 are essentially single-bodied in nature. Although the Golden Rule and Transfer Hamiltonian (T.H.) Formalisms give a generalisation as to the nature of the inelastic interaction occurring in the barrier, recent work on bias asymmetry has shown that the T.H. theory cannot accommodate such an asymmetry(156): as a result several many-bodied theories have also been recently proposed(153, 154, 155). However only further experimental investigation will decide which theory is most applicable. (Two review articles discussing recent theories are 157 and 158).

Instrumentation: The differential bridge of Colley and Hansma(133) which attempts to subtract an undoped spectrum from a doped one by analogue means, will prove very useful for examining absorptions within the phonon region where unambiguous identification is not always possible (See Section 5.9).

Computerisation: The development of computerised spectro-

meters (discussed in Chapter 4) is probably the fastest developing field: some of the important features such as multiple scanning and data storage, are featured in the spectrometer built for this project. Such advances are not only applicable to I.E.T.S. but also to all forms of spectroscopy.

More directly, there are several suggestions for improvements and future work which are applicable to the equipment used and techniques developed in this thesis. They are:

1. Substrate Roughness

A thorough in-depth investigation into the nature of the printed circuit board substrate and the relationship of surface roughness to penetration doping.

2. Junction Preparation Chamber

The modification of the junction preparation chamber to allow the manufacture of several (more than ten) junctions per substrate. This could be achieved by using a cross-hatching network of lead and aluminium strips as shown in Figure 7.1.1. Multiple electrical connections to the probe assembly could be made

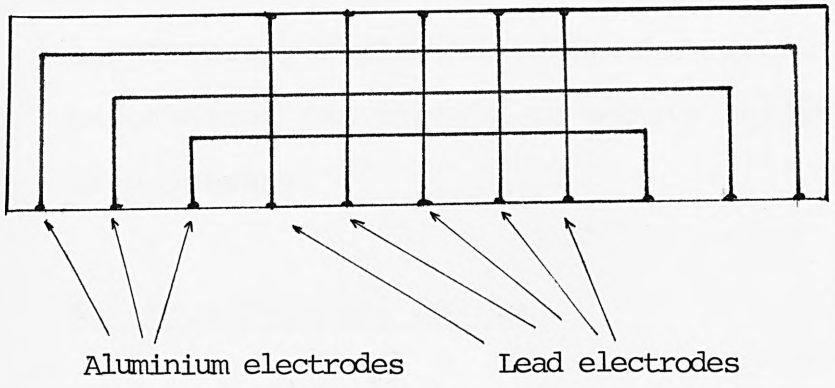

Figure7.1.1. Proposed multiple junction assenbly.

using a multi-way printed circuit-board edge connector similar to that used by Oxley et al. (159).

3. Silica Substrates

The reinstatement of silica or Pyrex-glass substrates is highly desirable at least for spectroscopy where the surface orientation information (as opposed to purely analytical) is necessary.

4. Four-Terminal Devices

The use of FOUR-terminal junctions (See Figure 7.1.1). The problem of lead resistance could be overcome if current conductors of large enough cross-section are used.

5. Computerisation

Many improvements in the computerised spectrometer would be advantageous. In general hardware modifications are limited only by lack of funds; whereas software modifications and innovations are limited only by the researchers' ability to write programmes (in both high and low level languages). Several suggestions are

listed as follows; those marked * are considered especially important.

5.1 Hardware

I) Ortec-Brookdeal now manufacture a lock-in amplifier which is fully microprocessor-controllable via a 16-way I.E.E.E. data bus. Use of such a lock-in together with the spectrometer and P.E.T. microprocessor would enable the entire spectrometer, including the lock-in amplifier to become fully automated; control of the spectrometer and the lock-in being handled by the microprocessor.

II) If multiple junctions were made using a modified preparation chamber (2 above), then selection of the appropriate junction could be made using a network of solid-state C.M.O.S. switches, which are directly controllable by a microprocessor.

5.2 Software

*I) Deconvolution

Deconvolution of an i.e.t. spectrum, using a Fast Fourier Transform (F.F.T.) algorithm, would prove extremely valuable for separating closely-spaced peaks, for removing the effects of thermal broadening and modulation broadening, and increasing resolution in general. Several deconvolution programmes are already available (see, Blass,Carrington: Bibliography), and an in-depth investigation of relevant literature and deconvolution in general, has been made(160, 161, 162, 163, 164). The results from this work suggest that deconvolution is not only feasible but highly desirable.

II) Difference spectrum

Use of a substraction programme to remove a standard undoped junction spectrum from a sample spectrum.

III) Data base

Using the large amount of storage space

available on the Honeywell to build up a library of standard tunnel spectra.

IV) Time-dependent spectra

With the present spectrometer software it is not possible to sample the variation in intensity of a particular peak with respect to time. Time dependence (at a fixed bias voltage) of a particular absorption would be useful for kinetic studies and junction ageing effects and essential if anti Stokes' phenomena are to be investigated.

*V) Noise removal

The inclusion of noise in spectra transmitted to and fro from the Pet to the Honeywell, via the telpehone lines is still a problem. Real-time noise removal at either the Honeywell or the Pet is impractical since this would involve modifying the Honeywell software (The "Topet" and "Frompet" commands), at the Pet software stored in the E.P.R.O.M. supplied with the interface. A much simpler programme would call each data point from the received

file, check it and decided if it was noise, and then re-store it in another file. This sort of programme could be easily implemented on the Pet in machine code using the assembler software available, and on the Honeywell in FORTRAN.

VI) Anti-Stokes' Electron Tunnelling (A.S.E.T.)

See Chapter 6, Section 6.4.

7.2 Conclusion

Perhaps one of the most important early findings of this research concerned the use of the turbomolecular pump in providing a contamination-free vacuum. Although turbomolecular pumps have been commercially available long before the discovery of inelastic electron tunnelling spectroscopy, the custom-built vacuum system used in this research is the first reported tunnel junction preparation chamber to utilise a turbomolecular pump. The advantages over conventional diffusion-pumped preparation chambers, can be seen from the published spectra already in the literature - all of which contain hydrocarbon contamination due to large molecular weight pump oil. Even the published "blank" spectra contain small hydrocarbon peaks. No such contamination is evident in the spectra produced using the turbomolecular-pumped vacuum system. Additionally,

I.E.T.S. is extremely sensitive to hydrocarbons and thus acts as its own hydrocarbon contamination monitor of the junction preparation chamber. It has, for example, proved fruitless to fit a quadrople mass spectrometer onto the preparation chamber in order to try and detect any contamination(106). I.E.T.S. is much more sensitive than mass spectrometry and the fact that no contamination has been detected on tunnel spectra is proof that the junction preparation chamber does not become contaminated as a result of any backstreaming from the turbomolecular pump.

An investigation of the upper electrode in a successful attempt to elucidate the mechanisms of electrode penetration doping revealed a number of large pores in the upper electrode through which the dopant molecules are thought to pass. The same investigation unexpectedly revealed the rough nature of the aluminium and lead electrodes. This roughness was found to be due to the use of a printed circuit board (p.c.b.) substrate which has a rough surface. As a result of these discoveries it has been possible to build up an accurate picture of the junction which has been deposited on a p.c.b. substrate. Using this picture it has been possible to plausibly explain junction instabilities and boosting which are believed to be due to the presence of metallic bridges forming between the electrodes through the oxide (see Section 3.5).

The rough surface nature of the oxide combined with electrode penetration doping suggested that the adsorbate species would not be in a single orientation, but disordered with several orientations present on the one oxide surface. Furthermore, this would imply that it would not be possible to deduce a unique surface orientation of the adlayer on the basis of the geometrical selection rules (Section 1.9) alone. These ideas, which apply to tunnel spectra run using a printed circuit board substrate, and/or have been doped by the electrode penetration doping method, were proved to be correct when the spectra in Chapter 5 were analysed. The spectra (all of which were run on junctions deposited on a printed circuit board substrate, and hence had a rough oxide surface) were found to yield ambiguous information concerning the geometry of the adsorbate. The only possible conclusions that could be reached from the results in Chapter 5 was that the adsorbate molecules had several different orientations on the alumina surface. This situation is exemplified by the results for penetration doped benzene in Section 5.8. Bogatina(58) calculated the active frequencies in a tunnel spectrum for two extreme orientations of the molecule: one with the molecular plane parallel to the metal-dielectric interface, the other with the molecular plane perpendicular to the metal-dielectric interface (see Table 5.8.3). When the results from the tunnel spectrum of benzene were compared with these theoretical results (Table 5.8.2), vibrational frequencies characteristic of <u>both</u> orientations were found

in the tunnel spectrum. This supports the idea that there are at least two molecular orientations present in the insulator as a direct consequence of using a rough substrate and penetration doping the junction.

The construction of the computerised spectrometer to enable real-time signal averaging has proved extremely useful not only for the reduction of low frequency (1/f) noise, but also as a spectrum storage and processing facility. However unless the noise analysis and the calculation of optimum time constants and scan times presented in Section 4.1 are fully understood and *correctly implemented by future spectrometer operators*, then the computerised spectrometer will not be working under optimum operating conditions for signal averaging which will result in the loss of detail in tunnel spectra.

The addition of the Pet/Honeywell interface will enable faster data processing, and the use of larger programmes such as third derivative calculations, peak integration and deconvolution. The increased storage space will enable a database of tunnel spectra to be formed.

Finally, the invention and preliminary investigation of anti-Stokes' electron tunnelling as a means to study the higher vibrational and electronic states of adsorbed species without dielectric breakdown problems, has yielded some very promising early results (Section 6.3), despite

the lack of stuiable equipment. These results indicate that alternative conduction mechanisms, via excited states of impurities (dopant molecules) within the barrier, are operative when the junction is irradiated with an external light source. It is hoped that despite the severe experimental difficulties, research into this effect will continue to eventually provide a new form of electron tunnelling spectroscopy.

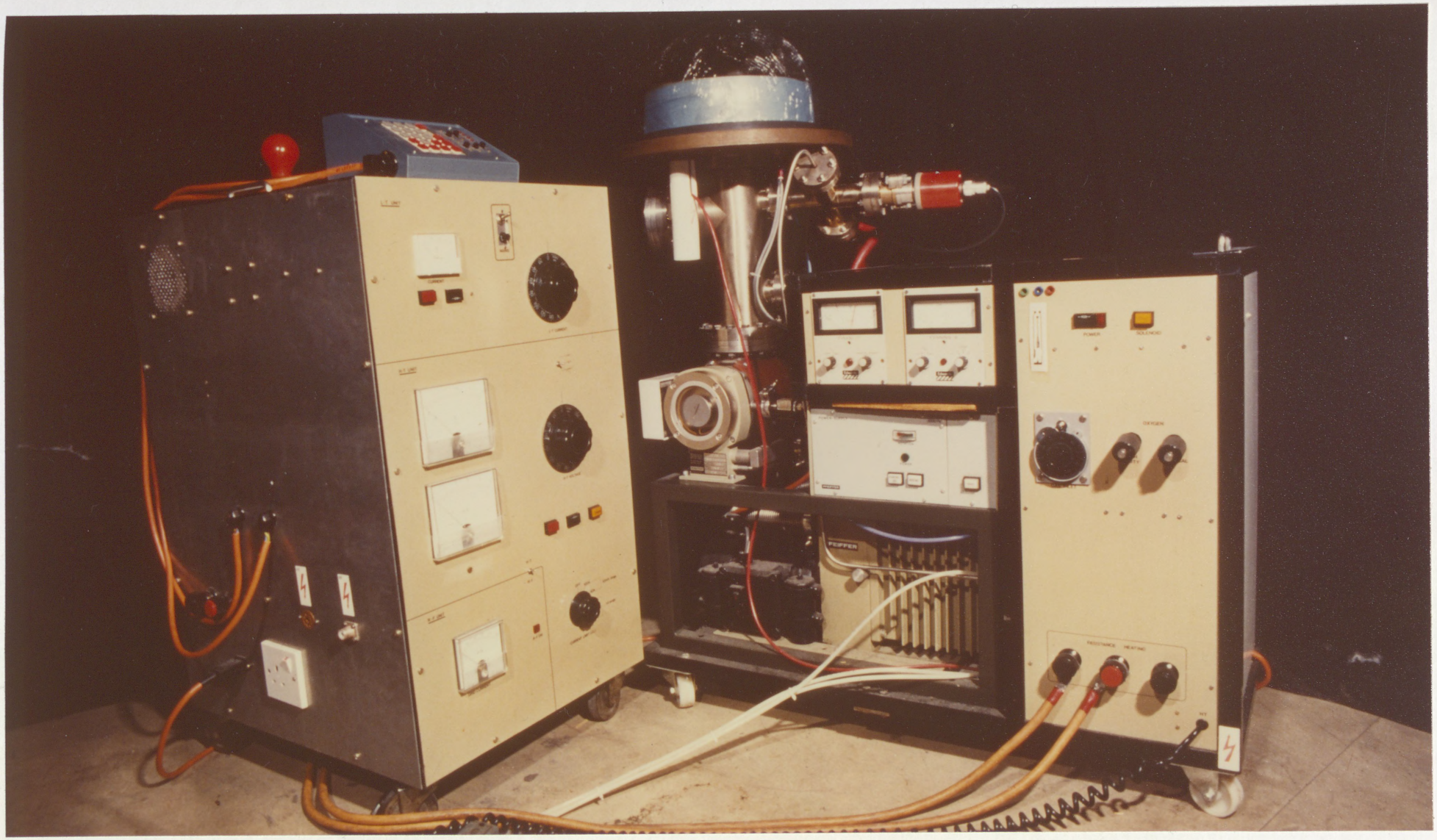

1. General view of vacuum system and power supply

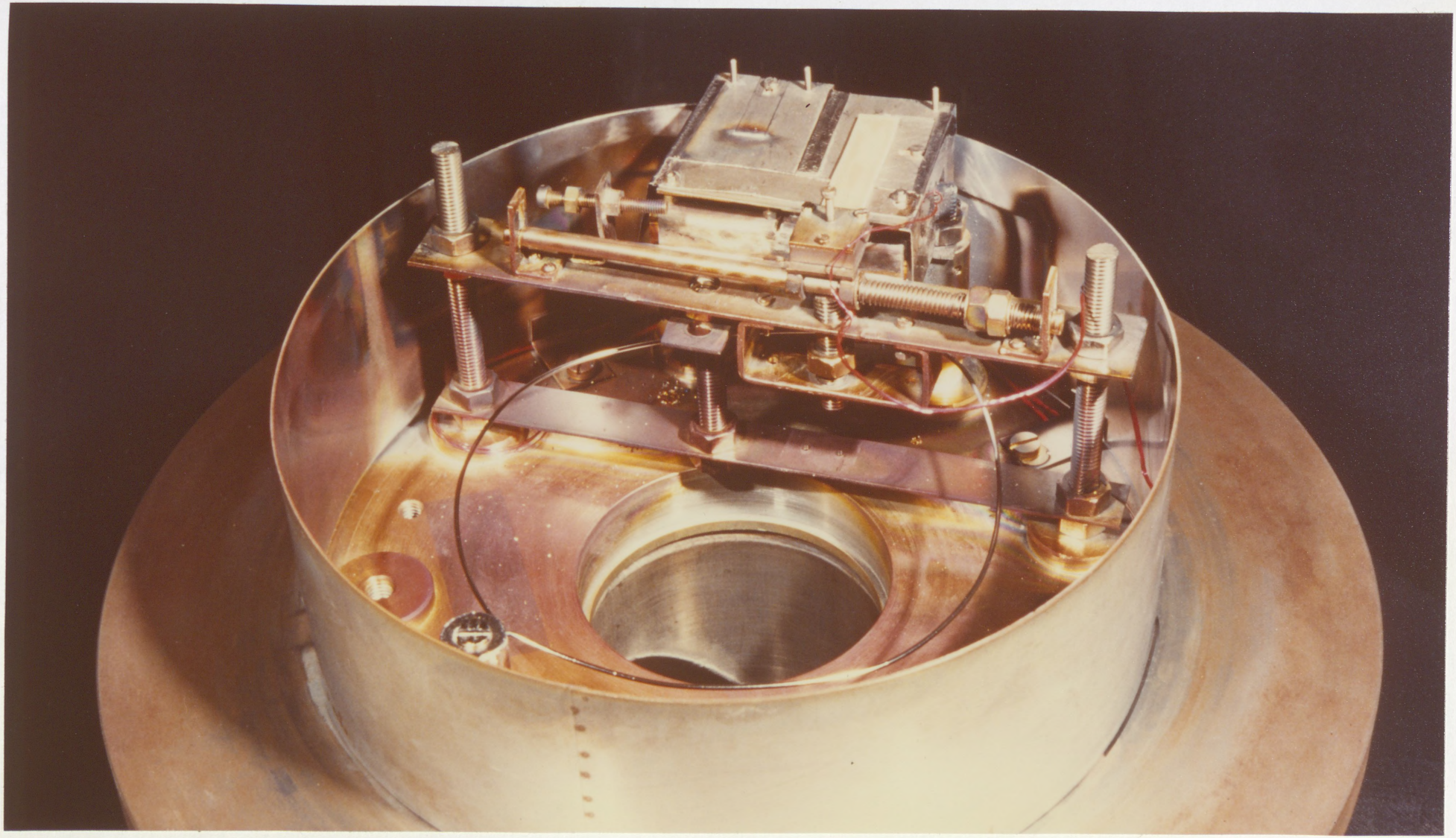

2. Close-up of preparation chamber

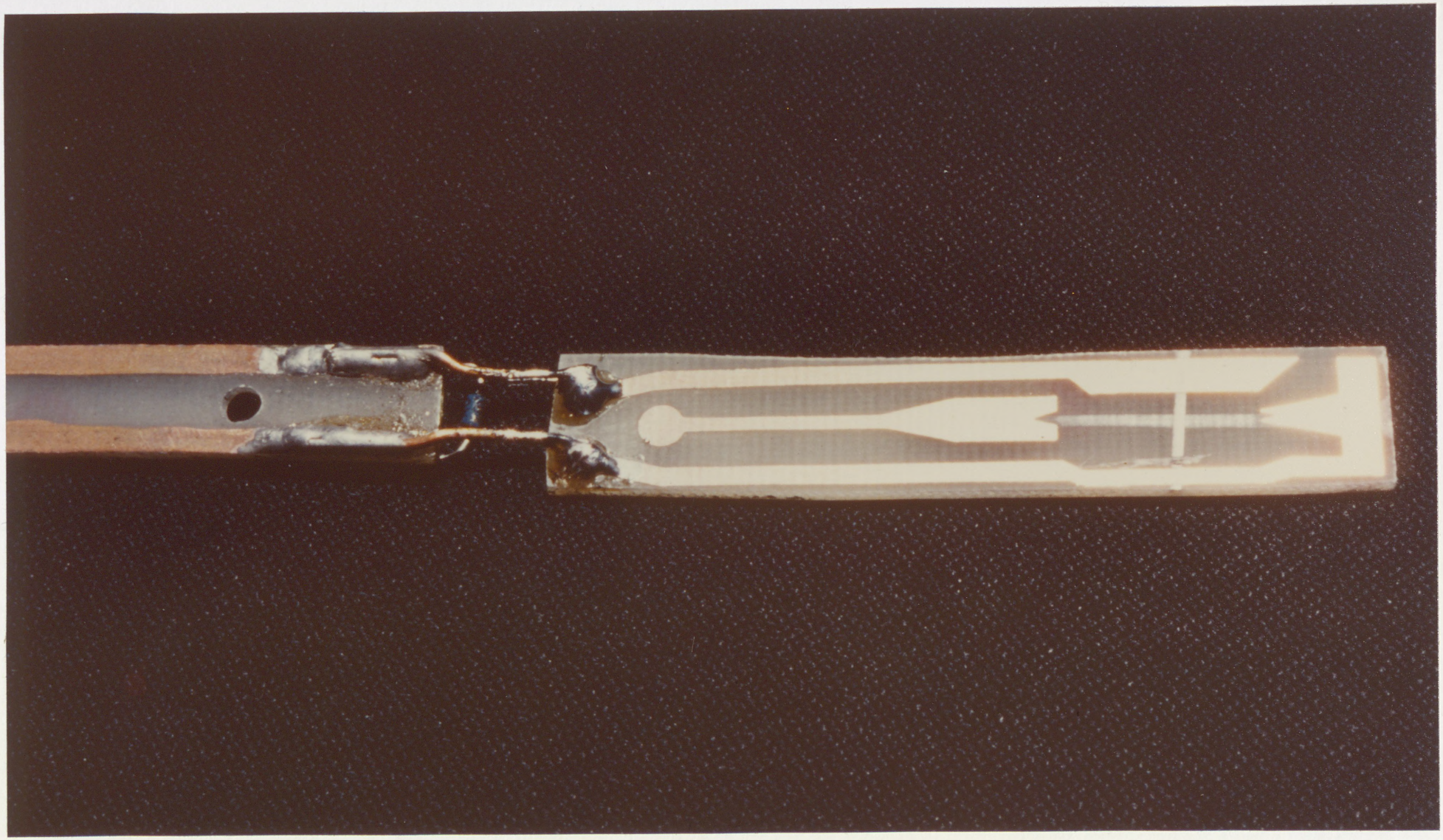

3. View of tunnel junction soldered to the probe assembly

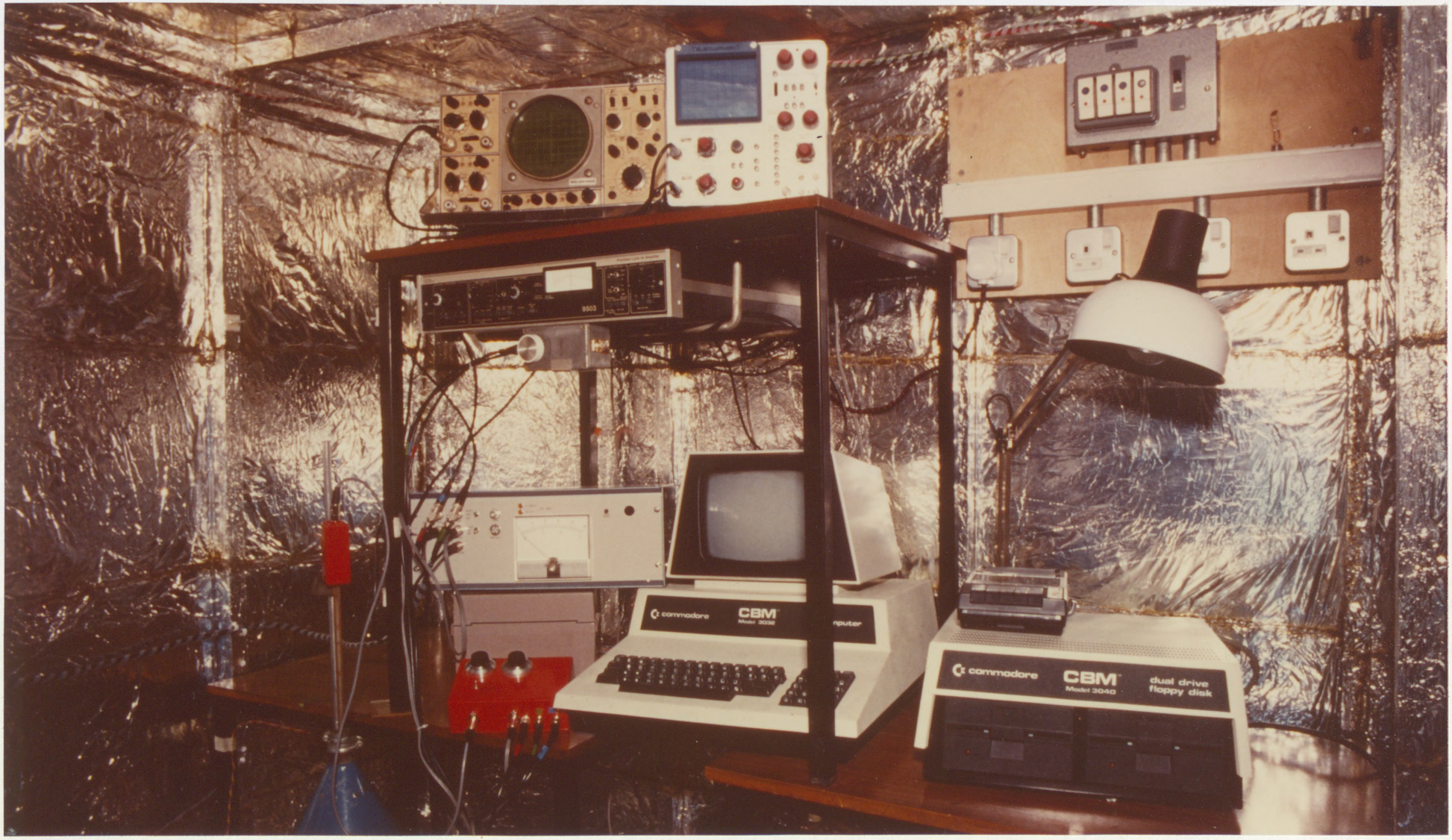

4. General View of the Computerised Spectrometer.

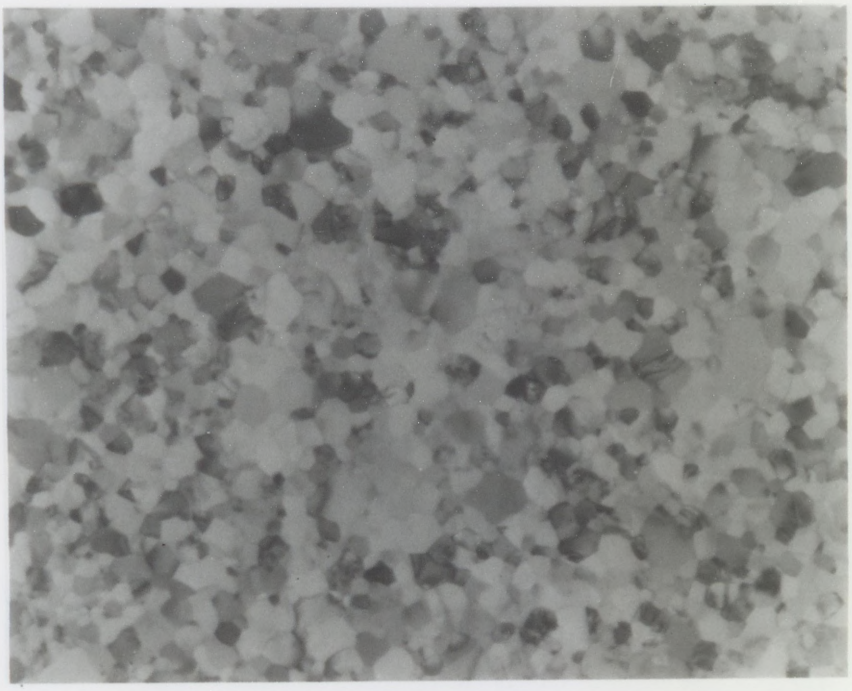

5. Aluminium Electrode : Thin region

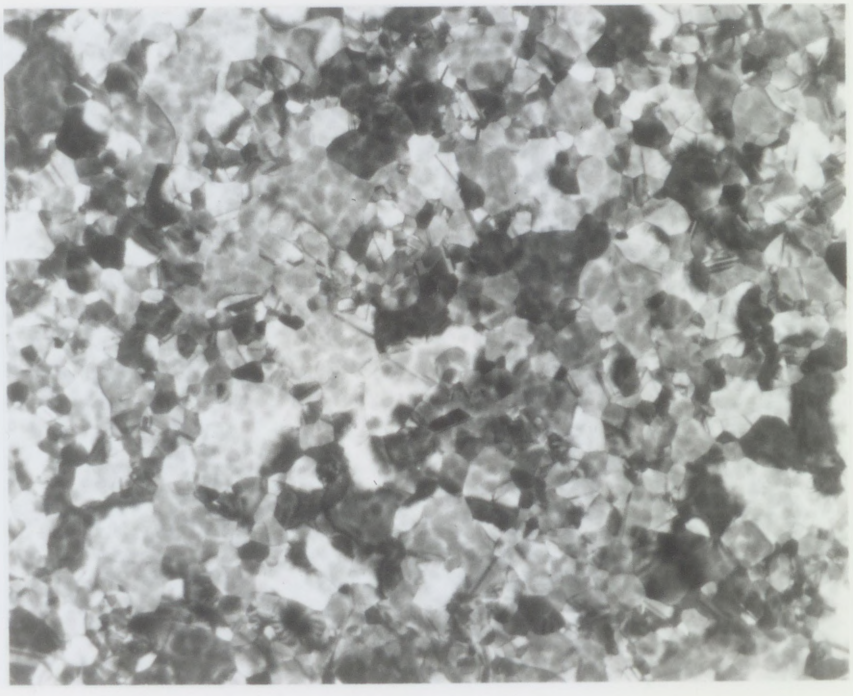

6. Aluminium Electrode : Medium thickness region

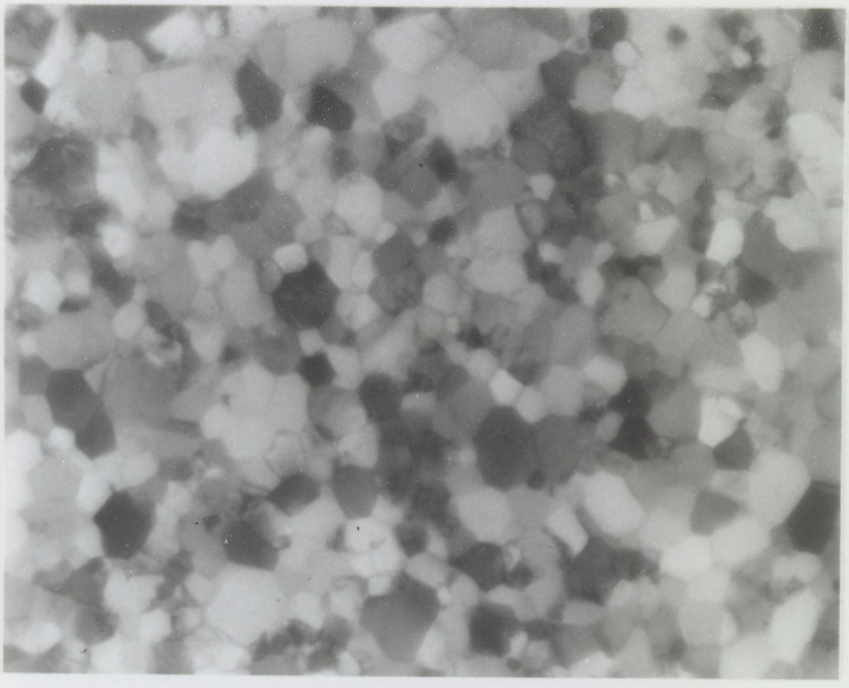

7. Aluminium Electrode : Thickest region

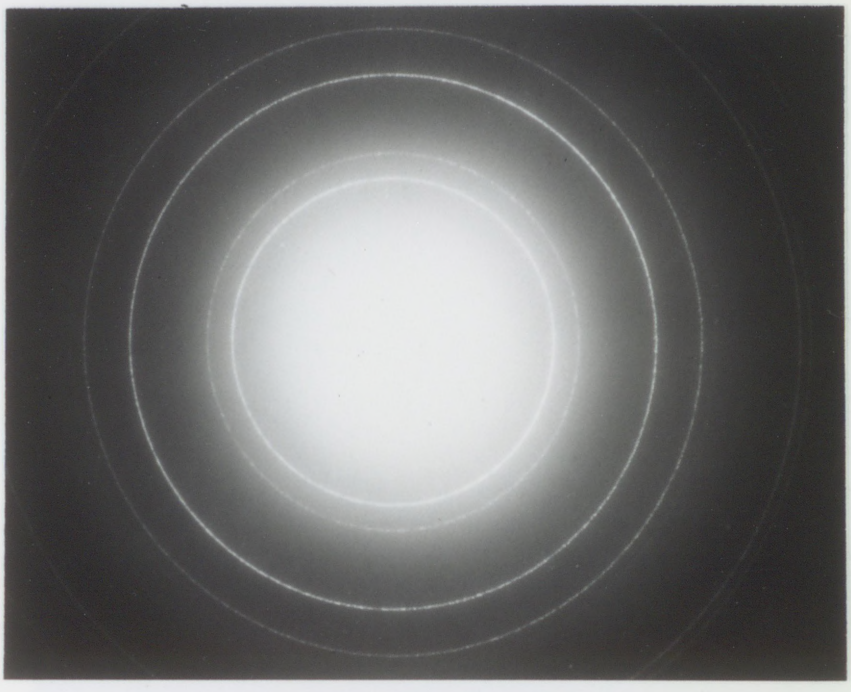

8. Aluminium Electrode : Electron diffraction
Specimen untilted

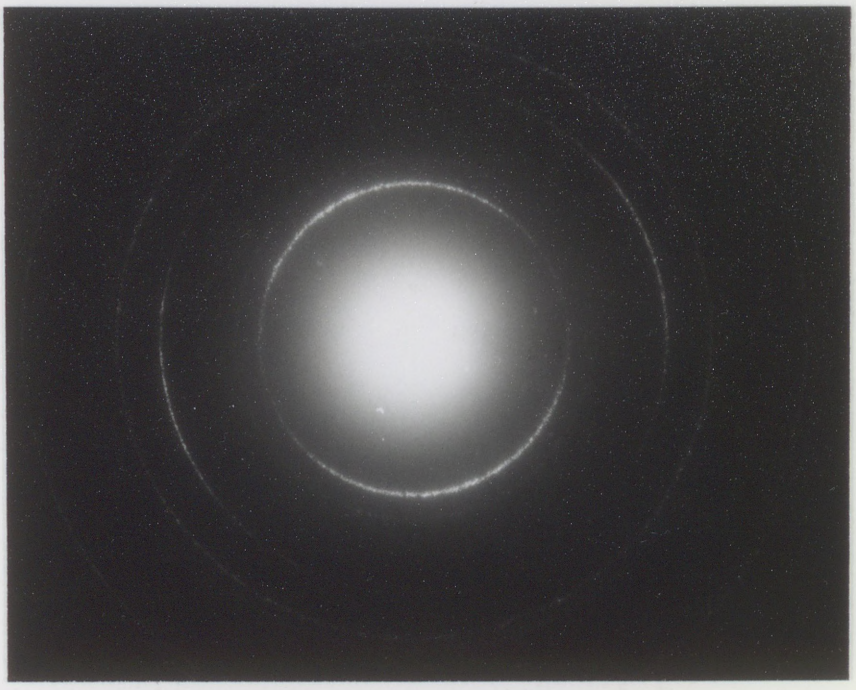

9. Aluminium Electrode : Electron diffraction
Specimen tilted 25°

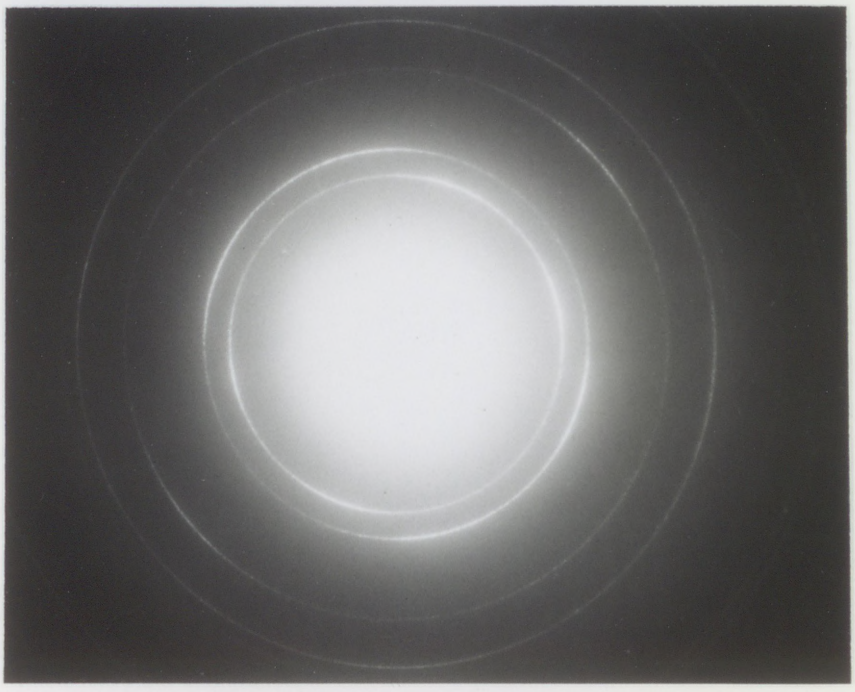

10. Aluminium Electrode : Electron diffraction
Specimen tilted 35·26°

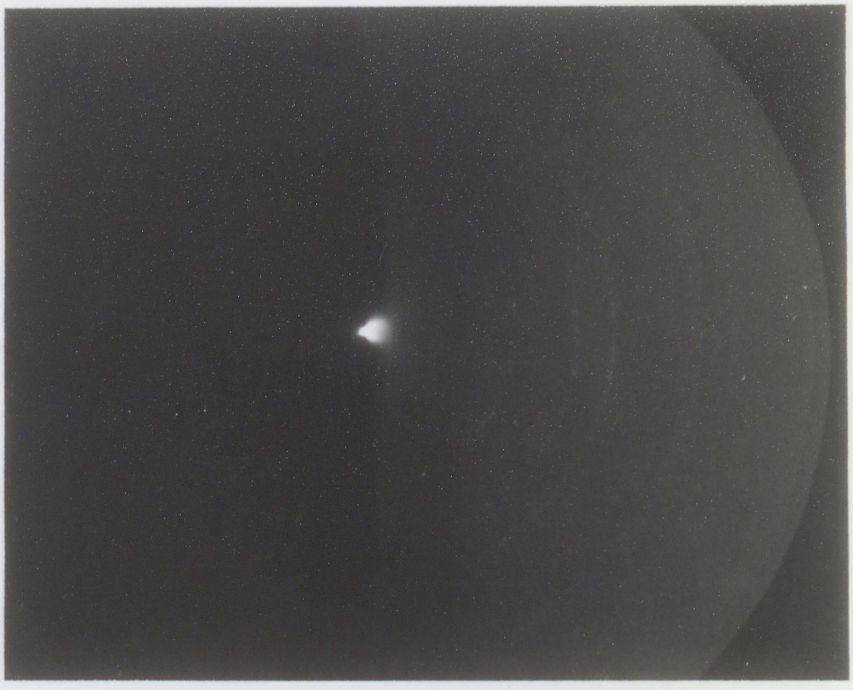

11.Reflection electron diffraction of Aluminium electrode

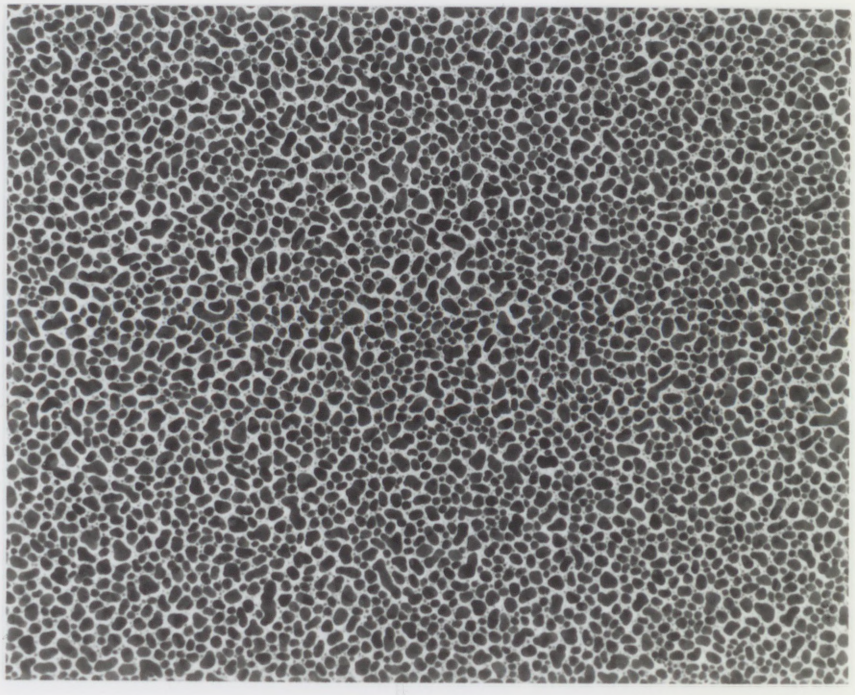

12.Lead Electrode. Thinnest region showing small islands

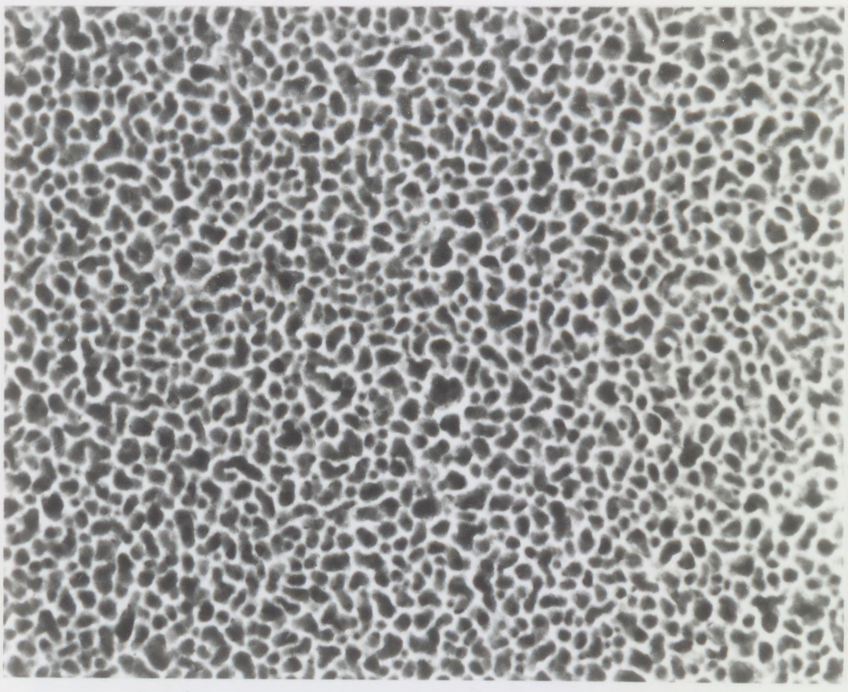

13. Lead Electrode Thicker region
Note increase in island size.

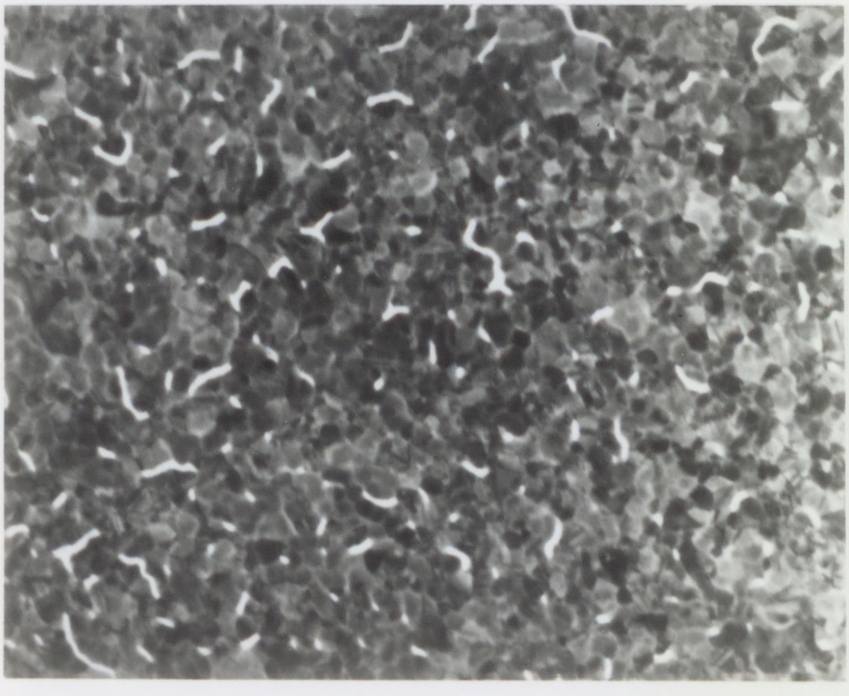

14. Lead Electrode Thickest crystalline region

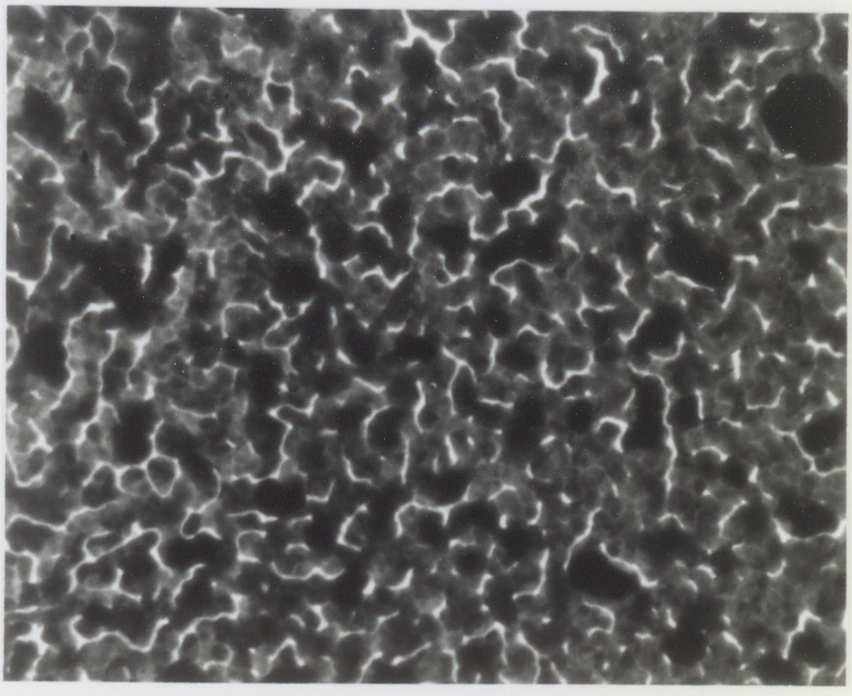

15. Lead Electrode showing pores in thinnest continuous region

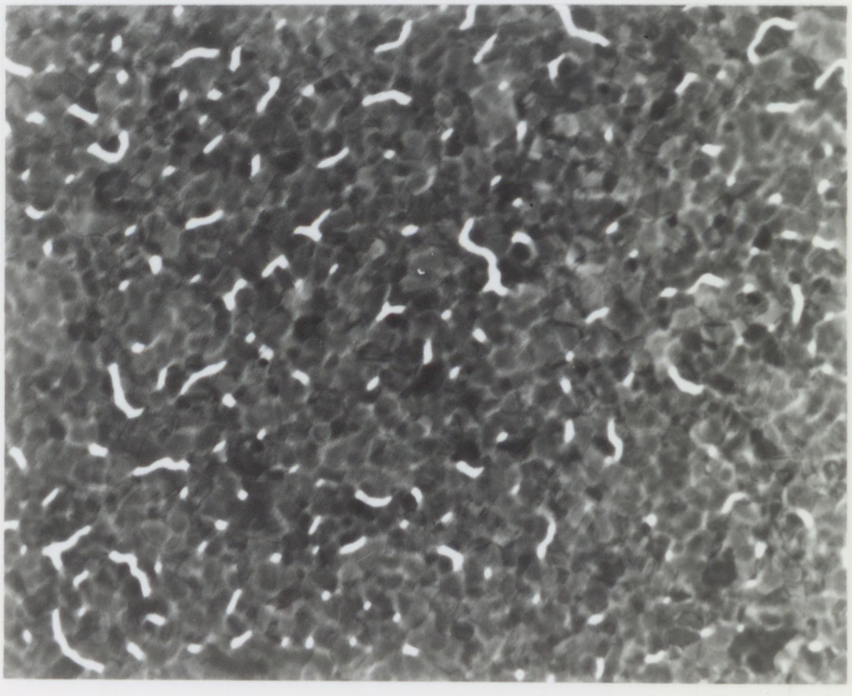

16. Lead Electrode showing pores in thicker region (see also photograph 14)

17. S.E.M of aluminium electrode on printed circuit board substrate

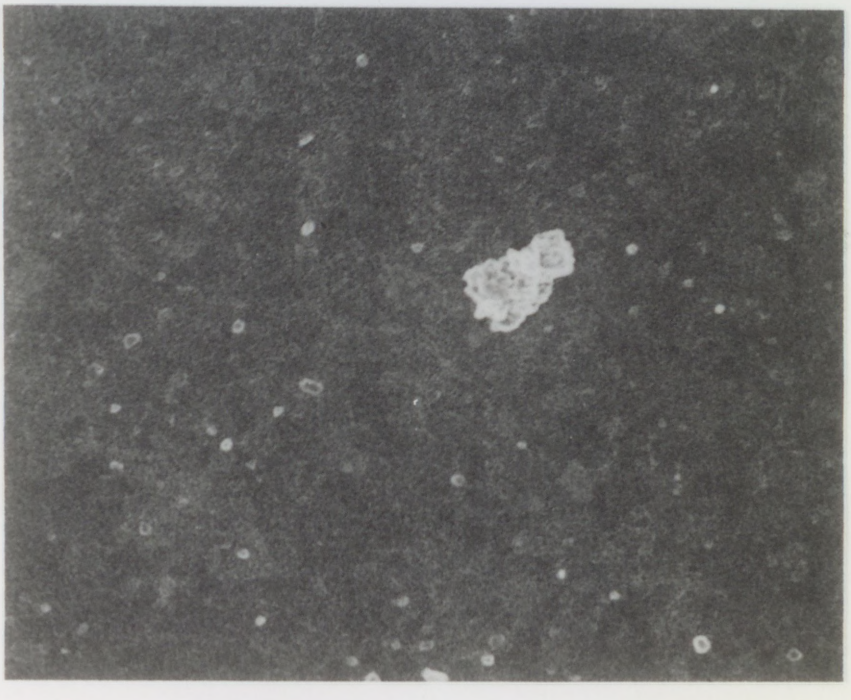

18.S.E.M of aluminium electrode on glass substrate

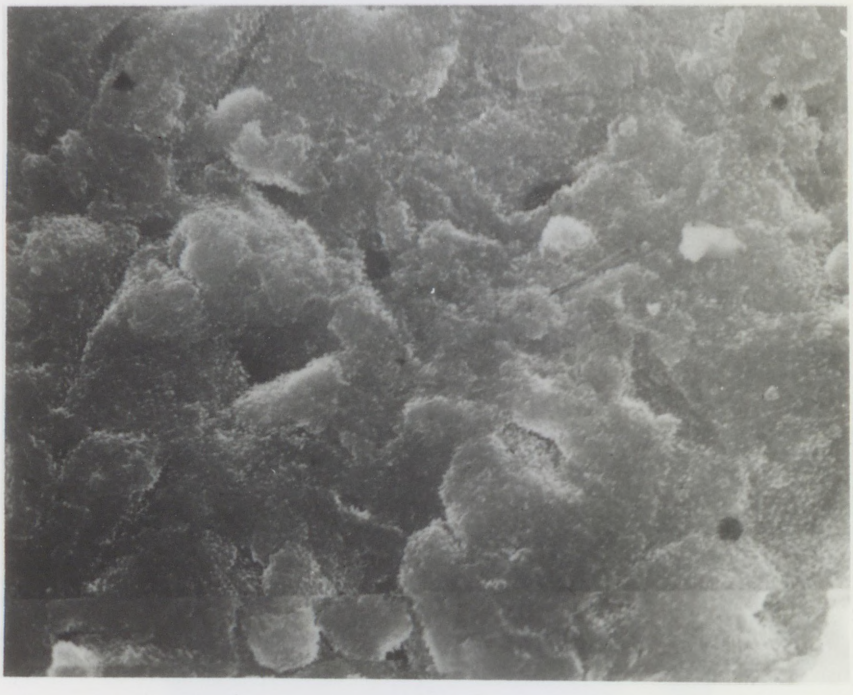

19. S.E.M of lead electrode (over aluminium) on printed circuit board substrate

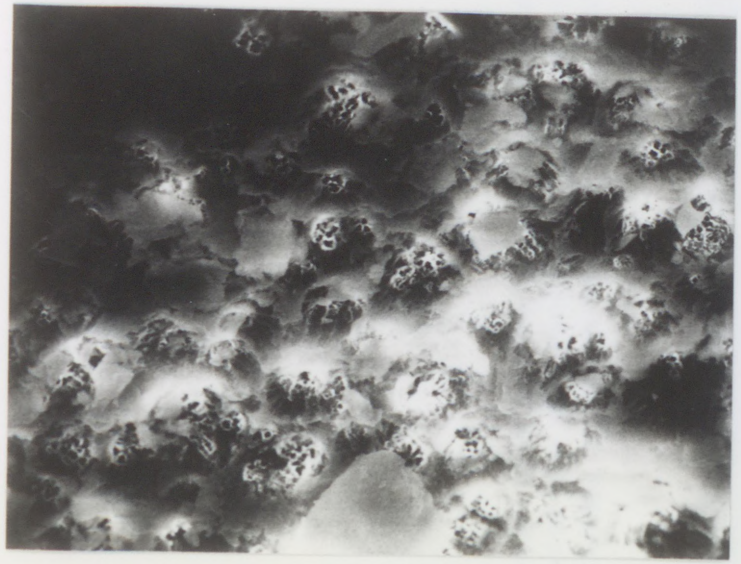

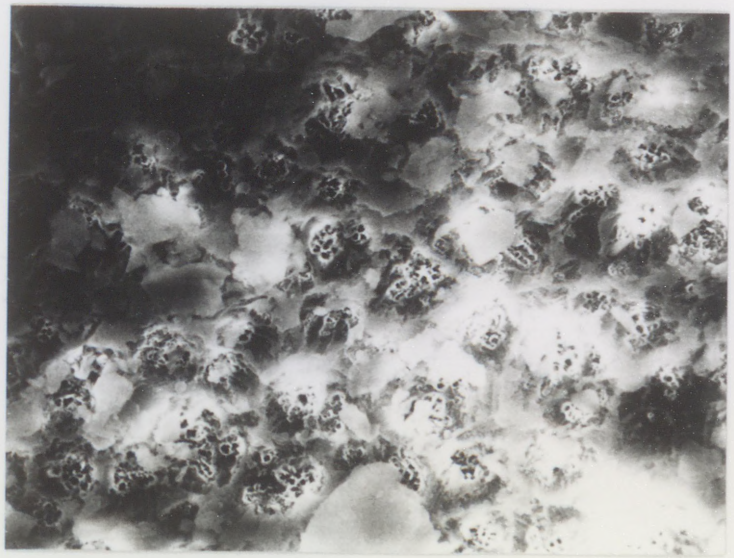

20. S.E.M of printed circuit board surface (Stereo - Pair)

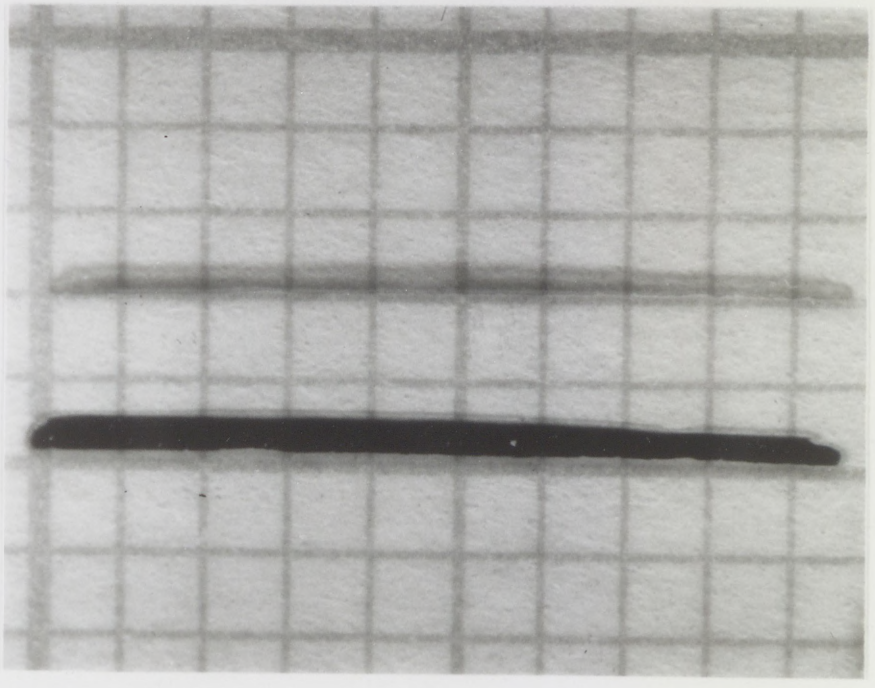

21. Translucent lead electrode shown in comparison with normal electrode. Both electrodes are deposited on pyrex glass (photographed over a 1m.m square grid)

APPENDIX 1

Derivation of Fermi's "Golden Rule"

Fermi's "Golden Rule" can be derived from time-dependent perturbation theory.

At t = 0 we assume the system is in a state ψn such that:

$$\hat{H}_o \psi_n = E^o_n \psi n \qquad (1)$$

and furthermore we assume that the Hamiltonian of the system depends on time and can be expressed as:

$$\hat{H} = \hat{H}_o + \hat{W}(t) \qquad (2)$$

where in general $\hat{H}_o$ is simple and $\hat{W}(t)$ is small and can be regarded as a perturbation on $\hat{H}_o$.

We now use the time-dependent Schrödinger equation:

$$i\hbar \frac{\partial \psi}{\partial t} = \hat{H}\psi \qquad (3)$$

As ψn varies with time we can no longer measure with certainty E_n, and have to expand $\psi n \equiv \psi(x,t)$ at a later time. Using the E^o representation:

$$\psi(x,t) = \sum_k Ck(t)\ \psi k(X)\ e^{-iE^o_k t/\hbar} \qquad (4)$$

where $\psi_k(x)$ depends on x only,

$e^{-iE_k^o t/\hbar}$ depends on t only,

and $|Cm(t)|^2$ is the probability of finding the system in state ψm.

Substituting (2) and (4) into (3) gives

$$\sum_{k=1}^{\infty} \left\{ i\hbar \dot{C}k(t)\psi k \; e^{-iE_k^o t/\hbar} + Ck(t)E_k^o \psi_k e^{-iE_k^o t/\hbar} \right\} \qquad (5)$$

$$= \sum_{k=1}^{\infty} \left\{ Ck(t) \; E_k^o \psi_k \; e^{-iE_k^o t/\hbar} + Ck(t)\hat{W}(t)\psi_k e^{-iE_x^o t/\hbar} \right\}$$

where $\dot{}$ represents differentiation with respect to time

multiplying through from the left-hand side by $\psi_m^* e^{iE_m^o t/\hbar}$ and integrating over all space (5) becomes:

$$i\hbar \int_{-\infty}^{\infty} \sum_{k=1}^{\infty} \dot{C}k(t)\psi_m^* e^{iE_m^o t/\hbar} \; \psi_k e^{-iE_k^o t/\hbar} \; dV$$

$$= \int_{-\infty}^{\infty} \sum_{k=1}^{\infty} Ck(t)\psi_m^* e^{iE_m^o t/\hbar} \; \hat{W}\psi_k e^{-iE_n^o t/\hbar} \; dV \qquad (6)$$

since $$\int_{-\infty}^{\infty} \psi_m^* \; \hat{W}\psi_k \; dV \equiv Wmk \quad or <m|W|k> \qquad (7)$$

and $$\int_{-\infty}^{\infty} \psi_m^* \psi_k \; dV \equiv \delta mk \qquad (8)$$

we can substitute (7) and (8) into (6)

Thus for k=m

$$i\hbar \dot{C}m(t) = \sum_{k=1}^{\infty} Ck(t)\, Wmk\, e^{i\omega_{mk}t} \qquad (9)$$

where $\omega_{mk} = \dfrac{E_m^o - E_k^o}{\hbar}$, the Bohr angular frequency

(Equation (9) is still an exact solution to the Schrödinger equation).

In order to obtain $|Cm(t)|^2$ to calculate the probability of finding the system in state ψm, we must solve (9) for $Cm(t)$. However we have an infinite system and therefore cannot solve exactly. We now use perturbation theory and express $Ck(t)$ as a power series:

$$Ck(t) = C_k^{(0)}(t) + \lambda C_k^{(1)}(t) + \lambda^2 C_k^{(2)}(t) + \ldots \qquad (10)$$

and replace.

$$\hat{W} = \lambda \hat{W} \qquad (11)$$

where λ is a small constant between zero and one.

We now assume that at t=0 the system is in a definite state ψn with energy E_n^o.

i.e.

$$\left.\begin{array}{ll} Ck(0) = 1 & \text{if } k=n \\ Ck(0) = 0 & \text{if } k\neq n \end{array}\right\} \delta kn \qquad (12)$$

and hence

$$|Cn(o)|^2 = 1$$

which is just another way of stating that the system is all in state ψn at t=O.

Therefore $|Cm(t)|^2$ at time t is the probability of transition from the initial state ψn at t=O to a state ψm at t=t. To calculate Cm(t) equations (lO) and (ll) are substituted into (9) and coefficients of equal powers of λ are equated.

(9) becomes

$$i\hbar(\dot{C}k^{(0)} + \lambda\dot{C}k^{(1)} + \lambda^2\dot{C}k^{(2)} + ..) = \sum_{k=1}^{\infty} (Ck^{(0)} + \lambda Ck^{(1)} + \lambda^2 Ck^{(2)} + ..)\lambda Wmke^{i\omega_{mk}t} \quad (13)$$

For the zeroth order approximation (λ=O)

$$\dot{C}^{(0)}k = O$$

Which shows the zeroth order coefficients $Ck^{(0)}$ are constant in time. Their values are the initial values of the problem and specify the state of the system before the perturbation.

In our case we have assumed that the system is initially in a definite unperturbed state and that

$$C^{(o)}k = \delta_{kn}.$$

The first order approximation (λ=1) gives (remembering to substitute (12) for $C_k^{(0)}$:-

$$\dot{C}_m^{(1)}(t) = \sum_{k=1}^{\infty} W_{mk}(t)\, e^{i\omega_{mn}t}\, (i\hbar)^{-1} \qquad (14)$$

hence

$$C_m^{(1)} = \frac{1}{i\hbar}\int_0^t W_{nm}(\tau)\, e^{i\omega_{mn}\tau}\, d\tau \quad (\text{for } m\neq n) \qquad (15)$$

Hence it is possible to calculate the probability ($=|C_m|^2$) between one initial state ψ_n and <u>one</u> final state ψ_m of $E_m^o \simeq E_n^o$. i.e. if $\hat{W}$ is of finite duration the amplitude of a state $C_m (n\neq m)$ after $\hat{W}$ has disappeared is proportional to the time Fourier component of the matrix element of the perturbation between ψ_n and ψ_m that corresponds to an angular frequency ω_{mn}.

We can now apply (15) more directly to inelastic tunnelling by assuming that the perturbation $\hat{W}$ depends harmonically on time, or more specifically we can regard $\hat{W}$ as being due to a particular vibrational frequency of an adsorbed impurity molecule in the barrier itself. We assume that $W_{nm}(t)$ acts only whilst the electron is in the barrier which is equivalent to saying $W_{nm}(t)$ is turned on at time t=0 when the electron at the barrier edge first experiences $\hat{W}$, and off at t=t when the electron has tunnelled into the second electrode.

We also assume that we can separate $W_{mn}(t)$ thus:

$$Wnm(t) = \langle n|W(t)|m\rangle = 2\langle n|\hat{W}|m\rangle \sin \omega t'$$

$$= 2\,\hat{W}nm \sin \omega t \qquad (16)$$

where $\hat{W}nm$ is time independent and

ω is positive

Substituting (16) into (15) gives:

$$C_m^{(1)}(t \geq t_o) = \frac{-Wmn}{i\hbar}\left(\frac{e^{i(\omega_{mn}+\omega)to}-1}{\omega_{nm}+\omega} - \frac{e^{i(\omega_{mn}-\omega)to}-1}{\omega_{mn}-\omega}\right) \qquad (17)$$

This suggests that the amplitude of ψk is appreciable only when the denominator of either of the two terms is practically zero. The first term is important when:

$$\omega_{nm} \cong -\omega$$

$$\text{or } E_m \simeq E_n - \hbar\omega$$

and the second term is important when:

$$\omega_{nm} \simeq \omega$$

$$\text{or } E_m \simeq E_n + \hbar\omega$$

Hence the first order effect of a sinusoidal perturbation (i.e. a molecular vibration in the barrier) with angular

frequency ω is to transfer or receive from the system on which it acts a quantum of energy $\hbar\omega$. Thus when a tunnelling electron is perturbed by a vibrational state (of energy $\hbar\omega$) of a molecule in the barrier the effect is for the molecule to transfer or receive one quantum of energy. In the case where the junction is maintained near absolute zero and the molecules are nearly all in their ground vibrational state, the effect is for the molecule to receive a quantum of energy from the electron (a Stokes' process).

Superficially at least, this is the quantum mechanical justification for the inelastic tunnelling process. (This is connected with the reason for the factor 2 in equation (16) in defining the time-dependent matrix elment $\hat{W}_{mn}$. A perturbation which is proportional to sin ωt or cos ωt contains both time factors $e^{i\omega t}$ and $e^{-i\omega t}$ with equal amplitude. Since only the factor $e^{-i\omega t}$ leads to transfer of energy from the perturbation to the system, insertion of the factor 2 ensures that the physically important matrix element of the perturbation is W_{mn} and not half this quantity).

We are considering only the case for $E_n^o > E_m^o$ and hence only the second term in (17), and assume that ψn is a discrete state and ψm is a continuous set of dissociated states. Thus the first-order probability of finding the system in state ψm after the perturbation has been removed is

$$\left|C_m^{(1)}\right|^2 = \left(C_m^{(1)} . C_m^{(1)*}\right) \qquad \text{for } t > t_o$$

hence:

$$|C_{nm}|^2 = \left|\frac{W_{nm}}{\hbar^2}\right|^2 (e^{i(\omega_{mn}-\omega)to}-1)(e^{-i(\omega_{mn}-\omega)to}-1)$$

$$= \left|\frac{W_{nm}}{\hbar^2}\right|^2 \frac{4.\sin^2(\omega_{nm}-\omega)t_o/2}{(\omega_{nm}-\omega)^2} \qquad (18)$$

The fact that the term $(\sin^2 x)/x^2$ in (18) behaves as a delta function can be seen by plotting

$$\frac{\sin^2(\omega_{mn}-\omega)to/2}{(\omega_{mn}-\omega)^2} \quad \text{against } \omega_{mn}-\omega \qquad \text{(Figure 1)}$$

The height of the main peak increases in proportion to t_o^2 and its breadth decreases as t_o^{-1} ; so the area under the curve is proportional to t.

(In fact for large t_o we notice

$$\lim_{t_o \to \infty} \frac{1}{\pi} \frac{\sin^2 \alpha t_0}{\alpha^2} = \delta(x) \qquad (19)$$

Thus if there is a group of states ψn that have energies nearly equal to $E_m + \hbar\omega$ and for which W_{mn} is roughly independent of ψn then the probability of finding the system in one or other of these states is proportional to t_o.

Thus the delta function term in (18) expresses the

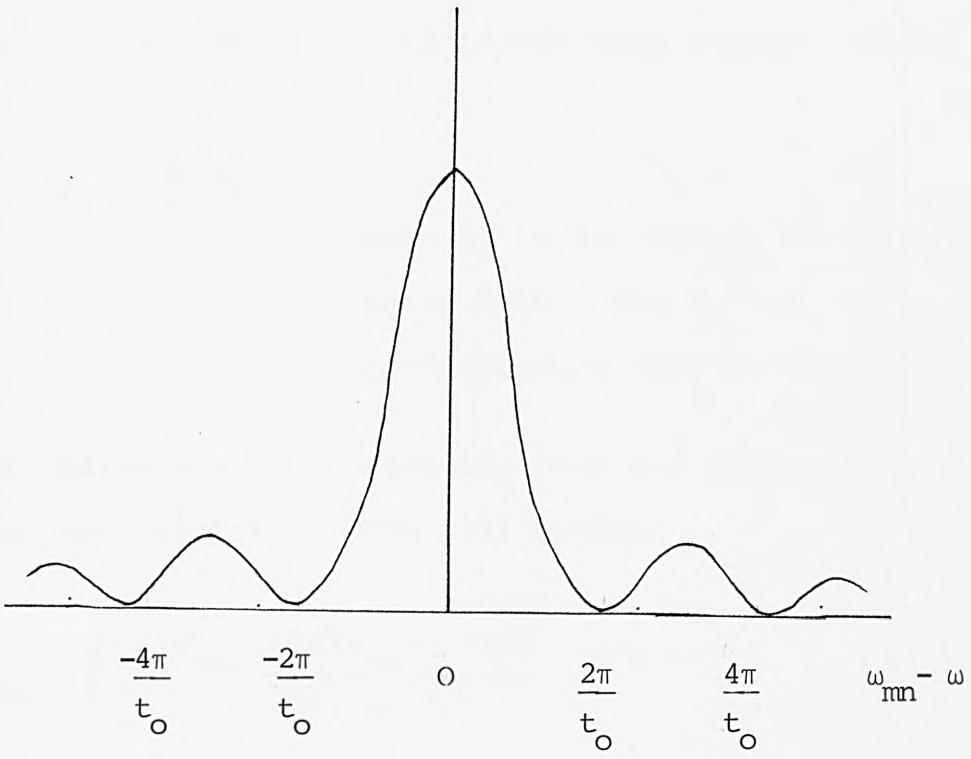

Figure 1. See text, equation 18.

need for conservation of energy inasmuch as there is a large probability for a transition in which $E_m = E^o n + \hbar\omega$ and effectively zero otherwise. Equation (18) just gives the transition probability from one initial state ψn to one final state ψm. The total probability of transition from ψn to all states ψm with energy E_m is found by integrating over all final states of the same energy: Since

$$E_f = \frac{\hbar^2 k_f^2}{2m}$$

when E_f is the energy at the Fermi level, and k_f the corresponding wave vector,

this is equivalent to integrating over all states with the same wave vector. Thus (18) becomes:

$$P_{TOT} = \int \frac{4|W_{mn}|^2 \sin^2(\omega_{mn}-\omega)to/2}{\hbar^2(\omega_{mn}-\omega)^2} \, d^3k \qquad (20)$$

where the integration is over all wave vectors of the Fermi surface at energy E_f (which is the surface of a sphere in reciprocal space of radius k_f).

Changing (20) to an energy integral we substitute

$$d^3k = \rho(e)\, dE_k \qquad (21)$$

where $\rho(E)$ is the density of states, equation (20) becomes:

$$P_{TOT} = 4|W_{mn}|^2 \rho(E) \int \frac{\sin^2(\omega_{mn}-\omega)t/2}{\hbar^2(\omega_{mn}-\omega)^2} \quad dE_k \qquad (22)$$

(having regarded W_{mn} and $\rho(E)$ as sufficiently independent of dE_k to be taken outside the integral sign).

Substituting $(\omega_{mn}-\omega)t/2 = X$

(and $dx = \frac{t}{2\hbar} dE$)

(22) becomes

$$P_{TOT} = 4|W_{nm}|^2 \rho(E) \int \frac{t}{2\hbar} \frac{\sin^2 x}{x^2} \quad dx \qquad (23)$$

$$\text{Thus } P_{TOT} = \frac{2\pi t}{\hbar} |W_{nm}|^2 \rho(E) \delta(E_n^o - E_m - \hbar\omega) \qquad (24)$$

(having made use of the result that

$\int x^{-2} \sin^2 x$ represents a delta function, i.e.

$$\frac{1}{\pi} \int_{-\infty}^{\infty} \frac{\sin^2 x}{x^2} \quad dx = 1)$$

We are interested in a transition probability per unit time, and should therefore strictly take the time derivative of (24) i.e.

$$\frac{d}{dt} (P_{TOT})$$

However in this case it is equivalent to dividing (24) by t. (Since additional terms, omitted from the substitution (16), on being divided by t tend to zero as $t \to +\infty$). Hence the probability of transition per unit time is:

$$W_{if} = \frac{2\pi}{\hbar} \left| W_{nm} \right|^2 \rho(E) \; \delta(E_f - E_i - \hbar\omega) \qquad (25)$$

Which is the golden rule[+] of Perturbation theory.

+(Golden Rule No. 2. E. Fermi, "Nuclear Physics p.142 University of Chicago Press, Chicago 1950).

REFERENCES

1. B.D. Josephson. Phys. Lett. 1, 251 1962

2. P.W. Anderson, J.M. Rowell. Phys. Rev. Lett. 10 (6), 230 1963

3. L. Esaki. Rev. Mod. Phys. 46 (2), 237 1974

4. B.D. Josephson.Rev. Mod. Phys. 46 (2) 251 1974

5. I. Giaever, K. Megerle. Phys. Rev. 122(4)1101 1961

6. I. Giaever. Rev. Mod. Phys. 46 (2), 245 1974

7. R.C. Jaklevic, J. Lambe. Phys. Rev. Lett, 17, 1139 1966

8. M.G. Simonsen, R.V.Coleman. Phys. Rev. B8 1369 1974

9. J.M. Clark, R.V. Coleman, Proc. Nat: Acad. 73,1589 1976

10. A.E.T. Kuiper, J. Medema, J.J.G.M. van Bokhoven, J. Catalysis 29, 40 1973

11. P.K. Hansma, M. Pirikh. Science 188, 1304 1975

12. P.K. Hansma, W. Kaska, R. Laine. J. Am. Chem. Soc. 98, 6064 1976

13. E. Schrödinger. Ann. Phys. (Leipzig) 4 Folge 79 631, 489 1926

14. J. Oppenheimer. Phys. Rev. 31,66 1928

15. R.H. Fowler, L.Nordheim. Proc. Roy. Soc. (London) A119 1973 1928

16. G. Gammow. Z.Physik. 51 204 1928

17. R.W. Gurney, E. Condon. Phys. Rev. 33, 122 1929

18. J. Frenkel. Phys. Rev. 36 , 1604 1930

19. A. Sommerfield, H.A. Bethé "Handbuck der Physik" (S. Flügge ed.) Springer, Berlin 24 150 1930

20. R. Holm, W. Meissner. Z. Phys. 74, 715 1932

21. R. Holm, W. Meissner. Z. Phys. 86, 787 1933

22. A. Braun, G. Busch. Helv. Acta. Phys. 15,571 1942

23. I. Dietrich. Z. Phys. 132, 231 1952

24. I. Dietrich. Z. Phys. 133, 499 1952

25. J.C. Fischer, I. Giaever, J. Appl. Phys. 32, 172 1961

26. A. Goldberg, H.M. Schey, J. Schwartz, Am. J. Phys. 35, 197 1967

27. D.J. Scalapino, S.M. Marcus, Phys. Rev. Lett, 18 (12) 459 1967

28. J. Bardeen, L.N. Cooper, J.R. Schrieffer, Phys. Rev. 106,162 1957

29. J. Bardeen, L.N. Cooper, J.R. Schrieffer Phys. Rev. 108, 175 1957

30. I. Giaever, H.R. Hart, K. Megerle. Phys. Rev. 126 (3), 941 1962

31. W.A. Harrison. Phys. Rev. 123, 85 1961

32. R.C. Jaklevic, J. Lambe. Phys. Rev. 165 (3) 821 1968

33. J. Kirtley, D.J. Scalapino, P.K. Hansma. Phys. Rev. 1314, 3177 1976

34. J. Bardeen. Phys. Rev. Lett. 6 (2), 57 1961

35. M. H. Cohen, L.M. Falicov, J.C. Phillips. Phys. Rev. Lett 8, 316 1962

36. B.D. Josephson. Phys. Lett. 1, 25 1962

37. B.D. Josephson. Adv. Phys. 14, 419 1965

38. J.R. Schrieffer: "Tunneling in Solids" Ed: Burnstein, S. Lundquist, Plenum Press Chapter 21 1969

39. J. Kirtley, P. Soven. Phys. Rev. B19 (4) 1812 1979

40. E.L. Wolf. Rep. Prog. Phys. 41, 1446 1978

41. C.P. Poole Jr. "E.S.R." Interscience, New York, pp.387, 775 1967

42. G.L. Green. Amer. Lab. 7, 15 1975

43. W.R. Patterosn, J.S. Shewman. Rev. Sci. Instr. 35, 1704 1964

44. D.E. Thomas, J.M. Rowell. Rev. Sci. Instr. 36, 1301 1965

45. J.G. Adler, J.E. Jackson. Rev. Sci. Instr. 37, 1094 1966

46. A.F. Hebard, P.W.Shumate. Rev. Sci. Instr. 45, 521. 1974

47. P.K. Hansma. Phys. Lett. C30 (2), 145 1977

48. J. Klein, A. Léger, M. Belin, D. Defourneau: Phys. Rev. B7, 2336 1973

49. R.J. Jennings, J.R. Merrill. J. Phys. Chem. Solids 33, 1261 1972

50. J. Lambe, R.C. Jaklevic. Phys. Rev. 165 (1) 821 1968

51. I. Giaever, K. Megerle. Phys. Rev. 122 (3) 1111 (Appendix 1) 1961

52. J.R. Schrieffer "Single Particle Tunneling into Superconductors" Chapter 21, page 287, of "Tunneling Phenomena in Solids" (Reference 38) 1969

53. I. Giaever, H.R. Hart, M. Megerle. Phys. Rev. 126, 941 1962

54. J. Kirtley "Vibrational Spectroscopies for Adsorbed Species" Eds: A.T. Bell, M.C. Hair. Am. Chem. Soc. Symposium Series No. 137. Chapter 11, (Washington, D.C.) 1980

55. B.O. Field, P.N. Shott, (Sec. 5.1) Spectrochimica Acta 36A, 549 1980

56. B.O. Field, P.N. Shott, (Sec. 5.4) Spectrochimica Acta 36A, 549 1980

57. N.I. Bogatina, I.K. Yanson, B.I. Verkin, A.G. Bartak. Sov. Phys. JETP 38 (6) 1162 1974

58. N.I. Bogatina. Opt. Spectrosc.38 (1). 43 1975

59. J. Klein. A. Léger. Phys. Lett. 28A (2)134 1968

60. J. Kirtley, P.K. Hansma. Surface Sci. 66, 125. 1977

61. T.T. Chen, J.G. Adler, S.S. Commun. 8,1965 1970

62. J.G. Adler. Phys. Lett. 29A, 675 1969

63. J.G. Adler. S.S. Commun. 7, 1635 1969

64. J.M. Rowell, A.G. Cynoweth, J.C. Phillips Phys. Rev. Lett.9 59 1962

65. I.K. Yanson, N.I. Bagotina, B.I. Verkin, O.I. Shklyarevskii. Sov. Phys. JETP 35 (3) 540 1972

66. J.R. Kirtley, P.K. Hansma. Phys. Rev. B12 531 1975

67. H. Spedding, D.H. Whiffen, Proc.Roy.Soc. A238, 245 1956

68. P.E. Cade. J. Chem. Phys. 17, 2390 1967

69. A.E.T. Kuipner, J. Medema, J.J.G.M. van Bokhoven. J. Catalysis 29, 40 1973

70. L.H. Little. "I.R. Spectra of Adsorbed Species". Academic Press 1966

71. H.E. Evans, W.H. Weinberg. J. Chem. Phys. 71,(4), 1537 1979

72. C.S. Korman, J.C. Lan, A.M. Johnson, R.V. Coleman. Phys. Rev. B19 (2), 994 1979

73. A. Léger, J. Klein, M. Belin, D. Defourneau. S.S. Commun. 11, 1331 1972

74. I. Giaever, H.R. Zella. Phys. Rev. Lett. 21 1385 1968

75. G. Burrafato, G. Faraci, G. Giaquinta, N.A. Mancini. Lettere Al Nuovo. Cimento 21,(16),547 1978

76. R. Magno, J.G. Adler, J. Appl. Phys. 49 (11) 5571 1978

77. H. Morawitz. Phys. Rev. 187, 1792 1969

78. S.L. Cunningham, W.H. Weinberg, Appl. Surface Sci. 2, 640 1979

79. R. Magno, J.G. Adler. Rev. Sci. Instr. 52 (2), 217 1981

80. M.F. Mouldoon, R.A. Dragoset, R.V. Coleman. Phys. Rev. B20 (2) 416 1979

81. D.G. Walmsley, I.W.N. McNorris, N.M.D. Brown. S.S. Commun. 16, 663 1975

82. D.G. Walmsley, I.W.N. McNorris, N.M.D. Brown. J. Chem. Soc. Faraday Trans. 2, 77, 337 1981

83. J.D. Langan, P.K. Hansma. Surface Sci. 52, 211 1975

84. C. Kittell "An Introduction to Solid State Physics" 5th Edn. Wiley 1976

85. T.J. Weiting, M. Schlüter (Eds.)"Electrons and Phonons in Layered Crystal Structures". Volume 3 of "Physics and Chemistry of Materials with Layered Structures" Pub. D.Reidel. Holland. 1979

86. S. de Cheveigné, J. Klein, A. Léger, M. Belin, D. Défourneau. Phys. Rev. B15 (2), 750 1976

87. S. de Cheveigné, A. Léger, J. Klein. Proc. 14th Int. Conf. Low Temp. Phys. Otenami, Finland V3. North Holland (Pub) 1975

88. A. Léger. Thesis: "Spectroscopie Par Effet Tunnel Inelastique". Université de Paris. 1971

89. G. Lewicki, C.A. Mead. Phys. Rev. Lett. 16, 939 1966

90. L. Esaki, P.J. Stiles, S. von Molnar. Phys. Rev. Lett 19, 852 1967

91. M. McColl, C.A. Mead. Trans. Met. Soc. AIME 233,502 1965

92. I.K. Yanson, N.I. Bogatina. Sov. Phys. JETP 32, 823 1971

93. McBride, G. Rochin, P. Hansma. J. Appl. Phys. 45, 2304 1974

94. R.C. Jaklevic, J. Lambe, Bull. Am. Phys. Soc. 14, 43 1969

95. D.C. Tsui, R.E.Dietz, L.R. Walker. Phys. Rev. Lett. 27 (25) 1792 1971

96. R.M. Handy. Phys. Rev. 126,1968 1962

97. A. Isin, J.E. Christopher, R.V. Coleman. J. Appl. Phys. 39, 704 1968

98. C. Nanney. Phys. Rev. Lett. 16, 313 1966

99. J.M. Rowell, L.Y.L. Shen. Phys. Rev. Lett. 17, 13 1966

100. A.F.G. Wyatt. Phys. Rev. Lett. 13, 401 1964

101. C.B. Duke. "Tunneling Phenomena in Solids" = Solid State Physics Supplement Number 10. Academic Press 1969

102. A. Adane, A.Fanconet, J. Klein, A. Léger, M. Bélin, D. Défourneau. S.S. Commun. 16, 1071 1975

103. W.R. Patterson, J. Shervan. Rev. Sci. Instr. 35 (12) 1704 1964

104. A.F. Hebard, P.W. Shumate Rev. Sci. Instr. 45 (4) 529 1974

105. J.L. Paterson, R.L. Caili, M.V. Moody, Rev. Sci. Instr. 50 (7) 903 1979

106. P.N. Shott. Thesis : The City University, London. 1979

107. Ortec Brookdeal. 9503 precision lock-in amplifier Instruction Manual. 1976

108. W. Gaede. Annln. Phys. 41, 337 1913

109. W. Becker, W. Nesseldrher Vacuum. 26 (7) 227 1976

110. W. Becker Vacuum 16(11) 625 1967

111. J. Henning Vacuum 28(10/11) 391 1978

112. "Turbomolecular pumps and Accessories" Balzers. P.M.800 035 PE 7910

113. H. Brove, A van Hengten. Vaccum 21(1/2) December 1970

114. "Turbomolecular Pumps" TPH 5000" Balzers Product Information P.M.800 004 RE

115. M. Pirani . Verk at. Phys. Ges. 8, 686 1906

116. F.M. Penning Physica, Eindhoven 4, 71 1937

117. Technical Data Sheet: Edwards' Fine Control Needle Valve M08636/31 1971
(Edwards High Vacuum, Manor Royal, Crawley, W. Sussex)

118. Tunneling Phenomena in Solids. Ed. E. Burnstein, S. Lundqvist. Plenum Press 1969

119. M.G. Simonsen, R.V. Coleman. Nature 244, 218 1973

120. M.G. Simonsen, R.V. Coleman. Phys. Rev. B8, 1369 1973

121. P.K. Hansma, R.V. Coleman. Science. 184 1369 1974

122. M.G. Simonsen, R.V. Coleman, P.K. Hansma. J. Chem. Phys. 61,3789 1974

123. Y. Skarlatos, R.C.Barker, G.L. Haller, A. Yelon. Surface Science 43, 353 1974

124. R.C. Jaklevic, M.R. Gaerttner. Appl. Surface Sci. 1, 479 1978

125. M.K. Konkin, J.G. Adler. Appl. Phys. Lett. 32,(7) 436 1978

126. = Reference 84, Page 54.

127. T.J. Coutts "Electrical Conduction in Thin Metal Films". Pub. Elsevier Chapter 8,1974

128. = Reference 84, page 586

129. Y. Skarlatos, R.C. Barker, A. Yelon. J. Appl. Phys. 47 (10) 4593 1976

130. D.R. Biggs. Project Report, Chemistry Department, The City University, London 1981

131. A. Léger, B. Delman, J. Klein, S.de Cheveigné. Revue de Physique Appliquée, 11, 304 1976

132. S. Reynolds, L.D. Gregson, C.C. Horley, D.P. Oxley, R.G. Pritchard. Surface and Interface Analysis 2, (6) 217 1980

133. S. Colley, P.K. Hansma, Rev. Sci. Instr. 48 (9) 1129 1977

134. K.W. Hipps, Ursula Mazur. J. Phys. Chem. 84, 3162 1980

135. A.B. Dargis. Rev. Sci. Instr. 52 (1) 46 1981

136. Roger Matthews Document E2. Honeywell/Pet Interface. University College of Wales, Aberystwyth, Computer Unit. 13th May 1981

137. P. Sigston. Project Report. Chemistry Department, The City University, London, June 1982

138. C.La.Lau, R.G. Snyder. Spectrochima Acta 27A, 2073 1971

139. Herzfeld, Ingold, Poole. J. Chem. Soc. (I), 222 1946

140. J.R. Scherer. Spectrochim Acta. 23A, 1489 1967

141. J.R. Scherer. Spectrochim Acta. 20, 345 1964

142. S.J. Daunt, H.F. Shurvell. Spectrochim Acta. 32A, 1545 1976

143. M.Ito, T, Shigeoka. Spectrochim Acta 22, 1043 1966

144. M. Moskovits, D.P. DiLella. J. Chem. Phys. 73,(12) 6068 1980

145. N.S. Gill, R.S. Nyholm. J. Inorg. Nucl. Chem. 18, 88 1961

146. N.Holonyak, D.L. Keune, R.D. Burnham, C.B. Duke. Phys. Rev. Lett. 24(11), 589 1970

147. I. Giaever, H.R. Zeller. Phys. Rev. Lett. 21(19) 1385 1968

148. C.B. Duke, G.G. Kleiman. 10th Proc. Int. Conf. Semiconductors. Otenami, Finland. Page 856 1970

149. A.M. Andrews, H.W. Korb, N. Holonak, C.B. Duke. Phys. Rev. B5(6), 2273 1972

150. I. Giaever. Phys. Rev. Lett. 20(23), 1286, 1968

151. J.C. Tsang, J.R. Kirtley. Solid State Communications 30 617 1979

152. J.C. Tsang, J.R. Kirtley, J.A. Bradley. Phys. Rev. Lett. 43(11), 772 1979

153. T.E. Feuchtwang. Phys. Rev. B20(2), 430 1979

154. C.B. Duke, G.G. Kleiman, T.E. Stakelon. Phys. Rev. B6(6), 2389 1972

155. G. Jona-Lasino, F. Martinelli, E. Scoppola. Commun. Math. Phys. 80, 223 1981

156. T.E. Feuchtwang. Page 129 "Inelastic Electron Tunnelling Spectroscopy". See Bibliography. 1978

157. T.E. Feuchtwang. Int. J. Quantum Chemistry: Quantum Chemistry Symposium 11, 607 1977

158. P.K. Hansma, J. Kirtley. Acc. Chem. Res. 11, 440 1978

159. D.P. Oxley, A.J. Bowles, C.C. Horley, A.J. Langley, R.G. Pritchard, D.L. Tunnicliffe. Surface and Interface Analysis 2(1), 31. (Figure 6) 1980

160. A.J. Kemp."Deconvolution". Research Memorandum Phys. Dept. City University, London. 1(October 1974

161. J.E.B. Ponsonby. Mon. Roy. Astr. Soc. 163, 369 1973

162. W.T. Cochran, J.W. Cooley, D.L. Savin, H.D. Helms R.A. Kaenel, W.L. Lang, G.C. Maling Jr., D.E. Nelson C.M. Reader, P.D. Welch. Audio and Electroacoustics AU - 15(2), 45 1967

163. K.R. Betty, G. Horlick. Appl. Spectrosc. 30(1), 23 1976

164. J.W. Brault, O.R. White. Astron.and Astrophys. 13, 169, 1971

165. Kazuo Nakamoto. "Infrared and Raman Spectra of Inorganic and Coordination Compounds." 3rd Edition. Wiley. 1978

Bibliography

The Principles of Quantum Mechanics 4th Edn. P.A.M. Dirac . (Oxford University Press) 1965

Quantum Mechanis Vol. 3. L.D. Landau, E.M. Lifshitz Pergamon. 1977.

Elements of Quantum Mechanicswith Chemical Applications. Jean Barriol. Plenum Press. 1962

Inelastic Electron Tunneling Spectroscopy. Springer Series and Solid-State Sciences. Vol. 4. Ed. T. Wolfram. Springer Verlag 1978.

Tunnelling Phenomena in Solids. Ed. E. Burnstein, S. Lundquist. Plenum Press 1969.

Tunneling in Solids. Solid State Physics Supplement 10. C.B. Duke (Academic Press 1969).

Solid State Physics Volume 30 1975. Eds. H. Ehrenreich, F. Seitz, D. Turnbull. (Academic Press).

Solid State Physcis Volume 11 1974. Ed. R.V. Coleman. (Academic Press).

Structure and Bonding Volume 38; Adsorbed Monolayers on Solid Surfaces. G.A. Somorjai, M.A. van Hove. Springer Verlag 1979.

Introduction To Ligand Field Theory. C.J. Ballhausen, McGraw-Hill 1962.

Chemical Applications of Group Theory. F.A. Cotton. (Wiley) 1971.

Introduction to Solid State Physics 5th Edn. C. Kittel. (Wiley) 1976.

The Architecture of Small Computer Systems. A.G. Lippiat (Prentice-Hall) 1978.

Infra Red Spectra and Characteristic Frequencies. F.F. Bentley, L.D. Smithson, A.L. Rozek. (Interscience) 1968.

Infra-red Spectra of Inorganic Compounds, R.A. Nyquist, R.O. Kagel. (Academic Press) 1971.

Deconvolution of Absorption Spectra. W.E. Blass, G.W. Halsey (Academic Press) 1981.

Spectroscopic References to Polyatomic Molecules. Verma Plenum Press 1981.

Computers for Spectroscopists. Edited by Carrington, Hilger. 1981.